



<https://theses.gla.ac.uk/>

Theses Digitisation:

<https://www.gla.ac.uk/myglasgow/research/enlighten/theses/digitisation/>

This is a digitised version of the original print thesis.

Copyright and moral rights for this work are retained by the author

A copy can be downloaded for personal non-commercial research or study,  
without prior permission or charge

This work cannot be reproduced or quoted extensively from without first  
obtaining permission in writing from the author

The content must not be changed in any way or sold commercially in any  
format or medium without the formal permission of the author

When referring to this work, full bibliographic details including the author,  
title, awarding institution and date of the thesis must be given

Enlighten: Theses

<https://theses.gla.ac.uk/>  
[research-enlighten@glasgow.ac.uk](mailto:research-enlighten@glasgow.ac.uk)

**GEOMETRICAL ANALYSIS AND RECTIFICATION  
OF THERMAL INFRARED VIDEO FRAME SCANNER  
IMAGERY AND ITS POTENTIAL APPLICATIONS  
TO TOPOGRAPHIC MAPPING**

**BY**

**AHMED MOHAMED AMIN**

**B.Sc., M.Sc**

**A Thesis Submitted for The Degree of  
Doctor of Philosophy (Ph.D.)**

**UNIVERSITY OF GLASGOW**

**October 1986**

ProQuest Number: 10995513

All rights reserved

INFORMATION TO ALL USERS

The quality of this reproduction is dependent upon the quality of the copy submitted.

In the unlikely event that the author did not send a complete manuscript and there are missing pages, these will be noted. Also, if material had to be removed, a note will indicate the deletion.



ProQuest 10995513

Published by ProQuest LLC (2018). Copyright of the Dissertation is held by the Author.

All rights reserved.

This work is protected against unauthorized copying under Title 17, United States Code  
Microform Edition © ProQuest LLC.

ProQuest LLC.  
789 East Eisenhower Parkway  
P.O. Box 1346  
Ann Arbor, MI 48106 – 1346

## ACKNOWLEDGMENTS

The author wishes to express his sincere gratitude to his supervisor, Professor G. Petrie, for suggesting this research topic and for his continuous advice and supervision throughout the period over which this research work was carried out. Indeed without his continuous help, this project would have never come to its present form.

The author also acknowledges the freedom granted by the two heads of the department, Professor I. B. Thompson and Professor J. Tivy, to use the facilities available in the department.

The help received from the Topographic Science staff members is gratefully acknowledged, in particular that from Mr. B.D.F. Methley and Mr. D.A. Tait.

Sincere thanks are also due to the following individuals and organisations;-

Barr & Stroud Limited (Glasgow) for providing their IR-18 MK II frame scanner for the aerial flying test and for the calibration tests. In particular, the very full collaboration of Mr. K. Boyle in supplying the necessary information about the scanner, and Mr. G. Sutherland for helping with the practical test as scanner operator were of great assistance to the author.

Dr. W. H. Ekin of Robert Gordon's Institute of Technology, Aberdeen, for flying the aerial test imagery together with Mr. S. Allan (navigator).

The National Engineering Laboratory (NEL) in East Kilbride for allowing the author to use its Ferranti monocomparator for the target plate calibration. The help of Mr. A. Nemo is gratefully acknowledged.

The Rank Pullin Controls, Rank Taylor Hobson, and AGA companies for allowing the author to use their thermal frame scanners for the geometrical calibration work.

The Environmental Remote Sensing Application Centre (ERSAC) for the use of their GEMS digital image processing system during the preliminary work to form the three-dimensional video model. In particular, Dr. C. Stove and Dr. N. Hubbard were extremely helpful.

The Remote Sensing Unit of the Macaulay Institute for Soil Research, Aberdeen for the use of their GEMS image processing

system for the actual formation of the three-dimensional video model. In particular, the full cooperation and help received from Mr. D. Miller is acknowledged with especial thanks.

The Audio-Visual Department of the University of Glasgow for assisting with some of the technical aspects of video, especially Mr. I. Long and Mr. B. Barrie.

The Chief Technician, Mr. I. Gerrard and his assistant, Mr. L. Hill, for their assistance in photographing some of the figures used in this thesis.

The Overseas Research Scheme (ORS) for their three consecutive awards which helped in reducing the required University fees to a home student level.

The Ministry of Higher Education in Egypt and the Suez Canal University for their financial support during the period of carrying out this research work.

# CONTENTS

	Page
1. Introduction .....	1
2. Video Technology .....	6
2.1 Introduction .....	7
2.2 Video Cameras .....	7
2.2.1 The Vidicon Tube .....	10
2.2.2 The Orthicon Tube .....	11
2.2.3 The Plumbicon Tube .....	11
2.2.4 The Return Beam Vidicon Tube .....	11
2.2.5 Colour Cameras .....	11
2.2.6 Standard Broadcast Television Systems....	12
2.2.7 Other Video Imaging Devices .....	14
2.3 Video Recording .....	14
2.3.1 U-matic VTR .....	15
2.3.2 VHS, Betamax, and Video 2000 VTR Systems..	16
2.3.3 Video Discs .....	16
2.4 Video Displays .....	17
2.4.1 Monochrome Displays .....	17
2.4.2 Colour Displays .....	18
2.4.3 Computer Graphics Displays .....	19
2.4.3.1 Raster-Driven Displays .....	20
2.4.3.2 Vector-Driven Displays .....	22
2.5 Video Frame Buffers .....	24
2.5.1 Black and White Frame Buffers .....	24
2.5.2 Colour Frame Buffers .....	25
2.5.3 Frame Buffer Resolution .....	27
2.6 Summary .....	28
3. Remote Sensing in the Optical Region of the Electromagnetic Spectrum .....	29
3.1 The Electromagnetic Spectrum .....	30
3.1.1 The Photographic Region of the EM spectrum .....	31
3.1.2 The Infrared Region of the EM Spectrum...	31
3.1.2.1 Basic Laws of Infrared Radiation.	31
3.1.2.2 Emissivity .....	33
3.1.2.3 Infrared Radiation from the Terrain .....	34
3.1.3 EM Spectrum and the Atmosphere .....	35

3.2	Detection and Recording of EM Radiation .....	35
3.2.1	Photography .....	36
3.2.2	Passive Scanning Systems .....	38
3.2.2.1	Optical-Mechanical Line Scanners.	38
3.2.2.2	Multispectral Line Scanners.....	40
3.2.2.3	Frame Scanners .....	41
3.3	Imaging Devices Employing Solid State Arrays ..	41
3.3.1	Imaging Devices Using Linear Arrays .....	41
3.3.2	Imaging Devices Using Areal Arrays .....	42
3.4	Detectors .....	43
3.4.1	Thermal Detectors .....	44
3.4.2	Quantum Detectors .....	44
3.4.3	Detector Cooling .....	45
<b>4.</b>	<b>Thermal Video Frame Scanners .....</b>	<b>46</b>
4.1	Basic Design of Thermal Video Frame Scanner..	47
4.1.1	The Telescope .....	47
4.1.1.1	Optical Materials .....	49
4.1.2	Scanning /Detector Configuration .....	51
4.1.2.1	Single Element Scanning .....	51
4.1.2.2	Serial Scanning .....	52
4.1.2.3	Parallel Scanning .....	52
4.1.2.4	Serial/Parallel Scanning.....	53
4.1.2.5	The SPRITE Detector .....	53
4.1.3	Scanning Mechanism .....	54
4.1.3.1	The Oscillating Plane Mirror ..	54
4.1.3.2	The Rotating Reflective Polygon	54
4.1.3.3	The Rotating Refractive Polygon	55
4.1.4	Radiometric Characteristics of Frame Scanners .....	55
4.2	The Modular Approach to Video Frame Scanner Design and Construction .....	56
4.2.1	UK Common Modules .....	57
4.3	Commercially Available Thermal Video Frame Scanners .....	58
4.3.1	AGA Thermovision.....	59
4.3.2	Inframatrix IRTV .....	60
4.3.3	Barr & Stroud IR-18 MKII Thermal Imager.	62
4.3.4	Rank Pullin Controls Thermal Imager ....	64
4.3.5	GEC Avionics/Rank Taylor Hobson TICM II.	65
<b>5.</b>	<b>Geometrical Analysis of Video Compatible Frame Scanner Imagery .....</b>	<b>67</b>
5.1	Introduction .....	68

5.2	Geometry of the Photogrammetric Frame Camera ..	69
5.3	Geometrical Characteristics of the Panoramic Frame Camera .....	70
5.4	Geometry of Vidicon Tube Camera Imagery .....	72
5.5	Geometry of Line Scanner Imagery .....	73
5.6	Geometrical Analysis of Video-Compatible Frame Scanner Imagery .....	74
5.6.1	Scanning Technique of the IR-18 Frame Scanner .....	75
5.6.2	Video Image Characteristics .....	77
5.6.3	Ground Resolution .....	78
5.6.4	The Effect of Ground Speed, Flying Altitude, and Field Scan Time on the Image Geometry .....	80
5.6.5	Effect of Scanning Technique .....	85
<b>6.</b>	<b>Calibration of Thermal Video Frame Scanners- Theoretical Basis and Actual Procedures .....</b>	<b>88</b>
6.1	Introduction .....	89
6.1.1	Calibration of Photographic Frame Camera. 6.1.1.1 The Multicollimator Method .....	89
	6.1.1.2 The Goniometer Method .....	92
	6.1.1.3 The Reseau Plate Method .....	93
6.1.2	Calibration of the Vidicon Tube Camera ..	93
6.1.3	Calibration of Thermal Video Frame Scanners .....	94
6.2	Design of the Target Plate .....	95
6.2.1	Manufacture of the Target Plate .....	96
6.2.2	Calibration of The Target Plate .....	98
6.3	Calibration Procedures Used for Each of the Frame Scanners .....	101
6.3.1	Calibration of Barr & Stroud IR-18 MKII Frame Scanner .....	101
6.3.2	Calibration of Rank Pullin Controls (RPC) Thermal Imager .....	102
6.3.3	Calibration of GEC Avionics/ Rank Taylor Hobson TICM II Frame Scanner .....	103
6.3.4	Calibration of AGA Thermovision .....	103
6.4	Video Image Coordinate Measurements .....	103
<b>7.</b>	<b>Results and Analysis of the Calibration of Video Frame Scanners .....</b>	<b>110</b>



7.1	Coordinate Transformation .....	111
7.1.1	Linear Conformal Transformation .....	111
7.1.2	Polynomial Transformation .....	112
7.1.2.1	Affine Transformation .....	113
7.1.2.2	Bilinear Transformation .....	113
7.1.2.3	Biquadratic Transformation .....	114
7.1.2.4	Bicubic Transformation .....	114
7.1.3	The Computer Programs .....	114
7.2	Systematic and Random Distortion .....	115
7.3	Determination of the Calibrated Focal Length (CFL) and the Principal Point Coordinates .....	117
7.4	Results and Analysis from the Barr & Stroud IR-18 Frame Scanner Calibration .....	117
7.5	Results and Analysis from the Rank Pullin Controls Frame Scanner Calibration .....	123
7.6	Results and Analysis from the TICM II Frame Scanner Calibration .....	126
7.7	Results and Analysis from the AGA Thermovision Frame Scanner Calibration .....	128
7.8	Overall Analysis .....	130
7.9	Systematic and Random Distortion .....	133
<b>8.</b>	<b>Analytical Photogrammetric Techniques Applied to Airborne Frame Scanner Imagery .....</b>	<b>134</b>
8.1	Introduction .....	135
8.1.1	Lack of Knowledge of Interior Orientation Elements .....	135
8.2	Formation of the Stereomodel .....	136
8.2.1	Characteristics of the Stereopair .....	137
8.3	Image Coordinate Refinements .....	139
8.3.1	Correction for the Imaging System Distortion .....	139
8.3.2	Correction for the Image Motion During the Field Scan Time .....	140
8.4	Possible Analytical Approaches .....	141
8.4.1	Space Resection/Intersection .....	141
8.4.2	Relative and Absolute Orientation .....	141
8.5	Space Resection/Intersection .....	142
8.5.1	Space Resection .....	143

8.5.1.1	Collinearity Condition for the Photogrammetric Frame Camera . . . .	143
8.5.1.2	Collinearity Condition for the Panoramic Frame Camera . . . . .	144
8.5.1.3	Collinearity Condition for the Optical-Mechanical Line Scanner. . .	146
8.5.1.4	Collinearity Condition for Frame Scanner Imagery. . . . .	147
8.5.2	Space Resection with Additional Parameters . . . . .	149
8.5.3	Space Resection Point by Point . . . . .	150
8.5.4	Space Intersection . . . . .	153
<b>9.</b>	<b>The Practical Test- Planning and Excuting the Flight Mission Using the IR-18 Frame Scanner. . . . .</b>	<b>155</b>
9.1	Introduction . . . . .	156
9.2	Diurnal Temperature Variations . . . . .	156
9.3	Ground Coverage and Ground Resolution . . . . .	158
9.4	Flight Planning for the Practical Test Using the Barr & Stroud IR-18 Frame Scanner . . . . .	159
9.4.1	The Test Areas . . . . .	159
9.4.1.1	Queenslie and Garrowhill Test Area . . . . .	159
9.4.1.2	Douglas Water Test Area . . . . .	160
9.4.1.3	Hunterston Test Area . . . . .	161
9.4.2	Preparing for the Flight Mission . . . . .	163
9.4.2.1	The Cessna 172 Aircraft . . . . .	163
9.4.2.2	The Mounting Rig . . . . .	164
9.4.2.3	The IR-18 Frame Scanner and Accessories . . . . .	165
9.4.2.4	The Crew . . . . .	166
9.4.2.5	Details of the Flight Mission . . .	166
9.5	Evaluation of the Flight Mission . . . . .	167
<b>10.</b>	<b>The Geometric Test- Provision Of the Control- Results and Analysis . . . . .</b>	<b>171</b>
10.1	Introduction . . . . .	172
10.1.1	Test Procedure . . . . .	172
10.2	Provision of the Control Points For the Geometric Test . . . . .	172
10.2.1	Video Image Coordinate Measurements . . .	174
10.2.2	Ground Coordinate Measurements. . . . .	174

10.3	Data Processing .....	175
10.4	Results and Analysis of the Geometric Test ...	177
10.4.1	Results from the Use of the Conventional Space Resection/Intersection Technique..	178
10.4.2	Results from the Use of Space Resection/ Intersection with Additional Parameters	179
10.4.3	Results from the Use of the Point-by- Point Space Resection/Intersection Technique .....	180
10.5	Overall Analysis .....	182
10.5.1	ISP Standard Test .....	182
10.5.2	IR-18 Test .....	184
10.5.3	Accuracy of Parallax Measurements.....	185
10.6	Conclusion .....	186
<b>11.</b>	<b>Interpretation of Thermal Frame Scanner Video Images for Topographic Mapping.....</b>	<b>187</b>
11.1	Introduction .....	188
11.2	Factors Affecting Interpretability of Thermal Images .....	189
11.2.1	Geometric and Radiometric Characteristics of the Scanning System.	189
11.2.2	Environmental Factors Affecting the Thermal Images .....	190
11.2.3	Thermal Characteristics of the Recorded Objects .....	190
11.2.4	The Video Monitor .....	191
11.3	Elements of Thermal Image Interpretation .....	191
11.4	Interpretation of Thermal Imagery for Topographic Mapping Purposes .....	193
11.5	Interpretation of the Thermal Video Images Covering the Hunterston Area .....	194
11.5.1	Man-Made Features .....	194
11.5.2	Hydrological Features.....	196
11.5.3	Vegetational Features .....	198
11.6	Interpretation of the Thermal Video Images Covering the Douglas Water Area .....	198
11.7	Interpretation of the Thermal Video Images Covering the Queenslie-Garrowhill Area .....	200
11.8	Conclusion .....	200

<b>12. Digital Geometric Rectification of Frame Scanner Imagery</b> .....	202
12.1 Introduction .....	203
12.2 Digitization of the Video Images .....	202
12.2.1 Digital Image Reduction and Enlargement	204
12.3 Digital Geometric Rectification .....	205
12.3.1 Analytical Rectification .....	205
12.3.1.1 Correction for the Effect of the Spherical Image Surface ..	206
12.3.1.2 Digital Correction for Scanner Attitude and Change of Attitude During the Image Scan Time ...	208
12.3.1.3 Correction for the Scanner Distortion Determined During the Calibration Process .....	209
12.3.1.4 Digital Correction for Image Motion During the Field Scan Time .....	210
12.3.2 Assignment of Digital Brightness Values	210
12.4 Resampling Methods .....	211
12.4.1 Nearest Neighbour Interpolation .....	212
12.4.2 Bilinear Interpolation .....	213
12.4.3 Bicubic Interpolation .....	214
12.5 Description of the Digital Rectification Process Carried out for the Video Frame Scanner Imagery .....	215
12.5.1 Computer Processing of the Digital Images .....	215
<b>13. Three Dimensional Video Viewing Using Airborne Video Frame Scanner Imagery</b> .....	218
13.1 Methods of Achieving Stereo-video Viewing....	219
13.2 Actual Implemented Procedure .....	225
13.2.1 The GEMS Image Processing System .....	226
13.2.2 Stereo-video Viewing Using the GEMS System .....	227
13.3 Flexibility and Limitations .....	229
13.4 Photographs of the Stereo-Model .....	230
<b>14. Conclusions and Recommendations</b> .....	233
14.1 General Conclusions .....	234

14.2 Assesment of The Video Technique .....	237
14.3 Recommendations for Future Work .....	238
14.4 A Final Note .....	239
<b>Bibliography .....</b>	<b>241</b>
<b>Appendix A The Computer Programs .....</b>	<b>247</b>
<b>Appendix B Vector Plots of Residual Errors from the Calibration of Thermal Video Frame Scanners.</b>	<b>305</b>
<b>Appendix C Vector Plots of Residual Errors from the Geometric Test .....</b>	<b>326</b>

## SUMMARY

This thesis is concerned with an investigation into the possibilities of generating metric information and carrying out topographic mapping operations from thermal frame scanner video images. The main aspects discussed within the context of this thesis are:-

- (i) the construction and operational characteristics of video frame scanners;
- (ii) the geometry of frame scanners;
- (iii) geometric calibration of thermal video frame scanners;
- (iv) the devising, construction and integration of a video-based monocomparator for video image coordinate measurements;
- (v) devising and implementing suitable analytical photogrammetric techniques to be applied to frame scanner imagery;
- (vi) the use of such frame scanners to acquire airborne video images for a pre-selected test area;
- (vii) the interpretation of thermal video frame scanners for topographic mapping;
- (viii) digital rectification of frame scanner imagery; and
- (ix) creation of a three-dimensional stereo model on a video monitor screen using the digitally rectified video images.

## CHAPTER I

### INTRODUCTION

## CHAPTER I

### INTRODUCTION

This thesis is concerned with an investigation of the possibilities of generating metric information and carrying out topographic mapping operations from video images acquired with a thermal frame scanner.

For mapping applications, photogrammetric cameras are commonly used. These cameras utilise photographic film and are designed, constructed and calibrated specifically to produce an image with a precisely known geometry. The interior orientation elements (i.e. the principal distance, the location of the principal point and the lens distortion characteristics) of each individual camera are determined with very high accuracy. An intra-lens shutter that allows simultaneous exposure of all image points is invariably used. In addition, most mapping cameras are designed to provide a favourable base-to-height ratio for accurate height determination. In fact, aerial photography has established itself as a very powerful and versatile tool for mapping purposes. Its high image resolution, geometric fidelity and stereoscopic analysis capabilities cannot be matched at this time by other remote sensing systems.

By contrast, thermal video frame scanners have been developed primarily for military purposes. The elements of inner orientation are not precisely known or determined. Instead, the foremost requirements are reliability and excellent image quality using a part of the electromagnetic spectrum (the thermal infrared) which permits day and night operation producing a video image in real time. Considerations of geometric fidelity are secondary and more attention is given to the radiometric side- in particular, the ability of the scanner to resolve small variations in temperature within the object field.

Taking an overall view, thermal video frame scanners have some interesting and even unique features such as:-

- (i) Their operation in the thermal part of the electromagnetic spectrum allows them to be used for day or night data acquisition.
- (ii) An enormous amount of data can be collected during the limited time of an aerial mission as a result of the high cycling rate of the scanner (usually 25 or 30 frames per second).



- (iii) Real-time viewing of the scanner images can be carried out during the aerial flight mission using an on-board video monitor.
- (iv) The recording and display of the acquired images is easily carried out using a video tape recorder.
- (v) On return from the flying mission, an immediate playback of the acquired images can be carried out for image review and assessment.
- (vi) The possibility exists for rapid image digitization and computer analysis.
- (vii) Video measuring and analysis equipment is available off the shelf at comparatively inexpensive prices.

Arising from these various factors, currently an increasing number of users have been considering the potential of thermal video based scanner systems to remote sensing applications. However, as far as the present author is aware, no serious attempt has been made to investigate the potential of these systems in the field of mapping. In order to carry out such a study, the procedures which are commonly used during the analysis and measurements of photogrammetric camera images must be applied to the video frame scanner images. These are:-

- (i) a geometrical analysis of the image generation technique;
- (ii) sensor calibration to determine the interior orientation parameters; and
- (iii) devising and using suitable analytical techniques for mapping purposes.

As will be seen later, the characteristics of video frame scanner images are so different to those of photographic film images, that a completely new set of techniques had to be devised to allow the thermal frame scanner images to be analysed geometrically and used for mapping purposes. These constitute the major part of the research work reported in this thesis.

It must also be emphasised in this introduction that the present project is not concerned with an in-depth analysis of the characteristics of the electronic circuits associated with image scanning and image generation, nor in the physics of the detector itself. Instead, the main interest will be in the geometry of the image generated by the scanner. However, whenever necessary, a simple explanation of the electronics and physics terminology as used within the text of this thesis is given within the limits of the author's background in these two fields.

The work reported in this thesis is organised along the following lines:-

Since the output from the frame scanner is an analogue video signal, and since one of the objectives of this project is to explore the use of an all-video imaging/measuring system, it was necessary to devote a complete introductory chapter (II) to review the current state-of-the-art in video technology under three major headings- video imaging, video recording and video display. Chapter III is concerned with remote sensing in the optical part of the electromagnetic spectrum with particular emphasis on the image acquisition systems operating in the thermal infrared region. This review opens the way to a detailed discussion of the design, construction and operational characteristics of the thermal video frame scanner itself in Chapter IV. The thesis then proceeds (in Chapter V) to a detailed analysis of the geometry of frame scanner imagery. The various types of distortion introduced to the image as a result of the scanning geometry are thoroughly investigated and set forth in this Chapter.

It will be seen in Chapter VI that the familiar calibration techniques commonly used with photogrammetric frame cameras and vidicon tube cameras cannot be used to calibrate thermal video frame scanners. In this Chapter, the method which has been devised and used specifically for the calibration of such a device is described. This leads to Chapter VII in which the mathematical procedures which have been used to establish the magnitude and pattern of distortion in the thermal video image are discussed, and the results of the calibration of several frame scanners are presented and analysed.

Analytical photogrammetric techniques which have been devised or adapted by the author for use with video frame scanner images with a view to establishing the potentials of these scanners in the field of topographic mapping are derived and explained in Chapter VIII. To establish the potential of these analytical techniques, an experimental test had to be carried out. The flight planning for the airborne thermal video imaging, the description of the actual flight mission and the evaluation of the flight test imagery are all described in Chapter IX. This aerial mission provided the required image data for the test. The provision of the control points from the single video images and the results of the application of the devised analytical techniques are presented and analysed in Chapter X. Chapter XI is devoted to an analysis of the factors which influence the interpretation of thermal video images for topographic mapping applications and to the results of some practical tests carried out by the author. Different factors which are likely to affect the appearance of various ground features in thermal video imagery are discussed, the elements of thermal image interpretation are presented and the results of the

interpretation of the video images which have been acquired specifically for the purposes of the interpretation is given.

One of the recently developed possibilities for the interpretation and measurement of remotely sensed data is that of three-dimensional video viewing. To implement this possibility, two overlapping frame scanner images were rectified digitally and then overlaid to produce a three dimensional video model. Chapter XII describes the digital rectification of the frame scanner imagery, while Chapter XIII describes and evaluates the different methods which can be used to generate a three-dimensional video model. The actual procedure which has been adopted in the present project using the facilities of the GEMS image processing system is also described.

Finally, the closing Chapter (XIV) summarises the conclusions reached through this work and makes recommendations for future research work.

## CHAPTER II

### VIDEO TECHNOLOGY

## CHAPTER II

### VIDEO TECHNOLOGY

#### 2.1 Introduction

In general conversation or in the popular press, the term "video" is considered to be equivalent to the word "television (TV)". However, originally video had a narrower meaning in that it was used in connection with the circuits and signals which deal with the picture information generated within a television system. It is still used in this sense in the specialist technical literature dealing with such circuits and signals even today. However, nowadays while the term television tends to be used in the specific context of transmission and reception of picture signals broadcast using radiowaves, "video" is often used to cover the broader uses of television techniques. Thus one reads of "video cameras" used in security surveillance systems and industrial monitoring, and "video recording" as used in the recording of broadcast or closed circuit television ( CCTV) systems.

Using the term in the last sense, a video system has three main parts: a video camera, a video tape recorder(VTR), and a video monitor, which function in the following way:-

- (i) the video camera picks up an image;
- (ii) the image is recorded on magnetic tape on the video tape recorder (VTR); and
- (iii) the video monitor can display on its screen the recorded image when it is played back from the VTR.

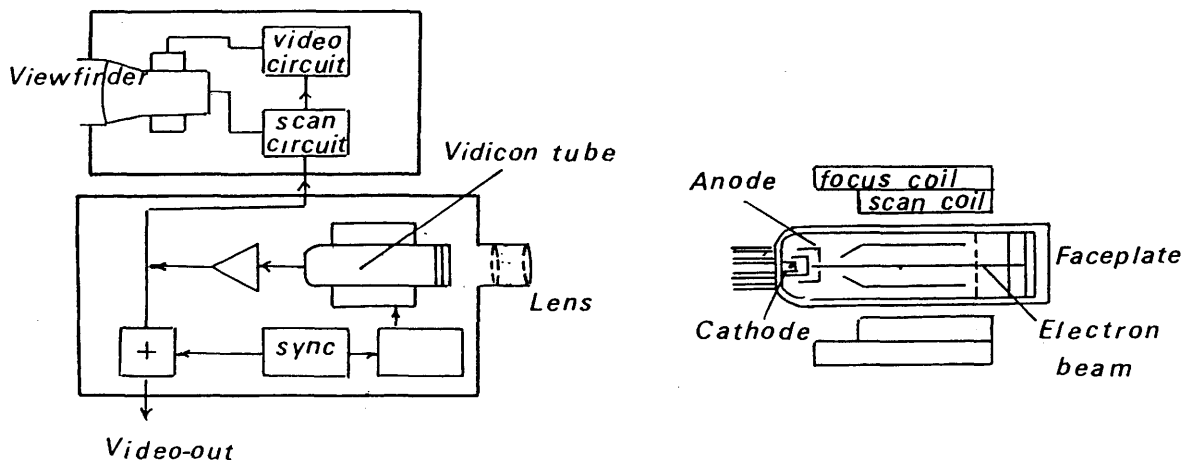
In this Chapter, the three main aspects of video imaging, recording and display are discussed in some detail. This will establish a useful background for the various aspects of video technology and terminology which are frequently discussed and used throughout the present thesis.

#### 2.2 Video Cameras

Optically, a video camera is similar to a film camera except that a light sensitive target takes the place of the photographic film. Fig.2-1a shows a schematic diagram of the construction of a video camera. The target together with its associated optical system and viewfinder are the principal components in a video camera. The target forms a part of a

scanning tube on which an optical image is focussed by the camera lens. This image is then sub-divided into picture elements (pixels) and scanned pixel by pixel in a certain order by an electron beam generated by the camera tube.

Fig.2-1b shows a cross section of a video camera tube. It consists of an evacuated glass tube of cylindrical form with the light sensitive target at one end and an electron gun at the other. The electron beam is generated by heating up a barium oxide coated cathode which emits a stream of electrons which are then accelerated along the tube in the direction of the target plate by a highly positive anode.



a) Main parts of the video camera

b) Cross-section of the camera vidicon tube

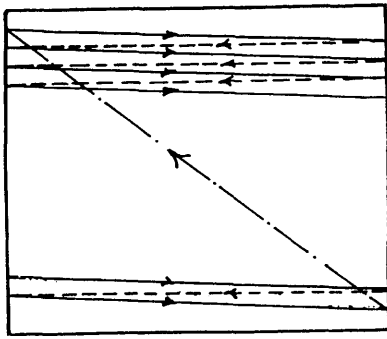
Fig.2-1 Construction of the video camera

Focussing and scanning coils are mounted around the glass tube to control the movement of the electron beam across the target plate.

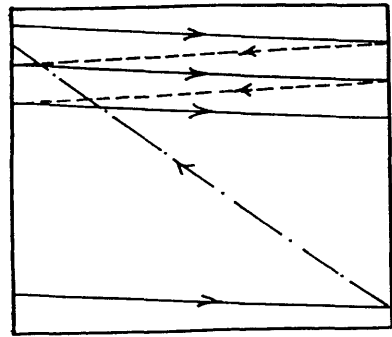
There are two methods by which the electron beam scans the image on the target plate of the camera tube:

- (i) non-interlaced scanning; and
- (ii) interlaced scanning

which are illustrated in Fig.2-2 below.



(a) Non-interlaced



(b) Interlaced

Fig.2-2 Image scanning by the camera vidicon tube

(i) Non-Interlaced Scanning:-

In this method, (Fig.2-2a), the electron beam of the camera tube moves with constant velocity along the standard straight line from left to right. As it reaches the right edge of the frame, it is stopped and blacked out while it re-traces its path from right to left to the starting position of the next line (i.e. at the left hand edge) which is contiguous to the starting point of the line just scanned. This process is repeated line after line until the beam has scanned the whole target plate. When it reaches the end of the frame, it is again blacked out while it retraces its path back to the start of the next frame.

(ii) Interlaced Scanning:-

In this type of scanning, (Fig.2-2b), basically the beam moves in the same manner as in non-interlaced scanning. However it scans first of all the odd numbered lines sequentially and then flies back to scan all the even numbered lines. Thus, every frame is divided into two interlaced fields. The first contains all the odd numbered lines and the second, all the even numbered lines. Such an arrangement is termed double interlaced scanning in the technical literature concerned with video technology.

Other methods of interlacing are also possible. For example, in the triple interlaced scanning, lines 1,4,7,.. would be scanned first in Field One, lines 2,5,8,.. would be scanned in Field Two, and finally, lines 3,6,9,.. would be scanned in Field Three.

The number of frames scanned per second is known as the frame frequency. While the number of lines scanned per second is referred to as the line frequency.

The electronic circuits associated with the video camera add a synchronising (sync) signal to the video signal. This is used to control the electron beam of the displaying monitor so that it moves in the same pattern as the scanning beam of the camera tube. These signals are added to the row video signal to form what is called a composite video signal

There are many different types of video camera tube ,some of which are listed below:

Iconoscope	Permachom
Orthicon	Plumbicon
Iscon	Silicon Charge Storage
Vidicon	Solid State Vidicon
Return Beam Vidicon (RBV)	

Of these, the most important are the vidicon, orthicon, plumbicon and the return beam vidicon.

### 2.2.1 The Vidicon Tube

The vidicon is the most commonly used tube in video cameras. The image of the scene is focussed on the target plate of the camera tube which is made of photoconductive material. The light falling on the target plate will cause the charges generated on the plate to vary in intensity in a direct relationship to the areas of light and shade in the object. Thus the plate will in effect carry a map of electrode charges corresponding to the picture seen by the lens. The brighter the image area, the higher the positive charge on the target. The charge pattern on the target plate is scanned systematically by the electron beam as described above in Section 2-2. When the electron beam strikes the target at any point, the positive charge at that point is discharged by the negative charge of the electrons hitting it. The greater the charge at any point, the more electrons are absorbed by it. The electrons which pass through the target plate fall on a signal plate and are used to generate a signal whose intensity varies directly with the intensity of light in the original picture. This signal is passed to the video circuitry which transforms it into a form suitable for the broadcasting, recording or display of the image.

The resolution of the vidicon tube is determined by the effective cross-section of the scanning beam when it touches the target plate. The average resolution of the vidicon tube is 1,000 TV lines . The main disadvantage of the vidicon tube is its relatively low sensitivity in terms of the range of brightness or intensities which can be described.



### 2.2.2 The Orthicon Tube

The image orthicon was the most widely used camera tube before the advent of the vidicon. The principle of the image orthicon is similar to that of the vidicon except that the target is made of a partially transparent photocathode on which the visual scene is imaged by the camera optics. The target then emits electrons of the same intensity pattern as that contained in the original image. An electron beam then scans the target in the same way as the vidicon to produce the video signal. The image orthicon has a better sensitivity to light than the vidicon, but its resolution is limited to 500 TV lines per frame.

### 2.2.3 The Plumbicon Tube

The plumbicon is identical in its construction to the vidicon in the operation of the electron gun and the target plate. However, instead of the photoconductive target, it uses a photosensitive layer of lead oxide. This type of tube is much more sensitive to light than the vidicon type. It is often used in the design of colour cameras used in professional broadcast studios.

### 2.2.4 The Return Beam Vidicon Tube

The Return Beam Vidicon (RBV) is a slightly modified version of the vidicon tube. The electron beam of the RBV scans the image on the target face plate in the same manner as with the vidicon tube, but is then reflected back into a photo-multiplier where it is amplified and used to produce the video signal. The cross-section of the scanning beam of the RBV is very small resulting in a very high resolution image (from 4,000 to 5,000 TV lines per frame). Television cameras equipped with RBV tubes have been used on board three LANDSAT satellites

### 2.2.5 Colour Cameras

The basic colour video camera used by professional broadcasting organisations utilises three separate vidicon tubes with colour filters in front of each, so that each one responds only to radiation in the Red, Green, or Blue (R, G, or B) windows of the visible spectrum. A diagram of the three tube camera is shown in Fig.2-3. While some video cameras may record directly the separate R G B signals, others will record the image in terms of its luminance (Y) and chrominance (C). A luminance signal (Y) which represents the overall brightness of the object element is generated by combining the intensities of the R, G and B components in

their correct proportions. At the same time, R-Y and B-Y colour signals are used to form a chrominance (C) signal which represents the colour of the object element.

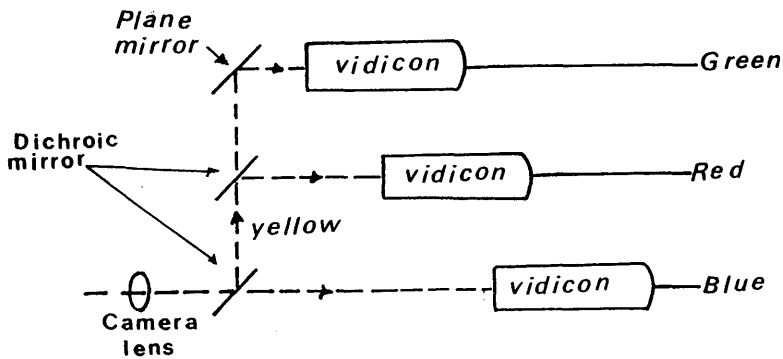


Fig.2-3 A three tube colour video camera

Most home video cameras use a simpler system having either one or two camera tubes. In the two-tube type of camera, the light from the lens is split equally between the two tubes. One tube is used to provide the luminance signal (Y), while the other is a special tube which has a striped colour filter bonded to the front of its target and consists of a series of narrow vertical stripes which alternately pass red or blue light. As the scanning beam passes over the target, the video output switches alternately between the red and blue signals and these are separated out by the camera electronics to produce the R and B output signals. The G video signal is generated by combining the R, B and Y signals.

In a single tube camera, the filter of the tube has alternating R, G and B filter stripes. The target is divided into vertical stripes grouped into three sets corresponding to the filter stripes. In effect the tube has three interlaced targets, each with its own colour filter. Three separate connections are brought out from the tube to give the three colour output signals from which the luminance and chrominance signals are generated.

### 2.2.6 Standard Broadcast Television Systems

As mentioned above, the colour video signal can be represented by the three colour primaries R, G and B, from which the luminance and chrominance signals are derived. The process of forming the luminance and chrominance signals is referred to as encoding. These two signals are modulated into a vision carrier and transmitted together. At the colour receiver, these combined signals are separated out again and are decoded into their individual R, G and B values which are applied to the colour display. The colour receiver and display could consist of a combination of three cathode ray

tubes (CRTs) viewed by a system of mirrors, but much more probably it will consist of a single CRT which can display all three colour primaries at once as will be explained later in Section 2.4.2.

There are three standard broadcast television systems:

- (i) Phase Alternation Line (PAL).
- (ii) National Television System Committee (NTSC).
- (iii) SEquential Colour And Memory (SECAM).

The PAL system has been adopted in most of the European countries, the NTSC standard has been adopted in the United States, Canada and Japan, while the SECAM system is used in France, the USSR and certain countries in the Middle East.

The main differences between the three systems occur during the signal modulation process which is used for transmitting the colouring signal. Another difference lies in their television format which is described by their line and frame frequencies. The format and specification of each of the three systems are shown below in Table 2-1.

System	PAL	NTSC	SECAM
Specifications			
Frame frequency (Hz)	25	30	25
Field frequency (Hz)	50	60	50
No. of Lines/frame	625	525	819
No. of active lines/frame	575	497	737
Line frequency (Hz)	15,625	15,750	20,475
No. of pixels/line	767	663	982
Line scan time ( $\mu$ s)	64.0	63.5	48.8

Table 2-1 Format specifications of the standard broadcast television systems

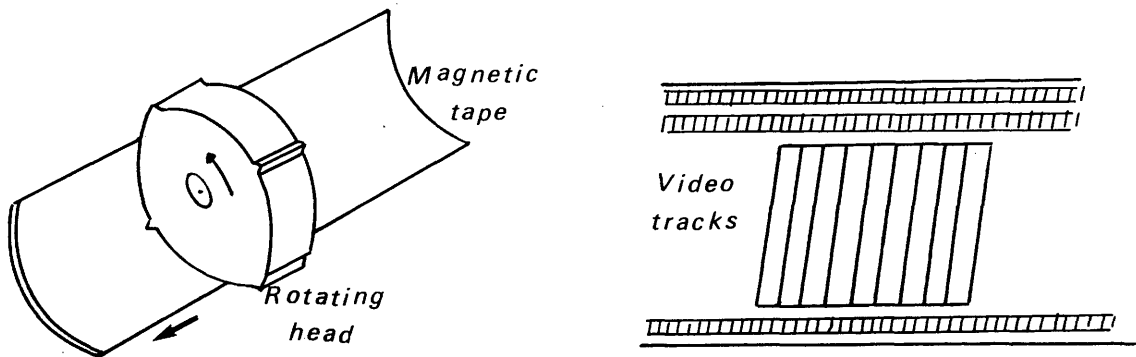
### 2.2.7 Other Video Imaging Devices:-

There are some other video imaging devices which do not use imaging tubes. Among them are those employing Charge Coupled Device (CCD) technology in which the vidicon tube is replaced by a large number of discrete electronic cells (diodes) mounted on an integrated circuit board. The cells are arranged in horizontal rows, one row for each scan line. Each cell in a row deals with one picture element (pixel) in the line. The cells of the CCD array and the complete sensor unit could be made smaller than the target of the vidicon tube. Another type of video imaging device is the video frame scanner which will be discussed in Chapter IV.

### 2.3 Video Recording

The video signal generated by a video camera may also be stored on a video tape using a Video Tape Recorder (VTR). The principle of operation of the video tape recorder is similar to that of the audio tape recorder where the audio tape is passed over a recording head which changes the pattern of the magnetism on the tape. There are two main techniques which are commonly used to write the video information on the video tape- Quadruplex Broadcast Standard and the helical scan.

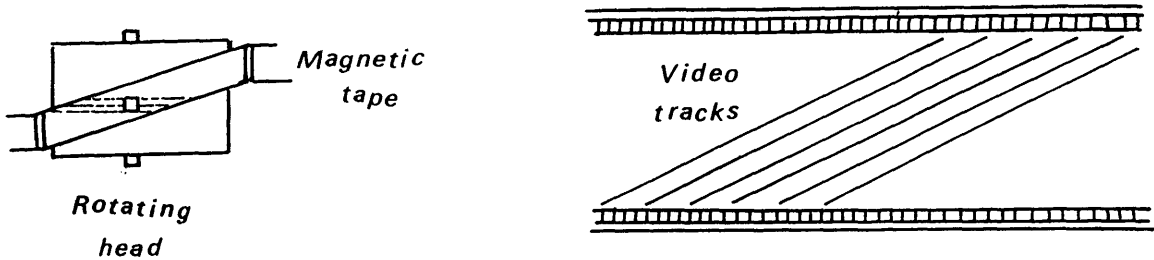
The Quadruplex Broadcast Standard uses a two-inch wide tape running over a head wheel carrying four recording heads mounted at 90° intervals around the wheel as shown in Fig.2-4a. As the head wheel rotates, each recording head writes a transverse track across the width of the tape. As the tape moves past the wheel, the successive head tracks are laid down side by side as shown in Fig.2-4b. This method is used only in professional broadcasting.



a) Recording head

b) Layout of tracks on the tape

Fig.2-4 The Quadruplex recording format



a) Recording head

b) Layout of tracks on the tape

Fig.2-5 The helical scan format

On the other hand, the Helical Scanning is used in almost all other video systems. In this method, two heads are mounted  $180^\circ$  apart on a rotating drum assembly as shown in Fig.2-5a. The tape is wrapped around the drum in a spiral path so that each head contacts the tape in turn for half a revolution of the drum. As a result, each head traces out a diagonal track across the tape as shown in Fig.2-5b.

Currently there are four main VTR systems using the helical scan technique. These are:-

- (i) U-matic , which is a professional system;
- (ii) Video Home System (VHS);
- (iii) Betamax;and
- (iv) Video 2000.

The last three are mainly for domestic use though they may also be found in industrial applications.

### 2.3.1 U-matic VTR

The U-matic machines are designed for industrial and professional use. They use  $3/4$ " (19 mm) wide magnetic tape and run at a writing speed of 8.54 m/sec which is faster than that of the other domestic systems. The dimensions of the U-matic cassettes are 219x138x31 mm. The dimensions of the

specific machine used in this project are 646x 425x 226 mm which is about twice the size of the biggest domestic system. Nevertheless, in terms of professional usage, U-matic recorders are regarded as being small, mobile, cheap, easy to use, and give good picture quality. Throughout the different stages of the present project, this type of video tape recorder has been used for image recording and playback.

### 2.3.2 VHS, Betamax and Video 2000 VTR Systems

These three systems are designed for home video use. All use 1/2" (12.5 mm) wide tape, but the cassettes used with such systems are each different in size. Betamax is the smallest, while the other two have the same size. In a VHS machine, the writing speed is 4.85 m/sec, in Betamax it is 6.6 m/sec, and in Video 2000 the speed is 5 m/sec. The three systems give similar picture quality but the formats are quite different so that the tape recorded on one system will not playback on machines of the other systems, since the layout of the video tracks across the tape is different.

### 2.3.3 Video Discs

A video disc consists of a plastic disc some 20 to 30 cm in diameter, on each side of which is a spiral track of grooves which carry the video information in much the same manner as a video tape. When inserted into a suitable player, the disc is rotated and a pick-up device follows the spiral track and detects the information to produce the video signal. Video information on a video disc is pre-recorded and the discs are pressed from a master. Thus they cannot be used to record an image from a video camera directly in the manner possible with a video tape recorder (VTR).

The information on a video disc is recorded using one or another of two main techniques. The first, uses capacitance variations between the disc tracks and a pick up stylus to read the video information. The tracks may be made as grooves in the disc in which case the system is called Capacitance Electronic Disc (CED). This was developed by RCA (Radio Corporation of America) and is known commercially as Selectavision. Alternatively, groovless tracks may be used to store the video information. This is known as Video High Density (VHD) which was developed by JVC (Japan Video Corporation).

The other system which was developed principally by Philips makes use of an optical system, where video signals are stored as a pattern of tiny shallow pits which are generated along the surface of the spiral track of the video disc. A helium neon laser is used to produce a very sharply focussed spot of light which is made to follow the spiral path of the signal track. The pits in the track cause variations in the

reflected light from the surface of the disc and these are picked up by a photocell and amplified to produce the video signal. These latter systems, which are sold mainly by Philips and Pioneer, are known commercially as Laservision disc players.

## 2.4 Video Displays

The video signal generated by the video camera or played back from a VTR or video disk player is fed through a cable to the display unit which is usually a video monitor or a domestic television receiver. Unlike broadcast television receivers, most video monitors are designed to run from a direct video input, e.g. from a video camera, a VTR or a home computer. Video monitors cannot tune to different channels nor can they play back sound like television receivers. On the other hand, the picture tube of the video display monitor is designed to give a smaller spot size and more accurate focussing over the whole screen, hence giving better resolution and a steadier picture. Also video monitors are not limited to the format and resolution of broadcast television systems. However, it should be observed that some of the newer designs of television receiver have a particular channel allocated specifically to receive video signals from a direct input, e.g. from a video camera, VTR or home computer, so that they can also act as video monitors.

### 2.4.1 Monochrome Displays

The main component of the monochrome video display monitor is a monochrome Cathode Ray Tube (CRT) shown in Fig.2-6. The body of the glass tube consists of a narrow cylindrical neck which flares out into a cone to end in a slightly curved glass face plate on which the picture is displayed. The air in the tube is evacuated and the tube itself is sealed to leave a vacuum inside. In the neck of the tube is an electron gun assembly similar to that of the camera tube explained in Section 2.2 above. A grid electrode mounted in front of the cathode is used to control the intensity of the beam and hence the brightness of the spot on the screen. Two anodes are used to focus the electron beam on the back of the screen. In addition, four deflection coils or plates are mounted around the neck of the tube to provide deflection fields. Two of these deflect the beam in the up and down directions, while the other two deflect the beam left and right. The electrons are focussed and impact on a phosphor material which covers the inside of the faceplate and forms the actual screen on which the picture is produced. When struck by the beam of electrons, the phosphor glows to produce a spot of light, the brightness of which depends on the intensity of the beam. To build up a complete image or picture, the electron beam must be scanned over the screen in a series of horizontal lines in the same way that the image of the original scene was scanned by the camera tube.

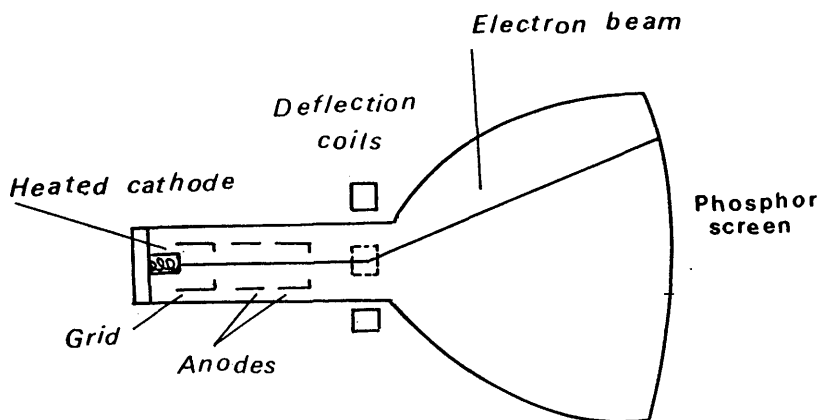


Fig.2-6 Construction of the monochrome CRT

The monochrome picture produced on the monitor screen usually consists of different shades or intensities of green or white on a black background, but black lines and text on a white background are also produced on certain high-quality monitors and an amber phosphor is also used in certain other types of monochrome monitors.

#### 2.4.2 Colour Displays

Colour monitors may have a composite colour video input or separate Red, Green, and Blue inputs. The most commonly employed display technology utilises a single tube with three electron guns, one for each of the three basic colours. These are mounted in the neck of the tube in a triangular lay-out in such a manner that their beams converge on the single phosphor-coated screen. The composite video signal received by the monitor is decoded into its three colour components and sync pulses by the video monitor electronics and each of the three colour components is used to drive the Red, Green or Blue gun as appropriate.

Instead of the normal monochrome phosphor coating, the whole screen is covered by an array of tiny Red, Green, and Blue phosphor dots which are arranged in groups of three, each group arranged in a triangular pattern to match the layout of the electron guns. Between the screen and the guns is a steel shadow mask, which contains a pattern of tiny holes, one for each group of dots on the screen. The holes on the mask are aligned relative to the dots on the screen and to the layout of the electron guns so that the beam from the red gun passing through a hole in the mask will fall on a red dot on the screen, while the green and blue beams passing through the same hole will hit only green and blue dots respectively as shown in Fig.2-7.



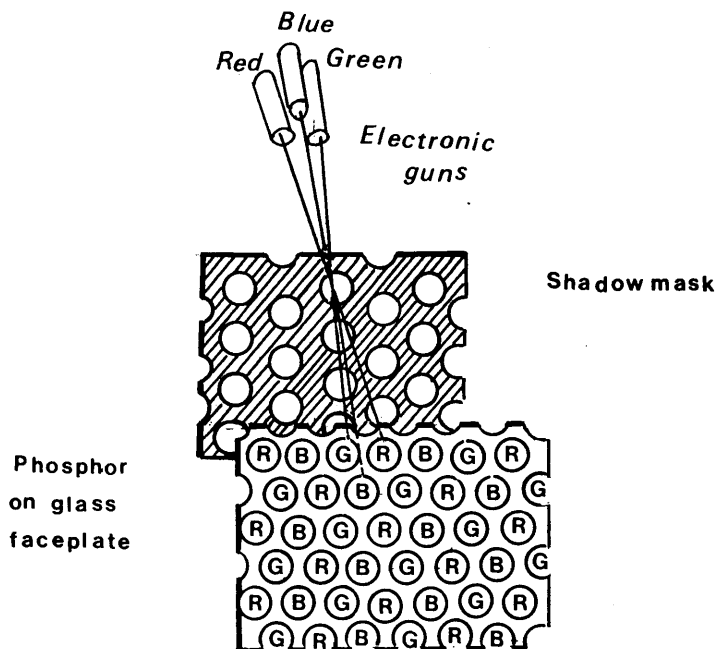


Fig.2-7 The shadow mask of the colour video monitor

When the video signal is applied for a specific position on the screen, the electrons from the red gun will produce a red spot image on the screen, while the green and blue guns will produce green and blue images respectively, which are adjacent to the red one. Since the three dots are very tiny and close to one another, a person observing them is unable to resolve the individual dots and his eye will merge the three images together to form a composite colour image at that position.

#### 2.4.3 Computer Graphics Displays

So far, the discussion in this chapter has been concerned only with the video images generated by video cameras and displayed on a video monitor. However, there are other cases where the images are represented digitally in a computer memory and are displayed on a video display monitor or computer terminal. An example of these is the computer simulation of pictures which create images of objects entirely mathematically. Another example is the image data from spacecraft and satellites which is recorded directly on to Computer Compatible Tapes (CCTs) which are read by a computer and then displayed on a video monitor. In the present project, some video images were digitized and stored in computer memory for processing. These have been displayed on a video monitor using an image processing system as will be explained later on.

In practice, there are two types of computer graphics displays- raster-driven, and vector-driven . The difference between them is mainly in how the image data is arranged and written on the video display. A display file in a vector driven device contains only information about the specific points, lines and characters to be drawn on the screen. The void areas of the screen are ignored and variations in the density of the displayed information are usually not possible. On the other hand, the raster-driven display involves the scanning of every dot or pixel on a rectangular matrix which covers the entire screen.

### 2.4.3.1 Raster-Driven Displays

A raster-driven graphics display device can be considered as a matrix of discrete cells, each of which can be made bright or dark. These devices can be divided into two categories:-

- (i) raster refresh displays; and
- (ii) raster storage displays.

#### (i) Raster Refresh Displays:-

These devices, which are essentially similar to the video monitors described above, are the most common type of computer display. As will be apparent, they do not have any inherent storage capabilities. The displayed image must therefore be passed repeatedly to the device at a high enough refresh rate to ensure a continuous image on the screen. The simplest example of these systems is a raster CRT utilizing a frame buffer as shown in the block diagram of Fig.2-8. Different types of frame buffer are discussed later in this chapter.

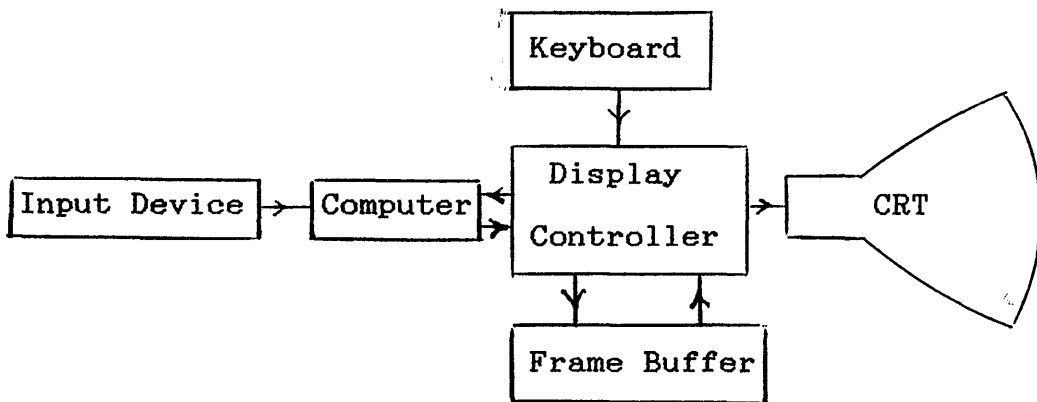


Fig.2-8 Raster refresh displays

Both interlaced and non-interlaced scanning may be encountered. The latter is preferable in terms of preventing flicker, but obviously it requires larger memories or frame buffers to refresh the complete frame at 50 or 60 Hz compared with the former where only each field has to be refreshed at 50 or 60 Hz.

For high resolution raster refresh tubes, the speed of transferring the data from the computer's memory to the display unit must be very high to prevent shaking of the image on the screen. This is done by building a specialized circuit which is designed to transfer data at the full memory speed. This is called Direct Memory Access (DMA).

Another very important point is that each pixel of the raster refresh display can be readily controlled in brightness or intensity in the same manner as described for video monitors. The whole technology is of course so akin to domestic television technology that it benefits greatly in terms of the intensive development and low production costs associated with the very competitive, high volume market for domestic television sets.

**(ii) Raster Storage Displays:-**

These are called matrix addressed storage devices. The best known example is the Plasma Panel. It is a non-CRT display device on which images can be written on the display surface point by point. It consists of two sheets of glass with thin, closely spaced, electrodes attached to the inner faces and covered with a dielectric material as shown in Fig. 2-9. The two sheets of glass are spaced a few microns apart and the intervening space is filled with a neon-based gas and sealed. By applying voltages between the electrodes, the gas between the panels is made to behave as if it were divided into tiny cells, each one independent of its neighbour. A cell is made to glow by placing a firing voltage across it. The gas between the cells is discharged and this develops very rapidly into a glow. Each cell on the screen can be individually turned on or off using a controller which responds to the signals received from the computer. Once turned on, the signal remains lit until turned off.

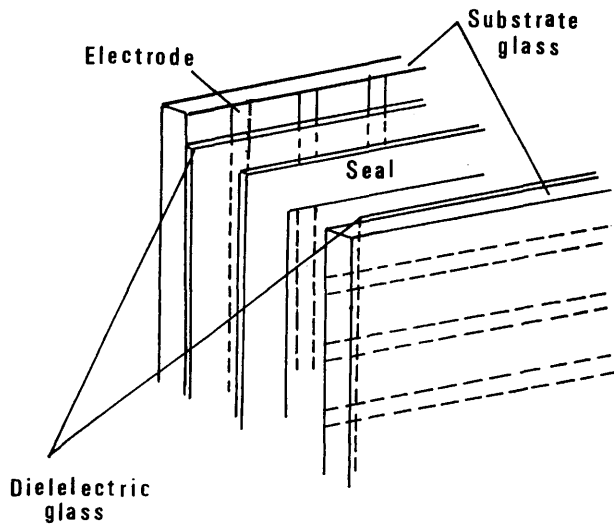


Fig.2-9 The Plasma Panel

The Plasma Panel produces a steady picture, totally free of flicker and is a less bulky device than a CRT of comparable screen size. Its main disadvantages are its poor resolution and its complex addressing or writing requirements. However, the Magnaxox Orion is a well known display device of this type which has been used as the basis of a computer terminal. Recently, the technology has also been adopted in high quality portable computers such as the Grid Compass and the Ericsson Portable computers to give high intensity displays superior to these using the more common Liquid Crystal Display (LCD) technology normally employed in such computers.

#### 2.4.3.2 Vector-Driven Displays

Vector-driven display systems draw and display pictures or graphic images by connecting specified line end points by a series of small lines or vectors. They are used in engineering applications and are excellent in displaying high resolution monochrome images of line drawings. Again these devices can be classified into two categories:-

- (i) vector refresh displays;and
- (ii) vector storage displays.

##### (i) Vector Refresh Displays:-

The vector refresh or calligraphic refresh tube is a CRT with a very short persistence phosphor. The picture is drawn on the CRT by a large number of tiny vectors refreshed at 40 to 50 Hz. The image is refreshed by using a controller to convert the computer's output

signals into deflection voltages to control the writing beam of the CRT. The image stored in the computer's memory may contain as many as 25,000 vectors, each of which must be passed to the controller during the 1/40 or 1/50 sec available for image display. This can be achieved by efficient access to the computer's memory by using a wide data path such as a DMA between the computer's memory and the controller.

(ii) **Vector Storage Displays:-**

An example of this type is the Direct Viewing Storage Tube (DVST), which is a CRT with a long persistence phosphor. The picture has to be drawn only once and then stays displayed without the need to be refreshed for at least one hour. In addition to the normal writing electron gun, the storage tube has flood guns as shown in Fig.2-10.

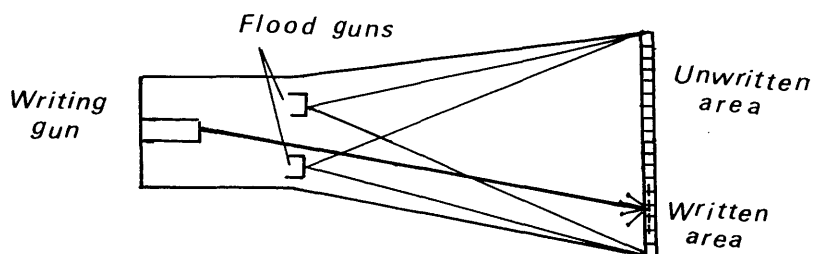


Fig.2-10 The direct viewing storage tube

These guns constantly emit low velocity electrons over the whole screen area. These electrons are too slow to dislodge electrons on unwritten areas and as a result, these areas merely collect electrons until they are made negative and can attract no more current. The written areas, being positively charged, attract flood electrons at such a velocity that sufficient secondary electrons are dislodged so that the phosphor target is held positive and continues to attract electrons. Thus the phosphor stays glowing. An example of the DVST is the well-known Tektronix 4010 series of computer display terminals.

The DVST is somewhat inferior to the refresh CRT in that only a single level of intensity can be displayed, and only green phosphor screens are available. On the other hand, very high resolution can be obtained (up to 4,000 X 4,000 lines), so it has had widespread use in the surveying and mapping industry.

In the present project, the aerial images were collected by an optical-mechanical type of scanner whose output is a video compatible signal. From the above discussion, it will be apparent that the only applicable method of display is the

raster refresh type with the capability of generating variable intensities or brightness values.

## 2.5 Video Frame Buffers

Most refresh displays, whether of the raster or vector types, incorporate a large digital memory or frame buffers to store the video information required to continually refresh the image displayed on the screen. Different kinds of memory have been used as frame buffers such as drums, disks, integrated circuits, shift registers, and core store. Nowadays, most frame buffers comprise Random Access Memories (RAM) implemented in integrated circuit technology.

The frame buffer accepts and stores data from the computer in a digital form while the CRT is an analogue device which accepts only analogue video signals. Thus conversion of the signal from its digital representation to an analogue representation must take place when the information is read from the frame buffer so that it can be displayed on the CRT. This is accomplished by a digital to analogue (D/A) converter which is fitted to the output end of the frame buffer.

### 2.5.1 Black and White Frame Buffers

The basic black and white frame buffer has one memory bit allocated for each location or pixel in the raster video image. Thus the overall memory dedicated to the display of the image or graphics is called a bit plane. If the resolution of the display is 512 X 512 pixels, it means that  $512 \times 512 = 262,144$  bits need to be stored or addressed in a single bit plane of memory. A single bit memory of this type can only control the spot at a specific location on the screen to be either on or off. So it is only suitable for the display of dots, lines or symbols, but not tonal images which require changes in the intensity or brightness at each position or location on the screen. The variation in the intensity levels can be achieved by using more bit planes as shown in Fig.2-11 below.

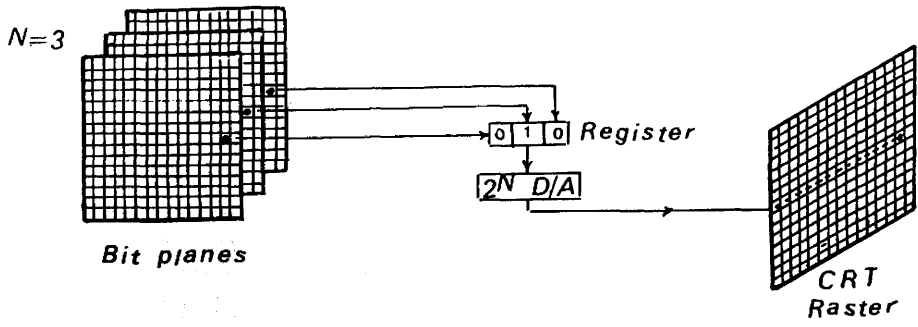


Fig.2-11 Black and white frame buffer

If N bit planes are used, the intensity of each pixel on the CRT is controlled by the corresponding pixel location in each of the N bit planes. The binary values in each of the N bit planes are loaded into their corresponding positions in a register and summed. The resulting binary number is interpreted as an intensity level between zero and  $2^N$  i.e. there are  $2^N$  intensity levels achieved with N bit planes. In Fig.2-11, three bit planes could be used to give eight ( $2^3 = 8$ ) intensity levels. Typically, eight bit planes giving  $2^8 = 256$  variations in intensity at each pixel addressed on the display might be employed to represent the tonal images obtained by an airborne or spaceborne imaging device.

In the present project, colour video imagery has not been acquired in flight since the thermal video frame scanner is essentially a monochrome device. Nevertheless, colour video displays have been used during the subsequent digital image processing carried out in this project. Thus a short account of the basic considerations relevant to this part of the project is also necessary in this introduction to video technology.

### 2.5.2 Colour Frame Buffers

A simple frame buffer to control a colour display can be implemented with three bit planes, one for each primary colour to give eight possible different colours. A diagram of such a simple colour frame buffer is shown in Fig.2-12.

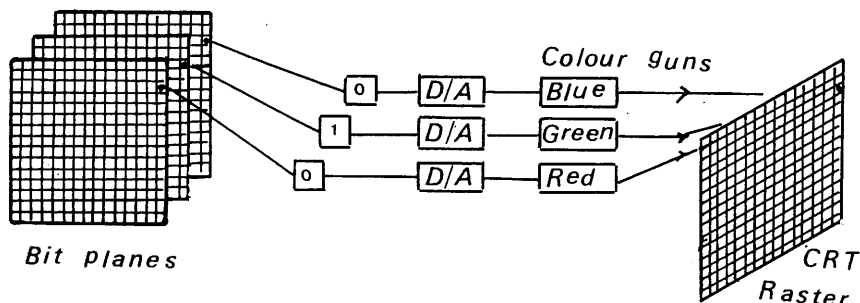


Fig.2-12 Colour frame buffer

Additional bit planes could be used for each of the three primary colours. Fig.2-13 shows a diagram for a colour frame buffer with multiple bit planes. In this case, eight bit planes per colour were used, each group of eight bit planes for a specific colour (Red, Green or Blue) giving 256 shades of that particular colour. In theory, a total of 16,177,216 ( $(2^8)^3 = 2^{24}$ ) possible colour shades could be produced. This is termed a full colour frame buffer.

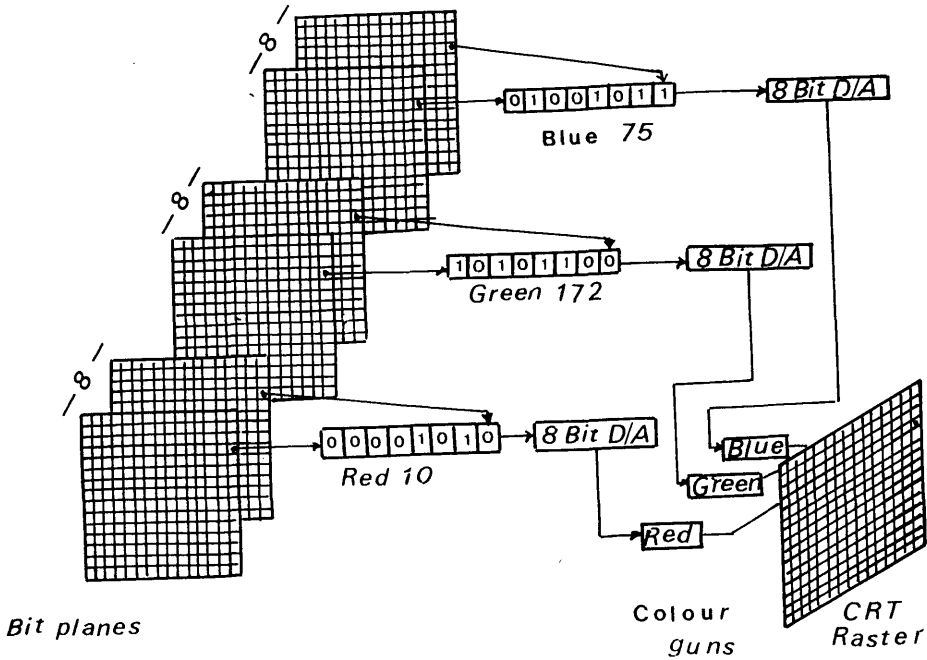


Fig.2-13 Full colour frame buffer

The full colour frame buffer can be further expanded by using the groups of bit planes as indices to colour look-up-tables. This is shown schematically in Fig.2-14. For  $N$ -bit planes per colour, and  $W$ -bit wide look-up-tables,  $(2^3)^N$  colours from a palette of  $(2^3)^W$  possible colours can be shown at any time. For example, for a 24-bit planes ( $N=8$ ) frame buffer, with three 10-bit wide look-up-tables ( $W=10$ ),  $2^{24} = 16,777,216$  colours from a palette of  $2^{30} = 1,073,741,824$  colours can be obtained.

Obviously, the approach of using 24 individual bit plane memories is an expensive item for a display device and even in these days of cheaper memories, many colour graphic terminals employ a smaller number of bit planes with a consequent reduction in the number of distinguishable colours.



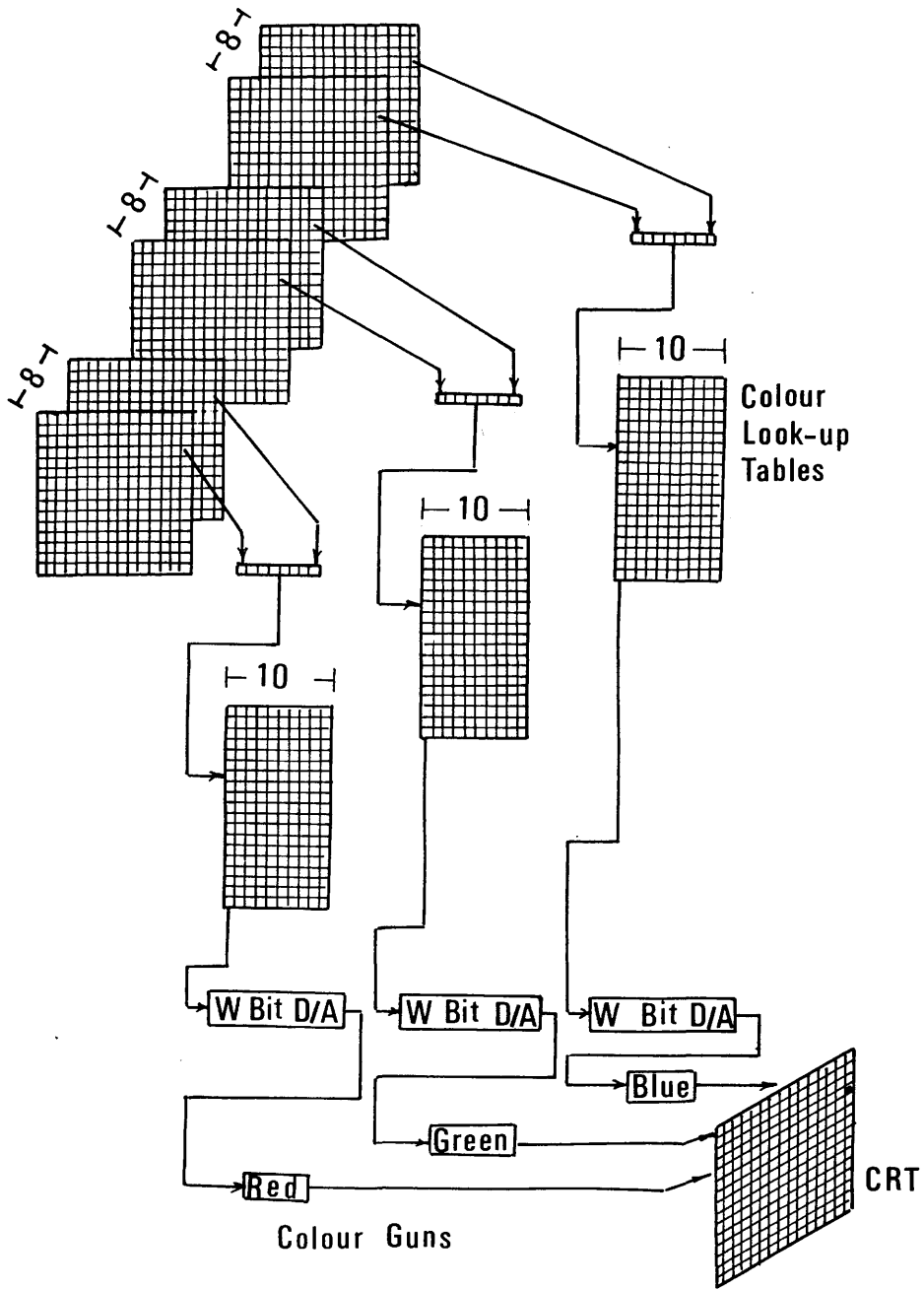


Fig.2-14 A 24-bit plane colour frame buffer with 10-bit wide-look-up table

### 2.5.3 Frame Buffer Resolution

The resolution of the frame buffer could be defined as the number of addressable pixels in the horizontal and vertical directions. Typical resolutions are 512 X 512, 1,024 X 1,024 and 4,096 X 4,096 pixels. Because of the large number of pixels stored in the frame buffer, achieving real-time performance could be difficult. For example, in a 512 X 512

pixels frame buffer, individual pixels would need to be accessed in 152 nanoseconds to produce a refresh rate of 25 frames/sec. The relevant access time for a 1,024 X 1,024 pixel frame buffer is 38 nanoseconds, while for 4,096 X 4,096 pixels it is 2.3 nanoseconds. The access time for each pixel is the time required to read the value of this pixel at each bit plane and produce a final value representing the intensity or colour of that pixel. Such a very short access time is very difficult to achieve in practice. However, if the pixels can be accessed simultaneously in groups of 16,32,64 or more, then real time performance for 512 X 512 and 1,024 X 1,024 pixel frame buffers is possible.

## 2.6 Summary

This chapter has served to introduce the main concepts of video technology which has been used throughout this research project in that the imaging sensor, the recording and display devices, the measuring equipment, etc. are all video-based. The next chapter will review the main characteristics of remote sensing devices operating in the optical part of the electromagnetic spectrum. The principles, concepts and technology discussed in these first two chapters will then be combined together in the form of video frame scanners which are the main concern of this project and which will be discussed in detail in Chapter IV.

## CHAPTER III

### REMOTE SENSING IN THE OPTICAL REGION OF THE ELECTROMAGNETIC SPECTRUM

REMOTE SENSING IN THE OPTICAL REGION  
OF THE ELECTROMAGNETIC SPECTRUM

3.1 The Electromagnetic Spectrum

The Sun and various artificial sources radiate electromagnetic (EM) energy of varying wavelengths. The frequency ( $f$ ) at which these waves are radiated is related to their wavelength ( $\lambda$ ) by the formula  $f = V/\lambda$  where  $V$  is the speed of EM energy ( $3 \times 10^8$  m/sec).

The EM spectrum may be subdivided into a number of regions. The range of wavelengths and frequencies and the names generally assigned to these regions is shown in Fig.3-1 below.

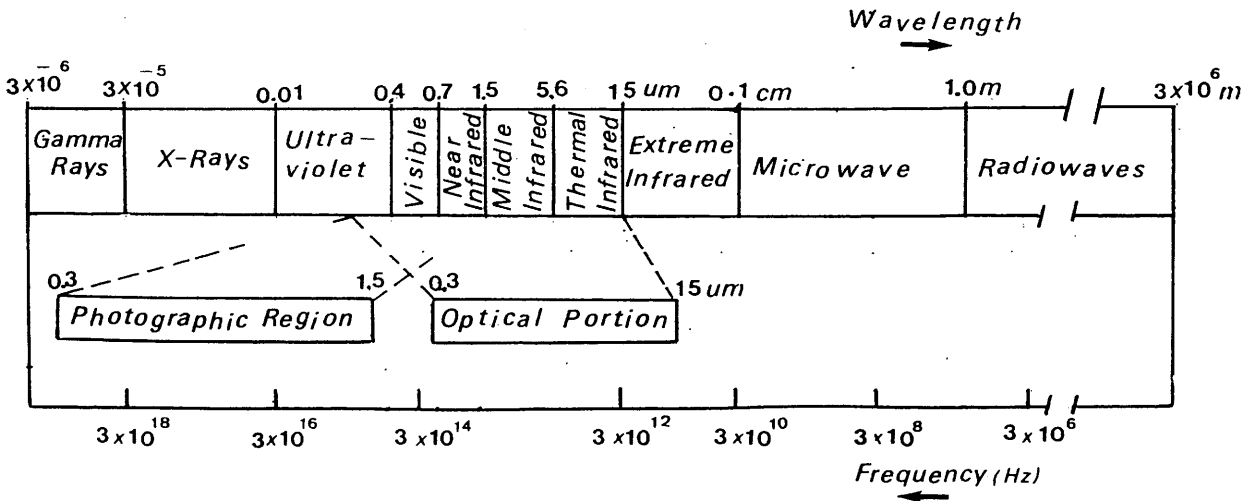


Fig.3-1 The electromagnetic spectrum

The human eye is sensitive to the visible region of the spectrum lying between 0.4 to 0.7  $\mu\text{m}$ . The entire band between 0.3 and 15  $\mu\text{m}$  in wavelength is referred to as the optical region of the EM spectrum, since EM waves may be refracted, reflected and focussed using lenses and prisms in this region. As can be seen from Fig.3-1 above, the optical region constitutes two main parts of the spectrum- the photographic part and the infrared part, which are overlapped in the near-infrared area.

### 3.1.1 The Photographic Region of the EM Spectrum

This is the portion of the spectrum having wavelengths between 0.3 and 1.5  $\mu\text{m}$ . Radiation in this area may be recorded using photographic emulsions. It is divided into blue, green and red. Colour or false-colour photography is possible in this area by using appropriate emulsions.

### 3.1.2 The Infrared Region of the EM Spectrum

The infrared spectrum lies between 0.7  $\mu\text{m}$  and approximately 1,000  $\mu\text{m}$  in wavelength, that is between the borders of the visible region at the shorter wavelength end and the microwave region at the longer wavelength end of the EM spectrum.

As a result of developments in detectors and optical materials, four quite natural though purely arbitrary divisions of the infrared spectrum are commonly used. These are:-

- (i) the near infrared region, from 0.7 to 1.5  $\mu\text{m}$ ;
- (ii) the middle infrared region, from 1.5 to 5.6  $\mu\text{m}$ ;
- (iii) the far infrared (thermal) region, from 5.6 to 15  $\mu\text{m}$ ;  
and
- (iv) the extreme infrared region, from 15 to 1,000  $\mu\text{m}$ .

Since the present project has a particular interest in the thermal infrared band, the basic physical laws of the infrared radiation will be discussed in detail.

#### 3.1.2.1 Basic Laws of Infrared Radiation

The amount of radiation emitted from an object at a certain wavelength is related to its temperature and to its emissivity. The higher the temperature of the object, the more the infrared radiation emitted from it.

Material that absorbs all incident energy, converts it to heat energy and transforms the heat back into radiant energy (thus emitting it) at the maximum possible rate allowed by the thermodynamic laws is known as a black body or a perfect thermal emitter. Selective absorbers and emitters are referred to as gray bodies.

The absolute temperature of the radiating object, the wavelength of the peak radiation emitted and the total radiated energy are related by the following fundamental laws of physics.

(i) **Plank's Law**

The relationship between the radiation intensity, spectral distribution and temperature of a black body is given by Plank's law which states that:-

$$W_{\lambda} = \frac{c_1}{\lambda^5} (e^{c_2/\lambda T} - 1)^{-1} \dots\dots\dots 3-1$$

Where:-

$W_{\lambda}$  is the amount of radiation emitted by the black body per unit surface area per unit wavelength interval into a hemisphere at a wavelength  $\lambda$ . It is measured in watts/cm per unit wavelength.

$T$  is the absolute temperature ( $^{\circ}K$ ) of the black body;

$\lambda$  is the wavelength of the emitted radiation;

$e$  is the base of natural logarithms = 2.718; and

$c_1, c_2$  are constants. Their values depend upon the unit of wavelength  $\lambda$  used.

Fig.3-2 below shows the spectral radiant emittance for black bodies at various absolute temperatures. It can be seen that, as the temperature of the black body increases, the intensity of the emitted radiant energy increases rapidly.

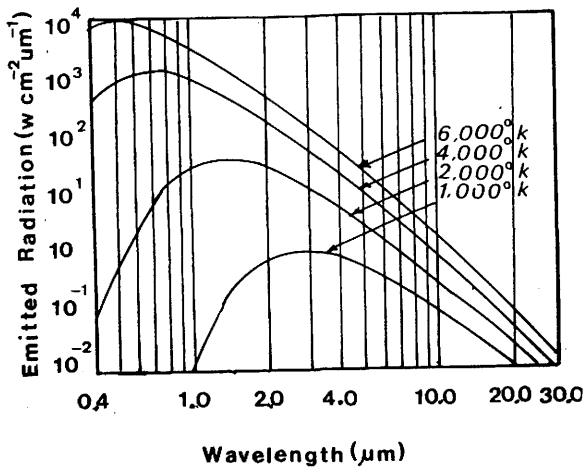


Fig.3-2. Black body radiation curves at various absolute temperatures

(ii) **Wien's Displacement Law**

This states that the wavelength of the peak radiation multiplied by the absolute temperature of the black body is equal to a constant. It is derived by differentiating equation 3-1 above with respect to  $\lambda$  and setting the derivative equal to zero;

$$\lambda_m T = K \dots\dots\dots 3-2$$

where:-

$\lambda_m$  is the wavelength at which  $W_\lambda$  is a maximum; and

K is a constant. ( K= 0.2897 cm deg. if  $\lambda$  is measured in centimetres).

Thus, as the temperature of a black body increases, its radiation peak shifts to shorter wavelengths as shown in Fig.3-2.

(iii) **Stefan-Boltzmann Law**

The total radiant emittance into a hemisphere from a black body at absolute temperature T is obtained by integrating  $W_\lambda$  in equation 3-1 with respect to  $\lambda$  between the limits  $\lambda = 0$  and  $\lambda = \infty$ .

$$W_\lambda = \int_{\lambda=0}^{\lambda=\infty} W_\lambda d\lambda = \sigma T^4 \dots\dots\dots 3-3$$

Where:-

$W_\lambda$  is the total black body radiant emittance, measured in watts/cm of the radiating surface; and

$\sigma$  Stefan-Boltzmann constant;  
=  $5.673 \times 10$  erg/(cm)(sec)(deg)  
=  $5.673 \times 10$  watts/(cm)(deg).

**3.1.2.2 Emissivity**

The above laws were all derived for a black body with an emissivity factor of 1.0. However, most bodies encountered in practice are not perfect black bodies. They are gray bodies which radiate or absorb less than what a black body would at the same temperature. Thus, their emissivity is always less than unity.

The emissivity factor of an object is a measure of its radiation (and absorption) efficiency. It is defined as:-

$$E_{\lambda} = \frac{\text{Radiant emittance at a given temperature}}{\text{Radiant emittance of a black body at the same temp.}}$$

Where  $E_{\lambda}$  is the emissivity factor of the object at a particular wavelength.

The emissivity factor is therefore an indication of the grayness of the radiating body. The lower the emissivity factor, the grayer the body; the higher the factor, the blacker the body. Because of emissivity variations, it is possible for objects to be at the same temperature and yet have completely different radiance emittance values.

### 3.1.2.3 Infrared Radiation from the Terrain

During daylight, the radiant energy from the terrain consists of two components—reflected solar radiation and emitted object radiation. Within the infrared region, it is apparent that, as the wavelength increases, the emitted infrared component becomes progressively more significant (Fig. 3-3).

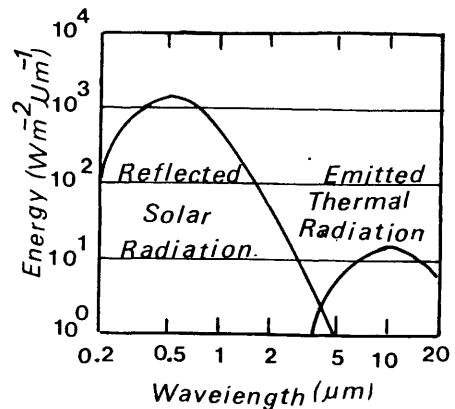


Fig.3-3 Reflected and emitted radiation from the terrain surface

As can be seen from Table 3-1 below, the main source of radiation in the near infrared region is the reflection of energy from the Sun incident upon the object. In the middle infrared region, the reflected solar radiation still represents about 80% of the total radiation from the object. In the far infrared, the emitted energy represents over 99% of the total energy from the object.

Wave Length Band $\mu\text{m}$	Solar Radiation watts/m <sup>2</sup>	Emitted Radiation watts/m <sup>2</sup>
0.3 - 3.0	750.0	0
3.0 - 5.6	24.0	6
5.6 - 15.0	1.5	150

Table 3-1 Radiation from the Earth in the visible and infrared regions of the spectrum



### 3.1.3 EM Spectrum and the Atmosphere

The atmosphere influences the EM radiation in two main respects- firstly by scattering and secondly by absorption. Scattering of the incoming radiation to the Earth and of the reflected radiation from the Earth's surface is caused primarily by tiny particles of dust, smoke, pollen and water suspended in the atmosphere. On the other hand, absorption occurs primarily as a consequence of the attenuating nature of molecules of ozone( $O_3$ ), carbon dioxide ( $CO_2$ ) and water vapour ( $H_2O$ ) in the atmosphere. Since these gases absorb EM radiation in specific wavelength bands, they govern the particular region of the spectrum which can be sensed by an airborne or spaceborne scanner.

Regions of the spectrum which are highly transmittive are referred to as atmospheric windows. It can be seen from Fig.3-4 that the atmosphere is highly transmittive in the visible part of the spectrum (0.4 to 0.7  $\mu m$ ). Other atmospheric windows present in the infrared part of the spectrum cover the ranges 0.7 to 1.3  $\mu m$ ; 1.5 to 1.8  $\mu m$ ; 2.0 to 2.6 ; 3.0 to 5.6  $\mu m$  and 8.0 to 14.0  $\mu m$ .

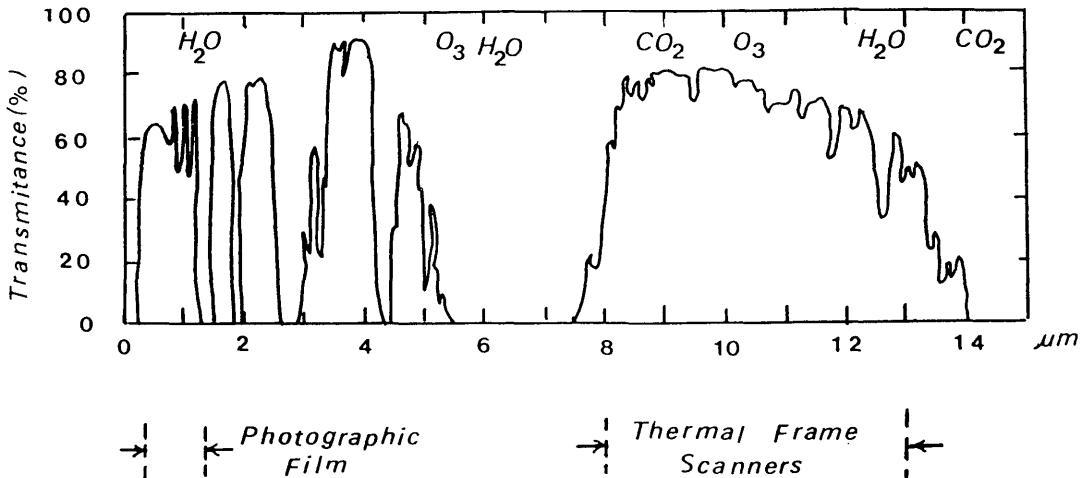


Fig.3-4 Atmospheric windows

### 3.2 Detection and Recording of EM Radiation

In principle, there are two main methods used in the detection, measurement and recording of the radiation in the optical part of the EM spectrum. These are photography and scanning. Photography can only be used in the photographic range of the EM spectrum (0.3 to 1.5  $\mu m$ ). Scanning on the other hand may be used over the whole of the optical part of the spectrum.

Scanners can be classified into passive and active. Within the optical range of the EM spectrum, passive scanning is

based on the use of solid-state detectors to convert the reflected and emitted radiation from the object into electrical signals which are used to generate a visual image of this object. Active scanning may be carried out using a laser as an illumination source instead of the Sun and collecting and measuring the resulting reflected energy from the terrain objects.

In the microwave region, passive scanning is based on the use of a receiver antenna to detect the emitted radiation from the object. On the other hand, active scanning is based on the use of a transmitter which emits EM radiation through an antenna and a receiver to receive the reflected radiation from the object, usually through the same antenna.

In the latter part of this chapter, passive sensors operating on the optical range of the EM spectrum will be discussed in more detail with particular emphasis on those utilizing optical-mechanical scanning techniques.

### 3.2.1 Photography

Photography is by far the most common and economical means of sensing and recording the visible and near infrared radiation reflected by the terrain.

A schematic diagram of a photogrammetric frame camera is shown in Fig.3-5. A lens and shutter assembly within the camera ensures that the incoming radiation is focussed and exposed instantaneously onto a photographic emulsion located in the camera's image plane. The latent photographic image is subsequently developed by chemical processing, so producing a conventional photograph.

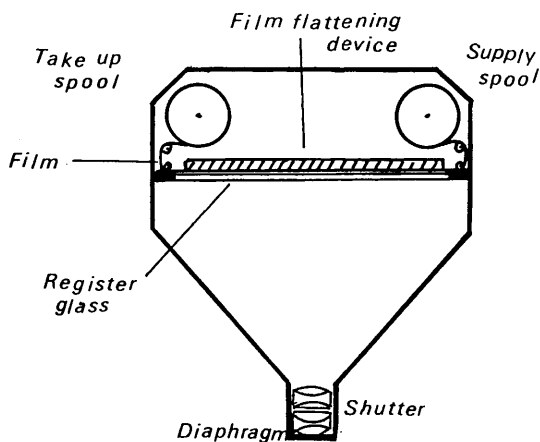


Fig.3-5 Design of the photogrammetric frame camera

Multispectral photography can also be obtained by using several spectral filters located in front of a number of lenses in combination with emulsions of different sensitivity. Alternatively and less commonly, a single lens camera supplied with a beam splitter may be used for the purpose. In both cases, several images of the same scene will be obtained simultaneously at different spectral wavelengths.

Another type of frame camera, which is of special interest in this discussion, is the panoramic frame camera. This type is mainly used for military reconnaissance purposes, since it can provide greater ground coverage per exposure with better resolution than a photogrammetric frame camera. This is achieved through the use of a long focal length lens while the wide angular coverage is achieved by causing the lens to rotate and so scan the terrain on either side of the flight line.

There are two main types of the panoramic frame camera:-

- (i) the direct scanning panoramic camera; and
- (ii) the rotating prism panoramic camera.

These are shown below in Fig.3-6

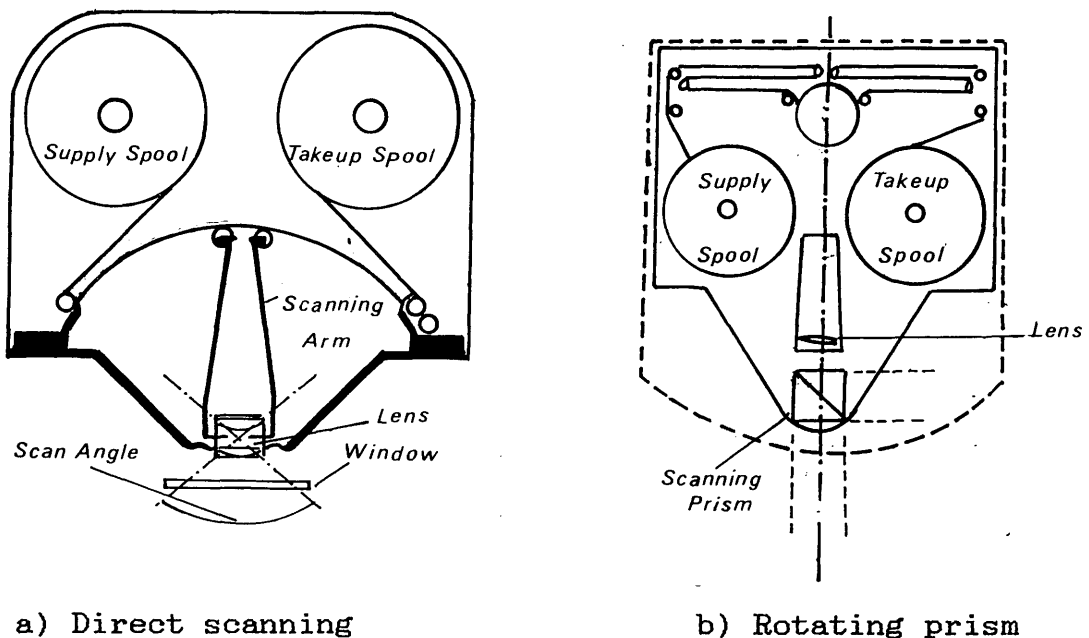


Fig.3-6 Design concept of the panoramic frame camera

**(i) The Direct Scanning Panoramic Camera:-**

The direct scanning panoramic camera contains a focal plane limited to a narrow slit which is oriented parallel to the direction of flight. A lens and the focal plane slit are rotated as a unit about the rear node of the lens. The axis of rotation lies in the vertical plane passing through the direction of flight. The film itself is stationary and is constrained to lie on a cylinder whose radius equals the focal length of the lens. The design concept of this type of panoramic frame camera is shown in Fig.3-6a.

## (ii) The Rotating Prism Panoramic Camera:-

In the rotating prism type, the lens-slit assembly remains stationary while a prism is rotated in front of the lens and the film is metered past the lens and slit at a velocity synchronised with the rotation rate of the prism. The concept and design of the rotating prism panoramic camera is shown in Fig.3-6b.

Photographic cameras can only operate in the visible or near infrared portions of the EM spectrum. The radiation from the middle and far infrared bands can only be recorded using scanners or other imaging devices equipped with suitable solid-state detectors.

### 3.2.2 Passive Scanning Systems

Passive scanning systems can be classified into line and frame scanners. Line scanners scan the object in one direction only and depend on the forward movement of the platform to provide the scan in the other direction. These devices can be sensitive to a single spectral band, as in the case of the simple optical-mechanical line scanner, or can be made sensitive to several spectral bands such as in the case of the multispectral line scanner (MSS). Both types have been widely used to acquire airborne or spaceborne imagery. On the other hand, frame scanners scan the object in two dimensions. In practice, they can only be made sensitive to a single spectral band. Frame scanners can also be operated from an airborne, spaceborne or ground based platforms. An example of such a system is the video-compatible optical-mechanical thermal infrared scanner.

#### 3.2.2.1 Optical Mechanical Line Scanner

The principle of operation and construction of the optical-mechanical line scanner is shown in Fig.3-7. An oscillating plane mirror is used to scan the ground line-by-line in the direction perpendicular to the flight path, while the forward motion of the platform allows the exposure of successive lines to build up a single strip image of the terrain. The radiation received from the ground is focussed onto the sensitive area of the detector. The detector transforms the received radiation into an electrical signal whose intensity is proportional to the amount of the received radiation.

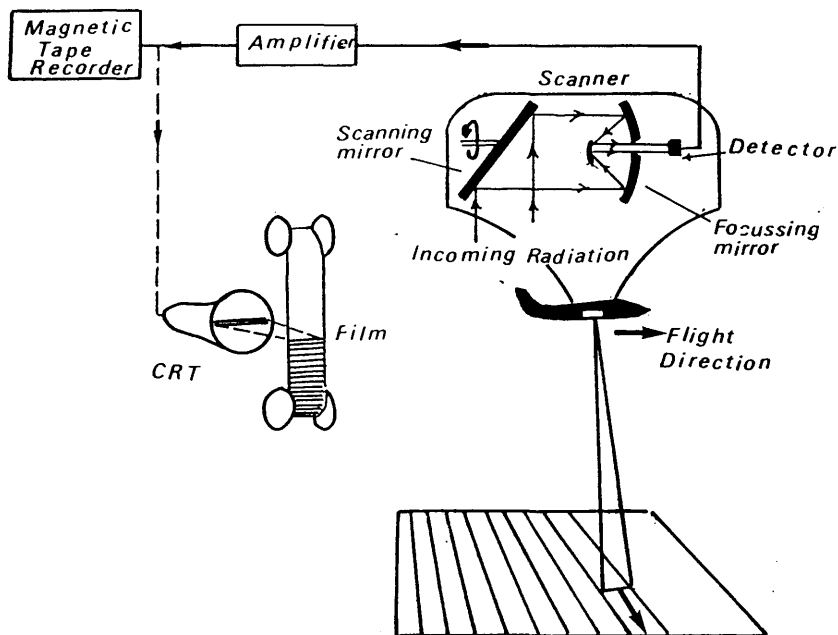


Fig.3-7 Construction of the optical mechanical line scanner

The mirror scans the ground through a scan angle  $\beta$  as shown in Fig.3-8. At any particular moment, the detector looks at a finite small area on the ground with a fixed angular size known as the instantaneous field of view (IFOV). The ground resolution of the scanner image is a function of the flying height, the scanner's IFOV and the scan angle. The output from the detector can be used to control the intensity of a bright spot moving across a CRT display at a velocity proportional to the velocity of the scanning mirror.

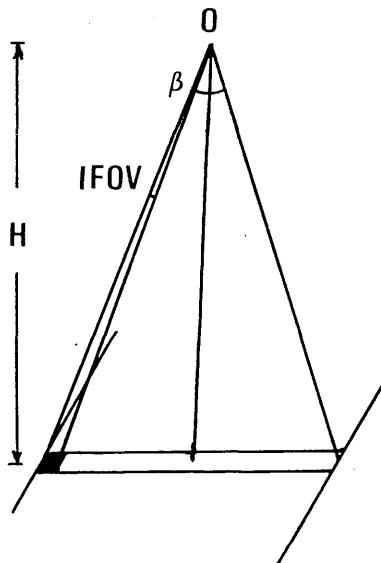


Fig.3-8 Scanning parameters

By this process, a line of varying intensity is swept across the CRT. By synchronising the velocity of a moving film placed in front of the CRT to match that of the platform, a continuous photographic image can be created (Fig.3-7). The outputs from the detector can also be recorded on a magnetic tape.

Among the well known aircraft-based thermal line scanners are the Daedalus DS 1230 and DS 1250, which cover the spectral range from 8 to 14  $\mu\text{m}$ , and the EMI Airscan which covers the spectral range from 3.5 to 5.5  $\mu\text{m}$ . The satellite-based line scanners include the Very High Resolution Radiometers (VHRR) mounted in the National Oceanic and Atmospheric Administration (NOAA) weather satellites which operate in the 10.5 to 12.5  $\mu\text{m}$  region, and the Heat Capacity Mapping Mission (HCMM) which carried scanners operating in the visible and near infrared (0.5 to 1.1  $\mu\text{m}$ ) and in the thermal infrared (10.5 to 12.5  $\mu\text{m}$ ) parts of the spectrum respectively.

### 3.2.2.2 The Multispectral Line Scanner

The multispectral line scanner (MSS) is similar in principle and operation to the simple optical-mechanical line scanner described in the previous paragraph. However, instead of having a single detector which is sensitive to a single spectral band, the MSS has multiple detectors, each of which is sensitive to a different spectral band. The principle, construction and operation of the MSS is shown in Fig.3-9.

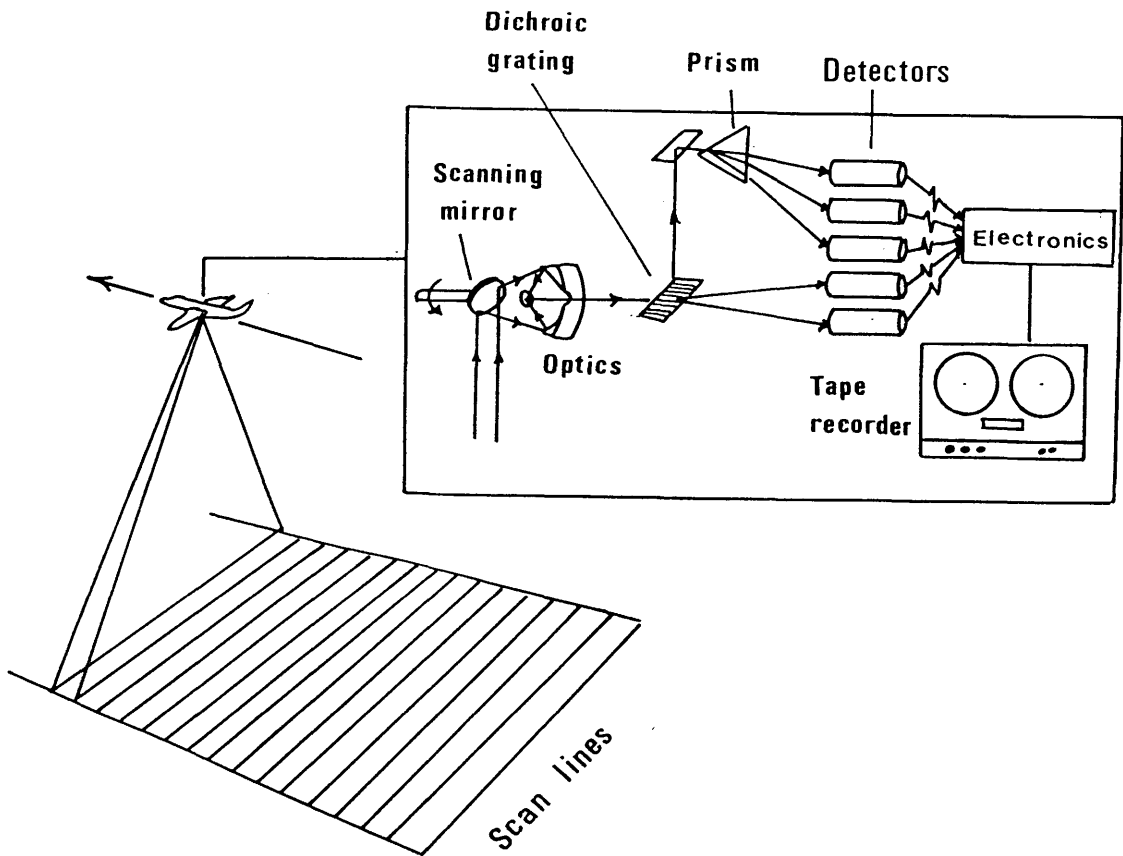


Fig.3-9 Basic construction of the multispectral scanner

Radiation from the scene is separated into discrete wavelength ranges by a grating and spectral filters so that the radiation from each spectral band is directed to the corresponding detector. The output signal from each detector can be recorded on magnetic tape or used to generate an image on a CRT in the same manner as with the simple line scanner.

Well known aircraft-based MSS devices include the Daedalus AADS 1268 (Airborne Thematic Mapper) which can be operated with up to 11 channels covering the spectrum range between 0.24 to 13.0  $\mu\text{m}$ , and the Programmed Neuro Cybernetics (PNC) scanner which operates in 4 channels within the far infrared band covering the spectrum range between 7.2 to 13.9  $\mu\text{m}$ . Among those mounted in Earth-orbiting satellites are the MSS and TM scanners in the Landsat series of satellites, and the Coastal Zone Colour Scanner (CZCS) on the Nimbus 7 satellite.

### 3.2.2.3 Frame Scanners

Unlike the line scanners which only scan the object in one direction, while the platform forward motion provides the scan of the object in the other direction, frame scanners scan the object in two directions using two optical mechanical scanning elements.

Since this type of scanner is the main subject of investigation in the present project, a detailed discussion of the design requirements of these systems, together with some examples of commercially available systems will be presented in the next chapter.

## 3.3 Imaging Devices Employing Solid State Arrays

Imaging devices also exist which employ an array of solid state detectors. These devices can use either a linear or an areal array.

### 3.3.1 Imaging Devices Using Linear Arrays

Instead of using a single element detector and a scanning mirror as the line scanner, an imaging device employing a linear array uses a number of discrete detector elements which are oriented across the flight path so that each detector receives radiation from a corresponding ground resolution element in the cross-track direction. Thus, the device images a complete line on the terrain simultaneously instead of sweeping it out sequentially as with the conventional line scanner. The ground coverage is produced in the normal way by the forward motion of the platform, hence the term "pushbroom" scanner (Fig.3-10) is commonly used. In

spite of the use of the term scanner, it will be noticed that these devices do not possess any of the optical mechanical scanning elements discussed above and strictly speaking they are not scanners.

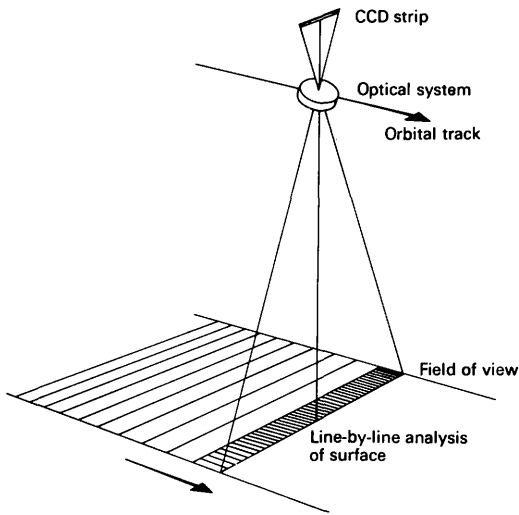


Fig.3-10a The pushbroom scanner

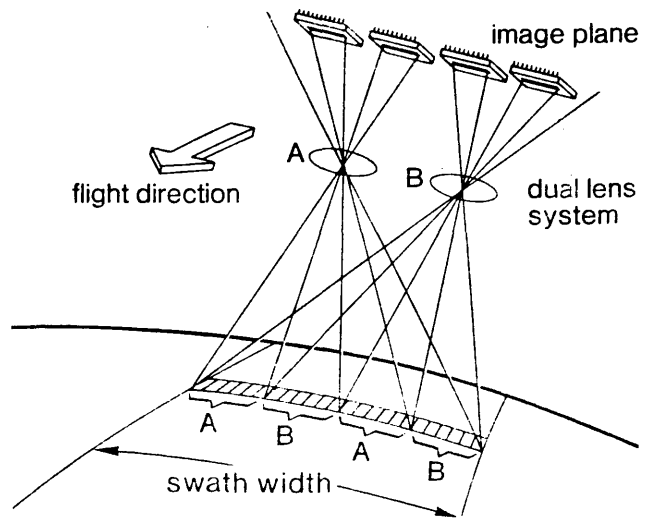


Fig.3-10b MOMS dual lens pushbroom scanner

The basic technology has mostly been developed for military reconnaissance purposes in the United States, from where the initial proposals for mapping satellites (Stereosat, Mapsat and others) using pushbroom scanners have originated. However, attention is currently focussed on the HRV linear array imaging device used in the French SPOT satellite and the German MOMS (Fig.3-10b), mounted in the SPAS platform deployed from the American Space Shuttle.

When compared to the basic line scanner, imaging devices employing solid state linear arrays produce an image of better geometric quality in the cross track direction. Also they will be lighter in weight, consume less power and be more reliable (Petrie, 1985).

### 3.3.2 Imaging Devices Using Areal Arrays

When used in a matrix form, solid state detectors are arranged so that the whole field of view is imaged simultaneously to produce a perspective view of the object. In geometric terms, the imaging process is similar to that of the photographic camera, except that the photographic emulsion is replaced by the matrix array of detectors. The signal from each of these detectors is then stored and read out in a serial mode to generate an image on a CRT. This type of imager is sometimes known as solid state framing camera or a staring device as opposed to a scanning device.



The solid state framing camera orbited in the small UOSAT (OSCAR-9) satellite uses an areal array of CCDs comprising 288 x 385 lines, manufactured by GEC in the U.K. (Fig.3-11). Also CCD areal arrays of 800 x 800 to 1125 x 1125 lines have been developed for high definition television (HDTV).

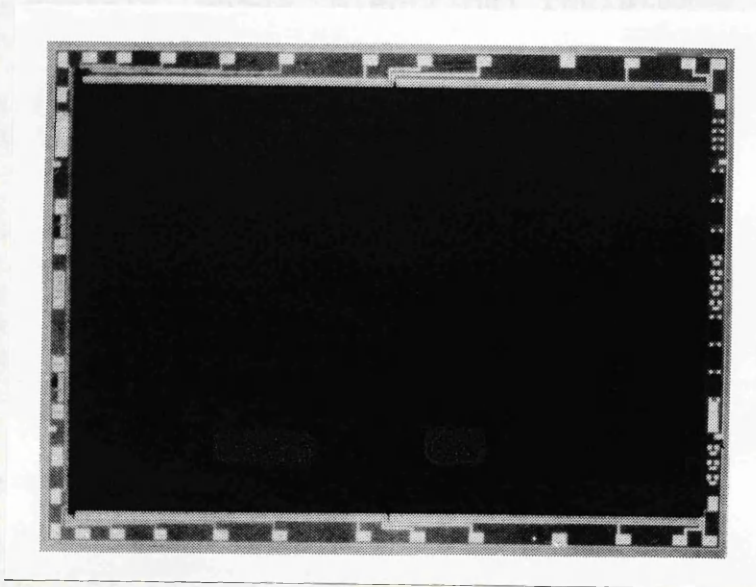


Fig.3-11 GEC Charged Coupled Device(CCD) areal imaging array for UOSAT camera

It can be seen that once again the so-called staring devices do not contain any of the scanning elements of a scanner, but only the solid state detector elements. Essentially therefore, they are non-photographic cameras and indeed are frequently described as CCD cameras.

Devices employing solid state areal arrays are expected to produce an image of very high geometric fidelity. Since the object is imaged instantaneously, all types of distortion introduced by the scanning effect such as scale change and image motion during scanning time should be completely eliminated.

### 3.4 Detectors

The heart of the imaging system is some form of detector which serves to measure the incident radiation levels and transform them into electrical signals. Two types of detector are commonly in use:-

- (i) thermal detectors;and
- (ii) quantum or photon detectors.

### 3.4.1 Thermal Detectors

These are solid state detectors which change their temperature in response to the absorption of incident radiation. This change in temperature within the detector is then measured electrically. Typically, thermal detectors contain materials whose electrical resistance depends on temperature. Thus, as the level of the incident radiation changes, the temperature of the detector material changes. In turn, the resistance of the material changes and the change in this resistance is measured through appropriate electrical circuitry.

Such detectors have the advantage of being extremely accurate; also they are sensitive to the whole range of the infrared spectrum. However, the major disadvantage is their comparatively long response time, which is the elapsed time between a change in the incoming energy level and the resulting change in the monitored electrical signal.

### 3.4.2 Quantum Detectors

In contrast to thermal detectors, quantum detectors are capable of very short response times. Basically, quantum detectors operate by direct interaction between the photons of the radiation incident upon them and the energy level of the electrical charge carried within the detector material. The spectral sensitivity range of the commonly used quantum detectors are listed below in Table 3-2.

Type of Detector	Chemical Abbreviation	Spectral Sensitivity Range ( $\mu\text{m}$ )
Silicon	Si	0.3-5.5
Indium Antimonide	In.Sb	3.0-5.5
Irium Arsenide	Ir.As	3.0-5.5
Mercury Doped Germanium	Ge. Hg	3.0-14.0
Cadmium Mercury Telluride (CMT)	Hg Cd Te	8.0-14.0

Table 3-2 Spectral range of quantum detectors

With their rapid response characteristics, quantum detectors are in widespread use in scanners of all types. Their major drawbacks are their narrow band spectral sensitivity and the necessity to cool them to a temperature approaching absolute zero.

### 3.4.3 Detector Cooling

At normal temperatures the signal output of an infrared quantum detector is very small and is swamped by thermal noise. To make the detector sensitive enough to resolve small temperature differences in the scene being observed, and to make the response clearly distinguishable from the thermal noise, the detector must be cooled to about  $193^{\circ}\text{K}$  ( $-80^{\circ}\text{C}$ ) for detectors working at 3 to  $5\ \mu\text{m}$ , and about  $80^{\circ}\text{K}$  ( $-193^{\circ}\text{C}$ ) for those working at 8 to  $14\ \mu\text{m}$  region of the EM spectrum. This is normally achieved using a Joule-Thomson mini-cooler with compressed gas bottles (air or nitrogen).

In the previous Chapter, the technical aspects of video technology, including video imaging, video recording and video display have been discussed. In this Chapter, different methods of detecting the EM radiation within the optical range of the spectrum have been presented with more emphasis on those employing an optical mechanical scanning technique. In the next Chapter (Chapter IV), the video technology and the optical mechanical scanning technique will be combined together in the form of the optical mechanical video frame scanner which is the main subject of interest in this project.

## CHAPTER IV

### THERMAL VIDEO FRAME SCANNERS

## CHAPTER IV

### THERMAL VIDEO FRAME SCANNERS

#### 4.1 Design of Thermal Video Frame Scanner

Thermal video frame scanners operate in the 8 to 14  $\mu\text{m}$  window of the EM spectrum. All frame scanners use the same principle in which an optical system is used to collect and focus the emitted radiation from the object onto the focal plane of the detector. The construction of the thermal video frame scanner is shown in the block diagram of Fig.4-1. An optical mechanical scanning mechanism is used to move the sensitive area of the detector so that it scans the whole object within the field of view of the scanner. Depending on the detector configuration and the scan mechanism speed, the output from the frame scanner could be a standard TV-compatible video signal which can be displayed directly on a conventional video monitor and recorded on a standard VTR. Alternatively with certain specialised types of scanner, the output may be in some other form of video signal which can be displayed and recorded on dedicated i.e. non-standard video devices. However in the latter case, it is possible to transform the video signal into a TV-compatible signal using some kind of frame buffer and conversion circuitry.

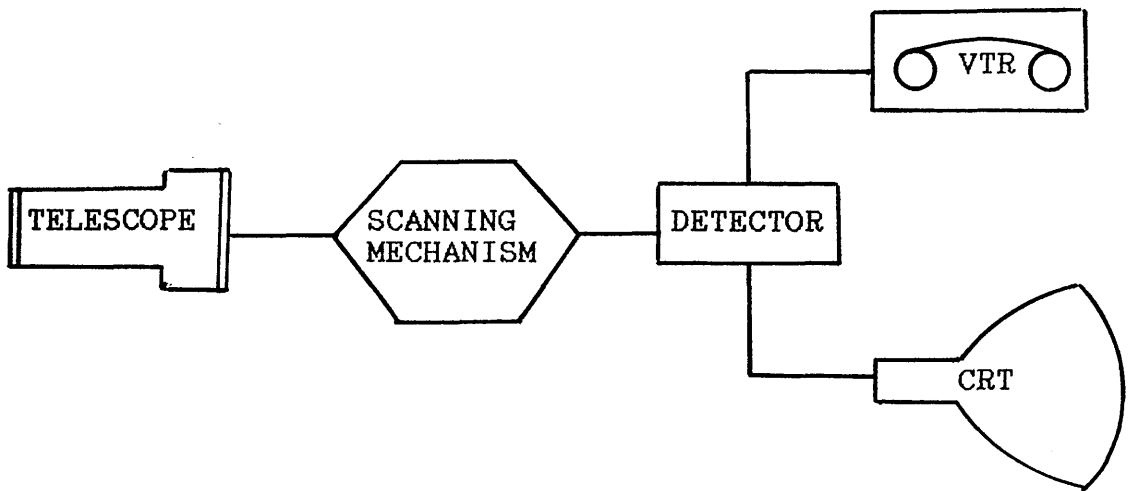


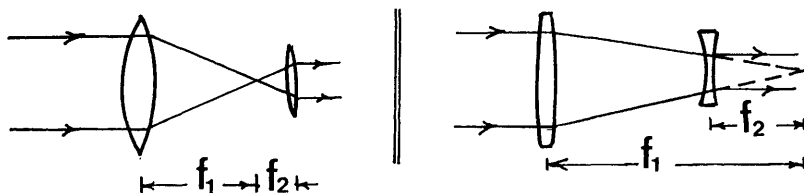
Fig.4-1 The construction of thermal video frame scanner

##### 4.1.1 The Telescope

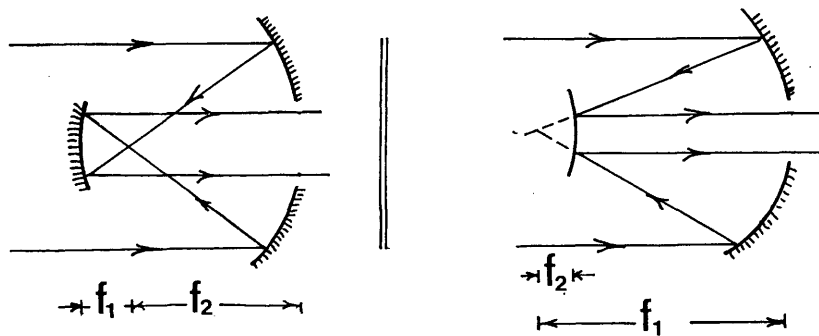
The frame type of scanner usually uses an afocal telescope to collect and focus the emitted radiation from the object onto the focal plane of the detector. The basic afocal telescope

consists of two lenses (the objective and the eyepiece lenses) separated by a distance equal to the algebraic sum of their two focal lengths. Such a system forms its image of an infinitely distant object at infinity. There are two types of afocal telescopes- astronomical and galilean. In the astronomical type there is a real focal plane between the objective and the eyepiece, while in the galilean type there is a virtual focal plane and the eyepiece is negative in power. Fig.4-2 shows the reflecting and refracting types of both telescopes.

Refractive Type



Reflective Type



a) Astronomical telescope

b) Galilean telescope

Fig.4-2 The afocal telescope

Galilean telescopes are much shorter in length than the astronomical ones. However, their objective lenses are larger in diameter than those of the astronomical and they are not in such common use in thermal frame scanners as the astronomical type.

The angular magnification of the afocal telescope is defined as the ratio between the angular size of the image and the angular size of the object. The linear magnification is the ratio between the linear size of the image and the linear size of the object.

#### 4.1.1.1 Optical Materials

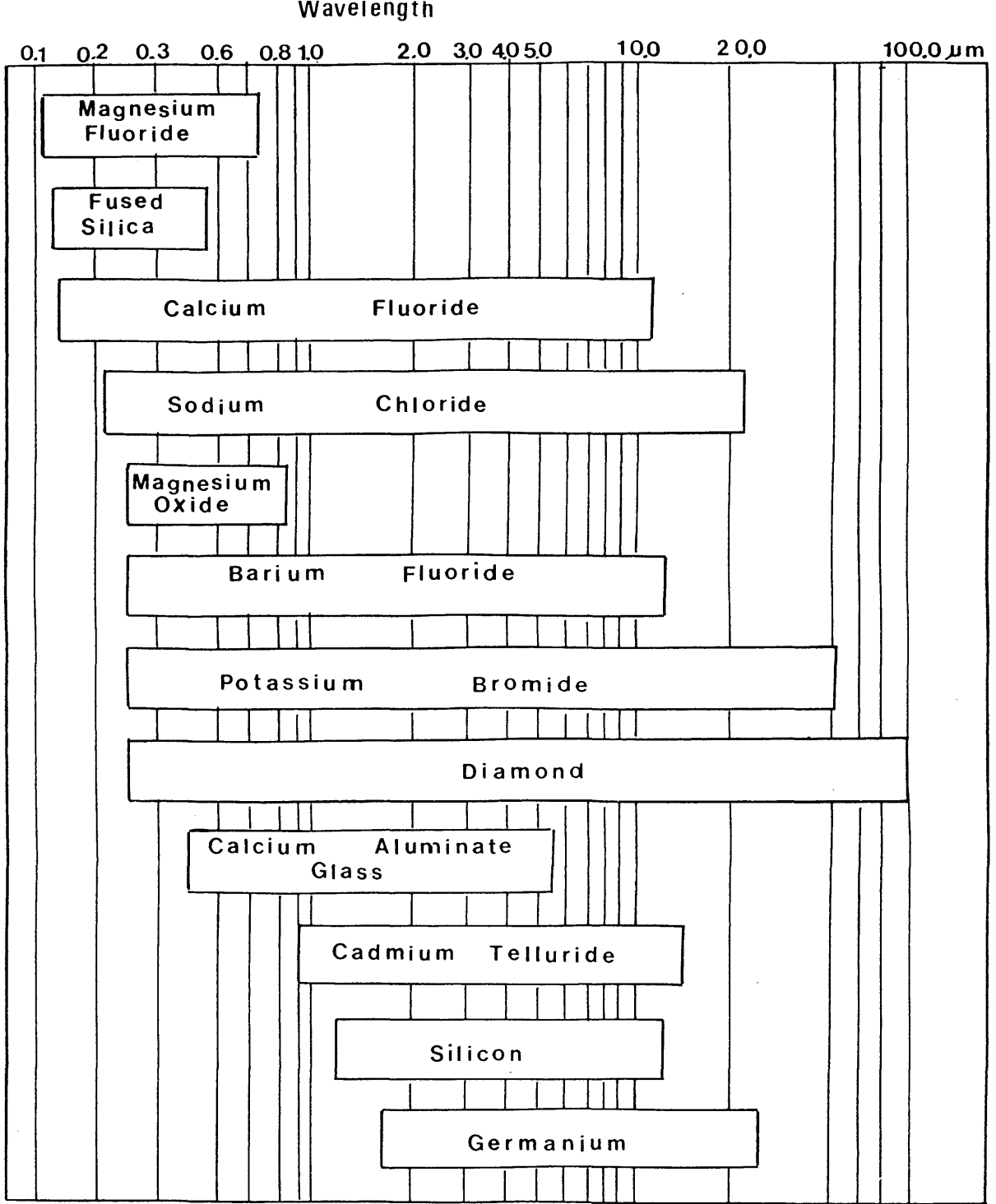
Among the optical properties required of an infrared optical material is that it should allow maximum transmission of infrared radiation in the desired thermal band. Fig.4-3 shows the transmission regions for the most commonly used optical materials. All optical materials should have a high degree of homogeneity and of freedom from birefringence. In materials used for mirrors, surface hardness, the ability to take a high polish and high reflectivity are desirable features.

The mechanical properties of the optical material such as Young's modulus, the elastic limit, the tensile, compression and torsional strength and hardness of the optical material are also of particular importance since these devices will be employed for airborne imaging where severe vibration and shock conditions exist.

Thermal properties are also of special importance. A low thermal coefficient of expansion and good thermal conductivity are required to prevent aberration unbalancing and focal length change with temperature change. Other required or desirable characteristics of optical components which are shared with photographic sensors are insolubility in water, compatibility with anti-reflection coatings and ease of acquisition and manufacture.

Either silicon or germanium-based materials can be used for the optical components employed in thermal imaging devices. Silicon is usually used in scanners operating in the 3 to 5.6  $\mu\text{m}$  band because it is cheaper than germanium and easier to obtain. However it is not as highly transmittive as germanium in the 8 to 14  $\mu\text{m}$  band.

On the other hand, germanium possesses most of the required characteristics for thermal imaging. It can be used in the middle infrared band (3 to 5.6  $\mu\text{m}$ ) or in the thermal band (8 to 14  $\mu\text{m}$ ). Arising from its favourable characteristics, germanium has been used as the principal material for the optical transmittive components of all the frame scanners considered or used in the research work reported in this thesis. However, it is a very expensive material and requires special techniques to machine it into the form of optical components.



Photography

Frame Scanners

Line Scanners

Fig.4-3 Transmission regions for optical materials



#### 4.1.2 Scanning/Detector Configuration

Depending on the required frame size and the scanning mechanism speed, the scanning configuration actually employed will include either a single element or a multiple element detector. With the latter, individual discrete elements may be arranged in a horizontal array to perform serial scanning; in a vertical array to perform parallel scanning; or in a small matrix array to perform serial/ parallel scanning.

##### 4.1.2.1 Single Element Scanning

In this method, the image is scanned pixel by pixel in a conventional raster mode as shown in Fig.4-4. The video image consists of a very large number of pixels, e.g. in a PAL TV compatible system, there are  $625 \times 833 = 520,833$  pixels/frame. Thus over 13 million pixels must be scanned every second, which requires a very high scanning speed (over 160,000 rpm ). In practice however, there are limits to the scan mechanism speed which is possible or practicable (around 45,000 rpm). Also within the practical limits of the scanning speed, the detector will be required to operate up to or even beyond its nominal cut-off frequency. In this case, the signal to noise ratio (SNR) will be very low. This is the ratio between the signal generated by the detector as a result of the incident radiation and the combined noises produced by the scanner and its associated electronics.

Experience showed that a 70 line image is the maximum that could be achieved with a single element detector within the practical limitations of the detector and the scan mechanism (Cuthbertson, 1983)

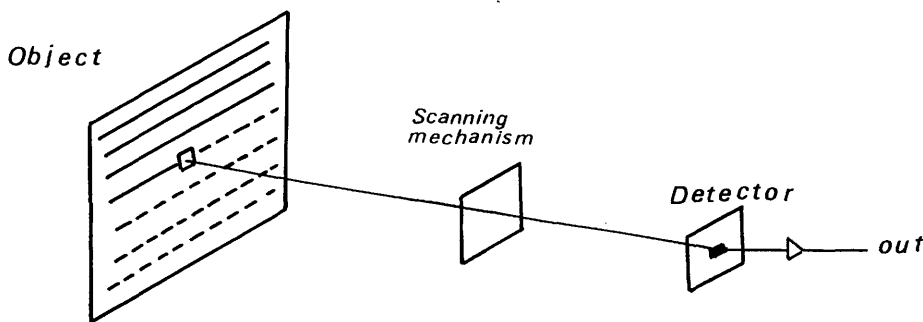


Fig.4-4 Single element scanning

### 4.1.2.2 Serial Scanning

In this technique, a serial array of detector elements is scanned over every line in the field in turn as shown in Fig.4-5. If  $N$  elements are used, each pixel will be scanned  $N$  times, and the output for the same pixel from each detector will be added by a process called time delay and integration (TDI). In this process, the signal from each detector is amplified, delayed by an amount proportional to the scan speed and inversely proportional to its position in the row and then added together to give an average value for a specific pixel.

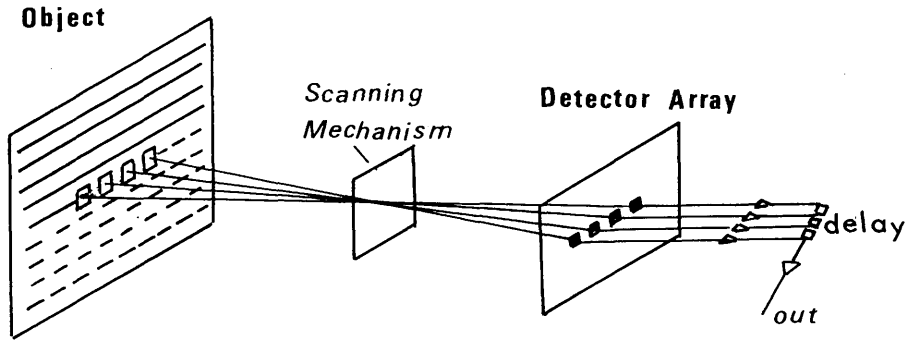


Fig.4-5 Serial scanning

The use of the serial scanning technique will yield an improvement in the SNR ratio proportional to  $\sqrt{N}$  where  $N$  is the number of serial detectors. However, it still requires an exceptionally high speed scanning mechanism.

### 4.1.2.3 Parallel Scanning

In this method, the image is scanned by a vertical array of detector elements as shown in Fig.4-6. Thus a number of lines in the image plane are scanned simultaneously i. e. in parallel. Since the CRT operates sequentially in a raster scan mode, the scanner must include a parallel to serial scan converter. In this case, the scanning mechanism will operate at a relatively slow speed. However, the SNR will be the same as that for a single element scanning mechanism since each pixel will be scanned only once.

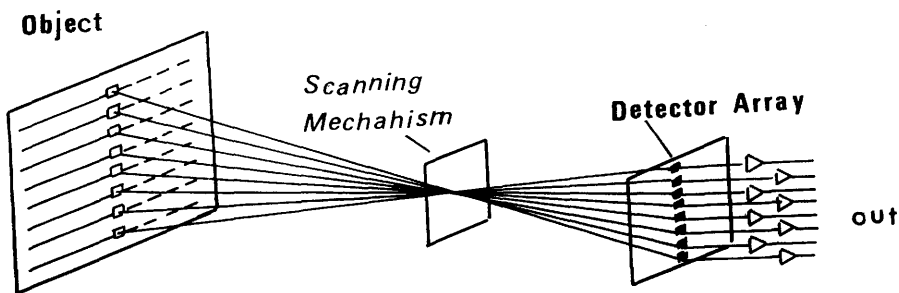


Fig.4-6 Parallel scanning

#### 4.1.2.4 Serial/Parallel Scanning

In serial/parallel scanning, a matrix of  $N \times M$  detector elements is used as shown in Fig.4-7 below. This will combine the SNR advantage of the serial scanning, together with the practical advantages of the slow mechanism speed of the parallel scanning technique. However, providing separate connections to all the detector elements requires a very complex electronic circuitry which is impractical. This problem was overcome by the use of the SPRITE detector devised by Dr.C.T. Elliott and developed at the Royal Signal and Radar Establishment.

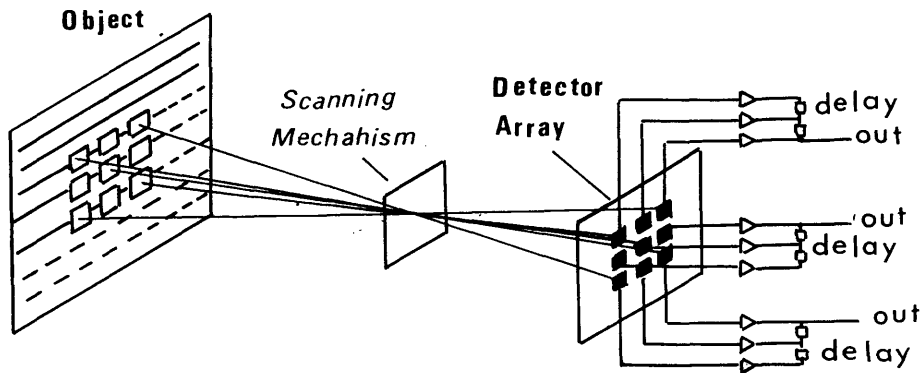


Fig.4-7 Serial/parallel scanning

#### 4.1.2.5 The SPRITE Detector

The name of this detector is an acronym derived from the words Signal PROCESSING In The Element (SPRITE). As shown in Fig.4-8, the detector takes the form of a CMT strip on which the incident thermal radiation is swept along in the form of charge carriers at the velocity which matches the scanning speed. In this case, the delay and integration procedure will take place in the bulk material to yield an output signal current equivalent to that which would have been obtained using a serial array of discrete elements after the TDI.

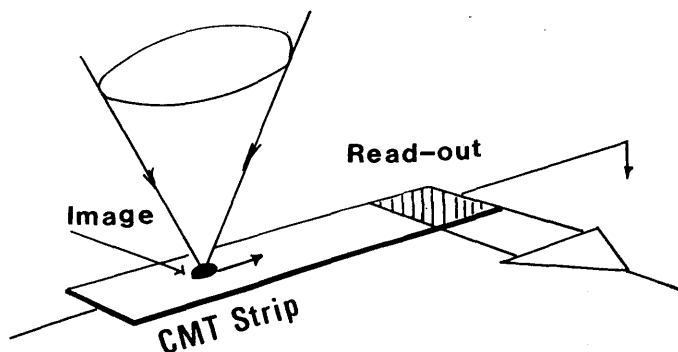


Fig.4-8 The SPRITE detector

If a number of these SPRITE detectors is used in parallel, then a serial/parallel scan will again be achieved. Thus the advent of the SPRITE detector made the serial/parallel scanning method the preferred one. The complexity of the required electronic circuitry was drastically reduced, since the TDI circuits were eliminated altogether and the number of amplifying channels was reduced. With this has come a reduction in the cost, weight, size and complexity of the latest thermal imager designs.

#### 4.1.3 Scanning Mechanism

The function of the scanning mechanism is to move the object image formed by the telescope in such a way that the detector sequentially scans the object within the field of view. Two scanning elements are required, one to scan the object line by line which is usually termed the frame scanning element, while the other scans each line pixel by pixel and is called the line scanning element. The most commonly used scanning elements are:-

- (i) the oscillating plane mirror;
- (ii) the rotating reflective polygon; and
- (iii) the rotating refractive polygon.

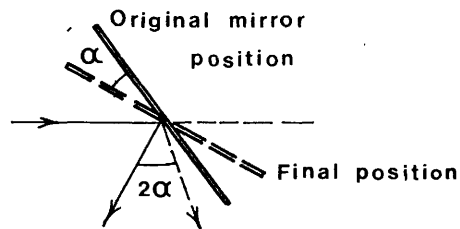


Fig.4-9 The oscillating plane mirror

##### 4.1.3.1 The Oscillating Plane Mirror

As shown in Fig.4-9, the oscillating plane mirror is a reflective device oscillating periodically in a systematic manner between two stops, so producing a ray angular deviation of twice the mirror scan angle. The oscillating plane mirror is commonly used as the frame scanning element located in front of the telescope.

##### 4.1.3.2 The Rotating Reflective Polygon

The scanning action of the rotating reflective polygon is similar to that of the oscillating plane mirror except that the centre of a facet moves in and out at the required rate thus producing a continuous scan of the object as shown in Fig.4-10.

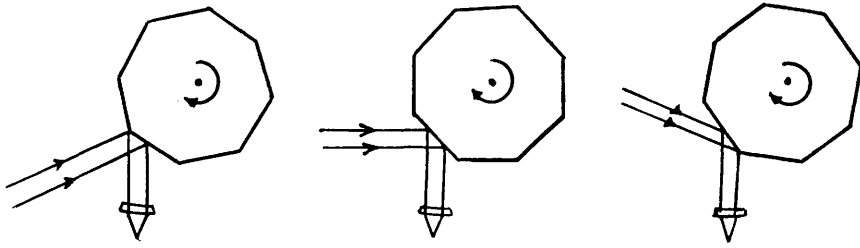


Fig.4-10 The rotating reflective polygon

#### 4.1.3.3 The Rotating Refractive Polygon

This type of scanning element is made of a transmitting material. It produces the scan by laterally displacing the incident ray and sweeping it across the detector or across the second scanning element. If the incident and exitant beams are in the same medium, the angles both beams make with the horizontal will be the same because the refraction at the first surface is reversed by the second surface. The scanning action of the refractive polygon is shown in Fig.4-11.

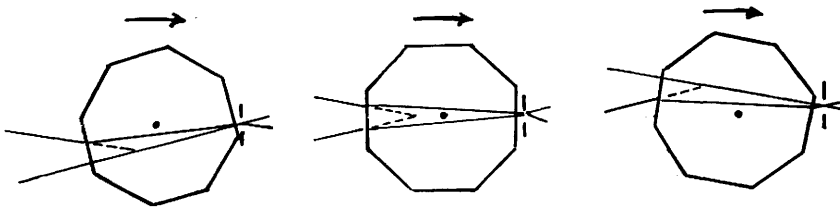


Fig.4-11. The rotating refractive polygon

In practice, the rotating polygon may have a maximum number of 10 facets. These polygons are commonly used as line scanning elements where they are driven to rotate at a very high speed. This speed depends on the number of facets on the prism together with the required frame size (i.e. number of pixels per frame). They are also useful in producing interlaced scanning, simply by canting the polygon faces to make them incline at different angles.

#### 4.1.4 Radiometric Characteristics of Frame Scanners

Several parameters are used to describe the radiometric performance of thermal frame scanners. The most important parameter is the temperature resolution. This is a measure of the smallest temperature difference in the scene that the scanner can resolve. In other words, it is the scanner's efficiency in detecting a small temperature variation within the object. This is known as the Minimum Resolvable Temperature Difference (MRTD). The MRTD is defined as the

minimum temperature difference between a standard four bar-target and its background which allows an observer to see the individual bars. It is measured by using the imager to look at bar targets comprising blackened metal plates with appropriately cut slots. The plates are kept at a well controlled temperature and viewed against a background which has its temperature altered until the observer can resolve the bars. The temperature difference between the bars and their background will be the MRTD at that situation. It is obvious that the smaller the MRTD, the more tonal shades within the object are obtained in the thermal image.

Current generations of thermal frame scanners normally incorporate an internal temperature reference. This takes the form of a black body radiation source positioned so that it is viewed by the line scanning mirror during each scan line. The temperature of this black body can be precisely controlled. This provides a continuously updated reference by which the other output values along the scan line can be related to the absolute radiant temperature.

Other performance parameters are related to the detector such as its responsivity (the ratio of the output voltage to the radiant input power) and detectivity, which is a figure of merit that takes account of responsivity, noise and detector size.

It must be mentioned here that frame scanners do not measure the object's temperature directly although it might be computed indirectly in terms of the object's emissivity and the use of temperature calibration targets. However this quantitative approach is outside the scope of the present project.

#### **4.2 The Modular Approach to Video Frame Scanner Design and Construction**

Arising from their capability of operating at night and at low radiation levels, thermal frame scanners have been developed rapidly for military applications such as pilot night vision, tracking, weapon aiming and navigation. This led to a growing realization in both the USA and Europe that the development of special thermal imagers for each specific application was impractical and uneconomic. In turn, this has led to the modular design approach, whereby sets of equipment building blocks have been designed which could be configured into complete systems to suit the special needs of individual projects. Not only does this approach result in the reduction in the cost of producing thermal frame scanners, but it also provides the opportunity to take advantage of technological developments during the life of the equipment, based on the substitution or replacement of individual modules, thus extending the performance and the service life of the scanner.

The USA was the first country to embrace the modular imager concept in 1974, The UK and France followed later in 1976. In the USA, after considering the different possibilities, the serial/parallel scan approach was adopted based on CMT detectors and a slow scanning speed. In Europe, an initial attempt to establish a collaborative programme failed. Thus Germany adopted the USA approach, while France and the UK proceeded with national programmes, each using a rather similar approach based on the serial/parallel scanning technique.

#### 4.2.1 UK Common Modules

The UK Thermal Imaging Common Module (TICM) programme defines three classes of module.

##### (i) UK Common Module Class I ( TICM I )

TICM I is intended for applications where low power consumption and weight are the main requirements. The displays used with this module are of the direct view type using an array of Light Emitting Diodes (LED) and the image is viewed directly through an optical telescope (viewfinder). The design in this module is based on using an array of 23 CMT detector elements and the image is displayed on 23 LED elements. This type of imager is mainly portable, an example of which is the Thorn EMI hand-held thermal imager.

##### (ii) UK Common Module Class II (TICM II)

The TICM II is intended for use in vehicles and in aircraft mounted systems. The display is a PAL TV-compatible image and the scanner operates in the 8 to 14  $\mu\text{m}$  band using 8 SPRITE detectors. Each of these is equivalent to 6 discrete elements, which are arranged to perform a serial/parallel scanning. An example of this module is the GEC Avionics/Rank Taylor Hobson TICM II thermal imager.

##### (iii) UK Common Module Class III (TICM III)

Any scanner in this class is essentially a scaled up version of the Class II scanners. Very high magnification is required, in which case the telescope length will be much larger than those of Class II.

### 4.3 Commercially Available Thermal Video Frame Scanners

There are many types of video frame scanners available for use in remote sensing applications. The design and characteristics of the following scanners will be discussed-

- (i) AGA Thermovision;
- (ii) Inframetrics IRTV;
- (iii) Barr & Stroud IR-18 MKII;
- (iv) Rank Pullin Controls (RPC) thermal imager; and
- (v) GEC Avionics/Rank Taylor Houbson TICM II.

The technical specifications of the above five scanners are given below in Table 4-1. The main source of information for each scanner was the manufacturer's brochure and the Patent specification. The main difference in the design of these scanners is the construction and operation of the scanning mechanism in conjunction with the detector configuration. In the remaining part of this Chapter, the scan mechanism of each of the above five scanners will be discussed in detail.

Scanner	AGA	Infra- metrics	IR-18	RPC	TICM II
Field of View	20°x20°	28°x21°	38°x25°	40°x30°	60°x40°
Spectral Band(μm)	8-14	8-12	8-13	8-13	8-13
IFOV (mrad)	3.4	2.0	1.73	2.1	2.27
MRTD (°C)	0.1	0.1	0.17	0.15	0.1
Detector	In Sb	CMT	SPRITE	SPRITE	SPRITE
No. of Detectors	1	2	4	8	8
Scanning Mode	Single	Par	Ser/Par	Ser/Par	Ser/Par
Video Format	Non-Stand	NTSC	PAL	PAL	PAL
Lines/frame	280	445	500	448	512
Pixels/line	70	400	384	333	384
Interlace	4:1	2:1	2:1	2:1	2:1

Table 4-1 Technical specifications of frame scanners



#### 4.3.1 AGA Thermovision

The AGA Thermovision (Fig.4-12) is a TV-incompatible thermal imager. As shown in Fig. 4-13a below, the scanning mechanism comprises two refractive prisms each with 8 facets. According to the manufacturer's brochure, the frame scanning element rotates at 180 rpm to scan the object line by line, while the line scanning element rotates at 18,000 rpm to scan each line pixel by pixel.



Fig.4-12 AGA Thermovision

The frame and line scanning elements are synchronised in such a way that four interlaced fields produce one complete frame of the scene as shown in Fig.4-13b. Each field comprises 100 lines, only 70 of which contain picture information. Each frame comprises 280 lines and each line contains 100 resolution elements. With 25 fields/sec, the framing rate is  $25/4 = 6.25$  frames/sec. This slow framing rate causes obvious difficulties when using the Thermovision from a moving platform such as an aircraft.

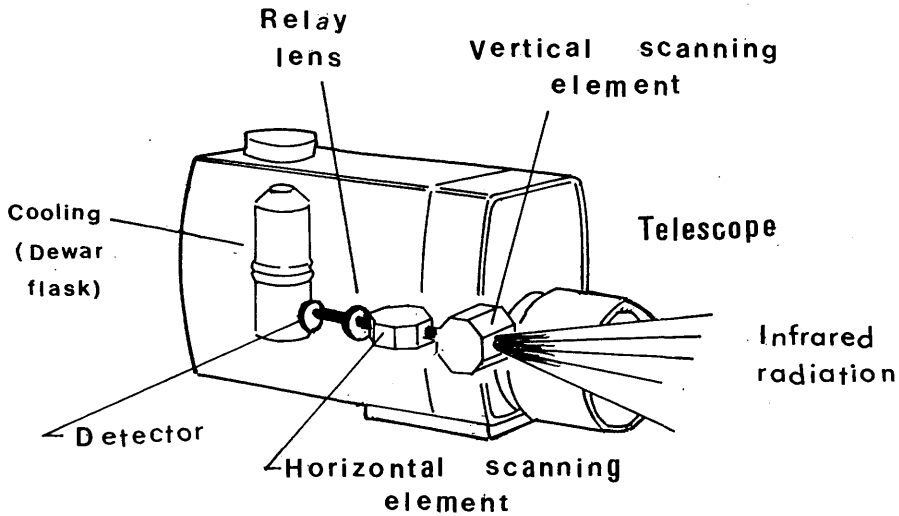


Fig.4-13a AGA Thermovision scan mechanism

The output from the scanner can be viewed directly on a 5" diagonal dedicated CRT or recorded on a non-standard VTR.

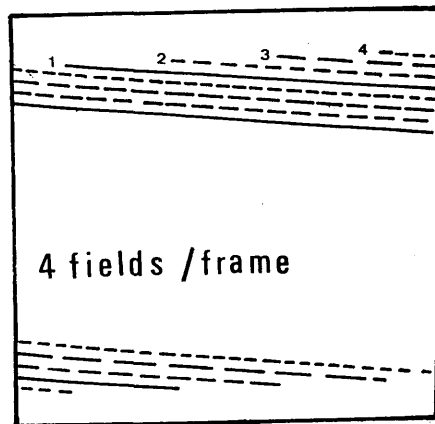


Fig. 4-13b AGA Thermovision scan pattern

#### 4.3.2 Inframetrics IRTV

The Inframetrics IRTV (Fig.4-14) is an American design, made originally to produce an NTSC video compatible image. Fig.4-15a depicts the scanning mechanism which, according to the patented design ( U.S. Patent No. 4,347,530), consists of two oscillating plane mirrors. The frame scanning mirror oscillates at a rate of 60 Hz, while the line scanning mirror is a resonant galvanometer oscillator which scans the object from left to right and then back from right to left at an oscillation rate of 3,933 Hz. The number of lines scanned per

frame is 445. Each line consists of 400 pixels. The scan pattern is shown in Fig.4-15b.



Fig.4-14 Inframetrics IRTV

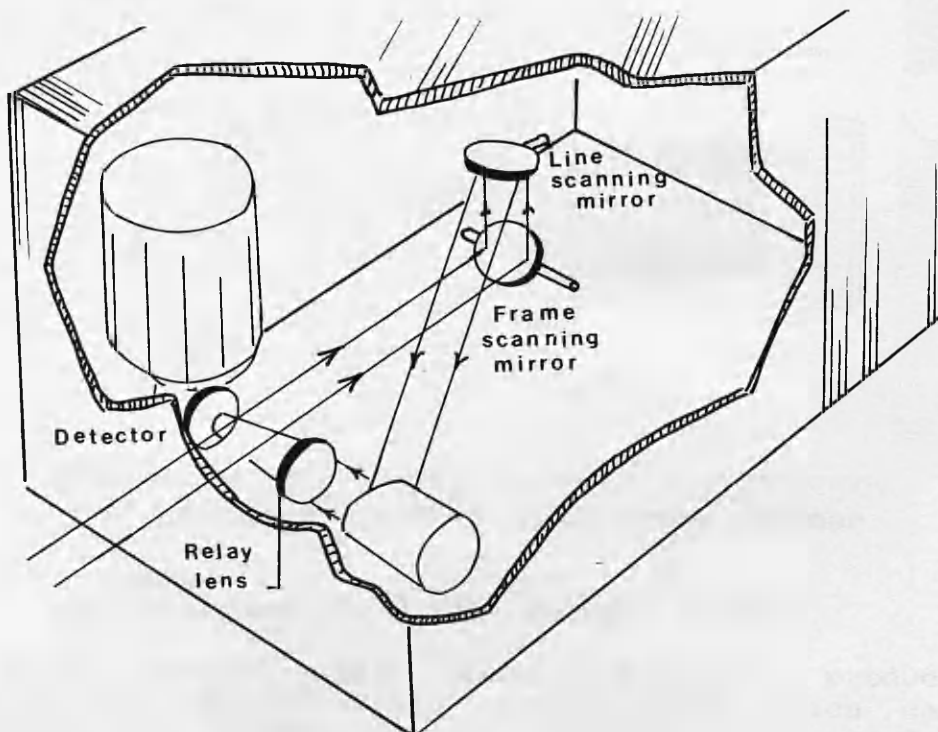


Fig.4-15a Inframetrics IRTV scanning mechanism

The outputs from the detectors are stored in RAMs and then read out in a raster mode to match the scanning characteristics of the NTSC standard TV system.

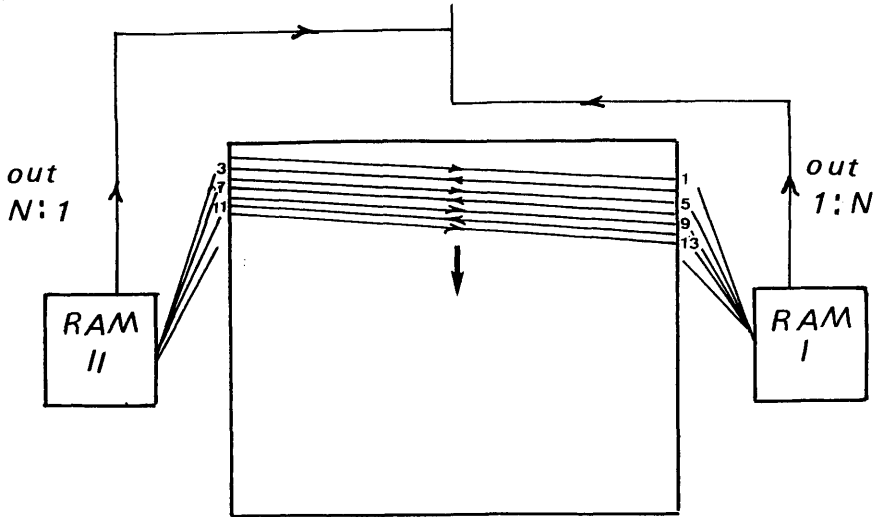


Fig.4-15b Inframetrics IRTV scan pattern

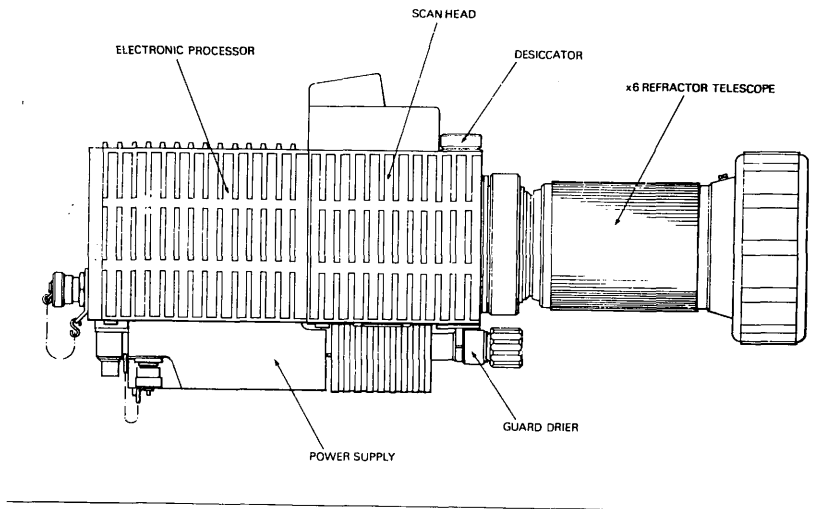


Fig.4-16 Barr & Stroud IR-18 frame scanner

#### 4.3.3 Barr & Stroud IR-18 MKII Thermal Imager

The IR-18 thermal imager, shown in Fig.4-16, produces a standard PAL TV-compatible video signal which can be displayed on a conventional video monitor or recorded on a standard VTR. The IR-18 is modular in design. However it does not use any of the TICM modules described above.

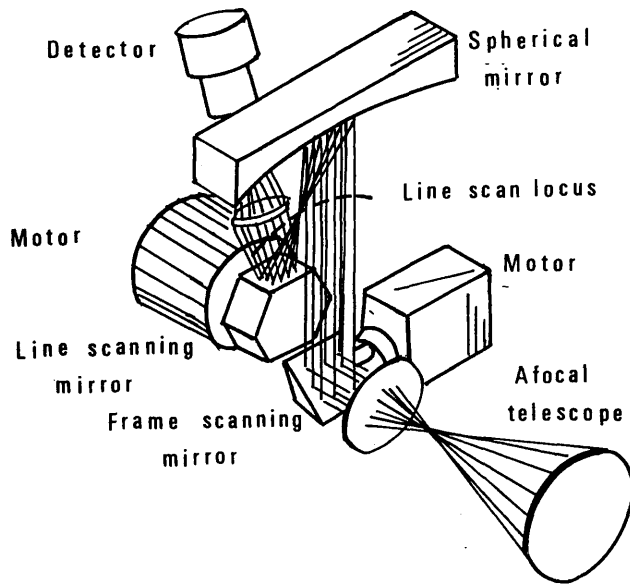


Fig.4-17a Barr & Stroud IR-18 scanning mechanism

The serial parallel scanning mechanism of the IR-18 (UK Patent no. 1,586,099) shown in Fig.4-17a, comprises an oscillating plane mirror and a 6 facet reflective prism. The oscillating plane mirror is a frame scanning mirror which oscillates at 50 Hz, while the reflective prism is a line scanning mirror which rotates at 39,000 rpm. With 4 detectors, the line scanning element completes the scanning of one field in 13 revolutions equivalent to 78 (13 x 6) facets. Each facet scans 4 lines simultaneously giving 312 lines/field, of which only 250 lines contain picture information. The scan pattern is shown in Fig.4-17b. The number of active lines scanned per frame is 500. Each line consists of 384 pixels.

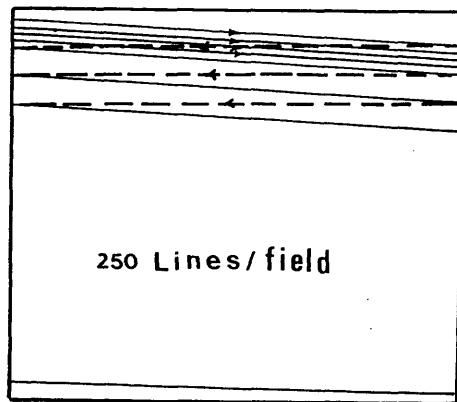


Fig.4-17b IR-18 scan pattern

#### 4.3.4 Rank Pullin Controls Thermal Imager

The configuration of the Rank Pullin Controls (RPC) thermal imager is shown in Fig.4-18 below. The scanning mechanism (UK Patents 2,110,897 and 2,1110,897 B) comprises two co-axial rotating reflective polygons as shown in Fig.4-19a.



Fig.4-18 Rank Pullin Controls thermal imager  
(two scanners with different telescopes)

The frame scanning is carried out by a 7 facet prism which rotates at 12,000 rpm, while the line scanning is achieved by an 8 facet prism rotating at 10,500 rpm. The rotations of the two polygons produce 56 (7x8) combinations of facets. With the use of 8 detectors, this results in 448 (56 x 8) lines/frame, of which only 416 lines contain picture information.

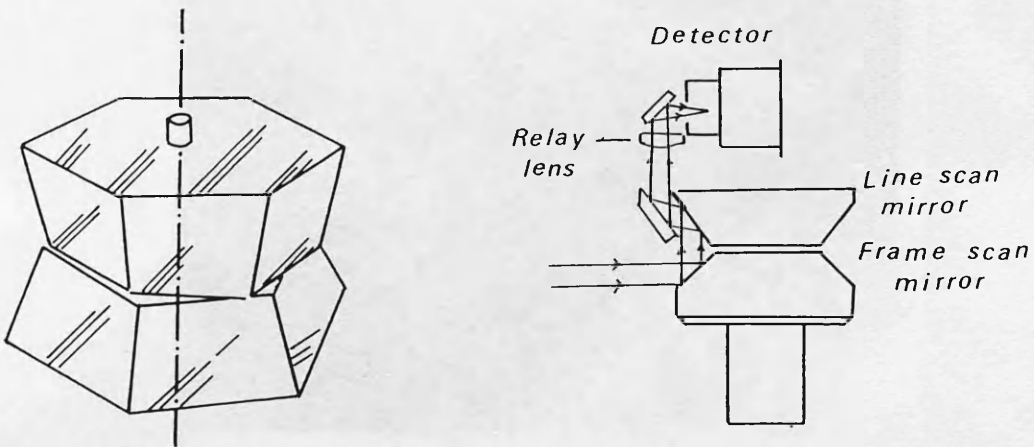


Fig.4-19a Scanning mechanism of the RPC frame scanner

As a result of the scanning method adopted, the output from the scanner is not a TV-compatible video signal since the scanning mechanism switches from odd to even field every four swaths of 8 lines as shown in Fig.4-19b. To display the image on a standard video monitor, the output from the scanner has first to be fed into a standard frame buffer, so that the odd and even fields of each frame are re-assembled and read out in the order which corresponds to the standard TV scan pattern.

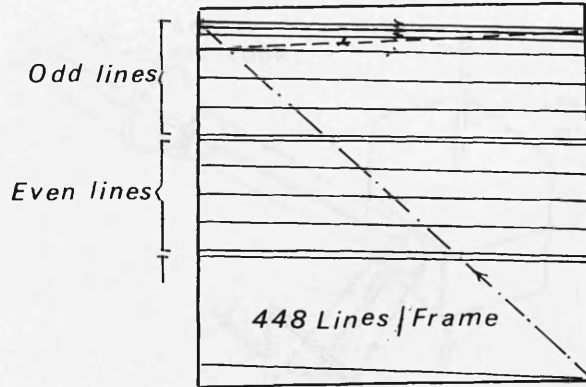


Fig.4-19b RPC scan pattern

#### 4.3.5 GEC Avionics/Rank Taylor Hobson TICM II

This imager is currently being produced jointly by GEC Avionics and Rank Taylor Hobson utilising Class II common modules. The design details were obtained from Crandon, 1985. The configuration of the scanner is shown in Fig.4-20.



Fig.4-20 GEC Avionics/ Rank Taylor Hobson TICM II

The scanning mechanism of the TICM II is shown in Fig.4-21a. The line scanning element is a 6 facet reflective prism which rotates at 19,500 rpm, while the frame scanning element is an oscillating plane mirror which oscillates at 50 Hz. The scanning mechanism produces 39 swaths per field, each swath consisting of 8 lines as shown in Fig.4-21b. This results in 312 lines/field of which only 256 contain picture information.

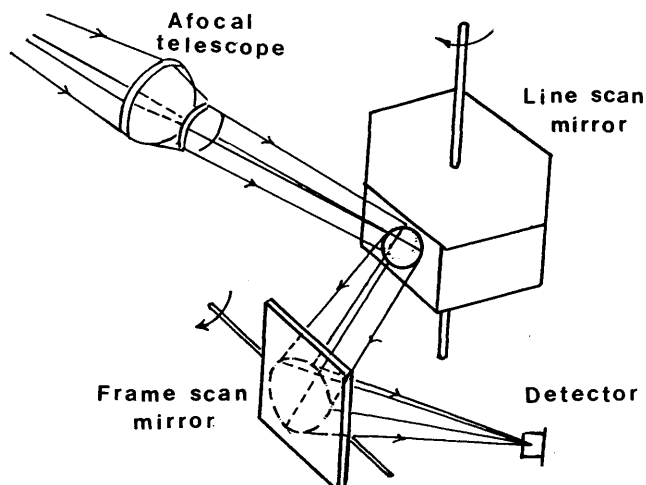


Fig.4-21a TICM II scanning mechanism

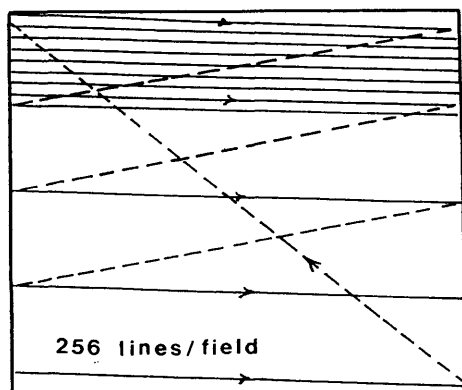


Fig.4-21b TICM II scan pattern

As can be seen from the above discussion, although the construction and hence the operation of the frame scanner, may be similar in one way or another to each of the other sensors discussed in the previous Chapters, in total it has its own unique geometrical characteristics. In the next Chapter, the analysis of these geometrical characteristics will be presented.



**CHAPTER V**  
**GEOMETRICAL ANALYSIS OF VIDEO COMPATIBLE**  
**FRAME SCANNER IMAGERY**

The first step in the analysis of video compatible frame scanner imagery is the identification of the geometric features that are present in the image. This is done by examining the image for lines, curves, and other geometric shapes. The next step is to measure the lengths and angles of these features. This is done by using a ruler and a protractor. The final step is to compare the measured values to the known values for the features. This is done by using a table of known values.

The second step in the analysis of video compatible frame scanner imagery is the identification of the geometric features that are present in the image. This is done by examining the image for lines, curves, and other geometric shapes. The next step is to measure the lengths and angles of these features. This is done by using a ruler and a protractor. The final step is to compare the measured values to the known values for the features. This is done by using a table of known values.

## CHAPTER V

### GEOMETRICAL ANALYSIS OF VIDEO-COMPATIBLE

#### FRAME SCANNER IMAGERY

##### 5.1 Introduction

In the previous chapters, the principle, construction and operational characteristics of the vidicon tube camera, the photogrammetric frame camera, the panoramic frame camera and the optical mechanical scanner were presented. From this prior discussion, the following points may be taken:-

- (i) Like the photogrammetric frame camera, frame scanners produce a perspective view of the object. However, while the photogrammetric camera images all the terrain objects simultaneously and almost instantaneously (exposure time between 1/500 to 1/1,000 sec in a single frame), frame scanners sequentially scan the object in a raster scanning mode over a scanning time of 1/25 sec per frame.
- (ii) Panoramic frame cameras produce a frame image by rotating a lens-slit assembly ( or prism in front of a fixed lens) to scan the terrain in the cross-track direction. By contrast, the frame scanner produces a frame video image by scanning the terrain in both the along-track and cross-track directions using two optical mechanical scanning mirrors, each of which scans in one direction.
- (iii) The output from the frame scanner is usually a TV-compatible video image which has many of the same characteristics as the video image produced by the vidicon tube camera. However, the vidicon tube camera scans the image of the object already exposed simultaneously onto the faceplate of the camera tube. Thus the scanning takes place in the image plane. On the other hand, the frame scanner sequentially scans in the object space using an optical-mechanical scanning mechanism, the intensity of each pixel being determined by a solid-state detector.
- (iv) Optical mechanical line scanners scan the object in one direction using a plane mirror oscillating in the object plane, while the forward motion of the platform advances the scan pattern to build up a

single strip image. By contrast, frame scanners scan the object in two dimensions in the object space using two scanning mirrors to produce individual video frame images which are not dependent on the motion of the platform.

It can be seen from the above discussion that, in certain specific ways, the principle and operational characteristics of the frame scanner have similarities to each of the above mentioned sensors. Therefore the geometrical characteristics of the frame scanner images will include certain characteristics of the images produced by all these varying different sensors. At the same time, the combination of these characteristics produces images with a geometry which is unique to frame scanners. The definition of, and investigation into these characteristics is an important part of the present research project.

### 5.2 Geometry of the Photogrammetric Frame Camera

The geometry of the frame camera is shown in Fig.5-1. The entire format is exposed through a lens whose optical axis is fixed relative to the focal plane. Exposure time is controlled by a shutter and the film is normally held stationary in the focal plane during the exposure time, although in appropriate circumstances it may be moved to compensate for image motion during the exposure time.

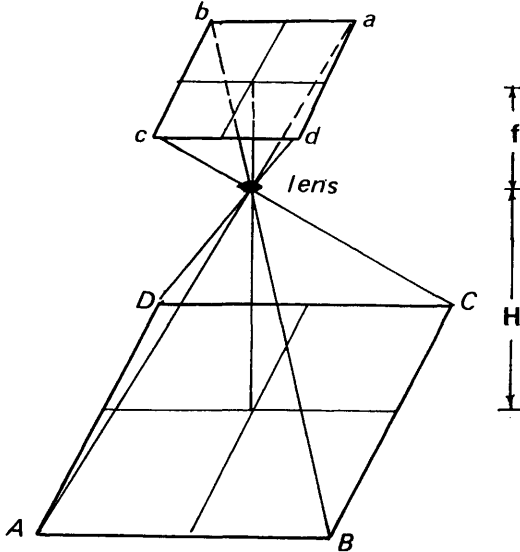


Fig.5-1 Geometry of the photogrammetric frame camera

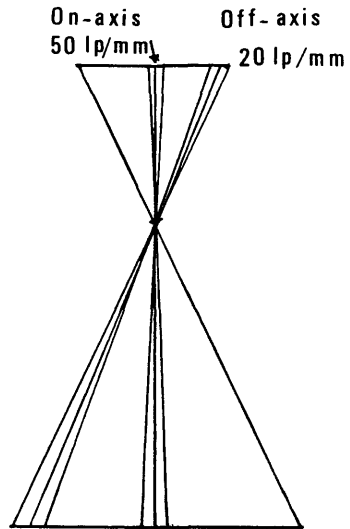


Fig.5-2 Image resolution

The resultant photograph will have a high resolution especially around the centre area of the format (typically 40 to 50 line pairs/mm for low contrast images) since the imaging is on-axis as shown in Fig.5-2 above. However, the image resolution will deteriorate towards the edges of the format where the imaging is well off-axis.

The image produced by a vertically pointing photogrammetric frame camera will also have a constant scale provided that the terrain lies in the horizontal plane. If relief is present, the resulting displacement is radial from the nadir point of the photograph. A most important point is that stereo-coverage is achievable by overlapping successive frame photographs in a suitable manner.

These characteristics have made the photogrammetric frame camera the most suitable form of aerial imagery if very high accuracy mapping is required.

### 5.3 Geometrical Characteristics of the Panoramic Frame Camera

The geometry of the panoramic frame camera is shown below in Fig.5-3.

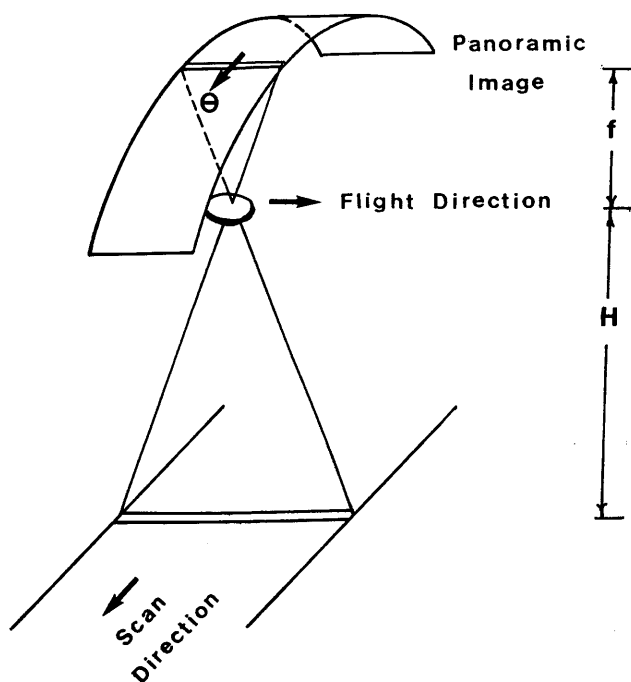


Fig.5-3 Geometry of the panoramic frame camera

The image produced by a panoramic frame camera has a very high resolution (around 100 line pairs/mm). However, the resolution of the panoramic frame camera does not deteriorate towards the edges of the photograph, since the imaging is always on-axis due to the rotation of the lens-slit assembly.

Arising from the geometry of scanning, the panoramic camera image has the following types of distortion:-

- (i) Panoramic distortion. This is the displacement of images of ground points from their normal perspective position due to the cylindrical shape of the negative film platen and the sweeping action of the optics. Considering a grid of unit-sized squares laid out on flat terrain, the resultant panoramic photograph will appear as in Fig.5-4a.

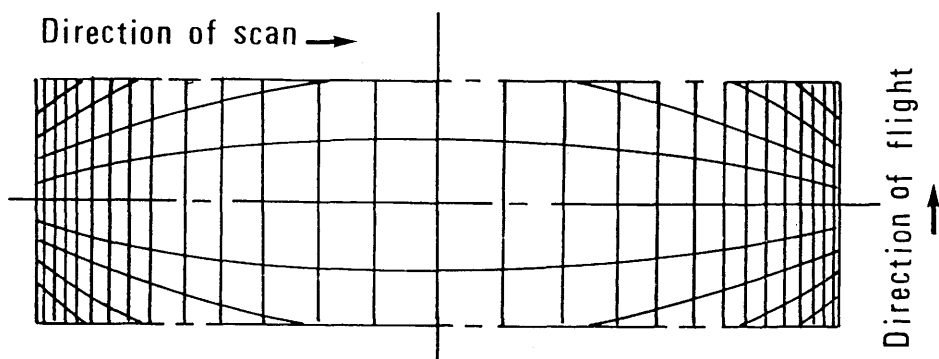


Fig.5-4a Panoramic distortion

- (ii) Sweep positional distortion. This is defined as the displacement of the images of ground points from their expected cylindrical position due to the forward motion of the platform during the frame scan time. This effect is shown in Fig.5-4b.

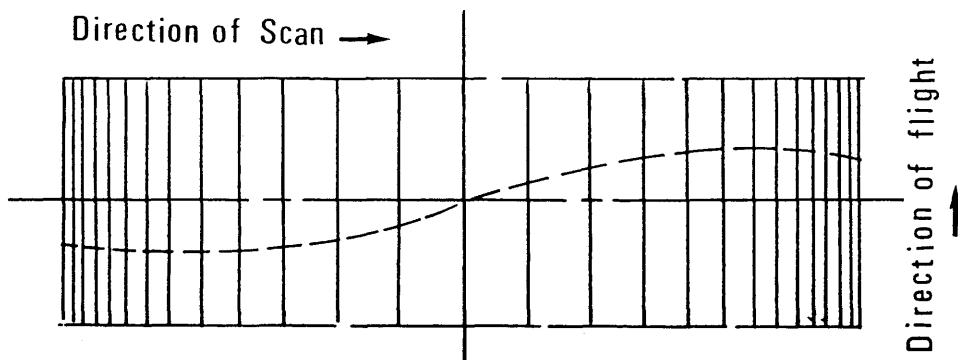


Fig.5-4b Sweep positional distortion

- (iii) Image motion compensation distortion. This results from the displacements of images of ground points from their expected cylindrical position due to the translation of the lens or the focal plane which is used to compensate for image motion during the frame scan time. This effect is shown in Fig.5-4c

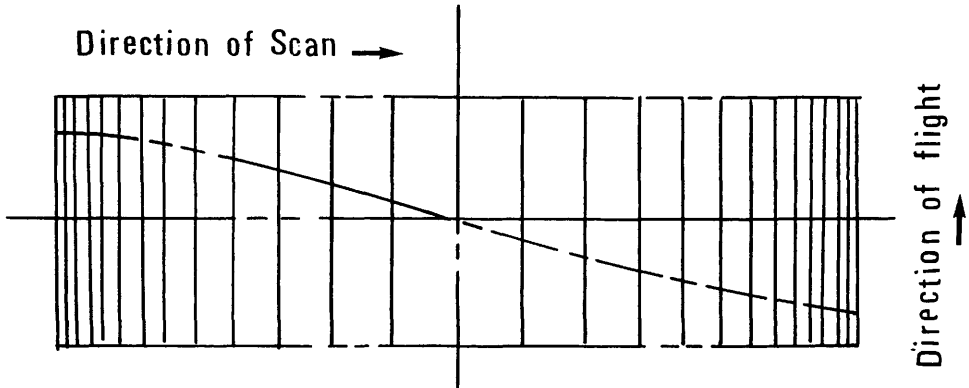


Fig.5-4c Image motion compensation distortion

The combined effect of the above mentioned types of distortion is shown below in Fig.5-4d

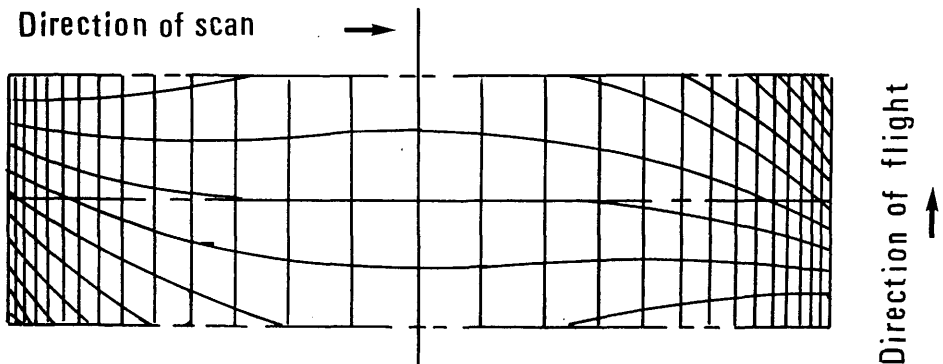


Fig.5-4d Combined geometrical distortion in panoramic frame camera imagery

#### 5.4 Geometry of the Vidicon Tube Camera Imagery

Vidicon tube camera imagery is generated instantaneously, since the image of the object is first focussed on the camera faceplate and stays there for 1/25 sec, during which the intra-lens shutter blocks any light from falling on the tube while the electron beam of the vidicon tube scans the camera faceplate

Thus basically, the geometry of the vidicon tube camera imagery corresponds to the geometry of the photogrammetric frame camera. Difficulties only arise from electronic distortion which must be eliminated by proper calibration. This area has been investigated thoroughly by Wong (1968, 1972).

### 5.5 Geometry of Line Scanner Imagery

The geometry of line scanner imagery is shown in Fig.5-5. The oscillating plane mirror scans in the cross track direction in a panoramic scanning mode, while the forward motion of the platform allows for the successive scan lines to build up a continuous strip image which will take a cylindrical shape.

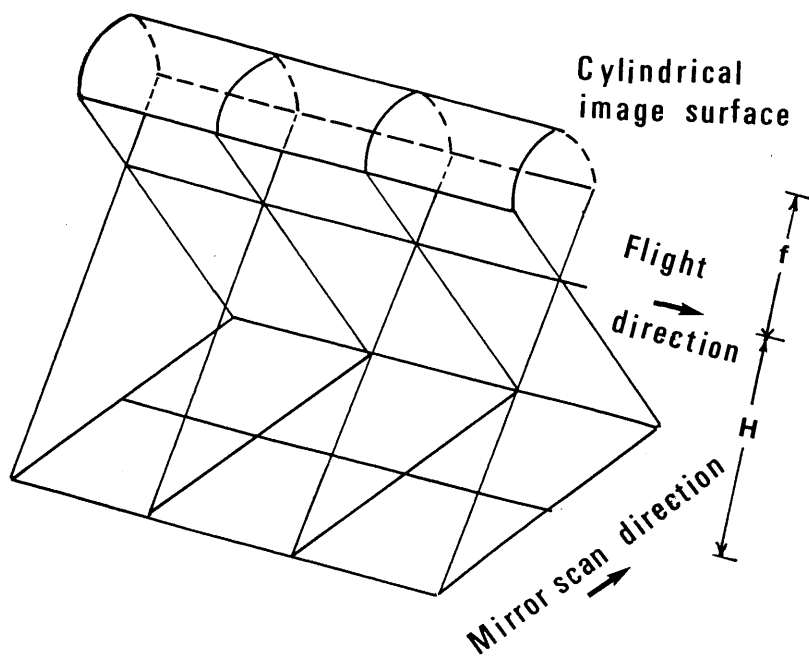


Fig.5-5 Geometry of the optical-mechanical line scanner

In the cross flight direction, (i.e. in the mirror scan direction) the instantaneous area scanned by the scanner is a function of the flying height ( $H$ ), the IFOV ( $\alpha$ ) and the scan angle ( $\beta$ ). This area is represented on the reproduced image by a constant pixel size equal to  $f\alpha$ , where  $f$  is the equivalent focal length of the scanner as shown in Fig.5-6a. This is done regardless of the scan angle. The result is a gradual decrease in the image scale away from the centre of the strip in the y-direction as shown in Fig.5-6b.

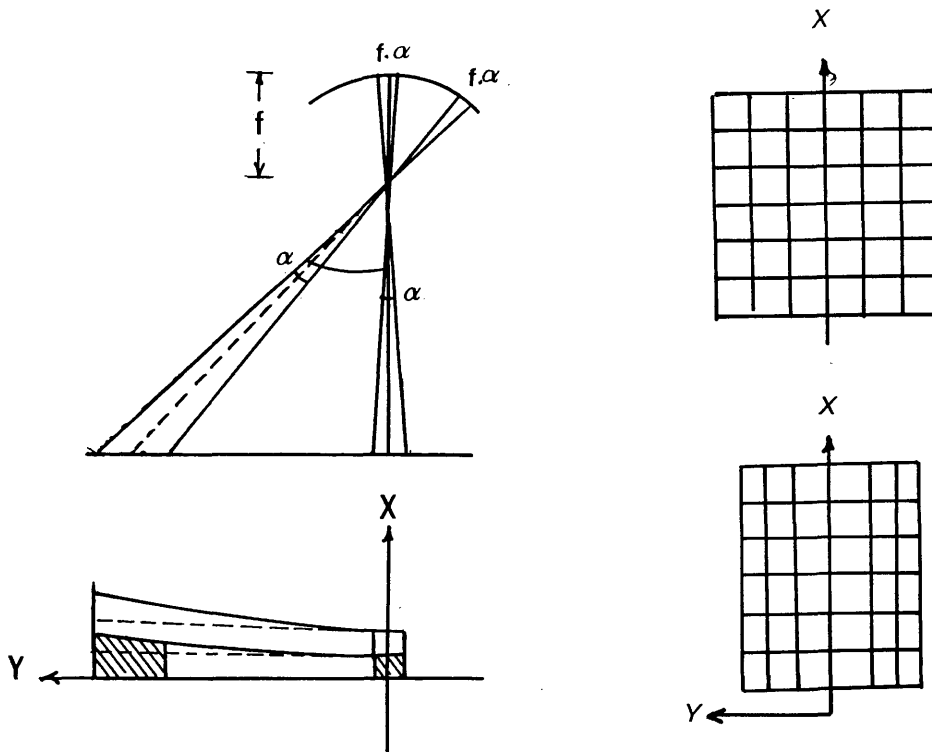


Fig.5-6a Panoramic scan effect. Fig.5-6b Scale change

In the flight direction (X-direction), the dimension of the instantaneous area imaged in a single scan also increases away from the centre of the strip. If the scanned strips are continuous on the ground along the centre line, successive scanned lines or strips will overlap away from the centre line and this will result in a constant scale along the image x-direction.

The image produced by line scanners will have low resolution when compared to the photogrammetric or panoramic frame camera since photographic films are far more sensitive than detectors. However, like the panoramic frame camera, the (angular) image resolution is constant over the strip since the scanning is always carried out on-axis.

In airborne line scanner imagery, the platform motion effects (pitch, yaw, roll and drift) may cause gaps or double imaging which is very difficult to deal with. However, these effects are not so serious with space-borne scanner imagery since the satellite moves in the near vacuum of space.

## 5.6 Geometrical Analysis of Video-Compatible Frame Scanner Imagery

Despite the differences in design between the various types of video compatible frame scanners, (e.g. in the arrangement and number of detector elements used or the type and speed of the scanning mechanism), they are all based on the same



principle in which two mirrors are used to move the sensitive area of the detector in the image space so that the image of the object formed by the telescope at infinity is completely scanned.

Thus, although the geometrical analysis in this section, is concerned especially with the Barr & Stroud IR-18 frame scanner, it should also be applicable to any other video compatible frame scanner.

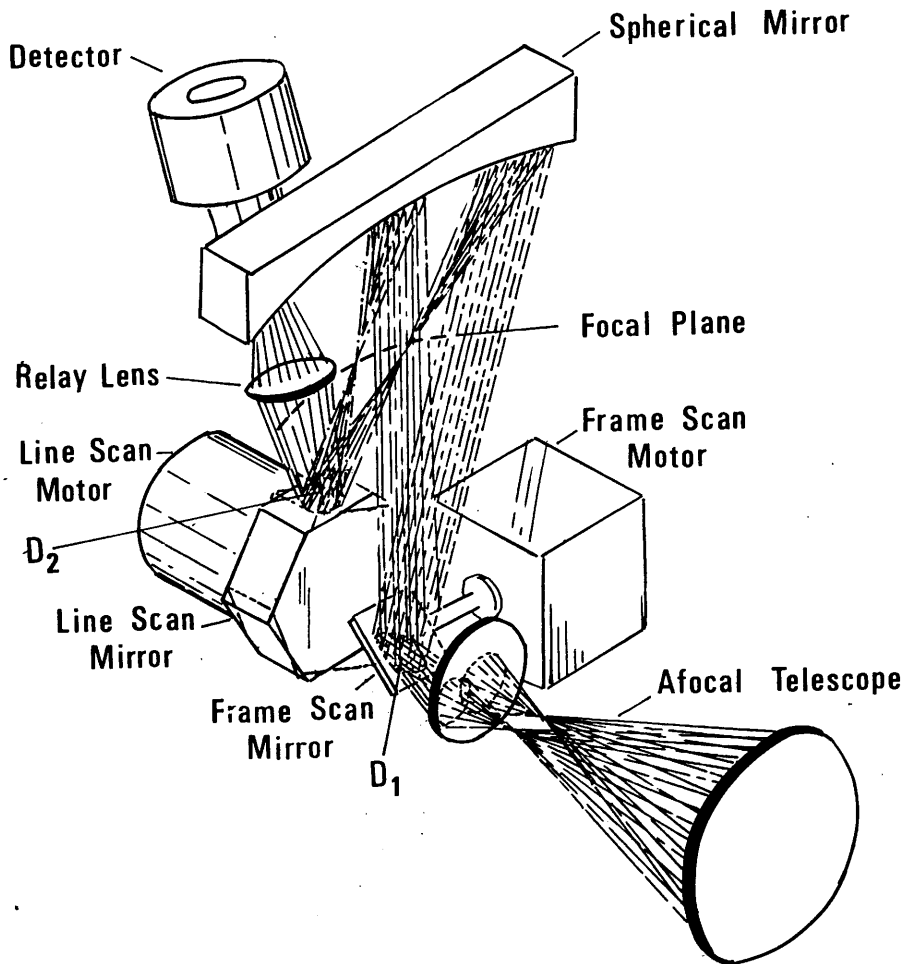


Fig.5-7 Barr & Stroud IR-18 scanning technique

### 5.6.1 Scanning Technique of the IR-18 Frame Scanner

According to the Patent lodged by the manufacturer (UK Patent number 1 586 099 ), the image of the objects within the field of view of the scanner is produced in the following way:-

- (i) An afocal telescope collects and focusses the emitted radiation from the object onto the frame scanning mirror which is driven to oscillate at 50 Hz. At any particular moment, the mirror will be directed towards a small area on the object whose angular size is defined by the scanner's IFOV. The size of the image of this elemental area on the frame scanning mirror is known as the frame scanning pupil (shown as  $D_1$  in Fig.5-7).
- (ii) The image  $D_1$  is reflected by the frame scanning mirror towards a spherical mirror which in turn focusses the image onto a spherical focal plane.
- (iii) The line scanning mirror, which is a hexagonal (6 faced) prism is caused to rotate about its axis by the line scan motor at a rate of 39,000 rpm, so that it scans the focal plane of the spherical mirror in such a manner that, at any rotational position, the principal axis forming the image defined on the frame scan pupil ( $D_1$ ) always passes through the centre of the line scan pupil (shown as  $D_2$  in Fig.5-7).
- (iv) The image reflected by the line scan mirror is focussed by the relay lens onto the sensitive area of the detector.
- (v) As mentioned in the previous Chapter, the IR-18 uses four SPRITE detectors. Thus, in effect, the line scan mirror is scanning 4 parallel lines at any moment. When the first four lines have been scanned, the frame scan mirror changes the angle of view so that the line scan mirror starts the scanning of the next four lines in the field pattern (since interlaced scanning is employed), until the whole field is scanned. Then the process is repeated to scan the next field.
- (vi) The outputs from the four SPRITE detectors are stored in analogue form in a CCD storage unit and then read out in a raster format which corresponds to the standard CRT scanning pattern.

As can be seen from the above discussion, the magnified image of the object formed by the telescope in the image space is scanned by the detector to produce a perspective image of the object. As this scanning is actually achieved by two mirrors, each of which scans in a similar manner to that of the line scanner mirror, the resultant video image will take the form of a spherical surface with all points equidistant from a single central point (O) as shown in Fig.5-8.

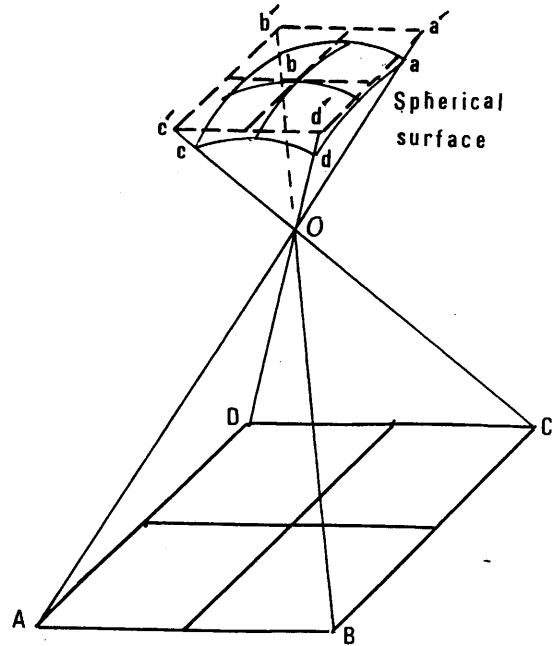


Fig.5-8 Image geometry of Barr & Stroud IR-18 frame scanner

### 5.6.2 Video Image Characteristics

The output from the IR-18 is a PAL TV-compatible video image. As has been mentioned in Chapter II, the PAL system produces two interlaced fields to form one complete frame. The number of lines in a single PAL frame is 625, of which only 575 contain picture information. Thus each frame will consist of 575 x 767 pixels, and each field will consist of 287.5 x 767 pixels on the video display.

However, the IR-18 frame scanner produces only 500 lines per frame leaving a further 75 blanked lines on the display to allow for the incorporation or addition of text or other symbols. This is a common feature in almost all frame scanners.

With 500 lines per frame, each field will consist of 250 x 767 pixels. The 250 lines are interlaced on the display by another 250 blank lines, which means that the actual size of the field on the display is 500 TV lines of which only 250 lines contain picture information, each line consisting of 767 pixels. On the other hand, the number of ground resolution elements scanned per line consists of 384 elements. Thus it can be seen that each ground resolution element is represented on the video display as two pixels.

It can also be seen from the scan pattern (Fig.4-17b) that the scan lines are not parallel to the edge of the frame. In

fact this seems to be a common feature in all video compatible images. This is likely to cause lack of orthogonality between the frame scan and the line scan directions on the display. However, it is not a serious matter and it can be easily corrected for by the use of a simple affine transformation.

As shown in Fig.5-9, the field of view of the frame scanner is defined by two angles. The smaller angle subtends the object in the frame scan direction while the bigger one subtends the object in the line scan direction. Throughout the discussion in this Chapter, these two angles will be defined as  $\beta$  and  $\theta$  respectively, while the IFOV will be defined as  $\alpha$ .

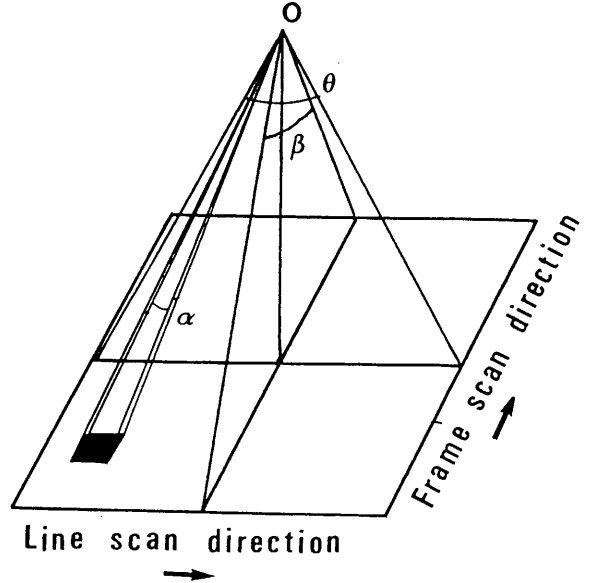


Fig.5-9 Field of view

### 5.6.3 Ground Resolution

The ground resolution at a specific point produced by a frame scanner is a function of the flying height ( $H$ ), the two scanning angles ( $\beta, \theta$ ) and the IFOV ( $\alpha$ ).

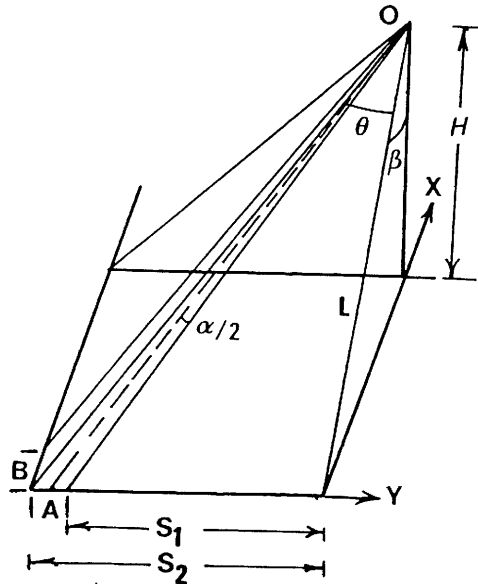


Fig.5-10 Ground resolution of frame scanners

In Fig.5-10, the size of the ground resolution element in the line scan direction ( $Y$ -direction) can be computed as

follows:-

$$L = H \sec \beta$$

$$S_1 = L \tan (\theta - \alpha/2)$$

Where L, S<sub>1</sub> and S<sub>2</sub> as defined in Fig.5-10.

$$S_1 = L \frac{\tan \theta - \tan \alpha/2}{1 + \tan \theta \tan \alpha/2}$$

$$S_2 = L \tan (\theta + \alpha/2)$$

$$= L \frac{\tan \theta + \tan \alpha/2}{1 - \tan \theta \tan \alpha/2}$$

Since  $\alpha/2$  is a very small angle,  $\tan \alpha/2$  may be substituted by  $\alpha/2$  ;

$$S_1 = L \frac{\tan \theta - \alpha/2}{1 + \alpha/2 \tan \theta}$$

$$S_2 = L \frac{\tan \theta + \alpha/2}{1 - \alpha/2 \tan \theta}$$

$$\text{Then } A = S_1 - S_2$$

where A is the size of the ground resolution element in the cross flight direction.

$$A = L \cdot \alpha \frac{1 + \tan \theta}{1 - \alpha^2 \tan^2 \theta}$$

In the above equation,  $\alpha^2 \tan^2 \theta$  may be neglected since  $\alpha^2$  is very small. Substituting for L, then

$$A = H \sec \beta \cdot \alpha (1 + \tan^2 \theta)$$

$$A = H \sec \beta \sec^2 \theta \cdot \alpha \quad \dots\dots\dots 5-1$$

In the same manner, the size of the ground resolution element in the frame scan direction (X-direction) can be found to be-

$$B = H \sec \theta \sec^2 \beta \cdot \alpha \quad \dots\dots\dots 5-2$$

Fig.5-11 below shows the changes in the ground resolution in both the line and frame scan directions for a given flying height (H=1,000 m) and a frame scanner having an angular resolution (IFOV) of 1.73 mrad.

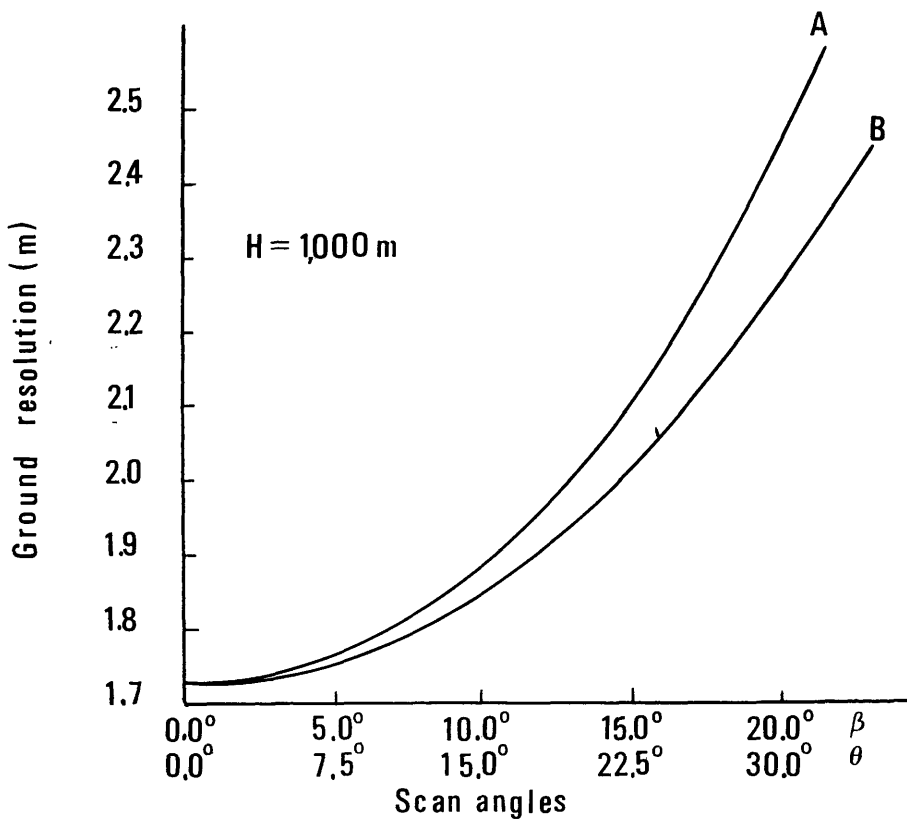


Fig.5-11 Ground resolution along the diagonal of the area covered by a single image of a frame scanner

#### 5.6.4 The Effect of Ground Speed, Flying Altitude, and Field Scan Time on the Image Geometry

An important factor that may well affect the geometry of the video image produced by the frame scanner is the image movement occurring during the field scan time. Any movement by the scanner during the scan time may cause a degradation of the image. This image degradation depends on the following factors:-

- (i) image scanning time;
- (ii) platform speed;
- (iii) flight altitude; and
- (iv) ground resolution of the scanner.

The scanner movements may be classified into two groups- angular movement and linear movement. An angular movement is a tilt of small order resulting from the aircraft vibrations and aerodynamic forces acting on the aircraft. This type of movement will be dealt with by analytical photogrammetric techniques in Chapter VIII. On the other hand, the linear movements, or translations of the frame scanner result mainly from the rapid forward movement of the aircraft, but smaller sideways linear movements are produced by the aerodynamic forces acting on the platform.

As mentioned above, the IR-18 produces 250 lines/ field. The scan time for a single line in the PAL standard systems is 64  $\mu$ s (microsecond). Thus the field scan time is 0.016 sec (excluding the framing mirror flyback time).

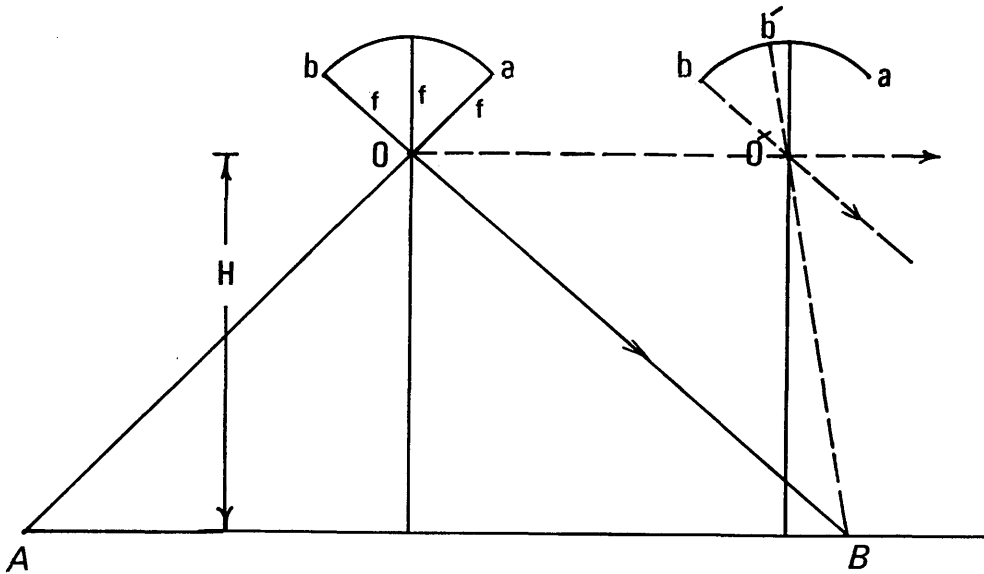


Fig.5-12 Image displacement caused by the platform forward motion during the image scan time

In Fig.5-12, if the whole object was scanned while the scanner was at position O, the perspective geometry of the image would not be disturbed and the ground points A,B would appear at their respective positions a,b in the spherical image plane. However, the scanning starts from the position where the image point a was recorded, but by the time the image point b is to be recorded, the scanner will have moved from position O to position O' and the image of the ground point B will be recorded at b' rather than at b as it would with a simple perspective projection.

Thus the forward motion of the aircraft has introduced a displacement in the x-direction of the spherical image plane equal to bb'. In effect, all the image points are displaced from their true perspective position. This displacement is a function of the image scale, the ground velocity of the platform and the scanning time. The x-image displacement is given by:-

$$dx_b = 1/S \cdot V \cdot T_b \dots\dots\dots 5-3$$

Where:-

$dx_b$  is the x-image displacement of point b;

S is the scale number;  
 V is the platform ground speed; and  
 $T_b$  is the scan time from the beginning of the field scan until the image point b has been recorded.

The scan time  $T_b$  can be divided into scan time in the frame direction and scan time in the line direction. Referring to Fig.5-13, the scan time in the frame direction is the time from the beginning of the field scan (i.e. when line  $L_a$  was recorded) until the line on which point b lies (line  $L_b$ ) is to be recorded, while the scan time in the line direction is the time from the scanning of the first pixel on line  $L_b$  until the image point b is recorded.

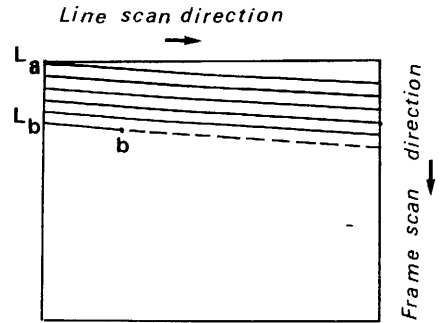


Fig.5-13 Line and frame scan time

The time required to scan a single line is  $64 \mu s$ , of which  $12 \mu s$  are used for the mirror flyback leaving  $52 \mu s$  for the actual scan. Thus:-

$$T_b = T_{f_b} + T_{l_b}$$

Where:-

$T_{f_b}$  is the elapsed scan time to reach point b in the frame scan direction; and

$T_{l_b}$  is the elapsed scan time to reach point b in the line scan direction.

and;

$$T_{f_b} = 64 \cdot x_b \mu s$$

$$T_{l_b} = 52 \cdot \frac{y_b}{384} \mu s$$

Then;

$$T_b = 0.135 (472.32 x_b + y_b) \mu s \dots\dots\dots 5-4$$

Substituting in equation 5-4, and considering the image coordinates in pixels, the focal length in pixels, the flying height in metres, and the ground speed in metres per second, then:-



$$dx_b = 1.35^{-7} \cdot f/H \cdot V \cdot (427 x_b + y_b) \quad \text{pixel} \dots\dots 5-5$$

Assuming a scanner focal length of 800 pixels, the maximum image displacement during the field scan time, and the line scan time, are shown below in Table 5-1 for airborne and spaceborne imagery.

Platform ground speed (m/sec)	Maximum displacement during the line scan time (52 μs) (pixel)	Maximum displacement during the image scan time (0.016 sec) (pixel)
100 (Airborne H = 1,000 m)	.005	1.28
8,000 (Spaceborne H = 200 Km)	.002	0.512

Table 5-1 Image displacement during the frame and line scan time

As can be seen from the table above, the image displacement during the line scan time is very small and can be neglected. Thus equation 5-5 can be reduced to the following form-

$$dx_b = 64^{-5} \cdot f/H \cdot V \cdot x_b \quad \text{pixel} \dots\dots\dots 5-6$$

However, the scanner can be mounted on the platform so that the frame scanning mirror may move in one of four directions relative to the flight direction. The image displacement in those four cases is shown in Fig.5-14 below relative to an image coordinate system in which the x-axis is taken as the frame scan direction, while the y-axis is taken as the line scan direction.

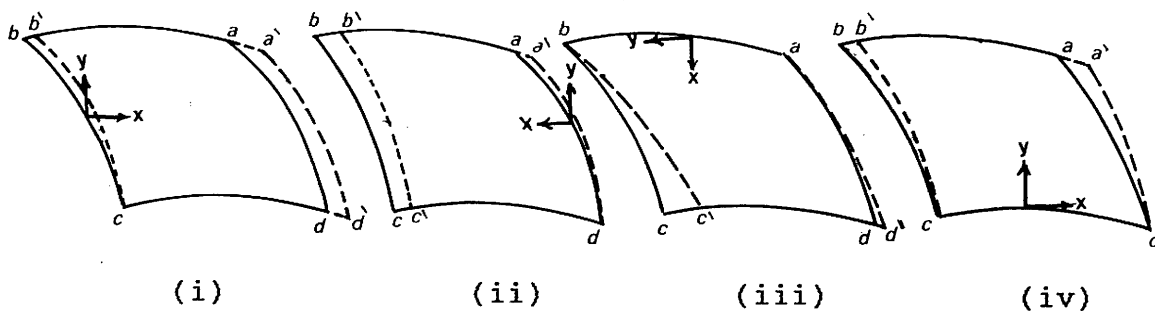


Fig.5-14 Effect of the craft forward motion on the image geometry at different scan directions

Since the video image has a rectangular format, in cases (i) and (ii) where the frame mirror scans parallel to the flight direction, the longer side of the format will be across the flight direction and the image will be elongated (case (i)) or compressed (case(ii)) along the x-direction. In both cases the image will be slightly twisted in the y-direction. In the other two cases where the frame mirror scans across the flight direction, the longer side of the format will be parallel to the flight direction and in both cases the image will be twisted along the x-direction.

In order to simplify the analysis, let the image displacement be expressed as a function of the image coordinates relative to the geometric centre of the video image. This situation is shown in Fig.5-15.

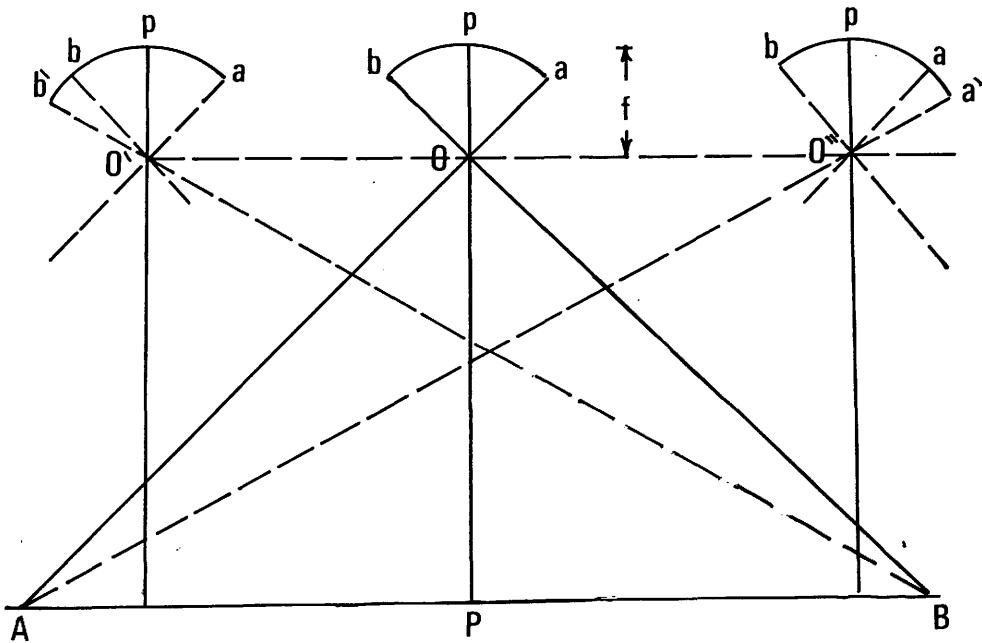


Fig.5-15 Scanning of the object during the platform forward motion relative to the geometric centre

The four cases (i) to (iv) considered above can now be replotted to produce the following diagrams.

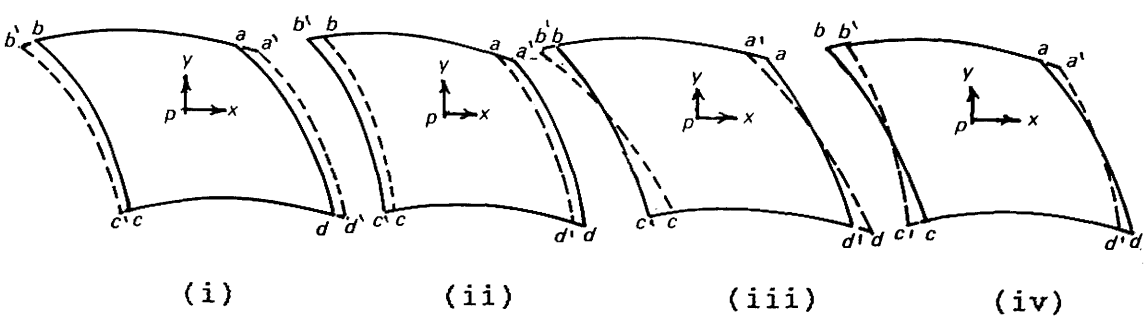


Fig.5-16 Image displacement due to the sequential scanning relative to the geometric centre of the video image

The above discussion was based on flat terrain. In the case of mountainous terrain however, the photo scale varies with the height ( $\pm dh$ ) of the point considered relative to the average terrain height and equation 5-6 will be rewritten as

$$dx_b = 64^{-5} \cdot f / (H + dh) \cdot V \cdot x_b \quad \text{pixel} \quad \dots\dots\dots 5-7$$

**5.6.5 Effect of Scanning Technique**

In Fig.5-17 point (a) was recorded in the spherical video image with coordinates  $x, y$ . Its corresponding image coordinates in the plane tangential to the video image at its geometric centre are  $x^{\bar{}}, y^{\bar{}}$ . The corrected image coordinates of any point (a) can be computed as follow:-

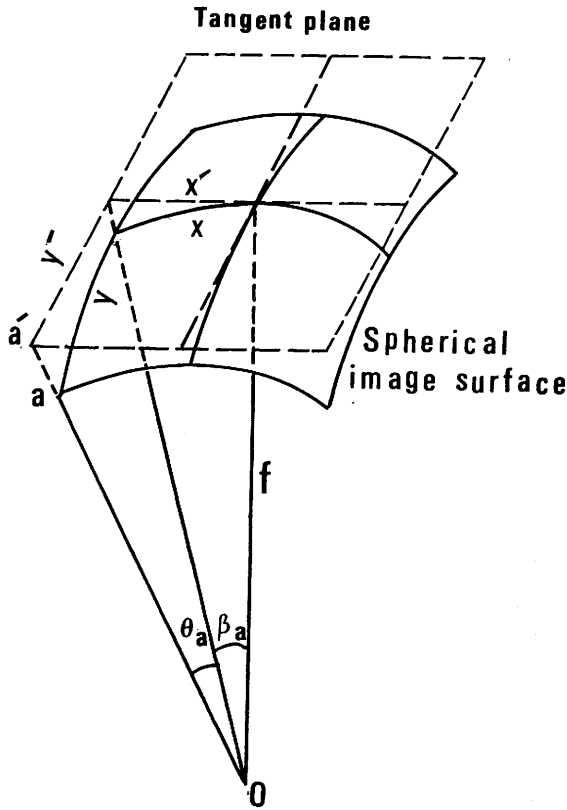


Fig.5-17 Spherical distortion in frame scanner image

$$\beta_a = x_a / f$$

$$\theta_a = y_a / f$$

$$x_a^{\bar{}} = f \tan \beta_a \quad \dots\dots\dots 5-8$$

$$y_a^{\bar{}} = f \tan \theta_a \sec \beta_a \quad \dots\dots\dots 5-9$$

Where:-

$\beta, \theta$  are the two scan angles for point a in the frame and line scan directions respectively; and

f is the equivalent focal length of the scanner.

The effect of the spherical distortion on the image is a gradual change in scale in the x and y directions from the geometric centre of the image as shown in Fig.5-18.

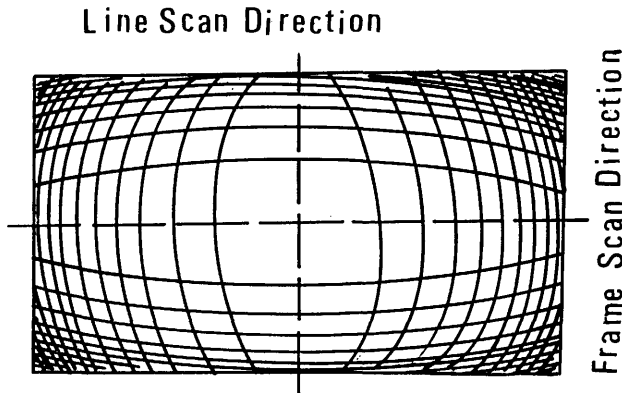


Fig.5-18 Spherical distortion of frame scanners

The combined effect of the spherical distortion and the image motion distortion is shown below in Fig.5-19.

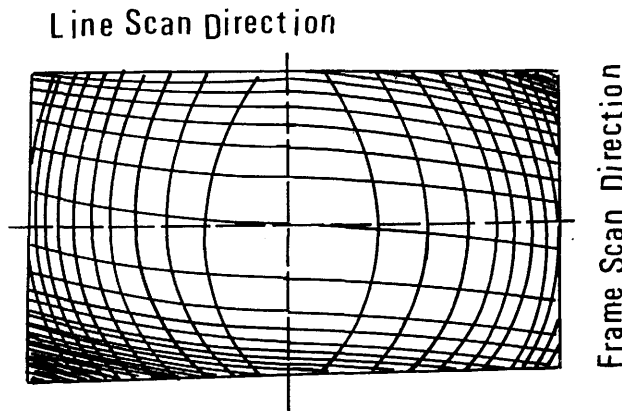


Fig.5-19 Combined effect of spherical and image motion distortion in frame scanner imagery

It can be seen from the above discussion that the video image produced by frame scanners will have the following characteristics:-

- (i) perspective geometry;
- (ii) spherical imaging surface;
- (iii) low image resolution when compared to the resolution of the photogrammetric frame camera images due to the use of solid-state detectors;
- (iv) image motion distortion caused by the forward motion of the platform during the image scan time;
- (v) electronic distortion caused by the scanner's electronic circuits;

For mapping applications, the sensor used for the acquisition of the aerial images must be calibrated precisely prior to the actual flight mission in order to determine the interior orientation parameters of this sensor. In the next Chapter, different methods of performing such a calibration for thermal video frame scanners will be discussed.

**CHAPTER VI**  
**CALIBRATION OF THERMAL VIDEO FRAME SCANNERS-**  
**THEORETICAL BASIS AND ACTUAL PROCEDURES**

The calibration of thermal video frame scanners is a complex task that involves the use of various techniques and equipment. The theoretical basis of the calibration process is based on the principles of radiometry and the geometry of the scanner's field of view. The actual procedures involve the use of a variety of calibration targets and the measurement of the scanner's response to these targets.

The calibration process is divided into two main parts: the theoretical basis and the actual procedures. The theoretical basis involves the derivation of the calibration equations and the determination of the scanner's response to the calibration targets. The actual procedures involve the measurement of the scanner's response to the calibration targets and the comparison of the results with the theoretical predictions.

The calibration targets are divided into two main categories: the theoretical targets and the actual targets. The theoretical targets are used to determine the scanner's response to a known radiance distribution. The actual targets are used to determine the scanner's response to a known radiance distribution in a real-world environment. The calibration process is completed when the scanner's response to the calibration targets is known and the calibration equations are used to determine the scanner's response to any other target.

## CHAPTER VI

### CALIBRATION OF THERMAL VIDEO FRAME SCANNERS-

#### THEORETICAL BASIS AND ACTUAL PROCEDURES

##### 6.1 Introduction

For mapping applications, photogrammetric cameras are usually calibrated to determine the following parameters of interior orientation :-

- (i) the calibrated or equivalent focal length (EFL);
- (ii) the position of the principal point; and
- (iii) the geometric distortion characteristics of the camera lens.

##### 6.1.1 Calibration of Photographic Frame Camera

Calibration techniques for the mapping frame camera are well established and are used to determine the interior orientation parameters to a very high accuracy. Laboratory, field, and stellar methods can all be employed for the purpose. The multicollimator method and the goniometer method are two types of laboratory procedure which are in common use for camera calibration.

##### 6.1.1.1 The Multicollimator Method

The multicollimator method employs a number of collimators mounted in a precisely known angular array as shown in Fig.6-1a. In addition, an autocollimator is used to line up the optical axis of the camera lens with the optical axis of the central collimator. Each individual collimator consists of a lens with a cross and some other resolution bar targets mounted in its plane of infinite focus. The process of calibration using the collimator method can be explained as follows:

- (i) Prior to the calibration procedure, the optical axis of the autocollimator (usually in an overhead position) is lined up vertically with the optical axis of the central collimator.
- (ii) The multicollimators are switched off and the camera to be calibrated is placed on its mount (between the autocollimator and the multicollimator). A plano-parallel glass plate with its rear surface silvered to act as a mirror is placed on the camera focal plane.

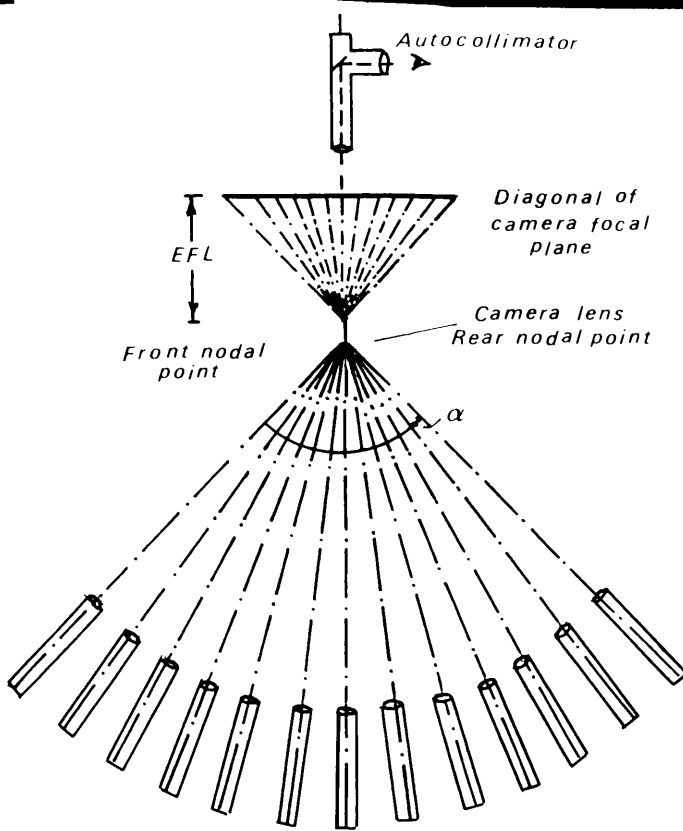


Fig.6-1a Bank of collimators for camera calibration

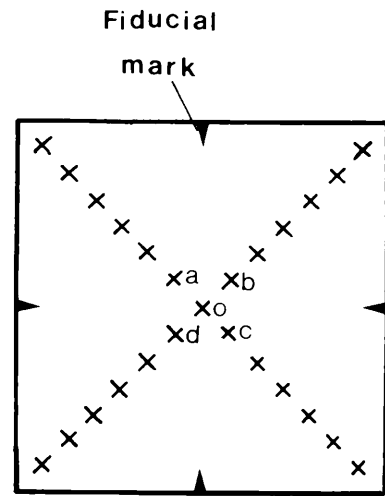


Fig.6-1b Images of photographed collimators

- (iii) The optical axis of the camera lens is then lined up with the optical axis of the autocollimator. This is achieved by continuous adjustment of the camera on its mount (by tilting and shifting the camera) until the projected cross of the autocollimator coincides with its image reflected back from the glass plate. This places the camera focal plane exactly normal to the axis of the central collimator.
- (iv) The autocollimator is then switched off, the plano-parallel plate is removed and a sensitized photographic plate is placed in the focal plane. The multicollimator array is switched on and the shutter is then opened and the image of the array of collimator crosses is recorded. The camera is then re-oriented about its vertical axis so that when further exposures are taken, the collimator crosses will be imaged along the diagonals of the camera format as shown in Fig.6-1b. The photographic plate containing the multiple exposures of the multicollimator crosses is then developed.
- (v) Finally, the fiducial marks on the camera focal plane are adjusted in position so that the point of intersection of each two opposite marks lies exactly on the image of the cross at the optical axis of the camera lens. This defines the principal point of autocollimation.



Distances on the exposed plate between imaged crosses are precisely measured using a monocomparator. The EFL is then computed as;

$$EFL = ( oa + ob + oc + od ) / 4 \tan \alpha$$

where oa, ob, oc and od are as shown in Fig.6-1b; and  $\alpha$  is the angle between the optical axes of each pair of adjacent collimators.

Based on the EFL value, theoretical distances from the central collimator image to all other collimator crosses can be computed. Radial lens distortion can then be computed by subtracting the calculated theoretical distances from the corresponding measured distances. The values of this radial distortion are then plotted (radial distortion versus radial distances from the central collimator image) to produce a curve describing the nature of the radial distortion of this particular lens. Fig.6-2 below shows the radial lens distortion curve for a Zeiss RMK aerial camera equipped with a Pleogon lens.

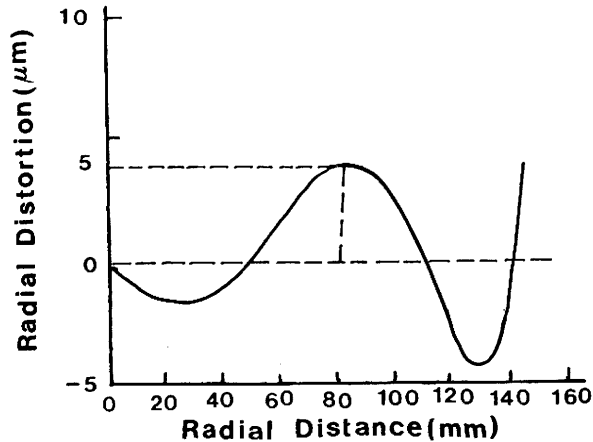


Fig.6-2 Radial lens distortion curve for Zeiss RMK aerial camera equipped with a Pleogon lens

The calibrated focal length (CFL) is then selected so that it produces a maximum positive radial distortion equal to the maximum negative radial distortion.

The images of the resolution targets of the collimators are imaged simultaneously with the crosses and are used to determine the camera's resolving power. These targets are made up of several line pairs (parallel black lines of a certain thickness separated by white lines of the same thickness). A typical pattern may consist of 10 - 80 lines/mm. The resulting images are examined under magnification to determine the finest set of parallel lines which can be clearly resolved.

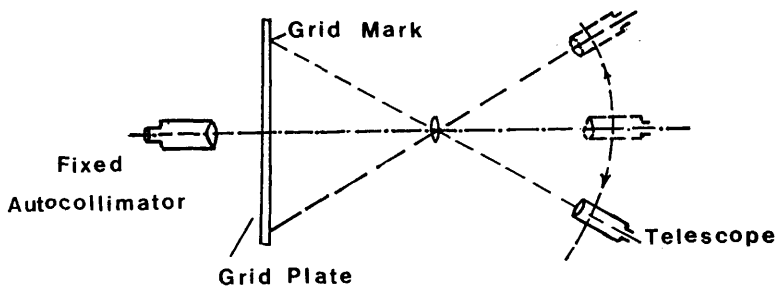


Fig.6-3 Goniometer method of camera calibration

### 6.1.1.2 The Goniometer Method

The main parts of a goniometer are a moving telescope and a fixed autocollimator (Fig.6-3). The moving telescope or goniometer is located in the object space in front of the camera and rotating around the centre of the entrance pupil of the aerial camera lens. The autocollimator is located behind the image plane of the camera being calibrated. The procedure of calibration can be described as follows:-

- (i) The movable telescope is rotated so that it is aligned with the fixed autocollimator. The camera body is then installed and oriented so that the entrance pupil of the lens is positioned on the vertical axis of rotation of the telescope;
- (ii) A plano-parallel grid plate is placed in the camera focal plane and the camera is aligned by autoreflection using the fixed autocollimator. This places the image plane perpendicular to the axis of the telescope when it is in its zero position.
- (iii) The grid plate is shifted in both directions until the central grid intersection lies on the line of sight of the telescope when it is in its zero position. The camera may be rotated about its optical axis in order to bring a diagonal row of grid intersections in line with the horizontal sweep of the line of sight of the telescope.
- (iv) The observations are made using the moving telescope or goniometer to measure the object space angles subtended by the central grid intersection and each of the diagonal grid intersections.

Since the grid spacings are precisely known from comparator measurements, the problem of determining the focal length and distortion reduces to the same as that using the multicollimators. However, it can be seen that in the

multicollimator method, the object space angles (between collimators) are known and the distances are measured by comparator (on the exposed plate), while in the goniometer method, the angles are measured (by the goniometer) and the distances are known (on the grid plate).

#### 6.1.1.3 The Reseau Plate Method

The reseau plate is a glass plate whose upper surface practically coincides with the surface of the camera focal plane frame. A grid or reseau of fine crosses is located on the upper surface of the plate. The crosses are distributed over the entire focal plane in a square array. The reseau pattern is calibrated (on a monocomparator) so that the distances between the crosses are known precisely.

In this method, the goniometer procedure described in the preceding Section is first carried out to determine the interior orientation parameters using the reseau plate which is fixed permanently in the camera focal plane. The reseau images in this case will appear on each photograph taken by the camera. The distances between these images can then be measured on each photograph and compared to their corresponding calibrated distances. In this way, the regular and irregular film deformations which have occurred between the time of exposure and the time of measurement can be determined.

#### 6.1.2 Calibration of the Vidicon Tube Camera

The situation with the vidicon tube camera is slightly different to that of the photogrammetric frame camera. In this case, the camera focal plane is replaced by the vidicon tube target plate. This target plate is scanned by the electron beam to produce a video signal as described in Chapter II. This signal may be used to generate an image on a flat screen monitor. To produce a hard copy image, the image on the monitor screen is then photographed by a photographic camera. Alternatively, an Electron Beam Recorder (EBR) may be used to write the image directly on to film. Because of the large electronic distortions which may be present in a TV-system, accurate calibration of the internal geometry must be considered in two stages:-

- (i) the determination of the internal geometry of the lens system including the focal length, principal point and the distortion characteristics as is done for a photogrammetric camera; and
- (ii) the determination of the geometric distortions introduced between the target plate of the TV-camera tube and the final photographic image as is done with the reseau camera described above.

Wong, 1968 carried out a comprehensive calibration of television systems for photogrammetric applications. He used a reseau grid which was etched onto the target plate of the vidicon tube. This allowed the use of the goniometer procedure explained above to determine the EFL, the position of the principal point and the distortion characteristics of the vidicon tube camera lens. Once the vidicon tube camera was calibrated and was used for imaging, the grid would undergo the same scanning procedure as the image on the target plate and would appear on each frame. By comparing the coordinates of the grid intersections on the reproduced frame with those on the target plate, it was possible to determine the image distortion pattern caused by the TV-system. In essence therefore, the procedure was similar to that used with film cameras equipped with a register plate on which reseau crosses had been marked.

### 6.1.3 Calibration of Thermal Video Frame Scanners

The methods described above for the calibration of the frame and vidicon tube cameras cannot be applied to thermal video frame scanners for the following reasons:-

- (i) thermal video frame scanners operate in the thermal band of the EM spectrum. Thus the array of targets to be used in the calibration must be made of a material of good thermal emissivity to ensure high contrast between the images of these targets and their background;
- (ii) frame scanners use several optical components such as the objective lens and eyepiece lens of the afocal telescope, the scanning mirrors, and the relay lens located in front of the detector. The calibration of each of these components individually is not practicable;and
- (iii) there is no target plate or image plane in which a photographic plate, a grid plate or a register glass equipped with a reseau can be placed.

An initial attempt was made to calibrate the IR-18 thermal scanner by imaging a glass grid plate which is normally used for the calibration of photogrammetric plotting machines. The plate was mounted vertically in contact with a tank of boiling water so that the heat transferred from the tank body to the glass grid plate. It was expected that, by raising the glass temperature, the difference in emissivity between the glass material and the lines forming the grid would be distinguishable so that a good contrast between their images would appear on the display. However, this method did not work as planned, most probably because the difference in emissivity was very small and also because the grid lines were much too thin to be resolved by the scanner.

So it was found that a target plate needed to be specially designed and constructed for the purpose of calibrating the video frame scanners taking into consideration the resolution limits and the performance of these scanners.

## 6.2 Design of the Target Plate

Although it was a failure, the initial glass plate test mentioned above gave a clear idea about the specifications of a target plate which could be used for calibration. It was apparent that it should be a metal plate in which a pattern of marks represented by etched holes (voids) would be distributed symmetrically over the plate. The positions of these marks could be measured accurately to give their linear coordinate values.

The target was designed specifically for the calibration of the IR-18 frame scanner which has a nominal field of view of  $38^\circ \times 25.5^\circ$ . A 1X magnification telescope was not available during the time of the test, and focussing without a telescope could not be achieved since the scanner is adjusted to view at infinity. Thus a 1.5X telescope with  $25.5^\circ \times 17^\circ$  field of view and an IFOV of 1.15 mrad was used instead. With these characteristics, the field of view at 1.0 m distance is  $450 \times 300$  mm, and the resolution is 1.15 mm.

A total of 150 X-shaped crosses arranged in a symmetric pattern of 10 rows by 15 columns was distributed over the plate with a 30 mm spacing between each pair of adjacent crosses in both the horizontal and vertical directions. The dimensions of each cross were 140 mm (diagonal length of the arm) by 2 mm (thickness of the arm)

The reason for choosing an X-shaped mark was that the pointing cursor of the video-based monocomparator which was to be used for the image coordinate measurements has a + shape. An X-shaped cross would be easier and more accurate to measure using such a measuring mark.

To test the resolution of the video image, a special resolution target (Fig.6-4) was photographed from a television test card. A total of 24 such targets was distributed at intervals across the target plate to test the resolution in both the horizontal and vertical directions.

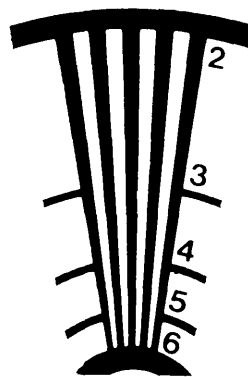


Fig.6-4 Video image resolution test target

Prior to the manufacture of the plate, different materials such as aluminium, stainless steel and copper were tested using the IR-18 scanner to decide which type of metal should be used in the manufacture of the test plate. These tests showed that copper exhibited the best contrast relative to its background followed by the stainless steel. However, the stainless steel was chosen since it is a better material to handle during manufacture or to use during calibration than copper. The final design of the target plate is shown in Fig.6-5 below.

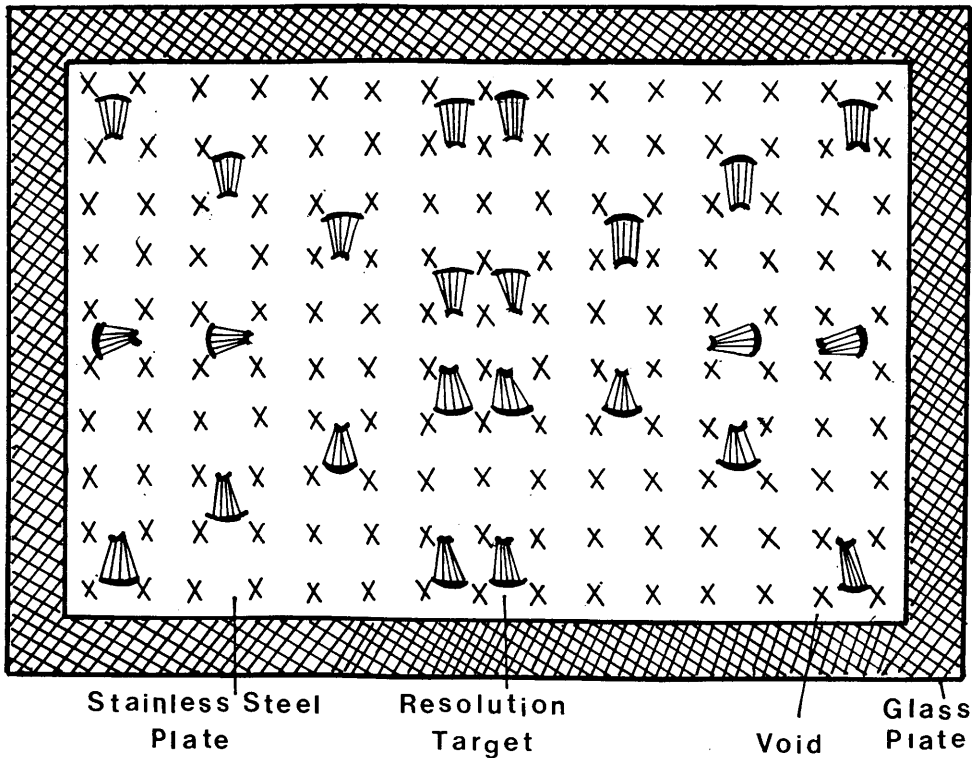


Fig.6-5 Design of the target plate for the calibration of the thermal video frame scanner

### 6.2.1 Manufacture of the Target Plate

The target plate was manufactured by a chemical milling process by the firm Photofabrication in Huntingdon. This process involved the following steps (Fig.6-6):-

- (i) A precise drawing on stable polyester material was made of the required pattern of test crosses. Photographic copies of the resolution targets were then added at the appropriate positions.
- (ii) A photographic film master was produced from the graphic drawing.
- (iii) A stainless steel metal plate was cut to the required

dimensions and then coated with photo-resist material.

- (iv) The pattern on the film master was copied onto the stainless steel plate.
- (v) The plate then went through an etching process in which the pattern of crosses and targets was dissolved out chemically.
- (vi) the photo-resist material was removed and the plate itself was washed and cleaned.

## THE CHEMICAL MILLING PROCESS

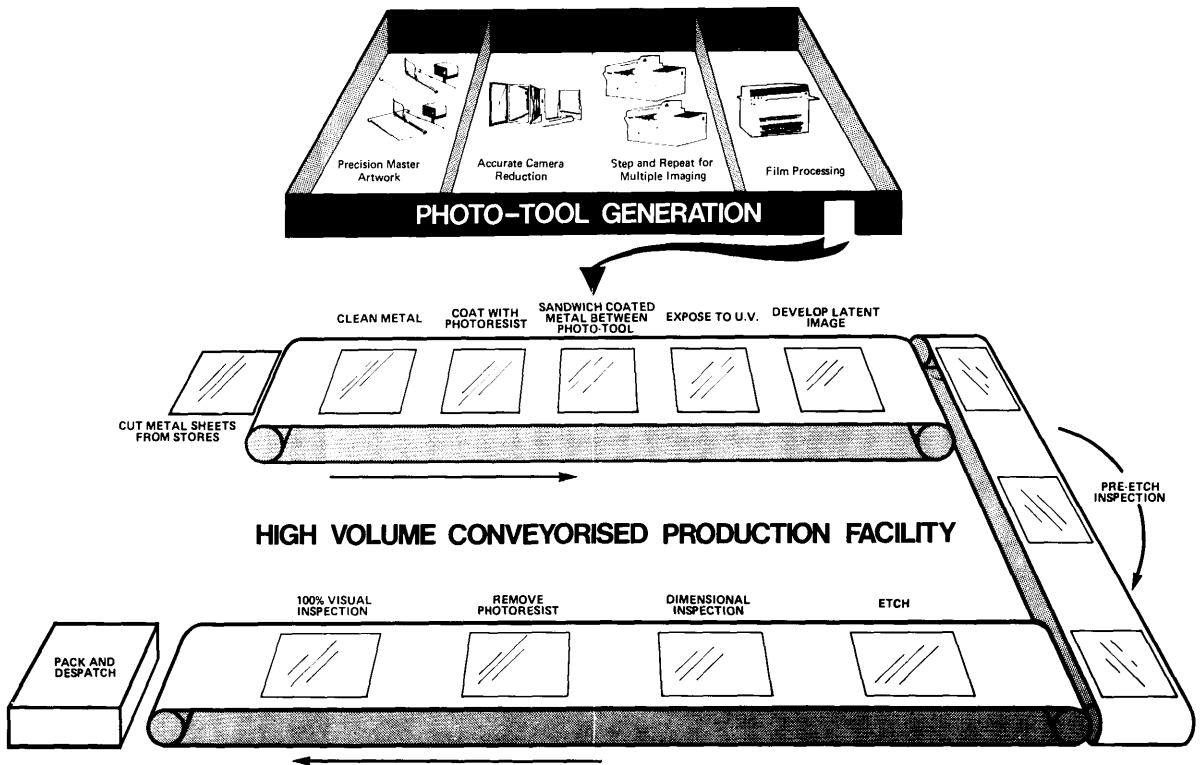


Fig.6-6 A block diagram for the chemical milling process used to manufacture the target plate

The thickness of the stainless steel plate originally manufactured by Photofabrication was 0.1 mm. This turned out to be too thin. Some parts in the middle of the plate began to exhibit buckling. On investigation, this buckling appeared to result from the process of manufacturing the stainless steel plate itself, during which the plate is rolled over a cylinder and subjected to high pressure to produce it in the required shape and form. An attempt was made to bond the target plate on to a thick glass plate to make it more stable, but this was not successful and the buckling

remained. It was then thought that a thicker stainless steel plate would resist bending during the rolling process over the cylinder. However, the manufacturers advised that there is a trade off between the plate thickness and the size of holes to be etched. If the plate was made too thick, the chemicals would etch deeper into the plate and the crosses would be unsharp. The manufacturers further advised that the best compromise would be to use a plate thickness of 0.2 mm. This solution was adopted and two examples of a second plate were manufactured to this specification. In this second plate, although the crosses were not quite as sharp as those of the first plate, the plate itself was very stable and exhibited negligible buckling, especially after being bonded on to a glass plate.

### 6.2.2 Calibration of The Target Plate

The glass plate was used not only to make the thin stainless steel plate rigid when mounted in a vertical position, but also because the glass itself has a very high thermal emissivity factor when compared to any type of metal. Compared to a perfect black body ( whose emissivity factor is 1.0) the glass material has an emissivity factor of 0.95 while the stainless steel's factor is 0.16. So if the glass plate was heated from behind, the voids being represented by the glass material would exhibit a high brightness against the background represented by the stainless steel material. Hence, it was necessary to calibrate the target plate at a temperature slightly higher than normal room temperature which would be representative of the conditions likely to occur during the later calibration of the frame scanner.

The glass plate was painted with a heat-resistant black paint and the target plate was stuck onto the painted side so that, when the glass is heated from behind, the energy does not transfer quickly to the stainless steel plate. The plate was then calibrated at the National Engineering Laboratories (NEL) in East Kilbride. The measurements were carried out on a large Ferranti monocomparator (Fig.6-7) which could accommodate the target plate. This monocomparator was equipped with a vidicon tube camera pointing vertically downwards on the plate and produced a 10 X magnified image on a 9" video monitor. A cross-hair cursor allows the observer to point to the target crosses accurately on the video monitor. The machine is equipped with linear encoders to give the measured plate coordinates (x,y) to a resolution of 1  $\mu\text{m}$  with an accuracy of  $\pm 7 \mu\text{m}$  as claimed by the manufacturers.

The plate was calibrated twice, firstly at the normal room temperature (about 20 °C ) and secondly by raising its temperature up to about 25°C. In each case, the 150 crosses were measured twice, forward and backward, in the x-direction to ensure consistency in the measurements and the mean coordinate value at each point was computed.



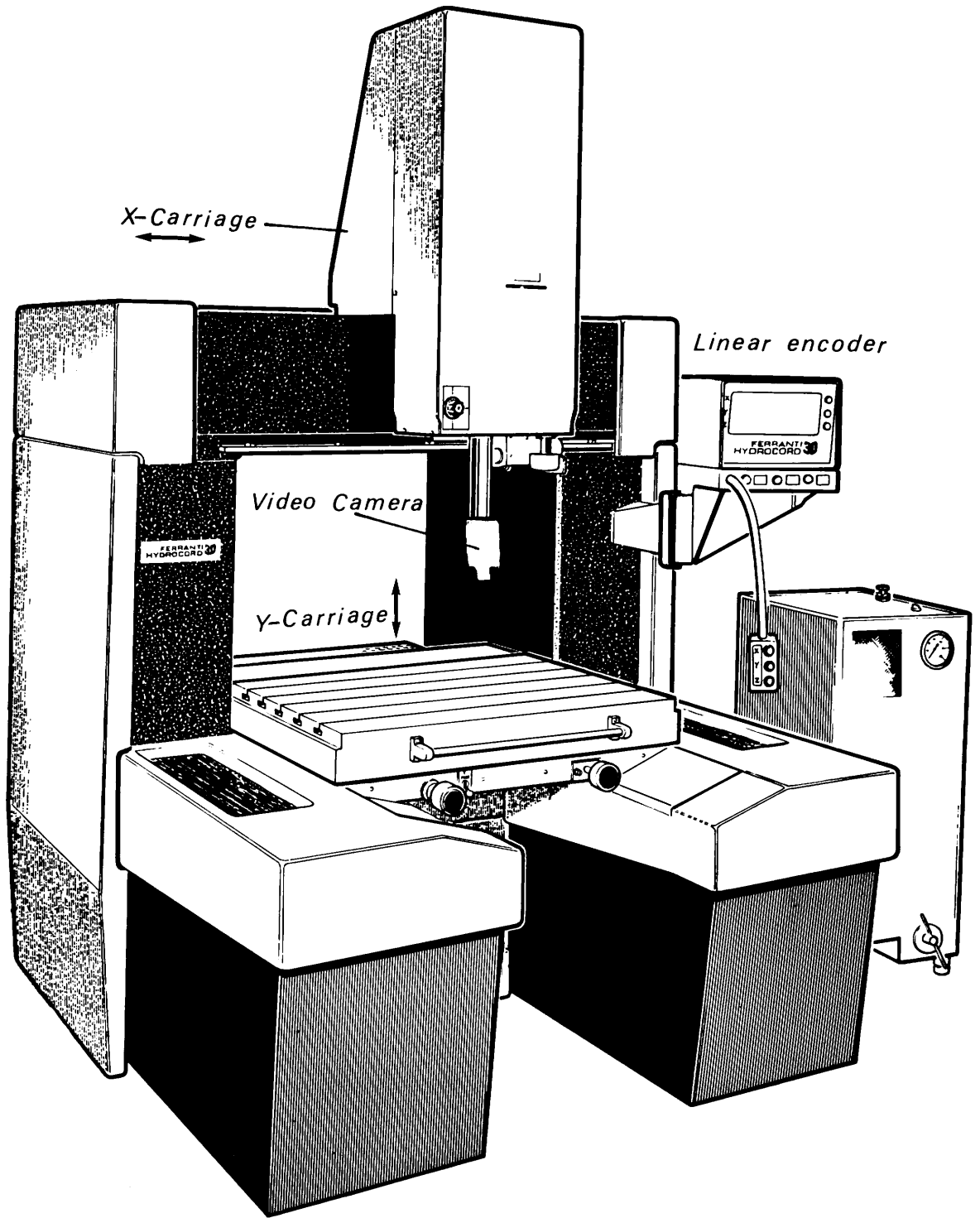


Fig.6-7 The Ferranti monocomparator

The precision of pointing to the crosses on the plate was computed as follows;

$$\begin{aligned} \bar{x}_a &= (Fx_a + Bx_a) / 2 \\ vx_a &= Fx_a - mx_a \quad \dots\dots\dots 6-1 \\ &= Bx_a - mx_a \end{aligned}$$

Where:-

$Fx_a, Bx_a$  are the forward and backward measured x-coordinates of point a;

$\bar{x}_a$  is the mean value of the forward and backward measured x-coordinates of point a; and

$vx_a$  is the residual between the mean value and each of the forward and backward measured x-coordinate of point a respectively.

The root mean square error (rmse) for all the 150 measured points can be computed using the formula:-

$$rmse (m_x) = \sqrt{\frac{[vv_x]}{n-1}} \quad \dots\dots\dots 6-2$$

The same procedure was used to compute the rmse in the y-direction ( $m_y$ ). The planimetric vector error ( $m_p$ ) can be derived from the expression  $m_p^2 = m_x^2 + m_y^2$ . The results are shown below in Table 6-1.

Plate Temperature	rmse	$m_x$ $\mu m$	$m_y$ $\mu m$	$m_p$ $\mu m$
20 °C		19	21	28
25 °C		23	19	30

Table 6-1 Precision of the target plate calibration

Thus, the calibration of the target plate resulted in a set of precisely calibrated x,y coordinates for each of the 150 crosses.

### 6.3 Calibration Procedures for Frame Scanners Using the Target Plate

Four representative frame scanners were calibrated using the target plate described above. These were:-

- (i) Barr & Stroud IR-18 MKII thermal imager;
- (ii) Rank Pullin Controls (RPC) thermal imager;
- (iii) GEC Avionics/ Rank Taylor Hobson TICM II; and
- (iv) AGA Thermovision.

In the first three cases, the calibration was undertaken in the factory where the scanner was made. The fourth device (the AGA Thermovision) was calibrated in the workshop/laboratory of the U.K. office of AGA.

#### 6.3.1 Calibration of Barr & Stroud IR-18 MKII Thermal Imager

To prevent emission or reflections from other ambient bodies during the calibration process, the calibration rig was mounted inside a wooden box. The scanner was mounted on one side of the box with the calibration plate on the other side. The interior walls of the wooden box were covered with a black paint to absorb any reflected or emitted radiation occurring inside the box. The distance between the scanner and the target plate was 1.0 m and the optical axis of the scanner telescope was adjusted to point directly at the centre of the plate. These arrangements are shown in Fig.6-8. The glass plate was then heated from behind by a hot air gun. It took about 10 minutes to get a good contrast between the images of the voids and their background on the video monitor screen.

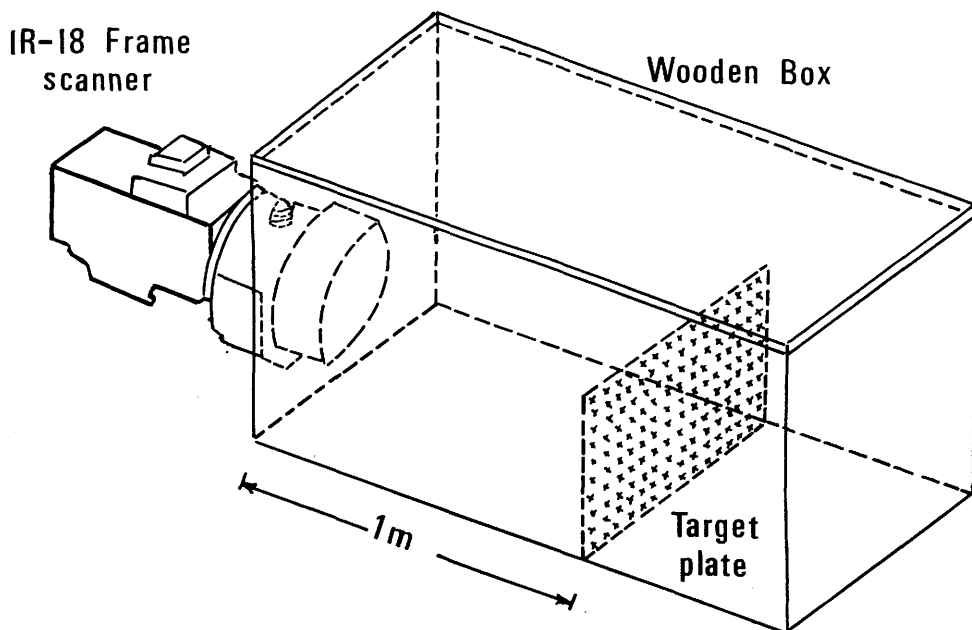


Fig.6-8 Calibration of Barr & Stroud IR-18 frame scanner

The contrast of the image which appeared on the video monitor (see Fig.6-14) was very good and the images of the crosses were very clear and quite sharp. The crosses being represented by the glass material appeared white, while their background appeared almost black. However, the images of the resolution targets intended to establish the resolution of the system did not turn out as desired, mainly because each target was formed by some very closely spaced lines (voids) which could not be resolved by the scanner. As mentioned earlier in this Chapter, these targets had been copied from a test card which was used originally to measure the resolution of the vidicon tube cameras. This shows that the resolution of these vidicon tube cameras is much better than that of the frame scanners. Since the plate had already been manufactured, it was not possible to change the form, size and characteristics of the resolution targets.

The output from the IR-18 frame scanner was recorded continuously on a U-matic VTR over a period of 20 minutes to allow the distortion to be established over a period of time. By measuring several frames taken at intervals over this period, it would be possible to see if the distortion pattern varied over this period.

Later, towards the end of this project, the 1X and 6X telescopes became available. Obviously it was of interest to calibrate the IR-18 scanner with telescopes of different magnification. With the 1X telescope, the same procedure described above was followed except that the plate was mounted vertically at 70 cm distance (instead of 1.0 m) from the scanner to fill the field of view ( $38^\circ \times 25^\circ$ ). In case of the 6X telescope which has a field of view of  $6.3^\circ \times 4.4^\circ$ , it was mounted outside the wooden box at a distance of 2.25 m.

### 6.3.2 Calibration of Rank Pullin Controls (RPC) Thermal Imager

The RPC thermal imager has a basic field of view of  $30 \times 40$ . The scanner had to be used with a 10X magnification telescope ( $3^\circ \times 4^\circ$ ). To achieve a compromise between filling the field of view and the resolution limits of the scanner (IFOV = 2.1 mrad) the target plate was placed vertically at 7 m distance from the scanner. At this distance, the resolution was 1.5 mm. The non-standard video signal from this scanner was first fed into a frame buffer and then converted into a PAL standard signal. As with the IR-18, the image of the test plate was recorded for 20 minutes on a U-matic VTR.

### 6.3.3 Calibration of GEC Avionics/Rank Taylor Hobson TICM II

#### Thermal Scanner

The TICM II has a nominal field of view of  $60^\circ \times 40^\circ$  and a 2.7 mrad IFOV. The scanner had to be used with 5X magnification telescope which has a field of view of  $12^\circ \times 8^\circ$ . Thus to fill the field of view and achieve a suitable resolution, the target plate was positioned vertically (with a horizontal optical axis) at a distance of 2.5 m from the scanner. The resolution at this distance was 1.4 mm. The standard video signal from the scanner was again recorded directly on a U-matic VTR for 20 minutes.

### 6.3.4 Calibration of AGA Thermovision

The nominal field of view of the AGA Thermovision is  $12^\circ \times 12^\circ$  and its IFOV is 1.9 mrad. The target plate was positioned vertically at 1.0 m distance from the scanner, at which distance the resolution is 1.9 mm. Since the scanner's output is not a standard video signal, it had to be fed into a special frame buffer to combine the four fields of each frame into two fields only (by adding the two odd fields together and the two even fields together). The resultant signal was then recorded on a U-matic VTR for 20 minutes.

### 6.4 Video Image Coordinate Measurements

The video image coordinates were measured on a video-based monocomparator specially designed for the project and assembled at the Department. This is shown in Fig.6-9 and consists of:-

- (i) a U-matic video tape recorder/playback unit;
- (ii) a frame memory;
- (iii) a video position analyser (VPA) which permits the introduction of the pointing cursor (+ shape cursor) and the direct measurement of its position on the image held in the frame memory in terms of x and y coordinates expressed in pixel counts;
- (iv) a video scaler which allows the superimposition of a grid to check metric accuracy; and
- (v) a standard PAL monochrome video monitor.



Fig.6-9 The video based monocomparator

Different formats of video tape recorders have been discussed in Chapter II. Any of these could be used in this assembly, provided the images to be measured have been recorded using the same format. However as mentioned earlier, U-matic is a high quality, semi-professional format and has been used throughout this project. A Sony model VO-2630 U-matic VTR was used in the video-based monocomparator.

The frame memory is similar to the frame buffer discussed in Section 2-5. It accepts analogue video data from the VTR and converts it into digital form using an analogue-to-digital converter (A/D). The digital data are then stored in the memory. If the image has to be displayed, it is converted into analogue form using a digital-to-analogue (D/A) converter and then sent to the display unit at a refresh rate of 50 fields per second.



Fig.6-10 FOR.A FM60 video frame memory

In this project, a FOR.A FM60 black and white frame memory (Fig.6-10) was used. The size of the digital memory is 512 x 512 pixels with a 6-bit resolution giving  $2^6 = 64$  grey levels of varying intensity.

A FOR.A VPA-1000 Video Position Analyser (Fig.6-11) was used for the coordinate measurements. It is connected directly to the frame memory and generates x,y coordinate axes which can be moved under the action of two control knobs (one for each axis) to any position on the video monitor screen. It also generates the measuring cursor (+ shaped mark) which is controlled by another two knobs. The x,y coordinates of this cursor are expressed in pixel counts with respect to the x and y axes to 1 pixel resolution. These coordinates can be displayed on the video monitor screen. The only drawback of this particular VPA is that it can only measure within 80% of the effective frame area stored in the frame memory.



Fig.6-11 FOR.A VPA-1000

A FOR.A VS-1000 video scaler was used to check the metric accuracy. A grid is generated electronically and superimposed on the image passing through the device. The separations between the grid lines can be altered between 9 and 45 pixels in each direction at 9 pixel intervals. The VS-1000 is shown below in Fig.6-12a while the electronically generated grid is shown in Fig.6-12b.



Fig.6-12a FOR.A VS-1000

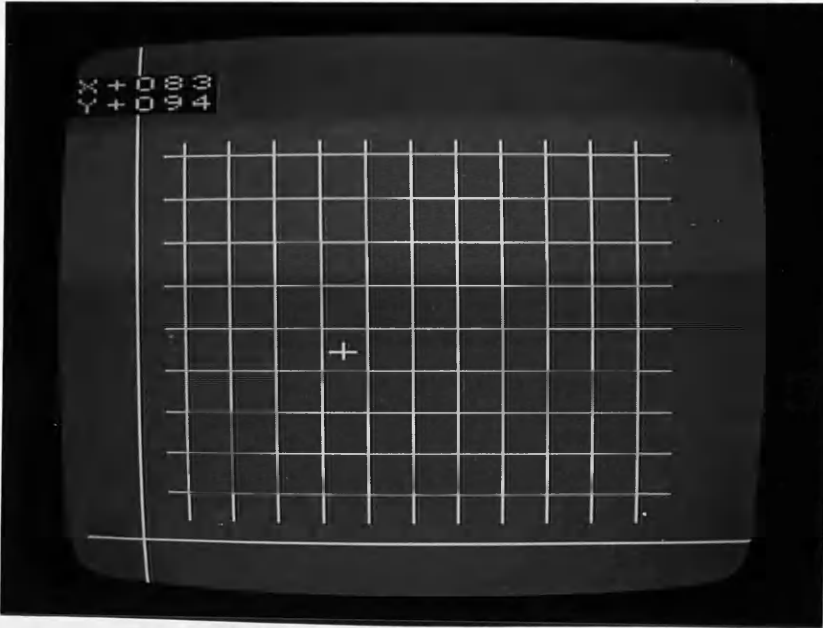


Fig.6-12b Image of the generated grid on the video monitor

A 14" Panasonic Model WV-5410 black and white monochrome video monitor (Fig.6-13) was used for image display. It is a very high resolution monitor (850 lines at the centre) with standard BNC type input and output connectors.



Fig.6-13 14" Panasonic video monitor



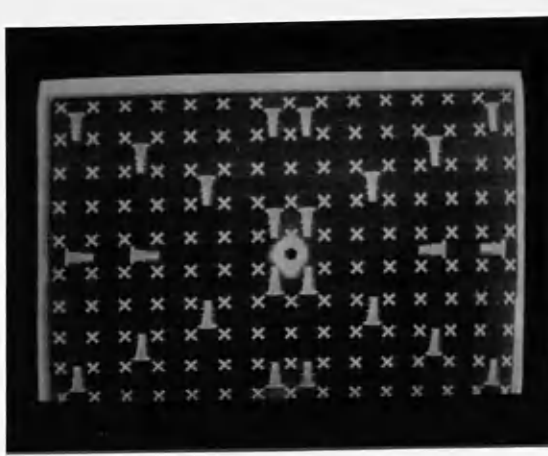
The system functions in the following way;-

- (i) The video images, previously recorded on the video cassette, are played back on the U-matic VTR.
- (ii) The video signal is passed from the VTR to the frame memory through a video cable. If it is required to freeze a specific image on the screen, (i.e. to carry out frame grabbing), then by simply pressing the freeze button, the image passing through the frame memory at that particular moment will be converted into digital form and stored temporarily in the frame memory until the freeze button is released. During the freeze time, the image held in the frame memory continues to be sent to the display unit at a 50 Hz refresh rate after being converted into analogue form.
- (iii) The VPA superimposes the x,y coordinate axes and the measuring cursor on the video image while it is passing through to the display monitor.

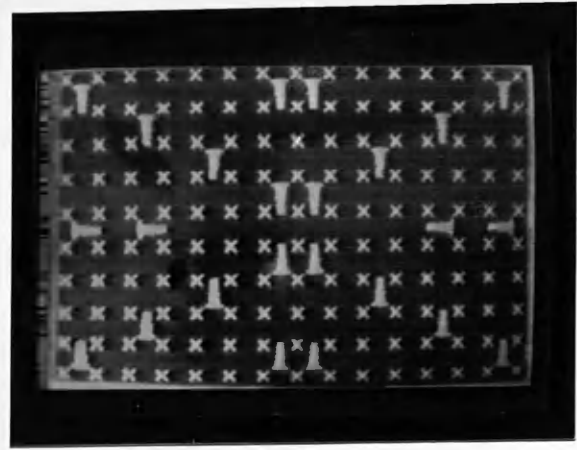
The most important advantage of this system is that the coordinate measurements actually take place inside the VPA and only the viewing takes place on the video monitor. Thus, distortions such as screen curvature or scale distortion which might be present on the monitor screen have no influence on the image measurement.

The accuracy of the whole video comparator system was first tested by measuring on the electronic grid generated by the video scaler. Different grids of different sizes were measured and the root mean square error in x and y was found to be  $m_x = m_y = \pm 0.1$  pixel (0.2 TV-lines). This showed that the internal measuring accuracy of the video monocomparator was very high.

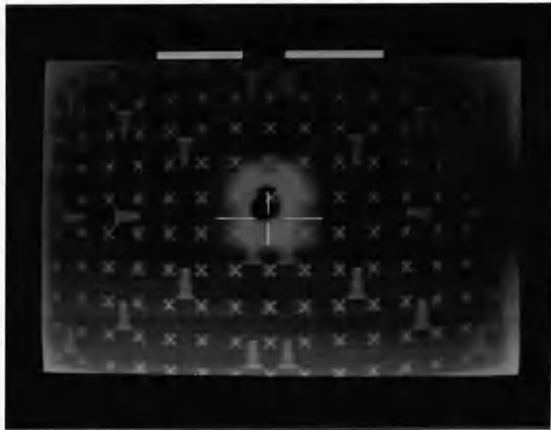
Five video frames were measured for each of the four calibrated frame scanners. These frames were chosen at regular intervals from the 20 minute recording of each scanner image. Each frame was measured in a systematic pattern in both the forward and backward directions. Out of the 150 crosses appearing on the screen, only 130 were measured since the remaining 20 crosses were outside the measuring range of the VPA. Fig.6-14 below shows the image of the target plate imaged by each of the calibrated four scanners. These images were taken off the video monitor screen for the purpose of presentation in this thesis. It must be mentioned that these hard-copy images have not been used for any type of measurement or analysis, which has invariably been carried out using the actual video images.



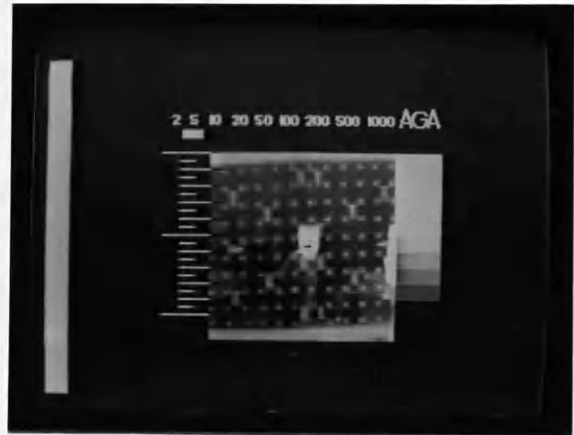
IR-18



RPC



TICM II



AGA

Fig.6-14 Images of the target plate as they appeared on the video monitor when imaged by the four scanners

The precision of measurements on each of the video images was determined in the same manner as explained above in Section 6.2.2 and the results are shown below in Table 6-2.

Scanner	Root Mean Square Error(rmse) in Pixels		
	$m_x$	$m_y$	$m_p$
IR-18	$\pm 0.35$	$\pm 0.25$	$\pm 0.33$
RPC	$\pm 0.50$	$\pm 0.40$	$\pm 0.64$
TICM II	$\pm 0.40$	$\pm 0.48$	$\pm 0.62$
AGA	$\pm 1.20$	$\pm 0.90$	$\pm 1.50$

Table 6-2 Precision of measuring the target plate coordinates on the video-based monocomparator

From inspection of the table above, it can be seen that the best precision was obtained with Barr & Stroud IR-18 frame scanner. This can be related to the following reasons:-

- (i) it has better resolution (smaller IFOV) than the other scanners;
- (ii) the target plate was designed specifically to match its characteristics;and
- (iii) the calibration procedure used was greatly aided by the use of the wooden black box. This helped to produce an image of superior contrast to that achieved with the others. The same procedure could not be used with the other scanners since the target plate had to be mounted at a long distance from each of the scanners and also a suitably dimensioned wooden box was not available. Considering the full collaboration and help received from each scanner manufacturer, it was not possible to ask them to prepare a box with suitable dimensions. It was also inconvenient to transport a 4 to 5 metres box to the place where the calibration was carried out in Southern England.

In the same table, it can be seen that the precision of measurement was very poor with the AGA Thermovision. This appears to be related mainly to its non-standard format, in which each frame is built up of four fields.

So far, the calibration procedure has resulted in two sets of coordinates, These are:-

- (i) the calibrated coordinates of the 130 crosses as measured by the Ferranti monocomparator;and
- (ii) the coordinates of the images of the same 130 crosses measured by the video monocomparator.

In the next Chapter, the methods which have been used to relate the two sets of coordinates and to solve for the interior orientation parameters are discussed, and the results of the calibration are presented and analysed.

## CHAPTER VII

### RESULTS AND ANALYSIS OF THE CALIBRATION OF VIDEO FRAME SCANNERS

CHAPTER VII

RESULTS AND ANALYSIS OF THE CALIBRATION  
OF VIDEO FRAME SCANNERS

The procedures discussed in the previous Chapter were used to calibrate the four representative thermal frame scanners. In this Chapter, the mathematical models used to relate the two sets of coordinates (calibrated target plate coordinates and measured video image coordinates ) are discussed. The results from the calibration are presented and analysed individually in order to discover the nature and magnitude of the distortion introduced by each scanner. Then an overall analysis is carried out in order to find out whether all frame scanners produce the same type and magnitude of distortion or not.

7.1 Coordinate Transformation

This procedure will be used to transform the calibrated coordinates from the target plate coordinate system into the video image coordinate system. Since the target plate coordinates had been calibrated, they are considered as error free and after the transformation, the measured video coordinates will be in a distorted position with respect to the transformed target plate coordinates.

In this way, it should be possible to determine the distortion values in the x and y directions at each of the 130 crosses in the video image. This is the difference between the measured coordinates of any cross on the video image and its corresponding transformed target plate coordinates.

7.1.1 Linear Conformal Transformation

This well known type of transformation comprises a scale change( $\lambda$ ), a rotation ( $\theta$ ) and two independent translations ( $a_0, b_0$ ). Let the position of any point i on the target plate be defined by its calibrated coordinates  $x_i, y_i$  measured by the Ferranti monocomparator. Correspondingly, let the position of the same point in the video image be expressed by its image coordinates  $x'_i, y'_i$  measured by the video monocomparator. The relationships between the two sets of coordinates can be expressed as follows:-

$x'_i = a_0 + a_1 x_i - a_2 y_i \dots\dots\dots 7-1$

$y'_i = b_0 + a_2 x_i + a_1 y_i \dots\dots\dots 7-2$

Where:-

- $x_i, y_i$  are the calibrated coordinates of point  $i$ ;
- $x'_i, y'_i$  are the measured video coordinates of point  $i$ ;
- $a_0, b_0$  are the the translation parameters in  $x$  and  $y$  respectively; and
- $a_1, a_2$  parameters which are functions of the rotation angle and the scale factor.

Assuming an error (distortion) value  $v_{x_i}, v_{y_i}$  at the image point  $i$ , equations 7-1, 7-2 can be re-written as:

$$x'_i + v_{x_i} = a_0 + a_1 x_i - a_2 y_i \quad \dots\dots\dots 7-3$$

$$y'_i + v_{y_i} = b_0 + a_2 x_i + a_1 y_i \quad \dots\dots\dots 7-4$$

Every measured point gives rise to two such equations. With the use of 130 image points, 260 equations will be formed and a least square adjustment procedure will be adopted since there are only four unknown parameters ( $a_0, b_0, a_1, a_2$ ) to be solved for.

In effect, this transformation does not change the basic relationship between image points; it merely transforms the calibrated coordinates of the target plate into the video image coordinate system. If the image coordinates have been measured accurately, the results from this transformation will show the geometric fidelity of the video images in their original state as produced by the frame scanner

### 7.1.2 Polynomial Transformation

A general 25-term polynomial equation having the form:-

$$\begin{aligned} x' = & a_0 + a_1 x + a_2 y + a_3 x y + a_4 x^2 + a_5 y^2 + a_6 x^2 y^2 + a_7 x^2 y + \\ & a_8 x y^2 + a_9 x^3 + a_{10} y^3 + a_{11} x^3 y + a_{12} x y^3 + a_{13} x^3 y^2 + a_{14} x^2 y^3 + \\ & a_{15} x^3 y^3 + a_{16} x^4 + a_{17} y^4 + a_{18} x^4 y + a_{19} x y^4 + a_{20} x^4 y^2 + a_{21} x^2 y^4 + \\ & a_{22} x^4 y^3 + a_{23} x^3 y^4 + a_{24} x^4 y^4 \quad \dots\dots\dots 7-5 \end{aligned}$$

$$y' = b_0 + b_1 x + b_2 y + \dots\dots\dots + b_{24} x^4 y^4 \quad \dots\dots 7-6$$

was also used to carry out transformation between the 2 sets of coordinate values.

This particular form is known as Biquartic polynomial since it includes all possible terms up to and including the fourth order terms. The reason for choosing such a high order polynomial was that the nature and extent of the distortions produced by the frame scanner's electronics were not known prior to the calibration procedure being undertaken.

Once again, if the distortion values  $v_x$  ,  $v_y$  at each of the 130 image points are considered, then the least squares adjustment procedure can be used to solve for the 50 unknowns ( $a_0$  to  $a_{24}$  and  $b_0$  to  $b_{24}$ ) included in equations 7-5 ,7-6.

If equations 7-5,7-6 can be programmed in such a manner that the user can specify the number of terms to be used in an individual run, then every possible variation in the number of terms used in a specific transformation could be implemented by truncating the unwanted terms from the general purpose polynomial equation. Among these forms are:-

- (i) the affine transformation;
- (ii) the bilinear transformation;
- (iii) the biquadratic transformation; and
- (iv) the bicubic transformation.

#### 7.1.2.1 Affine Transformation

This transformation has the form:-

$$x' = a_0 + a_1 x + a_2 y \dots\dots\dots 7-7$$

$$y' = b_0 + b_1 x + b_2 y \dots\dots\dots 7-8$$

Thus it employs only the first three terms from the general polynomial equations both in the x and y directions. It will be seen that in addition to the two translations and the general rotation of the linear conformal transformation, the affine transformation applies two discrete scale factors in the x and the y directions. Furthermore, one of the coordinate axes may be rotated to account for any lack of orthogonality in the image. The transformation procedure will solve for the 6 unknowns (  $a_0$  to  $a_2$  and  $b_0$  to  $b_2$  ).

#### 7.1.2.2 Bilinear Transformation

This simple 4-term expression has the form-

$$x' = a_0 + a_1 x + a_2 y + a_3 x y \dots\dots\dots 7-9$$

$$y' = b_0 + b_1 x + b_2 y + b_3 x y \quad \dots\dots\dots 7-10$$

In this case, there are 8 unknown parameters ( $a_0$  to  $a_3$  and  $b_0$  to  $b_3$ ) to be determined in total.

### 7.1.2.3 Biquadratic Transformation

This is a 9-term polynomial in the form-

$$x' = a_0 + a_1 x + a_2 y + \dots\dots\dots + a_8 x^2 y^2 \quad \dots\dots 7-11$$

$$y' = b_0 + b_1 x + b_2 y + \dots\dots\dots + b_8 x^2 y^2 \quad \dots\dots 7-12$$

It can be seen that this transformation employs only the first 9-terms (in  $x$  and  $y$ ) from the general polynomial equation. A total of 18 unknowns ( $a_0$  to  $a_8$  and  $b_0$  to  $b_8$ ) are to be solved for during the least square procedure.

### 7.1.2.4 Bicubic Transformation

A 16-term polynomial in the form-

$$x' = a_0 + a_1 x + a_2 y + \dots\dots\dots + a_{15} x^3 y^3 \quad \dots\dots 7-13$$

$$y' = b_0 + b_1 x + b_2 y + \dots\dots\dots + b_{15} x^3 y^3 \quad \dots\dots 7-14$$

In this case, there are 32 unknowns ( $a_0$  to  $a_{15}$  and  $b_0$  to  $b_{15}$ ) to be solved for.

However in order to monitor and discover the effective terms of the general polynomial, all possible cases were implemented, starting with the simple 3-term affine transformation, and increasing one term each time up to the full 25 terms. Thus for each image, 23 individual runs of the program were carried out. With 5 frames calibrated for each of the four scanners, and the IR-18 calibrated with 3 different telescopes, a total of 30 video frames were measured and used for the calibration, resulting in 690 program runs.

### 7.1.3 The Computer Programs

Two computer programs were written in standard Fortran 77 to perform the transformation procedures described above using the ICL 2988 mainframe computer of the University of Glasgow and running under the standard VME operating system.



CON is the linear conformal transformation program developed to run in interactive mode in which the operator has to respond to some queries such as the number of control points in each frame, the input and output data files name and the number of frames to be calibrated. It can also compute the systematic distortion for the system and the random distortion at each point of any specified frame. The program is very flexible and can be modified to accommodate any number of points and frames within the limiting storage of the operating system.

Poly25 incorporates the same features described above except that it performs polynomial transformation using the general polynomial (25-term equation). However, as mentioned earlier, the operator can specify any number of terms between 3 and 25 for each individual run. A detailed description of the two programs is given in Appendix A.

After carrying out a suitable coordinate transformation, the residual errors at each of the 130 positions of the calibrated crosses were plotted out as vectors using a special program written in FORTRAN 77 available in the Department. The program is called PLOTDT4 and was developed to plot the error vector at any number of points using subroutines from the GHOST general purpose graphics package available on the ICL 2988 mainframe computer at the University of Glasgow. This allowed the immediate graphical display of the pattern of errors either on a graphics terminal or in hard-copy form using an x/y plotter.

In this way, any gross error (blunder) could be detected and put right. After the elimination of all such gross errors, the plot of the errors as vectors gave an immediate view of the error pattern, e.g. whether it was systematic or not.

## 7.2 Systematic and Random Distortion

The distortion value at each point could be divided into its systematic and random components. Systematic distortion remains constant at the same image point of every frame, while random distortion follows a normal distribution with a mean value equal to zero. Thus-

$$(v_{x_i})_j = sv_{x_i} + (rv_{x_i})_j \quad \dots\dots\dots 7-15$$

$$(v_{y_i})_j = sv_{y_i} + (rv_{y_i})_j \quad \dots\dots\dots 7-16$$

Where:-

$(v_{x_i})_j, (v_{y_i})_j$  are the total distortion values at point i in frame j;

$sv_{x_i}, sv_{y_i}$  are the systematic distortion components at point  $i$  of every frame; and

$(rv_{x_i})_j, (rv_{y_i})_j$  are the random components of distortion at point  $i$  of frame  $j$ .

and

$$1/N \sum_{j=1}^N (rv_{x_i})_j = 0 \quad \dots\dots\dots 7-17$$

$$1/N \sum_{j=1}^N (rv_{y_i})_j = 0 \quad \dots\dots\dots 7-18$$

Where  $N$  is an infinite number of frames.

The systematic and random components of distortion may be determined for each scanner from the measurements made on  $N$  frames as follows:-

- (i) using any of the above mentioned transformation methods, the total distortion values  $v_x, v_y$  can be determined at each of the 130 crosses for each of the  $N$  video frames.
- (ii) the systematic component of distortion at each point can be computed using the formula;

$$sv_{x_i} = 1/N \sum_{j=1}^N (v_{x_i})_j \quad \dots\dots\dots 7-19$$

$$sv_{y_i} = 1/N \sum_{j=1}^N (v_{y_i})_j \quad \dots\dots\dots 7-20$$

- (iii) for any point  $i$ , the measured image coordinates  $\bar{x}_i, \bar{y}_i$  are corrected for the systematic distortion as follows-

$$cx_i = \bar{x}_i + sv_{x_i} \quad \dots\dots\dots 7-21$$

$$cy_i = \bar{y}_i + sv_{y_i} \quad \dots\dots\dots 7-22$$

Where:-

$cx_i, cy_i$  are the image coordinates of point  $i$  corrected for systematic distortion.

- (iv) the same transformation procedure used in (i) above is used again, but this time using the corrected image coordinates  $\bar{cx}$ ,  $\bar{cy}$ . The residuals resulting from this transformation will be the random components  $rv_{x_i}, rv_{y_i}$ .

### 7.3 Determination of the Calibrated Focal Length (CFL) and the Principal Point Coordinates

The position of the principal point of the frame scanner can not be precisely located since there are no fiducial marks or reseau crosses. On the other hand, the geometric centre of the image can be determined approximately using the video position analyser by measuring the frame dimensions on the screen and locating the centre of the frame.

The calibrated focal length of the scanner can be computed using the formula-

$$CFL = \frac{L \cdot d_i}{D_i} \quad \dots\dots\dots 7-23$$

Where:-

L is the distance between the target plate and the scanner measured during the calibration process;

$d_i = \sqrt{\bar{x}_i^2 + \bar{y}_i^2}$  where  $\bar{x}_i, \bar{y}_i$  are the measured video image coordinates of the cross point i corrected for distortion and expressed from the centre of the video image; and

$D_i = \sqrt{x_i^2 + y_i^2}$  where  $x_i, y_i$  are the calibrated coordinates of the cross point i on the target plate expressed from the centre of the plate.

### 7.4 Results and Analysis of the Barr & Stroud IR-18 Frame Scanner

The results from the calibration of the IR-18 are shown below in Table 7-1.

The results from the linear conformal transformation showed a big distortion occurring in the x and y directions at all the image points. The rmse was found to be  $\pm 5.8$  and  $\pm 7.5$  pixels in the x and y directions respectively. The error vectors at the 130 points were plotted using program PLOTDT4 and the plotting is shown in Fig.7-1. As can be seen from this figure, the distortion is symmetric all over the frame and the highest magnitude occurred towards the edges of the frame. This was expected due to the spherical surface shape

of the video image produced as a result of the scanning geometry. The same symmetric pattern was obtained from the plots of the error vectors for all five frames calibrated using the linear conformal transformation procedure

A drastic change in the magnitude of the distortion was obtained when the affine transformation was used. As shown in Table 7-1, the rmse was reduced from  $\pm 5.8$  (x),  $\pm 7.5$  (y) pixels using linear conformal transformation, to  $\pm 0.67$  (x),  $\pm 0.49$  (y) pixels when an affine transformation was used. This showed that the video image contained a big affinity and/or lack of orthogonality between the x and y axes. Again the results from this transformation were plotted and are shown in Appendix B.

The four parameter (bilinear), five parameter and six parameter transformations had very little or no effect on the results and the magnitude of distortion remained more or less the same at each point.

A sudden drop in the distortion value occurred in the y-direction when the 7-parameter transformation was employed by adding the  $x^2y$  term. The rmse was reduced from  $\pm 0.49$  to  $\pm 0.39$  pixel. The use of this transformation had no effect in the x-direction.

Again, a significant improvement in accuracy resulted in the x-direction when the  $xy^2$  term was added to the polynomial. The distortion was reduced from  $\pm 0.67$  to  $\pm 0.46$  pixels. This term had no effect on the y-direction.

The use of the 9-term (biquadratic) transformation showed no improvement in the accuracy.

Another improvement was obtained in the x-direction when the 10-parameter transformation was used by adding the  $x^3$  term. The rmse was reduced from  $\pm 0.46$  to  $\pm 0.34$  pixels.

The final significant improvement occurred in the y-direction when the term  $y^3$  was added to the polynomial. The rmse was reduced from  $\pm 0.39$  to  $\pm 0.30$  pixels.

The use of very high order polynomial transformations containing 4th and 5th order terms had absolutely no effect on the results obtained by the transformation procedure.

After each transformation, program PLOTDT4 was used to plot the error vector at each image point. A sample of these plots is shown in Appendix B.

As mentioned earlier, the Barr & Stroud IR-18 scanner was calibrated with telescopes of different magnification power to find out whether different telescopes will produce a different magnitude or pattern of distortion. The results from the calibration of the scanner with the 1 X and 6 X

telescopes are shown below in Tables 7-2 and 7-3 respectively.

It can be seen from the three tables below that the same terms were effective in improving the results for each of the three cases. This showed that the telescope magnification has no significant effect on the image geometry and that the magnitude of errors obtained is that resulting from the scanning geometry.

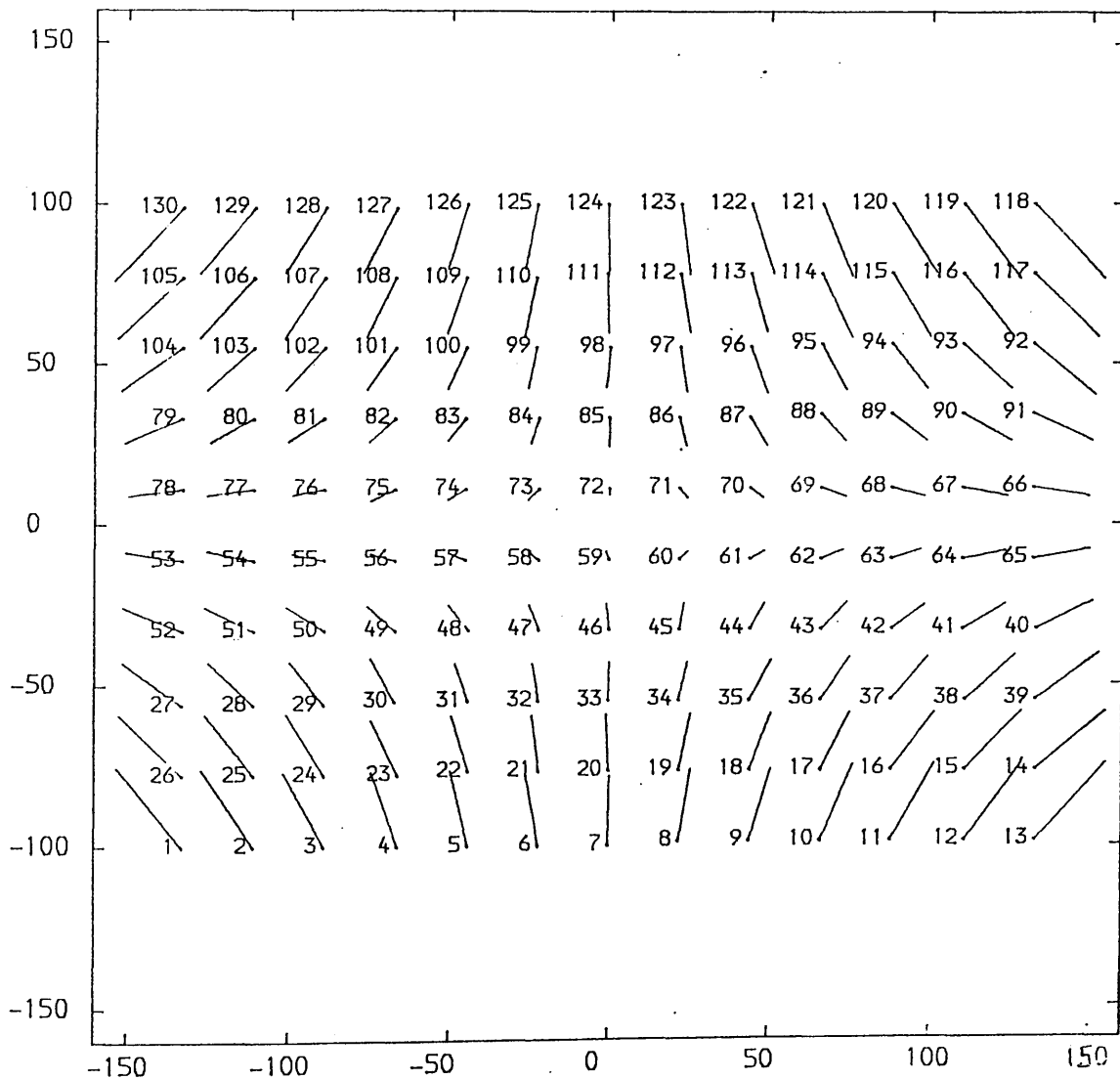


Fig.7-1 Vector plot for the IR-18 frame scanner.  
 Linear conformal transformation.  
 Vectors are 2 times magnified.

Transformation Procedure	R.M.S.E. (pixels)									
	Frame I		Frame II		Frame III		Frame IV		Frame V	
	$m_x$	$m_y$	$m_x$	$m_y$	$m_x$	$m_y$	$m_x$	$m_y$	$m_x$	$m_y$
Conformal	5.75	7.47	5.76	7.46	5.78	7.47	5.95	7.73	5.75	7.41
Affine	<u>0.63</u>	<u>0.48</u>	<u>0.67</u>	<u>0.51</u>	<u>0.68</u>	<u>0.46</u>	<u>0.67</u>	<u>0.46</u>	<u>0.72</u>	<u>0.57</u>
Polynomial										
Add. term										
4-Terms xy	0.63	0.47	0.61	0.49	0.67	0.45	0.65	0.44	0.71	0.57
5-Terms $x^2$	0.63	0.47	0.59	0.48	0.67	0.45	0.64	0.44	0.70	0.57
6-Terms $y^2$	0.61	0.46	0.58	0.48	0.63	0.42	0.63	0.41	0.68	0.57
7-Terms $xy^2$	0.62	<u>0.41</u>	0.58	<u>0.43</u>	0.63	<u>0.38</u>	0.63	<u>0.33</u>	0.67	<u>0.40</u>
8-Terms $y^2x$	<u>0.40</u>	0.41	<u>0.44</u>	0.43	<u>0.49</u>	0.38	<u>0.46</u>	0.33	<u>0.54</u>	0.40
9-Terms $xy^2$	0.40	0.41	0.44	0.43	0.48	0.37	0.46	0.33	0.54	0.40
10-Terms $x^3$	<u>0.28</u>	0.41	<u>0.33</u>	0.43	<u>0.38</u>	0.38	<u>0.31</u>	0.33	<u>0.39</u>	0.40
11-Terms $y^3$	0.29	<u>0.34</u>	0.33	<u>0.34</u>	0.37	<u>0.30</u>	0.31	<u>0.25</u>	0.39	<u>0.29</u>
12-Terms $xy^3$	0.29	0.33	0.32	0.34	0.36	0.30	0.31	0.25	0.39	0.29
13-Terms $xy^3$	0.29	0.33	0.32	0.34	0.35	0.30	0.31	0.25	0.39	0.29
14-Terms $xy^2$	0.29	0.33	0.32	0.34	0.36	0.30	0.31	0.25	0.39	0.29
15-Terms $xy^3$	0.29	0.33	0.32	0.34	0.36	0.30	0.31	0.24	0.39	0.29
16-Terms $x^2y$	0.29	0.33	0.32	0.34	0.36	0.30	0.31	0.24	0.39	0.29
17-Terms $x^4$	0.29	0.33	0.32	0.34	0.36	0.30	0.30	0.24	0.39	0.29
18-Terms $y^4$	0.29	0.33	0.32	0.33	0.36	0.29	0.31	0.25	0.37	0.28
19-Terms $xy^4$	0.29	0.33	0.32	0.33	0.36	0.29	0.31	0.25	0.37	0.28
20-Terms $xy^4$	0.29	0.33	0.33	0.32	0.35	0.30	0.31	0.25	0.36	0.28
21-Terms $xy^2$	0.28	0.33	0.33	0.33	0.35	0.31	0.31	0.25	0.36	0.28
22-Terms $xy^4$	0.28	0.34	0.33	0.33	0.34	0.30	0.33	0.25	0.36	0.28
23-Terms $xy^3$	0.28	0.33	0.33	0.33	0.34	0.30	0.30	0.25	0.36	0.28
24-Terms $xy^4$	0.28	0.33	0.33	0.33	0.34	0.30	0.31	0.25	0.36	0.28
25-Terms $xy^4$	0.29	0.34	0.33	0.33	0.34	0.30	0.31	0.24	0.36	0.28

Table 7-1 Calibration results for Barr & Stroud IR-18 frame scanner with 1.5 X telescope

Transform- ation	R.M.S.E. (pixels)									
	Frame I		Frame II		Frame III		Frame IV		Frame V	
	$m_x$	$m_y$	$m_x$	$m_y$	$m_x$	$m_y$	$m_x$	$m_y$	$m_x$	$m_y$
Conformal	5.76	6.45	5.76	6.46	5.78	6.47	5.95	6.73	5.75	6.41
Affine	<u>0.68</u>	<u>0.52</u>	<u>0.58</u>	<u>0.55</u>	<u>0.59</u>	<u>0.64</u>	<u>0.80</u>	<u>0.62</u>	<u>0.57</u>	<u>0.48</u>
Polynomial										
Add. term										
4-Terms $xy$	0.68	0.51	0.58	0.54	0.59	0.63	0.80	0.62	0.57	0.48
5-Terms $x^2$	0.68	0.50	0.59	0.54	0.59	0.63	0.79	0.61	0.57	0.48
6-Terms $y^2$	0.67	0.50	0.58	0.53	0.58	0.63	0.78	0.61	0.57	0.48
7-Terms $xy$	0.67	<u>0.41</u>	0.58	<u>0.45</u>	0.58	<u>0.49</u>	0.78	<u>0.48</u>	0.57	<u>0.42</u>
8-Terms $y/x$	<u>0.53</u>	0.41	<u>0.44</u>	0.45	<u>0.48</u>	0.49	<u>0.54</u>	0.48	<u>0.41</u>	0.42
9-Terms $xy^2$	0.53	0.41	0.44	0.44	0.48	0.49	0.54	0.48	0.41	0.42
10-Terms $x^3$	<u>0.39</u>	0.41	<u>0.33</u>	0.44	<u>0.38</u>	0.48	<u>0.36</u>	0.48	<u>0.33</u>	0.42
11-Terms $y^3$	0.39	<u>0.34</u>	0.33	<u>0.37</u>	0.38	<u>0.40</u>	0.36	<u>0.33</u>	0.33	<u>0.36</u>
12-Terms $xy^3$	0.39	0.34	0.33	0.37	0.38	0.40	0.36	0.33	0.33	0.36
13-Terms $xy^2$	0.39	0.33	0.33	0.37	0.38	0.43	0.36	0.33	0.33	0.36
14-Terms $x^2y^2$	0.39	0.33	0.33	0.36	0.38	0.39	0.36	0.33	0.33	0.36
15-Terms $xy^3$	0.40	0.33	0.33	0.36	0.38	0.39	0.35	0.33	0.33	0.35
16-Terms $x^3y^3$	0.39	0.33	0.32	0.36	0.38	0.39	0.35	0.32	0.33	0.36
17-Terms $x^4$	0.39	0.33	0.33	0.37	0.38	0.39	0.35	0.32	0.33	0.36
18-Terms $y^4$	0.39	0.33	0.33	0.37	0.38	0.40	0.35	0.32	0.33	0.36
19-Terms $xy^4$	0.39	0.33	0.33	0.37	0.37	0.39	0.35	0.32	0.33	0.36
20-Terms $xy^4$	0.38	0.33	0.34	0.37	0.37	0.39	0.35	0.32	0.33	0.36
21-Terms $xy^2$	0.39	0.33	0.33	0.37	0.37	0.39	0.35	0.32	0.33	0.36
22-Terms $xy^4$	0.39	0.34	0.33	0.37	0.37	0.39	0.35	0.32	0.33	0.36
23-Terms $xy^3$	0.38	0.33	0.32	0.37	0.37	0.39	0.35	0.32	0.33	0.36
24-Terms $xy^4$	0.38	0.33	0.32	0.37	0.36	0.39	0.35	0.32	0.33	0.36
25-Terms $xy^4$	0.38	0.34	0.32	0.37	0.36	0.39	0.35	0.32	0.33	0.36

Table 7-2 Calibration results for the Barr & Stroud IR-18 frame scanner with the 1X telescope.

Transformation Procedure	R.M.S.E. (pixels)									
	Frame I		Frame II		Frame III		Frame IV		Frame V	
	$m_x$	$m_y$	$m_x$	$m_y$	$m_x$	$m_y$	$m_x$	$m_y$	$m_x$	$m_y$
Conformal	6.74	7.93	6.63	7.89	6.70	7.76	6.80	7.73	6.84	7.94
Affine	<u>0.71</u>	<u>0.57</u>	<u>0.64</u>	<u>0.52</u>	<u>0.65</u>	<u>0.59</u>	<u>0.76</u>	<u>0.55</u>	<u>0.79</u>	<u>0.63</u>
Polynomial										
Add. term										
4-Terms $xy$	0.71	0.57	0.63	0.52	0.65	0.59	0.76	0.55	0.78	0.63
5-Terms $x^2$	0.71	0.57	0.63	0.52	0.65	0.59	0.75	0.55	0.78	0.63
6-Terms $y^2$	0.70	0.57	0.63	0.52	0.65	0.59	0.75	0.55	0.78	0.63
7-Terms $xy^2$	0.70	<u>0.43</u>	0.63	<u>0.40</u>	0.64	<u>0.45</u>	0.75	<u>0.47</u>	0.77	<u>0.51</u>
8-Terms $y^2x$	<u>0.49</u>	<u>0.43</u>	<u>0.52</u>	0.40	<u>0.51</u>	0.45	<u>0.53</u>	0.47	<u>0.55</u>	0.51
9-Terms $xy^2$	0.49	0.43	0.51	0.40	0.51	0.45	0.53	0.47	0.54	0.51
10-Terms $x^3$	<u>0.32</u>	0.42	<u>0.35</u>	0.40	<u>0.40</u>	0.45	<u>0.37</u>	0.47	<u>0.41</u>	0.51
11-Terms $y^3$	0.32	<u>0.28</u>	0.35	<u>0.32</u>	0.40	<u>0.36</u>	0.37	<u>0.35</u>	0.41	<u>0.39</u>
12-Terms $xy^3$	0.32	0.28	0.35	0.31	0.40	0.36	0.37	0.35	0.41	0.39
13-Terms $xy^3$	0.32	0.28	0.35	0.31	0.40	0.36	0.37	0.35	0.41	0.39
14-Terms $xy^2$	0.32	0.29	0.35	0.31	0.39	0.36	0.37	0.35	0.41	0.39
15-Terms $xy^3$	0.32	0.29	0.35	0.31	0.39	0.36	0.37	0.35	0.41	0.39
16-Terms $xy^3$	0.32	0.29	0.35	0.31	0.39	0.36	0.37	0.35	0.41	0.39
17-Terms $x^4$	0.32	0.29	0.35	0.31	0.39	0.37	0.37	0.35	0.41	0.39
18-Terms $y^4$	0.32	0.29	0.35	0.31	0.39	0.37	0.37	0.35	0.41	0.39
19-Terms $xy^4$	0.32	0.29	0.35	0.31	0.39	0.37	0.37	0.35	0.41	0.39
20-Terms $xy^4$	0.32	0.29	0.35	0.31	0.39	0.37	0.37	0.35	0.41	0.39
21-Terms $xy^2$	0.32	0.29	0.35	0.31	0.39	0.38	0.37	0.35	0.41	0.38
22-Terms $xy^2$	0.31	0.29	0.35	0.31	0.39	0.38	0.37	0.35	0.41	0.38
23-Terms $xy^3$	0.31	0.29	0.35	0.31	0.39	0.38	0.37	0.35	0.41	0.38
24-Terms $xy^4$	0.31	0.29	0.35	0.31	0.39	0.37	0.37	0.35	0.41	0.38
25-Terms $xy^4$	0.31	0.28	0.35	0.31	0.39	0.37	0.37	0.35	0.41	0.38

Table 7-3 Calibration results for the Barr & Stroud IR-18 frame scanner with the 6X telescope.



## 7.5 Results and Analysis from the Rank Pullin Controls Frame Scanner Calibration

The results for the RPC Thermal Imager are shown in Table 7-4. The linear conformal transformation resulted in a rmse of  $\pm 6.75$  and  $\pm 8.83$  pixels in the x and y directions respectively. The error vectors resulting from this transformation were plotted using the PLOTDT4 program. As can be seen in Fig.7-2, a similar pattern resulted to that produced from the plotting of the error vectors for the Barr & Stroud IR-18 frame scanner (Fig.7-1).

A significant improvement in the accuracy occurred when the affine transformation was used. The rmse was reduced to  $\pm 0.49$  and  $\pm 0.62$  pixels in the x and y directions respectively.

As can be seen from Table 7-4, again a substantial improvement in the accuracy occurred in the y-direction when the terms  $x^2y$  and  $y^3$  were added to the polynomial, while in the x-direction, the improvement occurred when the  $xy^2$  and  $x^3$  terms were added to the polynomial. As can be seen, the same terms had produced a significant improvement in the case of the Barr & Stroud IR-18 scanner.

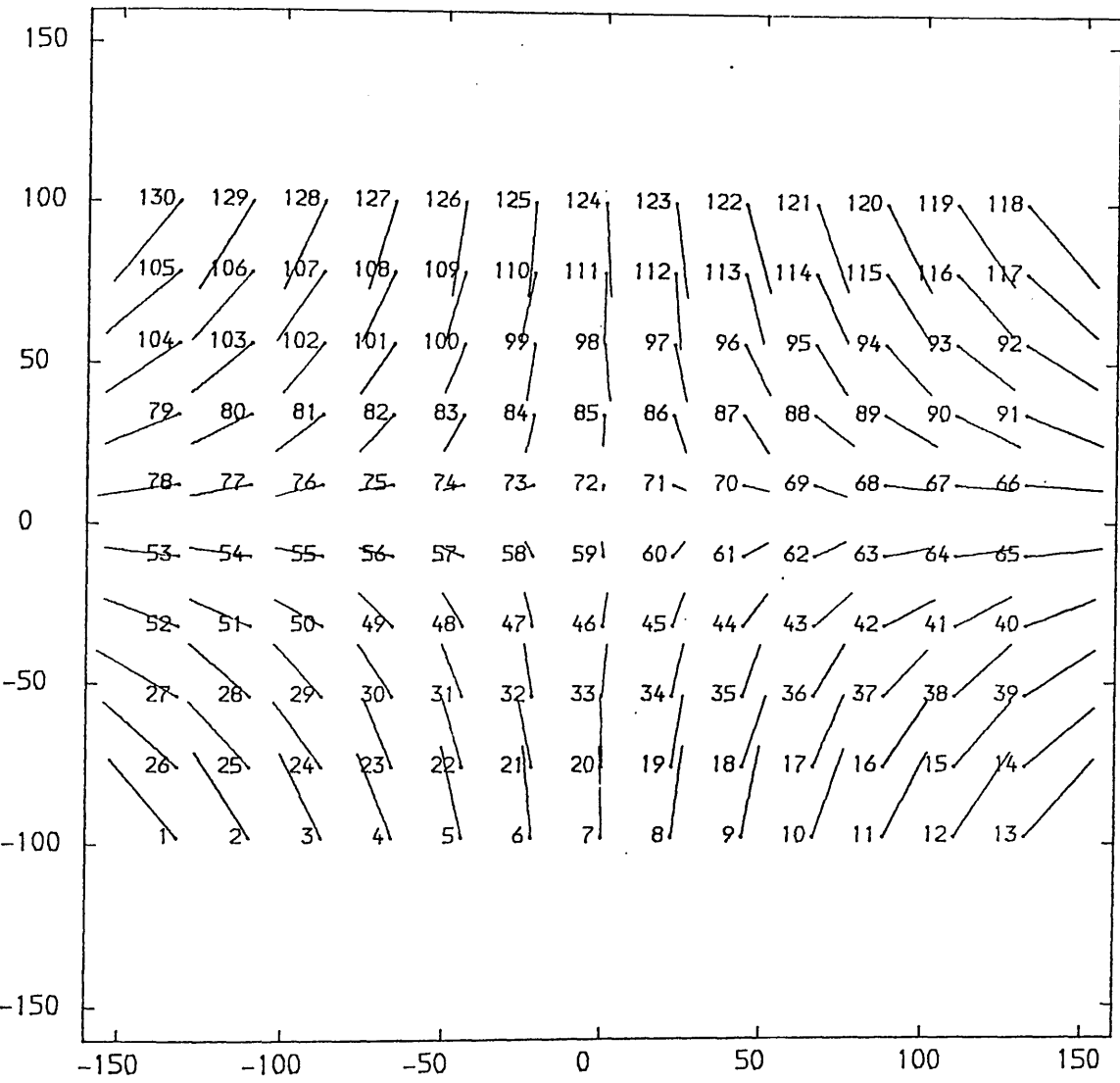


Fig.7-2 Vector plot for the RPC frame scanner.  
 Linear conformal transformation.  
 Vectors are 2 times magnified.

Transformation	R.M.S.E. (pixels)									
	Frame I		Frame II		Frame III		Frame IV		Frame V	
	$m_x$	$m_y$	$m_x$	$m_y$	$m_x$	$m_y$	$m_x$	$m_y$	$m_x$	$m_y$
Conformal	6.81	8.88	6.80	8.84	6.69	8.72	6.75	8.83	6.70	8.86
Affine	<u>0.46</u>	<u>0.64</u>	<u>0.49</u>	<u>0.55</u>	<u>0.52</u>	<u>0.64</u>	<u>0.54</u>	<u>0.61</u>	<u>0.47</u>	<u>0.67</u>
Polynomial										
Add. term										
4-Terms $xy$	0.46	0.64	0.49	0.55	0.52	0.64	0.54	0.61	0.47	0.67
5-Terms $x^2$	0.46	0.64	0.49	0.55	0.51	0.64	0.54	0.61	0.47	0.67
6-Terms $y^2$	0.46	0.63	0.49	0.55	0.52	0.64	0.54	0.61	0.47	0.67
7-Terms $xy^2$	0.46	<u>0.48</u>	0.50	<u>0.41</u>	0.52	<u>0.47</u>	0.54	<u>0.48</u>	0.47	<u>0.48</u>
8-Terms $y^3$	<u>0.41</u>	0.48	<u>0.47</u>	0.41	<u>0.47</u>	<u>0.47</u>	<u>0.49</u>	0.48	<u>0.42</u>	0.48
9-Terms $xy^2$	0.41	0.48	0.47	0.41	0.47	0.47	0.49	0.48	0.42	0.48
10-Terms $x^3$	<u>0.37</u>	0.48	<u>0.35</u>	0.41	<u>0.39</u>	0.47	<u>0.40</u>	0.48	<u>0.36</u>	0.48
11-Terms $y^3$	0.37	<u>0.42</u>	0.35	<u>0.36</u>	0.39	<u>0.44</u>	0.40	<u>0.41</u>	0.36	<u>0.43</u>
12-Terms $xy^3$	0.37	0.42	0.35	0.37	0.39	0.44	0.40	0.41	0.36	0.43
13-Terms $xy^3$	0.37	0.42	0.35	0.37	0.39	0.44	0.40	0.41	0.36	0.43
14-Terms $xy^3$	0.37	0.42	0.35	0.37	0.38	0.44	0.40	0.41	0.36	0.43
15-Terms $xy^3$	0.37	0.42	0.36	0.37	0.38	0.44	0.40	0.41	0.36	0.43
16-Terms $xy^3$	0.38	0.42	0.35	0.37	0.38	0.44	0.40	0.41	0.36	0.43
17-Terms $x^4$	0.38	0.42	0.35	0.37	0.38	0.44	0.40	0.41	0.36	0.43
18-Terms $y^4$	0.38	0.42	0.35	0.37	0.38	0.44	0.40	0.42	0.36	0.43
19-Terms $xy^4$	0.38	0.42	0.35	0.37	0.39	0.44	0.41	0.41	0.36	0.43
20-Terms $xy^4$	0.37	0.42	0.34	0.37	0.38	0.44	0.40	0.41	0.36	0.43
21-Terms $xy^4$	0.37	0.42	0.34	0.37	0.38	0.44	0.40	0.41	0.36	0.43
22-Terms $xy^4$	0.37	0.42	0.35	0.37	0.38	0.44	0.40	0.41	0.36	0.43
23-Terms $xy^4$	0.38	0.42	0.35	0.37	0.38	0.44	0.40	0.41	0.36	0.43
24-Terms $xy^4$	0.38	0.41	0.35	0.37	0.38	0.44	0.40	0.41	0.36	0.43
25-Terms $xy^4$	0.39	0.42	0.35	0.37	0.40	0.47	0.41	0.41	0.36	0.43

Table 7-4 Calibration results for the Rank Pullin Controls (RPC) frame scanner

## 7.6 Results and Analysis from the TICM II Calibration

The results from the calibration of the TICM II frame scanner are shown in Table 7-5 below. The sequence of improvements in the accuracy is similar to that which occurred with the previous two instruments. The affine transformation resulted in a drastic improvement in the accuracy followed by a significant change in the x-direction when the terms  $x y^2$  and  $x^3$  were used in the polynomial, while in the y-direction, the significant improvement occurred when the terms  $x^2 y$  and  $y^3$  were used. The vector plot for the linear conformal transformation is shown below in Fig.7-3.

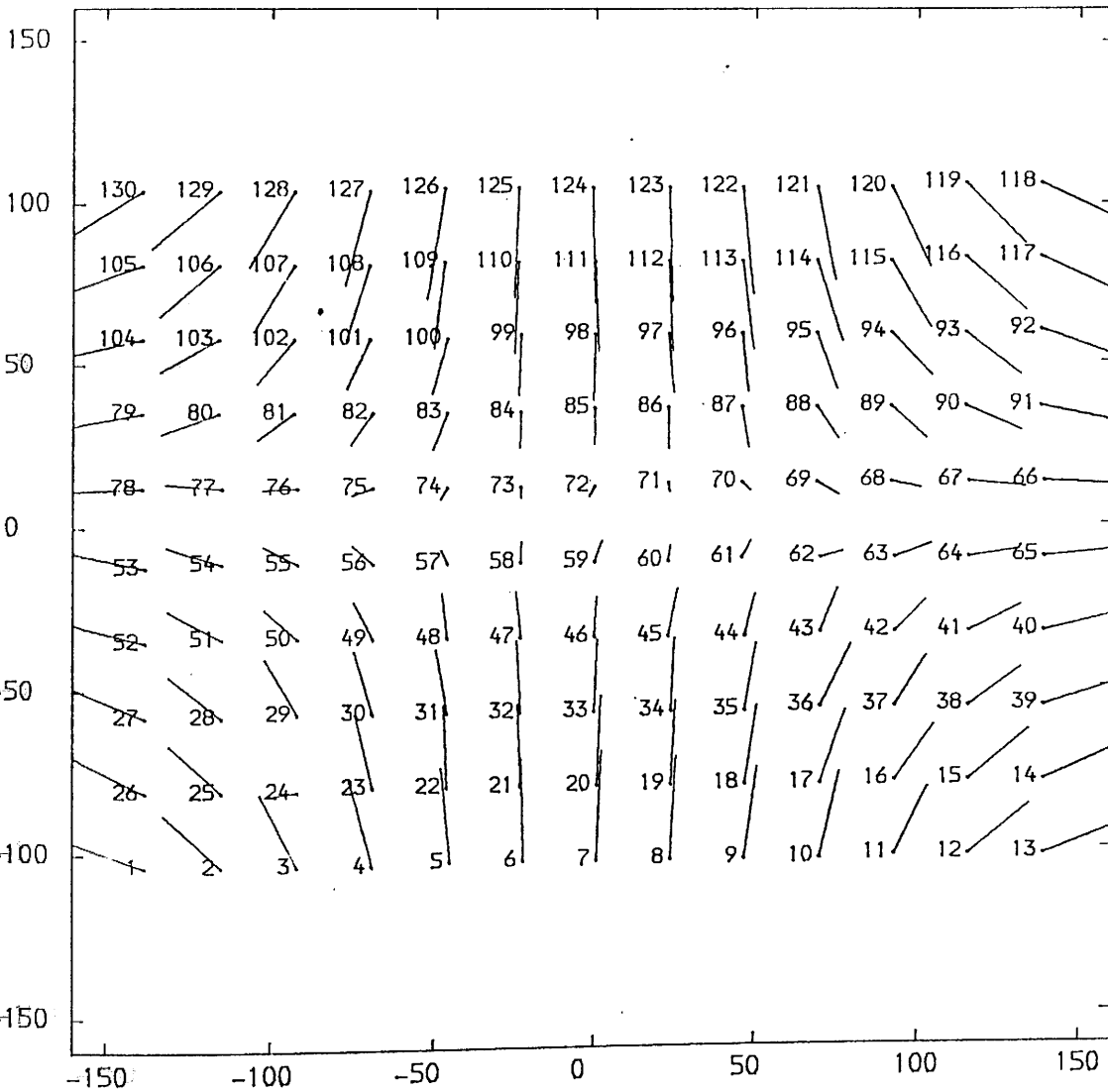


Fig.7-3 Vector plot for the TICM II.  
Linear conformal transformation.  
Vectors are 2 times magnified.

Transformation	R.M.S.E. (pixels)									
	Frame I		Frame II		Frame III		Frame IV		Frame V	
	$m_x$	$m_y$	$m_x$	$m_y$	$m_x$	$m_y$	$m_x$	$m_y$	$m_x$	$m_y$
Conformal	6.77	8.92	6.83	8.90	6.74	8.98	6.67	8.98	6.73	8.82
Affine	1.73	2.65	1.75	2.64	1.74	2.68	1.68	2.69	1.76	2.72
Polynomial										
Add.										
term										
4-Terms xy	1.73	2.66	1.75	2.64	1.74	2.68	1.69	2.69	1.76	2.72
5-Terms $x^2$	1.73	2.67	1.74	2.66	1.74	2.68	1.69	2.69	1.76	2.72
6-Terms $y^2$	1.74	2.62	1.74	2.65	1.74	2.68	1.69	2.68	1.76	2.72
7-Terms $xy^2$	1.74	0.77	1.74	0.73	1.74	0.75	1.69	0.76	1.75	0.70
8-Terms $y^2x$	0.80	0.76	0.78	0.73	0.78	0.75	0.74	0.76	0.76	0.70
9-Terms $xy^2$	0.80	0.76	0.78	0.73	0.78	0.75	0.74	0.76	0.76	0.70
10-Terms $x^3$	0.46	0.77	0.51	0.73	0.42	0.75	0.48	0.76	0.46	0.70
11-Terms $y^3$	0.45	0.55	0.51	0.53	0.42	0.50	0.48	0.58	0.46	0.53
12-Terms $xy^3$	0.45	0.55	0.51	0.53	0.42	0.51	0.48	0.58	0.46	0.53
13-terms $xy^3$	0.46	0.54	0.51	0.53	0.43	0.51	0.48	0.58	0.45	0.53
14-Terms $xy^2$	0.46	0.54	0.51	0.53	0.43	0.51	0.47	0.58	0.46	0.53
15-Terms $xy^3$	0.46	0.54	0.51	0.52	0.43	0.51	0.47	0.58	0.46	0.53
16-Terms $xy^3$	0.46	0.54	0.51	0.52	0.43	0.51	0.47	0.58	0.46	0.53
17-Terms $x^4$	0.46	0.55	0.51	0.52	0.43	0.51	0.47	0.58	0.46	0.53
18-Terms $y^4$	0.45	0.55	0.52	0.52	0.43	0.51	0.47	0.58	0.46	0.53
19-Terms $xy^4$	0.45	0.55	0.52	0.52	0.43	0.51	0.47	0.58	0.46	0.53
20-Terms $xy^4$	0.45	0.54	0.52	0.52	0.43	0.51	0.47	0.58	0.46	0.53
21-Terms $xy^4$	0.45	0.54	0.51	0.52	0.43	0.51	0.47	0.58	0.46	0.53
22-Terms $xy^4$	0.45	0.54	0.51	0.52	0.43	0.51	0.47	0.58	0.46	0.53
23-Terms $xy^4$	0.45	0.54	0.51	0.52	0.43	0.51	0.47	0.58	0.46	0.53
24-Terms $xy^4$	0.45	0.54	0.51	0.52	0.43	0.51	0.47	0.58	0.46	0.53
25-Terms $xy^4$	0.45	0.54	0.51	0.52	0.43	0.51	0.47	0.58	0.46	0.53

Table 7-5 Calibration results for the GEC Avionics/Rank Taylor Hobson TICM II frame scanner.

### 7.7 Results and Analysis from the AGA Thermovision

The results from the AGA Thermovision calibration are shown below in Table 7-6. As can be seen from this Table, the affine transformation still provides a big improvement in the accuracy while the terms  $x^2, x^3$  and  $x^2y, y^3$  are also producing a significant change in the accuracy in the x and y directions respectively. Again the vector errors from the linear conformal transformation were plotted as shown in Fig.7-4 below. A sample of the plots for other transformations is given in Appendix B.

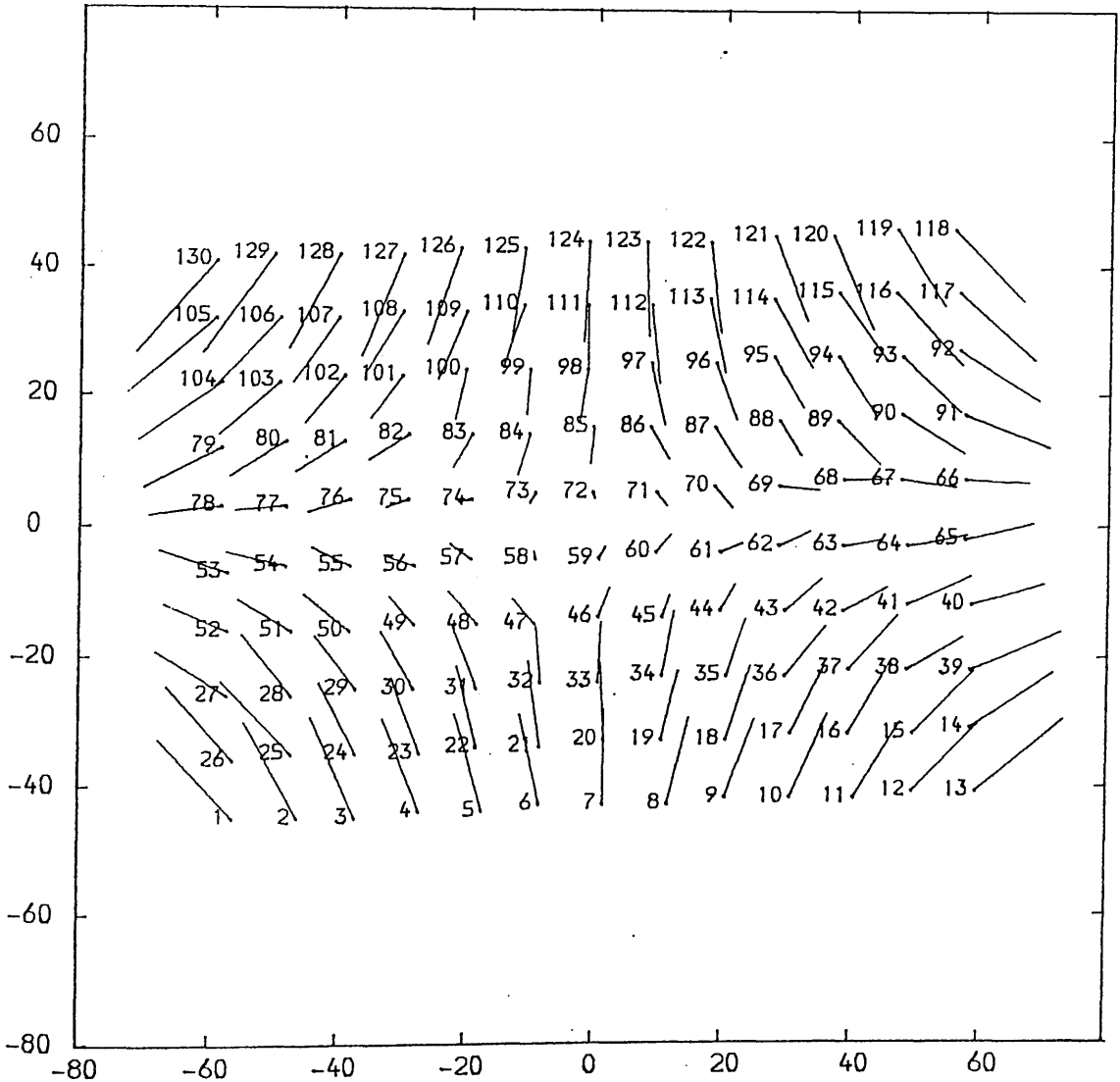


Fig.7-4 Vector plot for the AGA Thermovision.  
 Linear conformal transformation.  
 Vectors are 2 times magnified.

Transform- ation  Procedure	R.M.S.E. (pixels)									
	Frame I		Frame II		Frame III		Frame IV		Frame V	
	$m_x$	$m_y$	$m_x$	$m_y$	$m_x$	$m_y$	$m_x$	$m_y$	$m_x$	$m_y$
Conformal	6.81	8.88	6.80	8.84	6.69	8.72	6.75	8.83	6.70	8.86
Affine	<u>0.50</u>	<u>0.53</u>	<u>0.62</u>	<u>0.67</u>	<u>0.58</u>	<u>0.59</u>	<u>0.49</u>	<u>0.55</u>	<u>0.64</u>	<u>0.68</u>
Polynomial Add. term										
4-Terms $xy$	0.50	0.53	0.62	0.67	0.58	0.59	0.49	0.54	0.64	0.68
5-Terms $x^2$	0.50	0.53	0.61	0.62	0.58	0.59	0.48	0.54	0.63	0.67
6-Terms $y^2$	0.49	0.53	0.61	0.67	0.57	0.59	0.48	0.54	0.63	0.67
7-Terms $xy^2$	0.49	<u>0.49</u>	0.61	<u>0.57</u>	0.57	<u>0.51</u>	0.48	<u>0.50</u>	0.63	<u>0.59</u>
8-Terms $yx^2$	<u>0.46</u>	<u>0.49</u>	<u>0.55</u>	0.57	<u>0.50</u>	0.51	<u>0.44</u>	0.50	<u>0.58</u>	0.59
9-Terms $xy^3$	0.46	0.49	0.55	0.57	0.55	0.51	0.44	0.50	0.58	0.59
10-Terms $x^3$	<u>0.43</u>	0.49	<u>0.48</u>	0.57	<u>0.44</u>	0.51	<u>0.39</u>	0.50	<u>0.49</u>	0.59
11-Terms $y^3$	0.43	<u>0.45</u>	0.48	<u>0.51</u>	0.44	<u>0.43</u>	<u>0.39</u>	<u>0.43</u>	0.49	<u>0.50</u>
12-Terms $xy^3$	0.43	0.45	0.48	0.51	0.45	0.43	0.39	0.42	0.49	0.50
13-Terms $xy^3$	0.43	0.45	0.49	0.51	0.44	0.43	0.39	0.42	0.49	0.50
14-Terms $xy^2$	0.43	0.46	0.48	0.51	0.44	0.43	0.39	0.42	0.49	0.50
15-Terms $x^2y^3$	0.43	0.45	0.48	0.51	0.44	0.43	0.39	0.42	0.49	0.51
16-terms $xy^3$	0.44	0.45	0.48	0.51	0.44	0.43	0.39	0.42	0.49	0.50
17-Terms $x^4$	0.44	0.45	0.48	0.51	0.44	0.43	0.39	0.42	0.49	0.50
18-Terms $y^4$	0.43	0.45	0.48	0.50	0.44	0.43	0.38	0.42	0.49	0.50
19-Terms $xy^4$	0.43	0.45	0.48	0.51	0.44	0.43	0.38	0.42	0.49	0.50
20-Terms $xy^4$	0.43	0.45	0.48	0.51	0.44	0.43	0.39	0.42	0.49	0.50
21-Terms $xy^2$	0.43	0.45	0.48	0.51	0.44	0.43	0.39	0.42	0.49	0.50
22-Terms $xy^4$	0.43	0.45	0.48	0.51	0.43	0.43	0.39	0.42	0.48	0.50
23-Terms $xy^3$	0.43	0.45	0.48	0.51	0.44	0.43	0.39	0.42	0.48	0.50
24-Terms $xy^4$	0.43	0.45	0.48	0.51	0.43	0.43	0.39	0.42	0.49	0.50
25-Terms $xy^4$	0.43	0.45	0.49	0.51	0.43	0.42	0.40	0.42	0.48	0.50

Table 7-6 Calibration results for AGA Thermovision.

## 7.8 Overall Analysis

As can be seen from the Tables above, an enormous improvement in the accuracy of fit was obtained when an affine transformation was used instead of the linear conformal one. This indicates that all the video images from the four different frame scanners contain very substantial differences in scale between the x and y directions. This characteristic appeared in all 5 frames calibrated for each of the four scanners.

When higher term polynomials were used, a significant improvement in accuracy in the x-direction was obtained especially when the terms  $xy^2$  and  $x^3$  were used in the polynomial. In the y-direction, the improvement occurred when the  $x^2y$  and  $y^3$  terms were used. The use of very high (fourth and fifth) order terms did not result in any discernible improvement in accuracy.

Based on the results shown in the calibration tables, two equations could be formed and used as specific transformation polynomials for thermal video frame scanner imagery. This would be achieved by eliminating all the terms which have been shown to have no significant effect on the accuracy. These equations are-

$$x' = a_0 + a_1 x + a_2 y + a_3 x y^2 + a_4 x^3 \quad \dots\dots\dots 7-23$$

$$y' = b_0 + b_1 x + b_2 y + b_3 x^2 y + b_4 y^3 \quad \dots\dots\dots 7-24$$

Program POLY25 was modified to use equations 7-23 and 7-24 and then was used to perform another set of transformations and the results are shown below in Table 7-7.

Frame No. Scanner	R. M. S. E. (pixels)									
	I		II		III		IV		V	
	$m_x$	$m_y$	$m_x$	$m_y$	$m_x$	$m_y$	$m_x$	$m_y$	$m_x$	$m_y$
IR-18	0.30	0.36	0.34	0.39	0.41	0.33	0.30	0.22	0.43	0.31
RPC	0.39	0.45	0.35	0.36	0.37	0.45	0.40	0.42	0.37	0.45
TICM II	0.48	0.55	0.51	0.53	0.42	0.52	0.49	0.58	0.49	0.54
AGA	0.43	0.47	0.49	0.51	0.46	0.45	0.40	0.42	0.52	0.51

Table 7-7 Results from the reduced polynomial

As can be seen from the table above, the use of the specific polynomial equations (7-23 and 7-24), has produced almost the same accuracy obtained before for each scanner.



A set of simulated data was formed and used in equations 7-23,7-24. However, on this occasion the coefficients of the polynomial were considered to be known from the transformation procedure. The residuals at each point were computed and plotted. This was carried out in order to establish the exact shape of the image surface without the effect of the observational or random errors. The plot of this idealized shape is shown below in Fig.7-5

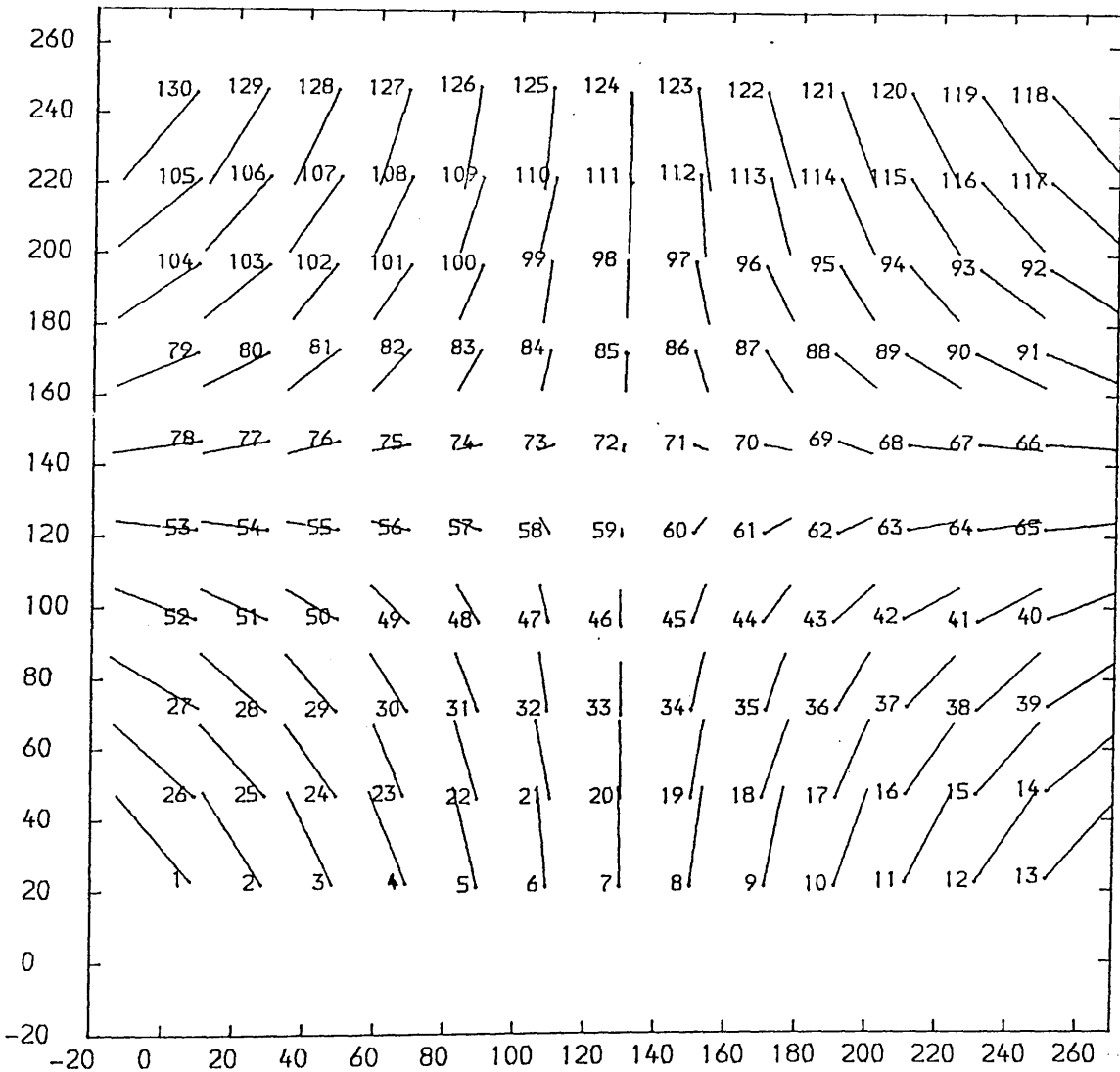
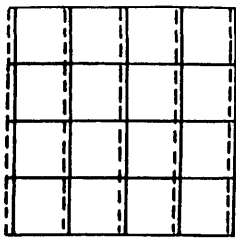
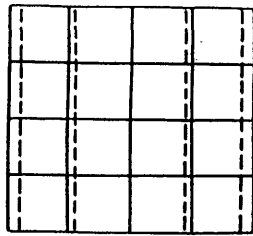


Fig.5-7 Plot of residuals using the simulated data

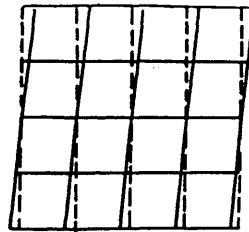
This reduced polynomial can now be used to describe the surface shape of the video image produced by any frame scanner employing the same technique of using two mirrors to scan the object in two orthogonal directions. Fig.7-6 below shows the effect of each term in these polynomials on the transformation procedure.



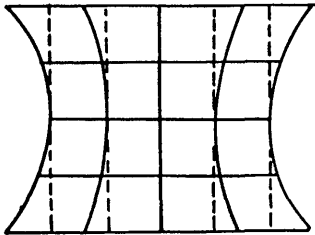
$$x' = a_0$$



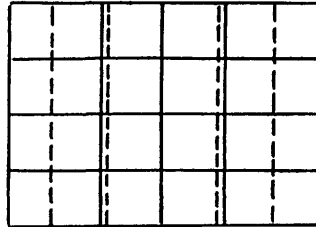
$$+ a_1 x$$



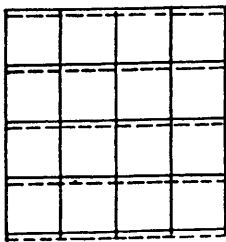
$$+ a_2 y$$



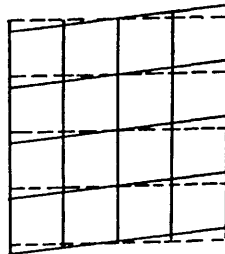
$$+ a_3 x y^2$$



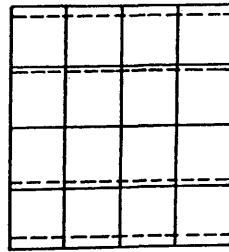
$$+ a_4 x^3$$



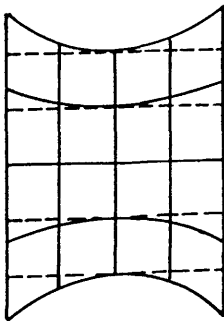
$$y' = b_0$$



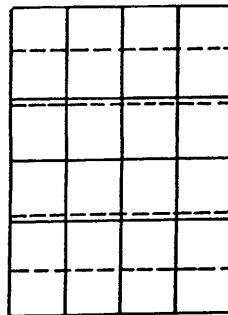
$$+ b_1 x$$



$$+ b_2 y$$



$$+ b_3 x^2 y$$



$$+ b_4 y^3$$

Fig.7-6 Effect of each term of the reduced polynomial on the video image geometry

## 7.9 Systematic and Random Distortion

The procedure described in Section 7.2 above for the determination of the systematic and random components of distortion was followed and the results are shown in the Table below:

Scanner	R.M.S.E. (Pixels)			
	Systematic Distortion		Random Distortion for Frame I	
	$m_x$	$m_y$	$m_x$	$m_y$
IR-18	5.80	7.50	0.28	0.31
RPC	6.75	8.82	0.38	0.47
TICM II	6.75	8.92	0.22	0.42
AGA	6.78	8.78	0.48	0.57

Table 7-8 Systematic and random distortion in each of the four frame scanners tested

As can be seen from the table above, the distortion is highly systematic, mainly due to the effect of scanning geometry. Thus the distortion produced by the frame scanners can be described as being both systematic and symmetric at the same time.

As can be seen in the previous Chapters, frame scanners have a different geometry and characteristics from the familiar imaging sensors which are commonly used in the field of remote sensing. In the next Chapter, the analytical photogrammetric procedures which can be applied to frame scanner imagery are discussed in detail, with a view to establishing their potential in the field of topographic mapping.

## CHAPTER VIII

### ANALYTICAL PHOTOGRAMMETRIC TECHNIQUES APPLIED TO AIRBORNE FRAME SCANNER IMAGERY

## CHAPTER VIII

### ANALYTICAL PHOTOGRAMMETRIC TECHNIQUES APPLIED TO AIRBORNE FRAME SCANNER IMAGERY

#### 8.1 Introduction

In the previous chapters, the geometrical theory of video frame scanners has been investigated in detail. Also a calibration procedure which can be employed with this type of scanner has been devised and used successfully. In this Chapter, the different approaches which may be used to reconstruct a three-dimensional model from two overlapping video images will be discussed. It is obvious that conventional analogue techniques using stereoplotting machines cannot be used with frame scanner images since these scanners produce a video image rather than a hard-copy image. Even if a hard-copy image is produced either by photographing the image displayed on the video monitor screen or using an electron beam writer to write the image on film, suitable stereoplotting machines which can correct for the types of distortion which exist in frame scanner images are not available. Instead, analytical techniques based on the use of ground control points whose coordinates are known in both the ground coordinate system and the video image coordinate system will be used to create a three-dimensional model of the terrain.

##### 8.1.1 Lack of Knowledge of Interior Orientation Elements

As mentioned earlier, frame scanners are not equipped with fiducial marks which allow the position of the principal point of the video image to be determined accurately. Also, the procedure which has been used to determine the scanners's calibrated focal length (CFL) is not very reliable since the distance between the scanner and the calibration target plate which was used to compute the CFL was measured by a surveying measuring tape to the nearest 0.5 cm. Any inaccuracy in the measurement of this distance will definitely produce an error in the computed CFL.

Since the frame size of the IR-18 frame scanner is 500 lines and each line consists of 768 pixels, the pixel which has coordinates of (250,384) was taken as the centre of the video image. In other words, this pixel has simply been adopted as the position of the principal point. Since it has not been determined by calibration, consequently there must be some uncertainty in its position.

Any error in the determination of the CFL and in the position of the principal point will be allowed for during the analytical procedures by using additional parameters to compensate for their effect. These will be included as unknowns in the formulation used for the analytical formation of the stereo-model.

Using analytical photogrammetric methods, the following procedure has been used to reconstruct the three-dimensional relationship between the image and ground points:-

- (i) The choice of the stereopair to be used to form the stereo model.
- (ii) Image coordinate refinements.
- (iii) Application of suitable analytical techniques to solve for the exterior orientation parameters and to derive the planimetric and height coordinates of the points whose coordinates are known in the two images forming the stereopair.

## 8.2 Formation of the Stereomodel

As mentioned in Chapter II, PAL TV-compatible systems produce an individual video image at a field rate of 50 Hz and a full (interlaced) format at 25 Hz. To form a suitable video stereomodel, it was required to capture two video images which have approximately a 60% overlap in the flight direction. Fig.8-1 shows these two images as they were recorded on the video tape during the flight test.

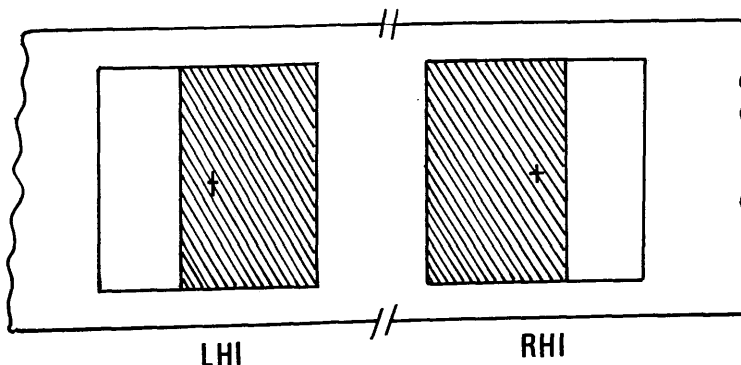


Fig.8-1 Two overlapping images on the video tape

The procedure which was used can be described as follows:-

- (i) The video cassette tape on which the images were recorded during the aerial flight test was played back on the VTR.

- (ii) The first image which covered the ground area of interest was frozen in the frame memory (FM). Thus the same image continued to be displayed on the video monitor screen at a refresh rate of 50 Hz.
- (iii) The video image frozen in the FM and displayed on the monitor was recorded on a blank video cassette tape for about 1 minute. This image will be called the left hand image (LHI) of the stereopair.
- (iv) A well defined object image on the LHI was chosen and its x-coordinate was measured by the VPA as shown in Fig.8-1. The corresponding x-coordinate of the same point on the second image (RHI) of the stereopair was computed assuming a 60% overlap. The measuring cursor of the VPA was moved to that position.
- (v) The freeze button of the frame memory was released and the video cassette tape containing the aerial images was put back into the VTR and allowed to continue to play back until the image of the same object defined in the LHI passed on to the measuring cursor of the VPA. At this moment, the image was frozen to form the right hand image (RHI) of the stereopair. This RHI was recorded for 1 minute onto the same tape as the LHI after leaving a short blank space on the tape between the two images.

The reason for the above procedure was to make sure that the same two video images of the stereopair can be accessed at any time. The same technique was used to form and record other stereopairs alongside the first one.

### 8.2.1 Characteristics of the Stereopair

One of the most important characteristics of stereo imagery is the base to height ratio (B/H). The B/H ratio is the ratio of the airbase of a pair of overlapping images to the average flying height above the terrain. The larger the B/H ratio, the greater the intersection angles between intersecting light rays to common points. These intersection angles are shown in Fig.8-2 below. In the vertical plane containing the exposure stations  $O_1$  and  $O_2$  at which the LHI and the RHI were taken, the greatest intersection angle ( $a_2$ ) will occur at the mid point (P) between their ground analogues  $N_1$  and  $N_2$ . Similarly, at the edge of the model, the greatest intersection angle ( $a_4$ ) will be at (R), the point where the perpendicular from (P) intersects the edge of the model.

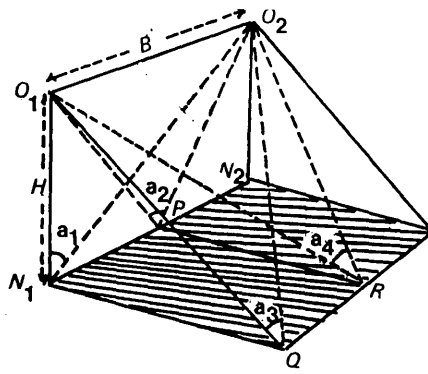


Fig.8-2 Intersection angles at common points (Petrie,1970)

For most topographic mapping based on the photogrammetric frame camera, photography is preferably taken with a wide or super-wide angle (short focal length) lens and camera, so that a large base to height ratio is obtained. This ensures a maximum theoretical accuracy in height measurement and contouring.

As mentioned in Chapter V, frame scanners have a rectangular field of view. Thus the scanner could be fitted in the aircraft so that:-

- (i) the wider angle is set across the flight direction; or
- (ii) the narrower angle is set across the flight direction.

It is obvious that the B/H ratio for case (ii) will be larger than that of case (i). Petrie, 1970 computed the intersection angles ( $a_1, a_2, a_3$  and  $a_4$ ) at the four specific points N, P, Q and R respectively for a single stereopair with 60% overlap taken by different imaging devices and with different B/H ratios. These are shown below in Table 8-1 together with the corresponding values for the IR-18 frame scanner.

Type	Photographic Frame Cameras				Frame Scanners	
	Super Wide	Wide	Normal	Narrow	IR-18	
					(i)	(ii)
Angular Coverage	122°	95°	56°	30°	20.4°	20.4°
B/H Ratio	1.02	0.61	0.31	0.15	0.12	0.18
Intersection Angle						
$a_1$	45.9°	31.5°	17.1°	8.7°	6.8°	10.4°
$a_2$	54.1°	34.1°	17.4°	8.8°	6.8°	10.5°
$a_3$	32.2°	25.5°	16.0°	8.5°	6.7°	10.2°
$a_4$	35.0°	27.3°	16.2°	8.6°	6.8°	10.4°

Table 8-1 Intersection angles at points N,P,Q,R



These figures show the poor intersection angles at the terrain for a stereo-model formed from IR-18 frame scanner imagery taken with a vertical position of the optical axis.

### 8.3 Image Coordinate Refinements

In conventional mapping techniques using photogrammetric frame camera images, the measured image coordinates are usually corrected for the following types of distortion:-

- (i) Radial lens distortion.
- (ii) Atmospheric refraction.
- (iii) Earth curvature.
- (iv) Film deformation.

The situation with airborne video frame scanner images is slightly different. The flying altitude is usually very low (500 m to 10,000 m), in which case, the effects of the atmospheric refraction and the Earth curvature can be neglected, bearing in mind the low resolution (pixel size) of this type of imaging device. Also the aspect of the film deformation is not applicable since these scanners produce a video image. Thus, based on the geometrical analysis presented in Chapter V, the measured video image coordinates must be corrected for the following types of distortion:-

- (i) Imaging system distortion. This is the sum of the distortions present in the frame scanner images such as those generated by the optical elements, scan geometry distortion and any distortion caused by the electronic circuits. The magnitude and extent of this distortion has been established in the previous Chapter.
- (ii) Image motion during the image scan time.

#### 8.3.1 Correction for the Imaging System Distortion

The measured video image coordinates  $x_j$ ,  $y_j$  of any point  $j$  can be corrected for the system distortion using the simple affine transformation which will be applied to a patch of the image subtended by four crosses whose coordinates and magnitude of distortion are known from the scanner calibration. The affine transformation will be used first to solve for the 6 unknown parameters ( $a_0, a_1, a_2, b_0, b_1$  and  $b_2$ ). These parameters will then be used to correct the measured image coordinates of any point lies within the vicinity of the area between the four crosses. This could be achieved as follows:-

- (i) A distortion table is formed containing the x,y coordinates of the 130 cross images of the target plate as measured by the VPA together with the mean distortion  $v_x$  ,  $v_y$  at each cross image.
- (ii) A search is made through the distortion table to locate the closest four cross images to point j and the distortion values at these four points are retrieved.
- (iii) The coefficients of the following equations are then computed-

$$v_{x_i} = a_0 + a_1 x_i + a_2 y_i \dots\dots\dots 8-1$$

$$v_{y_i} = b_0 + b_1 x_i + b_2 y_i \dots\dots\dots 8-2$$

- (iv) Having determined the coefficients  $a_0$  ,  $a_1$  ,  $a_2$  ,  $b_0$  ,  $b_1$  and  $b_2$  , the distortion values at any point j can be computed as follow:-

$$v_{x_j} = a_0 + a_1 x_j + a_2 y_j \dots\dots\dots 8-3$$

$$v_{y_j} = b_0 + b_1 x_j + b_2 y_j \dots\dots\dots 8-4$$

- (v) Finally, the measured image coordinates of point j are corrected as follows:-

$$x_j^- = x_j + sv_{x_j} \dots\dots\dots 8-5$$

$$y_j^- = y_j + sv_{y_j} \dots\dots\dots 8-6$$

Where  $x_j^-$  ,  $y_j^-$  are the corrected image coordinates of point j.

### 8.3.2 Correction for the Image Motion During the Image Scan Time

The mathematical basis for the correction of this type of distortion is given in Section 5.6.4. A computer program was written to correct the measured video image coordinates for the two types of distortion. The details of this program are given in Appendix A.

## 8.4 Possible Analytical Approaches

There are two common photogrammetric techniques which are usually applied for aerial imagery-

- (i) space resection/intersection; or
- (ii) relative and absolute orientation.

### 8.4.1 Space Resection/Intersection

The problem of space resection/intersection involves two separate stages:-

#### (i) Space Resection:-

An individual space resection of each image by which the coordinates of the perspective centre ( $X_0, Y_0$  and  $Z_0$ ) may be determined relative to the ground coordinate system and the three rotations ( $\omega$ ,  $\phi$  and  $\kappa$ ) about the three coordinate axes  $x, y$  and  $z$  respectively, which were present at the moment of exposure, may be determined.

#### (ii) Space Intersection:-

In which the measured image coordinates, the now known coordinates of the perspective centre and the rotation parameters from each of the two overlapping images are combined to give the terrain coordinates.

### 8.4.2 Relative and Absolute Orientation

This procedure involves two distinct stages-

#### (i) Relative Orientation:-

In this process, the positions and orientations of both exposure (scan centre) stations are determined with respect to an arbitrary object reference coordinate system. In addition, the object positions of the measured image coordinates are determined in this reference system. The solution which is usually adopted is based on the coplanarity condition. This condition states that, when two photographs are in correct relative orientation, rays from corresponding image points intersect; the two corresponding image points and the two projection centres lie on these intersecting rays and must lie in a single plane (the epipolar plane).

(ii) **Absolute Orientation:-**

Absolute orientation is the process by which a pair of relatively oriented photographs and the corresponding three-dimensional model are related to the ground control system. This consists of solving for seven absolute orientation parameters. These are the scale of the three dimensional model, three translations and three rotations. The solution of these seven parameters is based on the known orientation parameters of each of the two images forming the stereo-model which have been derived during the relative orientation phase.

As can be seen from the above discussion, the two main techniques which are commonly used in analytical photogrammetry can be applied to the video imagery acquired by frame scanners. However, the space resection intersection procedure is more flexible and can be easily modified to account for the unique characteristics of the video frame scanner imagery. Another reason which made this technique attractive was the availability of a suitable computer program in the Department (El Hassan, 1978). This program had been written and used for the processing of reconnaissance camera imagery using the additional parameters technique. The program was modified by the present author to account for the special geometrical characteristics of video frame scanner imagery. In the remaining part of this Chapter, the space resection/ intersection technique and the possible modifications required to account for the additional characteristics of frame scanner imagery will be discussed in more detail.

### 8.5 Space Resection

As mentioned above, the problem of resection in photogrammetry is concerned with the determination of the position of the perspective centre of a single image in space and its tilts based on the known positions (X,Y) and elevations (Z) of at least three non-linear objects. The solution which is usually used to solve for these parameters is based on the collinearity condition. This states that "every object, its image and the camera exposure station must all lie on a common straight line" (Moffit & Mikhail, 1980). This method allows the use of a least squares adjustment procedure when redundant data is available to minimize the random observational discrepancies.

### 8.5.1 Collinearity Condition

Although the definition of the collinearity condition is the same for almost all imaging systems utilizing a perspective centre, the mathematical equations which are used to satisfy this condition may differ from one imaging system to another according to its geometry.

This point will become apparent by discussing the collinearity condition for the main imaging systems whose geometry has been discussed in Chapter V. These are the photogrammetric frame camera, the panoramic frame camera, the optical-mechanical line scanner and the video frame scanner.

#### 8.5.1.1 Collinearity Condition for the Photogrammetric Frame Camera

The situation with the frame camera is shown in Fig.8-3 below, in which the exposure station L of an aerial photograph has coordinates  $X_0, Y_0$  and  $Z_0$  with respect to the ground coordinate system  $X, Y$  and  $Z$ . The image point (a) of the object point (A) shown in a tilted image plane, has image space coordinates  $x_a, y_a$  and  $-f$  with respect to an image coordinate system  $x, y$  and  $z$  based on the exposure station L.

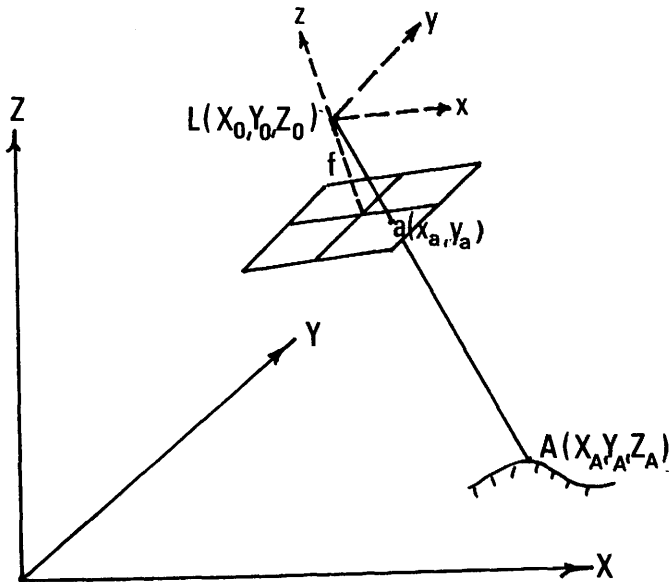


Fig.8-3 The principle of collinearity

The projective transformation equation which relates the two systems of coordinates can be expressed as follows:-

$$\begin{pmatrix} X_A \\ Y_A \\ Z_A \end{pmatrix} = A \lambda \begin{pmatrix} x_a \\ y_a \\ -f \end{pmatrix} + \begin{pmatrix} X_0 \\ Y_0 \\ Z_0 \end{pmatrix} \dots\dots\dots 8-7$$

Where:-

$X_A, Y_A, Z_A$  are the coordinates of the object point with respect to the ground coordinate system;

$x_a, y_a$  are the coordinates of the corresponding image point with respect to the image coordinate system with the principal point as origin;

$f$  is the camera focal length;

$\lambda$  is a scale factor;

$A$  is an orthogonal orientation matrix which relates the image coordinate system to the ground coordinate system with its elements formed by the three rotational angles omega ( $\omega$ ), phi ( $\phi$ ) and kappa ( $\kappa$ ); and

$X_0, Y_0, Z_0$  are the coordinates of the exposure station with respect to the ground coordinate system.

Equations 8-7 above can be used to derive the following two collinearity equations which will be valid for any point  $i$  on the photograph;

$$x_i = -f \frac{m_{11}(X_i - X_0) + m_{12}(Y_i - Y_0) + m_{13}(Z_i - Z_0)}{m_{31}(X_i - X_0) + m_{32}(Y_i - Y_0) + m_{33}(Z_i - Z_0)} \dots\dots\dots 8-8$$

$$y_i = -f \frac{m_{21}(X_i - X_0) + m_{22}(Y_i - Y_0) + m_{23}(Z_i - Z_0)}{m_{31}(X_i - X_0) + m_{32}(Y_i - Y_0) + m_{33}(Z_i - Z_0)}$$

Where  $m_{11}$  to  $m_{33}$  are the elements of the orthogonal matrix  $A$

Since the whole format was exposed instantaneously, the camera parameters determined from equations 8-8 are valid for any point on the photograph.

### 8.5.1.2 Collinearity Condition for the Panoramic Frame Camera

The geometry of the collinearity condition for the panoramic frame camera is shown below in Fig.8-4.

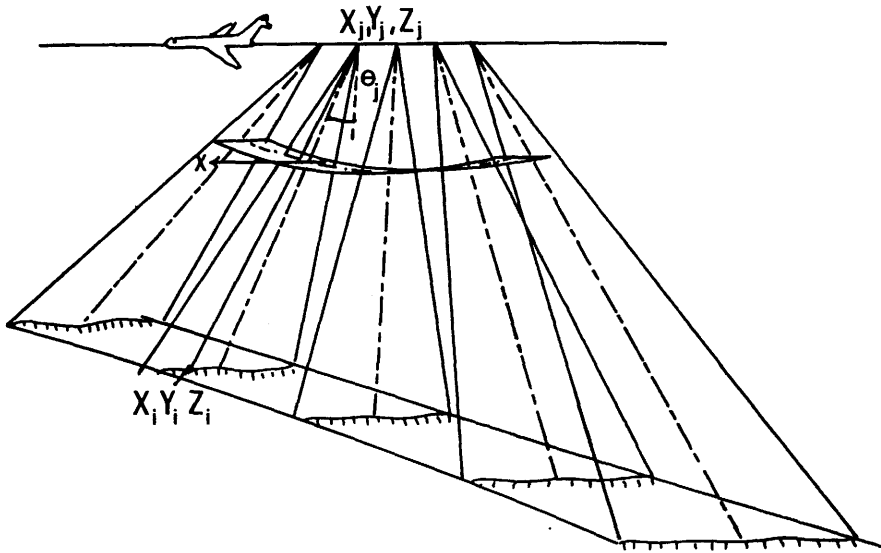


Fig.8-4 Geometry of the collinearity condition for the panoramic frame camera

Since the panoramic camera scans the terrain through a scan angle ( $\theta$ ) using the lens-slit assembly, the instantaneous focal plane will be limited to the line exposed by the slit at any instant of time. In this case, the camera position and attitude will be changing from one slit line to the other across the frame.

Considering an image coordinate system limited to the focal line (Fig.8-4), in which the origin is the centre point  $j$  of this focal line, the projective transformation equations must take into account the scan angle ( $\theta$ ) as an additional rotation about the  $x$ -direction (Case, 1967)

Thus, the projective equations for the panoramic camera imagery can be expressed as follows:-

$$\begin{vmatrix} X_i \\ Y_i \\ Z_i \end{vmatrix} = \begin{vmatrix} 1 & 0 & 0 \\ 0 & \cos\theta_j & -\sin\theta_j \\ 0 & \sin\theta_j & \cos\theta_j \end{vmatrix} A_j \lambda_j \begin{vmatrix} x_i \\ y_i \\ -f \end{vmatrix} + \begin{vmatrix} X_j \\ Y_j \\ Z_j \end{vmatrix} \dots\dots 8-9$$

Where ( $\theta_j$ ) is the scan angle for slit  $j$  on which the image point  $i$  lies.

In the above equation, the  $y$ -coordinate is considered to be zero since it lies in the narrow direction of the slit.

The collinearity equations for panoramic photography derived from equation 8-9 are as follows:-

$$\begin{aligned} \bar{x}_i &= -f \frac{m_{11}(X_i - X_j) + m_{12}(Y_i - Y_j) + m_{13}(Z_i - Z_j)}{m_{31}(X_i - X_j) + m_{32}(Y_i - Y_j) + m_{33}(Z_i - Z_j)} \\ \bar{y}_i &= -f \frac{m_{21}(X_i - X_j) + m_{22}(Y_i - Y_j) + m_{23}(Z_i - Z_j)}{m_{31}(X_i - X_j) + m_{32}(Y_i - Y_j) + m_{33}(Z_i - Z_j)} \end{aligned} \dots\dots\dots 8-10$$

Where:-

$$\begin{aligned} \bar{x}_i &= x_i / \cos \theta_i; \text{ and} \\ \bar{y}_i &= f \tan \theta_i \end{aligned}$$

### 8.5.1.3 Collinearity Condition for the Optical-Mechanical Line Scanner

In this case, the scanner scans the object sequentially pixel by pixel in the cross-track direction and the instantaneous focal plane will be limited to a point. Again, the projective equation must take into account the mirror scan angle  $\theta$  as an additional rotation about the x-direction (Konecny, 1972). The geometry of the collinearity condition for line scanner imagery is shown in Fig.8-5 below.

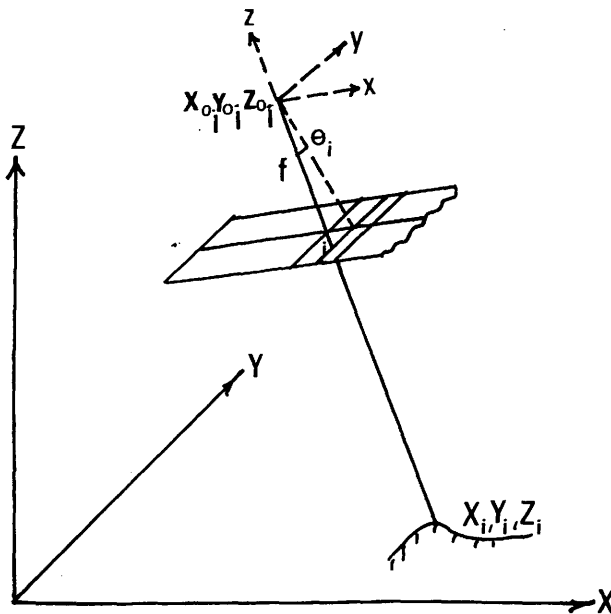


Fig.8-5 Collinearity condition for line scanner imagery

Thus the projective equations will be in the following form:-

$$\begin{vmatrix} X_i \\ Y_i \\ Z_i \end{vmatrix} = \begin{vmatrix} 1 & 0 & 0 \\ 0 & \cos \theta_i & -\sin \theta_i \\ 0 & \sin \theta_i & \cos \theta_i \end{vmatrix} A_i \lambda_i \begin{vmatrix} 0 \\ 0 \\ -f \end{vmatrix} + \begin{vmatrix} X_0 \\ Y_0 \\ Z_0 \end{vmatrix} \dots\dots 8-11$$



The collinearity equations for the line scanner imagery derived from equations 8-11 are as follows:-

$$0 = -f \frac{m_{11}(X_i - X_{o_i}) + m_{12}(Y_i - Y_{o_i}) + m_{13}(Z_i - Z_{o_i})}{m_{31}(X_i - X_{o_i}) + m_{32}(Y_i - Y_{o_i}) + m_{33}(Z_i - Z_{o_i})} \quad \dots 8-12$$

$$f \tan \theta_i = -f \frac{m_{21}(X_i - X_{o_i}) + m_{22}(Y_i - Y_{o_i}) + m_{23}(Z_i - Z_{o_i})}{m_{31}(X_i - X_{o_i}) + m_{32}(Y_i - Y_{o_i}) + m_{33}(Z_i - Z_{o_i})}$$

#### 8.5.1.4 Collinearity Condition for Frame Scanner Imagery

Frame scanners sequentially scan the object pixel by pixel in two directions. Thus the instantaneous focal plane will again be limited to a point and the exterior orientation parameters are likely to change from one point to the other. Also, the projective equations must take into account the two scan angles (about the x-direction and about the y-direction). The geometry of the collinearity condition for frame scanner imagery is shown in Fig.8-6 below.

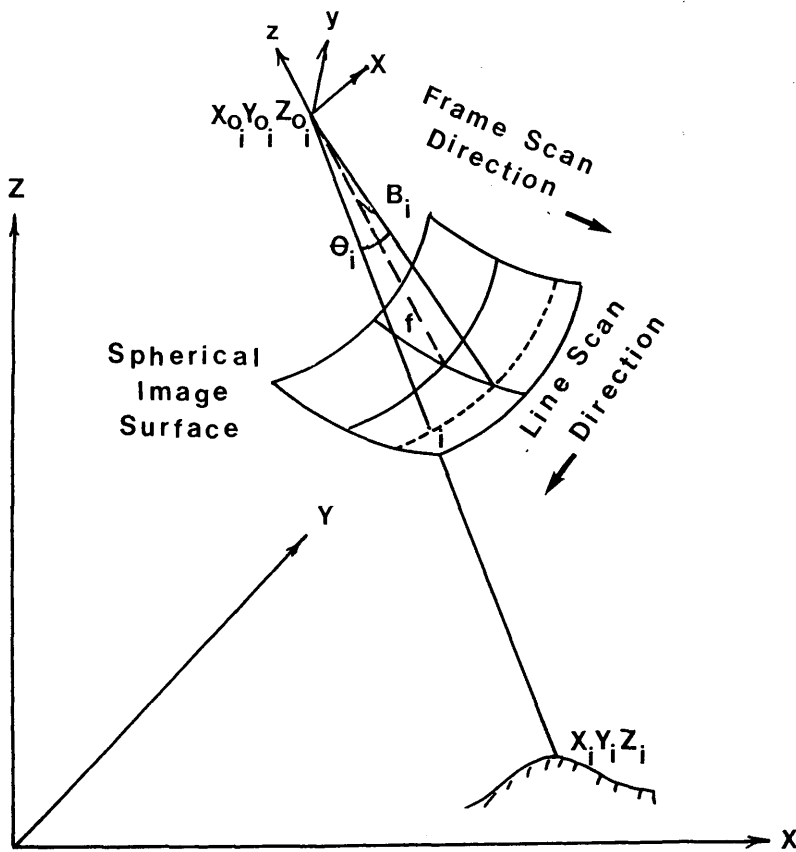


Fig.8-6 Geometry of the collinearity condition for the frame scanner imagery

The projective equations will take the form:-

$$\begin{vmatrix} X_i \\ Y_i \\ Z_i \end{vmatrix} = \begin{vmatrix} 1 & 0 & 0 \\ 0 & \cos\theta_i & -\sin\theta_i \\ 0 & \sin\theta_i & \cos\theta_i \end{vmatrix} \begin{vmatrix} \cos\beta_i & 0 & \sin\beta_i \\ 0 & 1 & 0 \\ \sin\beta_i & 0 & \cos\beta_i \end{vmatrix} \lambda_i A_i \begin{vmatrix} 0 \\ 0 \\ -f \end{vmatrix} + \begin{vmatrix} X_{o_i} \\ Y_{o_i} \\ Z_{o_i} \end{vmatrix} \dots\dots\dots 8-13$$

The collinearity equations for the frame scanner imagery derived from equations 8-13 are as follows:-

$$\bar{x}_i = -f \frac{m_{11}(X_i - X_{o_i}) + m_{12}(Y_i - Y_{o_i}) + m_{13}(Z_i - Z_{o_i})}{m_{31}(X_i - X_{o_i}) + m_{32}(Y_i - Y_{o_i}) + m_{33}(Z_i - Z_{o_i})} \dots 8-14$$

$$\bar{y}_i = -f \frac{m_{21}(X_i - X_{o_i}) + m_{22}(Y_i - Y_{o_i}) + m_{23}(Z_i - Z_{o_i})}{m_{31}(X_i - X_{o_i}) + m_{32}(Y_i - Y_{o_i}) + m_{33}(Z_i - Z_{o_i})}$$

Where:-

$$\bar{x}_i = f \tan\beta_i$$

$$\bar{y}_i = f \tan\theta_i \sec\beta_i$$

It is of interest to notice that the above two equations are the same as equations 5-8,5-9 (Chapter V) derived from the projection of the spherical image surface onto an equivalent frame image tangential to the spherical plane at its centre i.e. at scan angles  $\beta = \theta = 0$ .

As can be seen from the above discussion, there are two main points which have to be dealt with during the space resection phase using frame scanner imagery. These are:-

- (i) the uncertainty in the determined values for the interior orientation parameters (i.e. the principal distance and the position of the principal point) of an individual image;and
- (ii) the changes in the exterior orientation parameters which may occur during the image scan time.

There are two possible solutions which can be used in this situation:-

- (i) conventional space resection with additional parameters can be used to model for the systematic

errors introduced as a result of any error in the interior orientation parameters and also for the change in the exterior orientation parameters during the image scan time; or

- (ii) space resection point-by-point in which each image point will be considered individually. In this method, the exterior orientation parameters are expressed as functions of the image coordinates measured from the geometric centre of the frame scanner image.

### 8.5.2 Space Resection with Additional Parameters

This technique has been applied particularly to aerial triangulation using the bundle method (Bauer and Muller, 1972 and Brown, 1976) when it is called a self-calibration block adjustment method. In this method, no prior system calibration is carried out. Instead, the calibration is actually achieved by suitable procedures while forming the model itself.

The principle of the self-calibration method is to add specific parameters to the projective equation (equation 8-14) which will act as corrections to the measured image coordinates for the appropriate distortion. The solution for the additional parameters is then carried out simultaneously with the sensor exterior orientation elements. The space intersection phase is then carried out using the corrected image coordinates. It is obvious that the use of this method would require more control points to solve for the correction parameters as well as for the exterior orientation parameters.

The following error model was suggested by Brown, 1976 to be applied as a solution for reconnaissance frame photography:-

$$\Delta x = a_1 x + a_2 y + b_1 x y + b_2 x y^2 + b_3 x^2 y + c_1 x r^2 + c_2 x r^5 + d_1 \dots\dots\dots 8-15$$

$$\Delta y = -a_1 x + a_2 y + b_1 x y + b_2 x y^2 + b_3 x^2 y + c_1 y^2 r + c_2 y r^5 + d_2 \dots\dots\dots 8-16$$

In this model:-

- the term  $a_1$  corrects for the change in image scale;
- the term  $a_2$  corrects for rotation of the photograph;
- the b-terms correct for film deformation;
- the c-terms correct for radial lens distortion; and
- the d-terms correct for the position of the principal point.

The terms concerned with the distortion and deformation in the above error model ( the b and c-terms ) can be replaced by the terms of the reduced polynomial determined through the calibration procedure described in the previous Chapter. Thus by eliminating these terms from equations 8-15,8-16 and combining the remaining terms with those of equations 7-23 and 7-24, the following error model can be used with frame scanner images:-

$$\Delta x = a_0 + a_1 x + a_2 y + a_3 x y^2 + a_4 x^3 \dots\dots\dots 8-17$$

$$\Delta y = b_0 + b_1 x - b_2 y + b_3 x^2 y + b_4 y^3 \dots\dots\dots 8-18$$

The above error model contains 10 unknowns. Thus a total number of 16 unknown parameters (these 10 plus the normal 6 parameters) have to be determined for an individual frame scanner image during the space resection phase. Since each control point (with known X,Y and Z coordinates) gives rise to two equations, a minimum number of 8 control points is required to solve for the unknown parameters for a single frame scanner image.

### 8.5.3 Space Resection Point by Point

In this method, the scanner parameters and attitude will be computed for each point individually. This can be achieved by considering approximate exterior orientation parameters corresponding to the central point of the video image and then modelling the change in the orientation parameters between the time of recording this central point and the time of recording any other point.

Equations 8-8 can be linearised by Taylor's series and can be written in the form:-

$$\begin{aligned} V_{x_i} = & \frac{\partial x_i}{\partial \omega_i} d\omega_i + \frac{\partial x_i}{\partial \phi_i} d\phi_i + \frac{\partial x_i}{\partial \kappa_i} d\kappa_i + \frac{\partial x_i}{\partial X_{0_i}} dX_{0_i} + \frac{\partial x_i}{\partial Y_{0_i}} dY_{0_i} \\ & + \frac{x_i}{\partial Z_{0_i}} dZ_{0_i} - J_i \dots\dots\dots 8-19 \end{aligned}$$

$$\begin{aligned} V_{y_i} = & \frac{\partial y_i}{\partial \omega_i} d\omega_i + \frac{\partial y_i}{\partial \phi_i} d\phi_i + \frac{\partial y_i}{\partial \kappa_i} d\kappa_i + \frac{\partial y_i}{\partial X_{0_i}} dX_{0_i} + \frac{\partial y_i}{\partial Y_{0_i}} dY_{0_i} \\ & + \frac{y_i}{\partial Z_{0_i}} dZ_{0_i} - K_i \dots\dots\dots 8-20 \end{aligned}$$

Where:-  $V_{x_i}, V_{y_i}$  are corrections to the measured image coordinates;

$J_i, K_i$  are the discrepancies of the measured image coordinates from the values computed using approximate orientation elements experienced at the moment of exposure of the centre point. The partial derivatives of  $x, y$  are also evaluated at the approximate values of the exterior orientation elements.

If the approximate values of the exterior orientation elements corresponding to the central point (p) of the video image (p) are given by  $\omega_p, \phi_p, \kappa_p, X_{0p}, Y_{0p}$  and  $Z_{0p}$ , then the approximate exterior orientation elements  $\omega_i, \phi_i, \kappa_i, X_i, Y_i$  and  $Z_i$  corresponding to any point i on the video image will be:

$$\begin{vmatrix} \omega_i \\ \phi_i \\ \kappa_i \\ X_{0i} \\ Y_{0i} \\ Z_{0i} \end{vmatrix} = \begin{vmatrix} \omega_p \\ \phi_p \\ \kappa_p \\ X_{0p} \\ Y_{0p} \\ Z_{0p} \end{vmatrix} + \begin{vmatrix} d\omega_i \\ d\phi_i \\ d\kappa_i \\ dX_{0i} \\ dY_{0i} \\ dZ_{0i} \end{vmatrix} \quad \dots\dots\dots 8-21$$

Where  $d\omega_i, d\phi_i, d\kappa_i, dx_{0i}, dY_{0i}$  and  $dZ_{0i}$  are the changes in the exterior orientation elements between the instant of recording the central point (p) and the recording of point (i). These changes are functions of the aircraft speed S (with components  $\bar{X}_{0i}, \bar{Y}_{0i}, \bar{Z}_{0i}$ ) and the roll ( $\bar{\omega}$ ), yaw ( $\bar{\phi}$ ) and pitch ( $\bar{\pi}$ ) of the aircraft. Thus:-

$$\begin{vmatrix} d\omega_i \\ d\phi_i \\ d\kappa_i \\ dX_{0i} \\ dY_{0i} \\ dZ_{0i} \end{vmatrix} = t_i \begin{vmatrix} \bar{\omega}_i \\ \bar{\phi}_i \\ \bar{\kappa}_i \\ \bar{X}_i \\ \bar{Y}_i \\ \bar{Z}_i \end{vmatrix} \quad \dots\dots\dots 8-22$$

The time ( $t_i$ ) can be expressed as a linear function in  $x$  and  $y$  (see equation 5-4). Thus equation 8-22 can be written in the following form:-

$$\begin{aligned}
d\omega_i &= a_0 + a_1 x_i + a_2 y_i \\
d\phi_i &= b_0 + b_1 x_i + b_2 y_i \\
d\kappa_i &= c_0 + c_1 x_i + c_2 y_i \\
dX_{0i} &= d_0 + d_1 x_i + d_2 y_i \\
dY_{0i} &= e_0 + e_1 x_i + e_2 y_i \\
dZ_{0i} &= f_0 + f_1 x_i + f_2 y_i
\end{aligned}
\tag{8-23}$$

Equation 8-23 can now be substituted in equations 8-19,8-20 to give:-

$$\begin{aligned}
V_{x_i} &= \frac{\partial x_i}{\partial \omega_i} a_0 + \frac{\partial x_i}{\partial \omega_i} a_1 + \frac{\partial x_i}{\partial \omega_i} a_2 + \frac{\partial x_i}{\partial \phi_i} b_0 + \frac{\partial x_i}{\partial \phi_i} b_1 \\
&+ \frac{\partial x_i}{\partial \phi_i} b_2 + \frac{\partial x_i}{\partial \kappa_i} c_0 + \frac{\partial x_i}{\partial \kappa_i} c_1 + \frac{\partial x_i}{\partial \kappa_i} c_2 + \frac{\partial x_i}{\partial X_{0i}} d_0 \\
&+ \frac{\partial x_i}{\partial X_{0i}} d_1 + \frac{\partial x_i}{\partial X_{0i}} d_2 + \frac{\partial x_i}{\partial Y_{0i}} e_0 + \frac{\partial x_i}{\partial Y_{0i}} e_1 + \frac{\partial x_i}{\partial Y_{0i}} e_2 \\
&+ \frac{\partial x_i}{\partial Z_{0i}} f_0 + \frac{\partial x_i}{\partial Z_{0i}} f_1 + \frac{\partial x_i}{\partial Z_{0i}} f_2 - J_i \tag{8-24}
\end{aligned}$$

$$\begin{aligned}
V_{y_i} &= \frac{\partial y_i}{\partial \omega_i} a_0 + \frac{\partial y_i}{\partial \omega_i} a_1 + \frac{\partial y_i}{\partial \omega_i} a_2 + \frac{\partial y_i}{\partial \phi_i} b_0 + \frac{\partial y_i}{\partial \phi_i} b_1 \\
&+ \frac{\partial y_i}{\partial \phi_i} b_2 + \frac{\partial y_i}{\partial \kappa_i} c_0 + \frac{\partial y_i}{\partial \kappa_i} c_1 + \frac{\partial y_i}{\partial \kappa_i} c_2 + \frac{\partial y_i}{\partial X_{0i}} d_0 \\
&+ \frac{\partial y_i}{\partial X_{0i}} d_1 + \frac{\partial y_i}{\partial X_{0i}} d_2 + \frac{\partial y_i}{\partial Y_{0i}} e_0 + \frac{\partial y_i}{\partial Y_{0i}} e_1 + \frac{\partial y_i}{\partial Y_{0i}} e_2 \\
&+ \frac{\partial y_i}{\partial Z_{0i}} f_0 + \frac{\partial y_i}{\partial Z_{0i}} f_1 + \frac{\partial y_i}{\partial Z_{0i}} f_2 - K_i \tag{8-25}
\end{aligned}$$

The above equations contain 18 unknown orientation parameters ( $a_0$  to  $f_3$ ), three for each of the six orientation elements. Thus, a minimum number of 9 control points (known in X,Y and Z) are needed to determine the required orientation parameters

### 8.6 Space Intersection

Having determined the two sets of exterior orientation parameters for each of the two video frame scanner images of the stereo-model using either of the two space resection procedures described above, the X,Y and Z ground coordinates of any point whose image appears in the overlap area of the stereopair can be computed using the space intersection procedure. In this method, corresponding rays to the same object point from two overlapping images must intersect at the same ground points as shown in Fig.8-7.

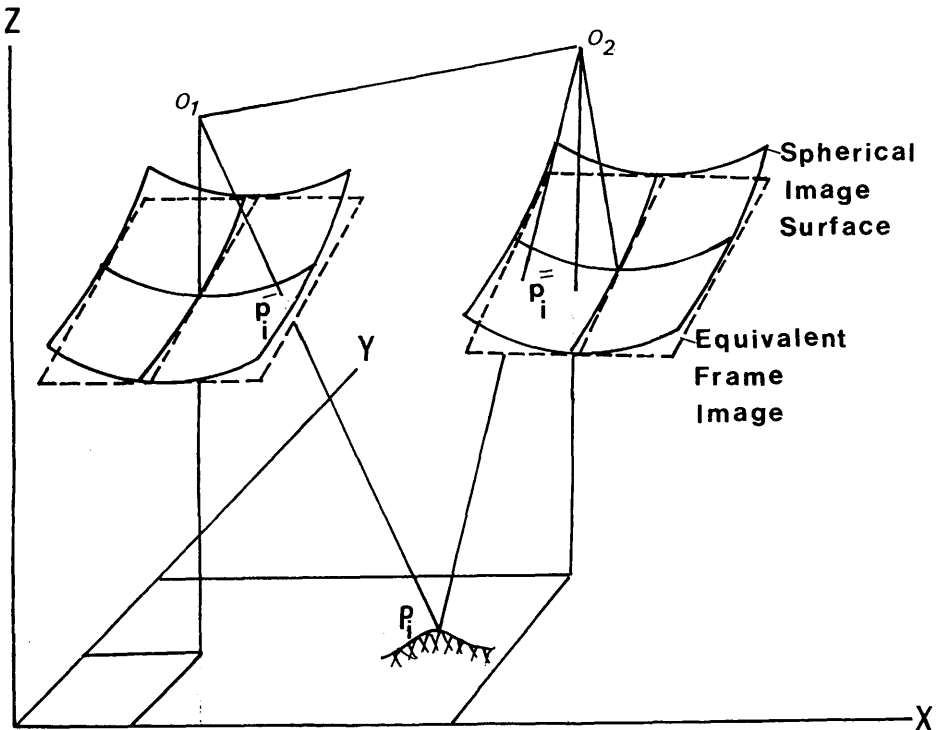


Fig.8-7 Space intersection

The projective relationships between the object on the ground and its corresponding images on the two video frame scanner images are given by:-

$$\begin{vmatrix} X_i - X_{o_i} \\ Y_i - Y_{o_i} \\ Z_i - Z_{o_i} \end{vmatrix} = A_i \lambda_i \begin{vmatrix} x_i \\ y_i \\ -f \end{vmatrix} \dots\dots\dots 8-26$$

and;

$$\begin{vmatrix} X_i - X_{0_i} \\ Y_i - Y_{0_i} \\ Z_i - Z_{0_i} \end{vmatrix} = \begin{vmatrix} \bar{A}_i \bar{\lambda}_i \\ y_i^- \\ -f \end{vmatrix} \dots\dots\dots 8-27$$

Where the terms with a single prime correspond to the left hand image and the terms with double prime correspond to the right hand image.

From these two equations, the respective scale factors will be given as follows (Konecny, 1975):-

$$\bar{\lambda}_i = \frac{(X_{0_i}^- - X_{0_i}^{\bar{}}) W_i^{\bar{}} - (Z_{0_i}^- - Z_{0_i}^{\bar{}}) U_i^{\bar{}}}{U_i^- W_i^{\bar{}} - U_i^{\bar{}} W_i^-} \dots\dots\dots 8-28$$

and

$$\bar{\lambda}_i = \frac{(Z_{0_i}^- - Z_{0_i}^{\bar{}}) U_i^- - (X_{0_i}^- - X_{0_i}^{\bar{}}) W_{0_i}^-}{U_i^- W_i^{\bar{}} - U_i^{\bar{}} W_i^-} \dots\dots\dots 8-29$$

where;

$$\begin{vmatrix} U_i^- \\ Y_i^- \\ W_i^- \end{vmatrix} = \bar{A}_i \begin{vmatrix} x_i^- \\ y_i^- \\ -f \end{vmatrix} \dots\dots\dots 8-30$$

and;

$$\begin{vmatrix} U_i^{\bar{}} \\ Y_i^{\bar{}} \\ W_i^{\bar{}} \end{vmatrix} = \bar{A}_i \begin{vmatrix} x_i^{\bar{}} \\ y_i^{\bar{}} \\ -f \end{vmatrix} \dots\dots\dots 8-31$$

Substituting for the scale factor and the given values of the image coordinates and the orientation elements in equations 8-26 and 8-27, the ground coordinates X, Y and Z of any point i can be computed.

In this chapter, the theory and analytical procedures which can be used to reconstruct a three-dimensional model from two overlapping video frame scanner images have been discussed. However, these techniques should be tested using practical data in order to ascertain their validity and to evaluate their effect. The method of performing such a practical test using airborne thermal video frame scanners will be discussed in the next Chapter.



## CHAPTER IX

### THE PRACTICAL TEST- PLANNING AND EXECUTING THE FLIGHT MISSION USING THE IR-18 FRAME SCANNER

## CHAPTER IX

### THE PRACTICAL TEST-

#### PLANNING AND EXECUTING THE FLIGHT MISSION

#### USING THE IR-18 FRAME SCANNER

##### 9.1 Introduction

Flight planning for the acquisition of thermal infrared imagery or thermography using a video frame scanner is very similar in many respects to that carried out for aerial photography using a conventional photogrammetric camera. In both cases, the following two items have to be supplied to the flying crew:-

- (i) a flight plan showing the exact area of interest and the proposed flight lines; and
- (ii) the required specifications of the imagery, such as forward (longitudinal) and side (lateral) overlap, flying altitude, aircraft ground speed, etc.

However, the flight planning also requires a decision as to the best or most suitable time of day for the acquisition of the imagery. For aerial photography, the best time is usually during daylight between 10 a.m. and 2 p.m. to give maximum solar illumination and minimum shadow. For aerial thermography, the situation is often completely different. This will become apparent by discussing the variations in diurnal temperature which have a profound effect on the images acquired by a thermal video scanner.

##### 9.2 Diurnal Temperature Variations

As has been mentioned in Chapter III, all objects above  $0^{\circ}$  K ( $-273^{\circ}$  C ) radiate EM energy at different wavelengths. The amount of the emitted thermal radiation detected by a scanner from a certain object depends on the following factors:-

- (i) the object temperature;
- (ii) the object emissivity; and
- (iii) the wavelength at which the scanner operates.

The temperature of an object is a measure of its heat energy possessed in the form of the kinetic motion of its constituent molecules. As these particles collide, part of their thermal energy is converted to electromagnetic energy. The higher the temperature, the more electromagnetic energy the object emits.

The energy incident on the surface of the terrain object can be absorbed, reflected or transmitted so that:-

Where:-

$$E_i = E_a + E_r + E_t$$

$E_i$  is the energy incident on the surface of the terrain object;

$E_a$  is the component of the incident energy absorbed by the terrain element;

$E_r$  is the component of the incident energy reflected by the terrain element;

$E_t$  is the component of the incident energy transmitted by the terrain element.

It can be seen from the above equation that the higher the object's reflectance, the lower its emissivity. For example, metallic surfaces are highly reflective, so they have a low emissivity factor. By contrast, water is highly absorptive, thus it has a high emissivity factor.

Typical diurnal or daily variations in radiant temperature for different materials are shown in Fig.9-1 (Sabins, 1973).

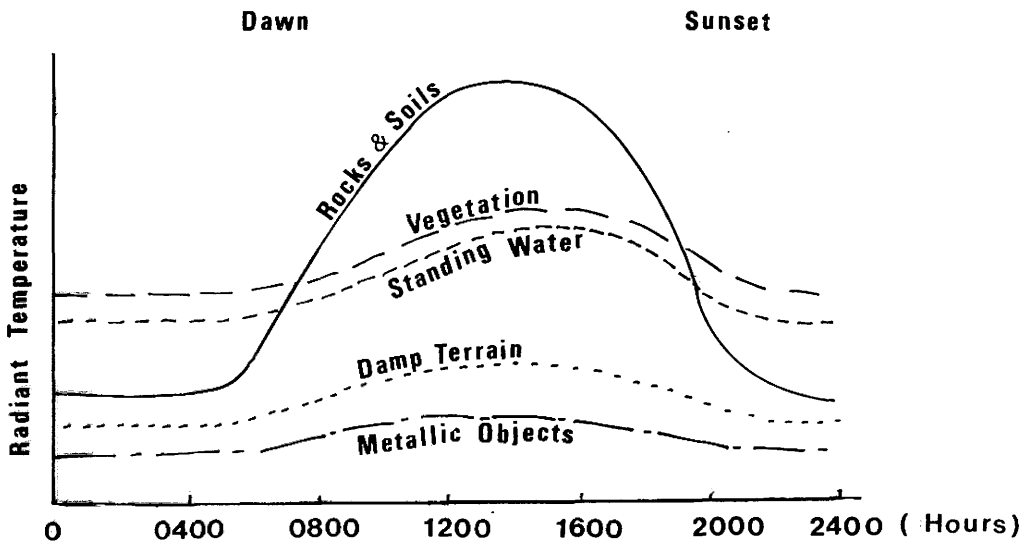


Fig.9-1 Diurnal radiant temperature curves

During the daytime, direct sunlight differentially heats terrain objects according to their thermal characteristics and their sunlight absorption. Although reflected sunlight has virtually no direct effect on imagery in the 8 to 14  $\mu$ m band, daytime imagery contains thermal shadows in cool areas shaded from direct sunlight by other objects such as trees, buildings and some topographic features.

It is always recommended that aerial thermography should be conducted during the period at least 4 hours after sunset until predawn time since this time of the day provides the longest period of reasonably stable temperature and minimum shadow effect. However, aircraft navigation over areas selected for thermal imaging is more difficult during periods of darkness, when ground features cannot be readily seen by the pilot, although in some cases the aircraft may be equipped with night time navigation equipment such as Radar or Forward Looking Infrared (FLIR) systems which would permit accurate navigation during night time operations.

### 9.3 Ground Coverage and Ground Resolution

The ground coverage of a frame scanner is a function of the aircraft's flying height and the scanner's field of view, while the ground resolution is a function of the flying height and the scanner's IFOV.

Table 9-1 below shows the maximum ground coverage (i.e. without any telescope or with 1X telescope magnification) for a single video frame and the ground resolution at a given flying height of 1,000 m, for the four video frame scanners discussed in this project.

Scanner	Field of View	Ground Coverage (m)	IFOV (mrad)	Ground Resolution (m)
IR-18	38.0° x 25.5°	668 x 443	1.73	1.73
RPC	40.0° x 30.0°	727 x 535	2.10	2.10
TTCM II	60.0° x 40.0°	1154 x 727	2.27	2.27
AGA	40.0° x 40.0°	727 x 727	5.40	5.40

Table 9-1 Ground coverage and resolution

However, unlike the photogrammetric frame camera where the ground coverage is obtained by a series of separate photographs taken at constant intervals of time (of the order of 1 per 5 seconds to 1 per minute) along the flight line, a frame scanner produces continuous coverage in the flight direction in the form of a series of successive heavily overlapping frames taken at a frequency of 25 frames per second (for PAL standard video systems).

The choice of the flying height will determine the image scale and hence the number of flight lines required to cover a certain area. For interpretation purposes, the highest resolution and largest image scale are usually required to facilitate the task of the interpreter. This will require flying at a low altitude and hence more flight lines. On the other hand, budget considerations press for a high flying altitude in order to reduce the number of flight lines. For mapping applications, the flight altitude is usually determined by the required map scale and the specified accuracy of height measurement and contouring. Obviously, some compromise regarding these various conflicting requirements must be arrived at so that a suitable flight plan can be contrived.

#### **9.4 Flight Planning for the Practical Test Using the Barr & Stroud IR-18 Frame Scanner**

The flight planning was made for the IR-18 when fitted with the 1.5X telescope since at the time of running the test, the 1X telescope was not available. With this telescope, the scanner's field of view is  $25.5^\circ \times 17^\circ$  and the angular resolution (IFOV) is 1.15 mrad.

##### **9.4.1 The Test Areas**

It was convenient to choose certain of the test areas nearby in Glasgow so that these areas could be visited for the purpose of establishing the ground control test field. Also this meant that only a very short flight was necessary from Glasgow Airport to the test area with consequent economy in flying time and in expense. The choice was limited to the east side of Glasgow to avoid the approaching tracks to Glasgow Airport which lies to the west of the city. Other areas located further from the city were selected which would allow the interpretational characteristics of the video frame scanner imagery to be evaluated. In total, three areas were chosen for the purpose of the test.

##### **9.4.1.1 Queenslie and Garrowhill Test Area**

This area was chosen mainly for the purpose of carrying out the geometrical test since it is an industrial and residential area which can provide suitable ground features such as road intersections and corners of houses which can be used as check and control points. The flight planning for this area was made for a flight altitude (H) of 2,500 ft (750 m) above mean sea level and 20% side lap.

At this flying height, the resulting image scale is approximately 1:1,200 and the ground resolution is 0.85 metre. The planimetric coordinates of the ground control points were to be scaled from the Ordnance Survey (O.S.) 1:1,250 large scale maps, while the ground elevations were to be established by running level lines using a surveyor's tilting level. At 1:1,250 scale, 1 mm on the map = 1.25 m on the ground. If 0.1 mm is the smallest amount that can be specifically scaled, this is equivalent to 0.12 m on the ground. If the flying height is 750 m, then if the accuracy of spot heighting was  $1/5,000$  of the flying height (H), this would be equal to 0.15 m. Fig.9-2 shows the test area with the planned flight lines drawn on a 1:50,000 scale O. S. map.

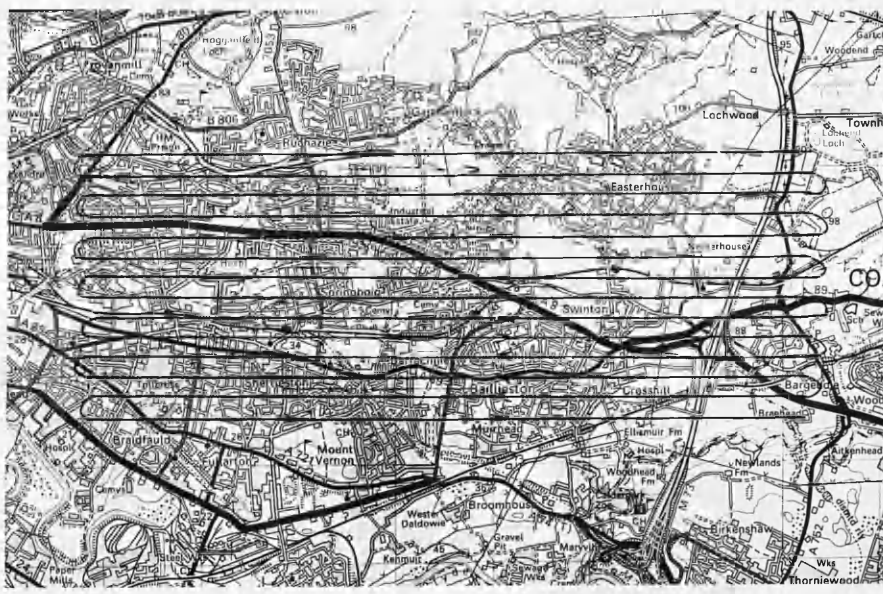


Fig.9-2 Flight lines for Queenslie and Garrowhill test area

Obviously, it would have been more convenient to have acquired the imagery at a higher altitude to achieve reasonable ground coverage which would allow more flexibility in the choice of the check and control points. However, due to the restrictions from the air-traffic control, the imagery had to be acquired at this low flying altitude.

#### 9.4.1.2 Douglas Water Test Area

This area was chosen mainly for the purpose of interpretation. There are several coal mines in this area and it would be interesting to see how the bings or special heaps associated with these would appear on the thermal imagery since it is known that they are subject to spontaneous internal combustion and indeed in some instances they have to be cooled down by continuously spraying water on them. The

flying height (H) for this area was 3,000 ft. (915 m) above m.s.l. This results in an image scale of 1:1,500 and a ground resolution of 1.05 metre. The flight plane for this area is shown below in Fig.9-3.

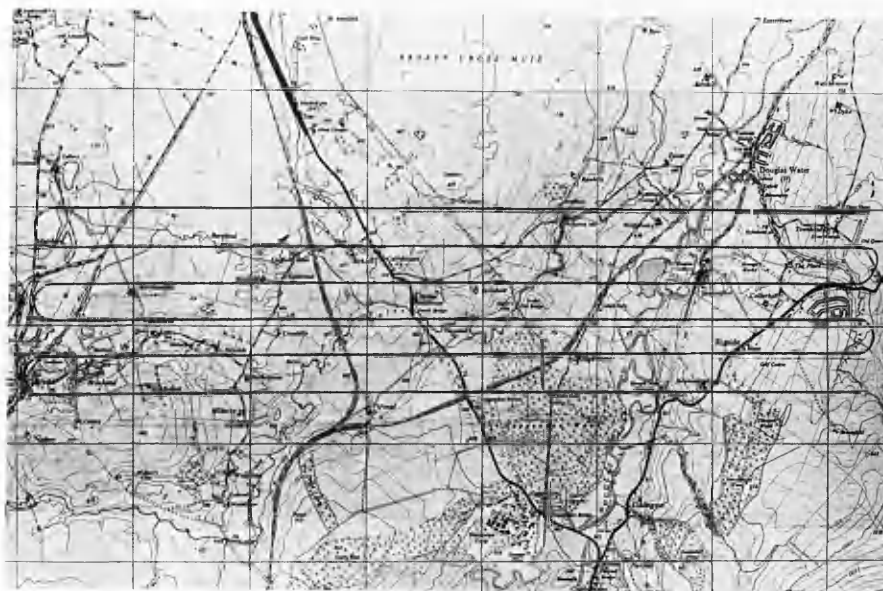


Fig.9-3 Flight map for Douglas Water test area

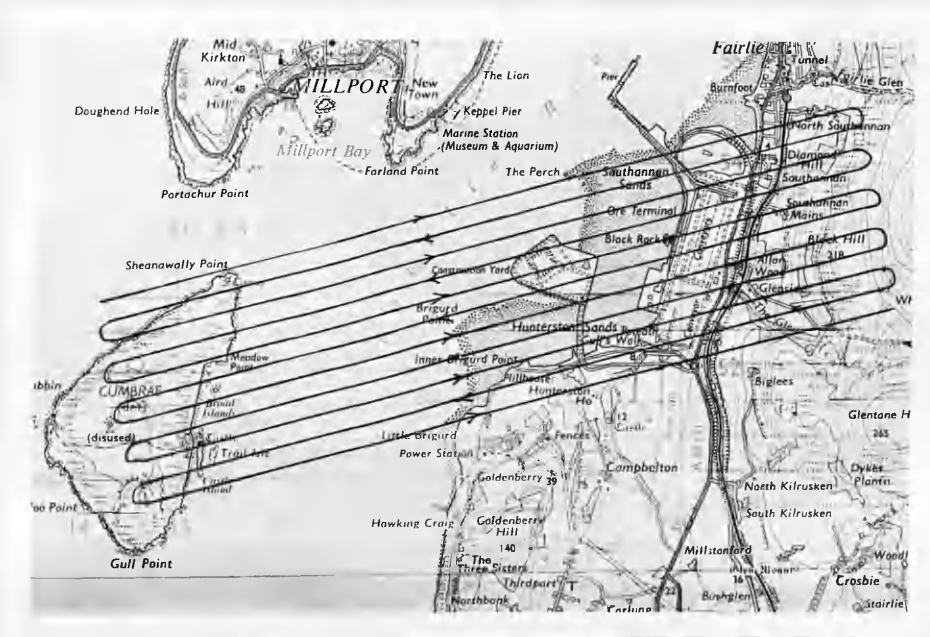
#### 9.4.1.3 Hunterston Test Area

This area was also chosen for an interpretation test. The area is located directly adjacent to the Firth of Clyde. The thermal behaviour of the sea water would be of special interest since the area contains the two large nuclear power stations at Hunterston, with largely outfall pipes allowing the discharge of thermally heated water from the stations into the sea.

The distribution of this heated water at different times within a tidal cycle would be of considerable interest. This area was in fact flown twice for reasons which will be explained later. The first flight was carried out at 6,000 ft (1,830 m), while the second was flown at 3,000 ft (915 m). At the former flying height ( $H=6,000$  ft), the image scale is 1:3,000 and the ground resolution is 2.1 metre. while at the latter flying height ( $H=3,000$  ft), the image scale is 1:1,500 and the ground resolution is 1.05 m. The flight plan for this area is shown below in Fig.9-4



(a) First flight



(b) Second flight

Fig.9-4 Flight map for Hunterston area



#### 9.4.2 Preparing for the Flight Mission

Due to budget considerations, a professional surveying company could not be used to carry out the flights and the acquisition of the imagery. At the time of planning the flights, an article appeared in the Photogrammetric Record written by Dr. W.H. Ekin (1984) describing an inexpensive retractable vertical camera rig for a light aircraft. Dr. Ekin is a lecturer in mechanical engineering at Robert Gordon's Institute of Technology (R.G.I.T.), Aberdeen, who is a keen amateur pilot and owns a Cessna 172 light aircraft. He had already been collaborating with the Remote Sensing Unit of the Macaulay Institute for Soil Research, Aberdeen in the acquisition of ground data using aerial photography. For this purpose, he had devised a method of mounting a 70 mm Hasselblad 500 EL/M camera in his Cessna 172 aircraft which allowed it to be used to acquire photographic images. Dr. Ekin was approached and agreed to carry out the test flights required for the project. After a slight modification, the same method was used to mount and operate the IR-18 frame scanner using the Cessna 172 light aircraft. In the following Section, the description of the aircraft, the mounting rig and the actual preparation for the flight mission are given in detail.



Fig.9-5 The Cessna 172 light aircraft

##### 9.4.2.1 The Cessna 172 Aircraft

The Cessna 172 (Fig.9-5) is a single engined, high-wing light aircraft, i.e. one in which the wings are located above the windows of the crew compartment. It is a four seater aircraft which has two passenger access doors, one on each side, plus a luggage compartment with an access door in the left hand side of the aircraft behind the rear seat. Normally, the

pilot's door (the left hand door) has an opening window, but Dr. Ekin has modified his aircraft to incorporate an opening window in the right hand door to allow the navigator to put his head out into the airstream to help in locating the aircraft position with respect to the ground features during a survey flight.

In his article, Dr. Ekin claimed that there are four main advantages of using the Cessna 172 for aerial photography. These are:-

- (i) the wings are located above the windows of the crew compartment which allows better downward visibility for the crew;
- (ii) the window in each door can be opened in flight for navigation purposes;
- (iii) the luggage compartment containing the camera or scanner is easily accessible from the rear seat; and
- (iv) there are no obstructions to downward visibility just outside the luggage compartment doorway.

#### 9.4.2.2 The Mounting Rig

The mounting rig consists of a camera carriage fixed on four wheels which can slide on top of two rails 250 mm apart. Attached to the camera carriage is the luggage door so that when the carriage is in its retracted position, the luggage door is closed. When it is in its working position, the luggage door is moved 220 mm laterally outwards into the air stream. The imager is protected by a rudimentary windshield. The carriage is controlled to move inwards or outwards by a simple hand lever. By leaning over the back of the rear seat, the camera or scanner operator is readily able to extend and retract the imager carriage. Fig.9-6a shows the rig with the scanner mounted on its carriage, while Fig.9-6b shows how the rig is mounted to the aircraft including the position of the luggage compartment door.

Since the camera carriage was originally designed to accommodate the Hasselblad camera, it had to be slightly modified by the Barr & Stroud technicians to accommodate the IR-18 frame scanner. Two steel bars were welded into the rig to hold the scanner between them.



Fig.9-6a The rig with the scanner mounted on its carriage



Fig.9-6b The Cessna 172 and the retractable rig

#### 9.4.2.3 The IR-18 Frame Scanner and Accessories

The maximum allowable load in the luggage compartment of the Cessna 172 is 120 lb. The following equipment and accessories had to be loaded in the aircraft for the purpose of capturing and recording the video scanner images:-

Item	Weight (lb)
Rig .....	10
Scanner with X1.5 telescope .....	21
Portable U-matic VTR .....	16
8" video monitor .....	17
Air bottle for detector cooling .....	36
Battery .....	13
Remote box and cables .....	4
View finder .....	1
<hr style="border-top: 1px dashed black;"/>	
Total weight .....	118

As can be seen, this was a rather critical matter since the weight was approaching the maximum permissible limit. The problem was solved when Barr & Stroud were able to provide a smaller air bottle, approximately the size of a rugby ball which weighed only 10 lb instead of the 36 lb of the standard air bottle provided for use with the scanner. In this way, the total weight in the compartment was reduced to about 90 lb.

#### 9.4.2.4 The Crew

The crew for the aerial mission consisted of the following personnel:-

Dr. W. Ekin, (R.G.I.T)	Pilot
Mr. S. Allan (R.G.I.T)	Navigator
Mr. G. Sutherland (Barr & Stroud)	Scanner Operator

With the weight of this crew plus the scanner and accessories, this light plane was fairly heavily loaded so that its performance was affected. In particular, it resulted in a slow rate of climb to the desired altitudes from which the images had to be obtained.

#### 9.4.2.5 Details of the Flight Mission

The initial plan was to conduct the aerial flying on Thursday, 23rd August, 1984. However, due to a bad weather, it had to be postponed for 48 hours. On Saturday, the 25th, the weather conditions had improved, the wind was moderate and the sky was almost clear from clouds but it was very sunny which is not recommended for aerial thermography. However, it was decided to collect some trial images under these circumstances with a view to repeating the flight over the same area at the predawn time next day in order to compare the thermal behaviour of the terrain objects at different times of the day.

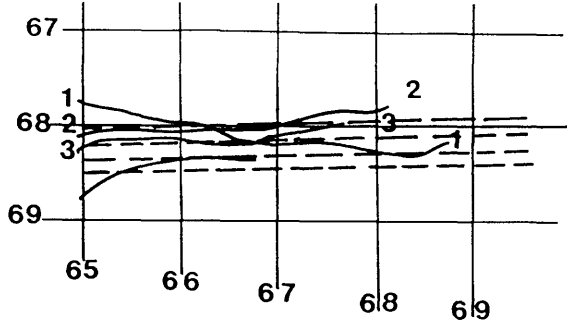
Two areas were imaged during the afternoon of this first day - the residential area of Queenslie and Garrowhill intended for the geometric test and the Hunterston area intended for thermal interpretation. It took the crew almost three hours, from 3 to 6 p.m., to complete the imaging of these two areas. The images from each area were recorded on a 20 minute U-matic video cassette tape. When the aircraft and crew returned, the recorded tapes were played back immediately to check the success of the mission and were found to be satisfactory.

On the next day, Sunday the 26th, the whole group met at Glasgow Airport at 4 a.m. and went directly to the Airport weather centre to inspect the weather conditions for the early hours of the morning. Unfortunately, the weather forecast predicted that there would be very low cloud and fog (at about 500 ft above the ground). The staff at the weather centre advised that the flight should be postponed until at least 9 am which of course was not what was planned and would mean that the sun's thermal heating effect would come into play.

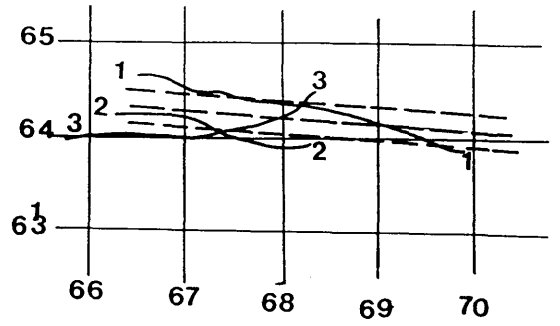
Starting at 9 a.m. a flight was made over Hunterston area for the second time and later over the Douglas Water area. The flight line directions for Hunterston area had to be changed (from northeast to southwest) for reasons which will be explained later. It took more than 3 hours to fly over these two areas. The images for Hunterston area were recorded on one and a half video tapes (30 minutes), while the images for Douglas Water were recorded on a single tape (20 minutes). Again the images were checked immediately after the crew returned and were found to be satisfactory.

## 9.5 Evaluation of the Flight Mission

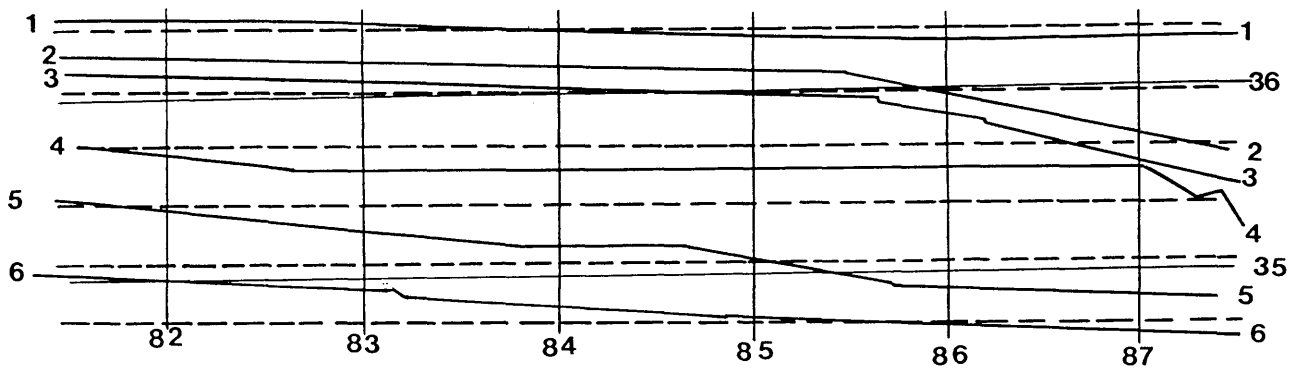
In order to evaluate the flight mission, the flight lines which were actually flown over each area were plotted on a plastic sheet overlaid on a map covering the area. This was done simply by playing back the recorded video tape and freezing the image on the video monitor every minute or so and then marking the position of the video image centre on the plastic sheet. By connecting the successive marks on the plastic sheet, it was possible to define the actual flight lines. By comparing these actual flight lines with the corresponding planned flight lines, it was possible to evaluate the whole mission. Fig.9-7 shows the plots of the two sets of flight lines with respect to the British National Grid for all the areas flown.



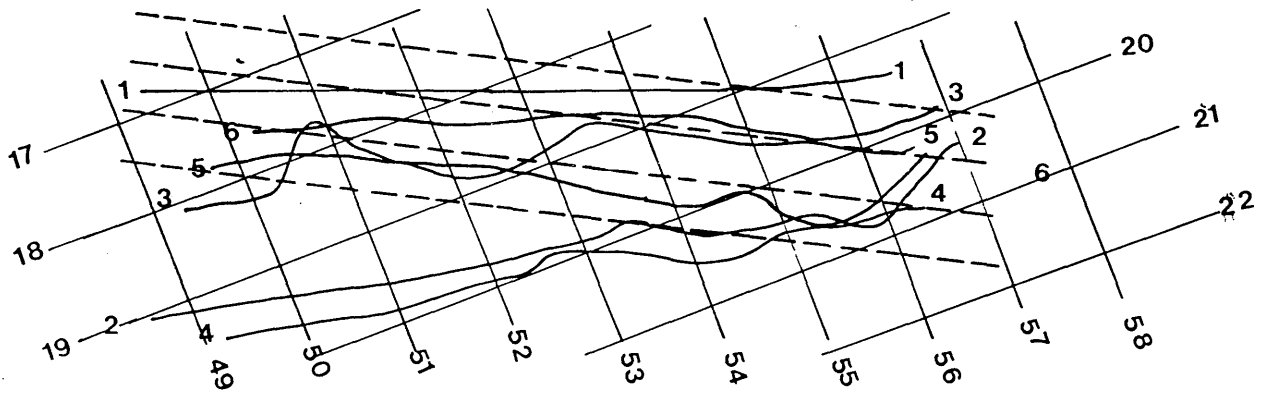
(a) Queenslie Industrial Estate  
(H = 2,500 ft.)



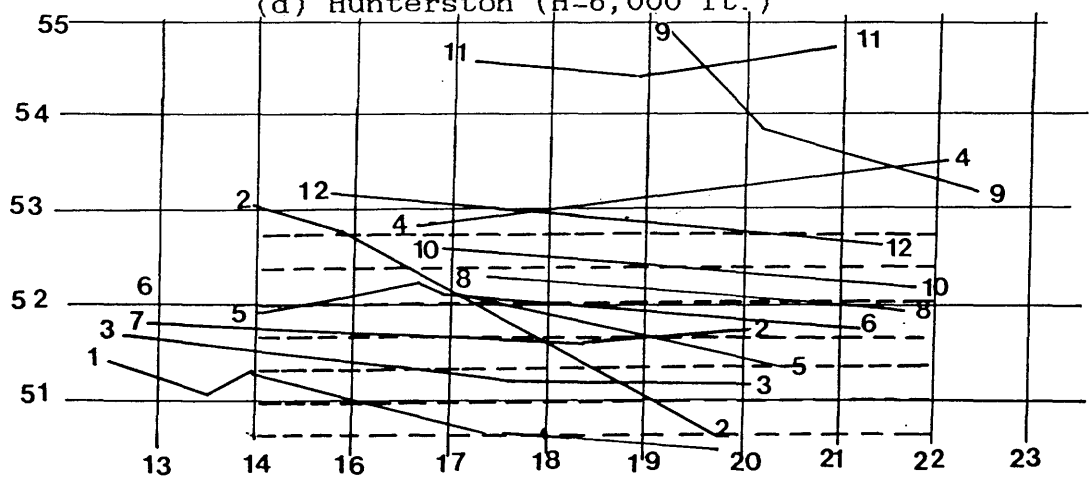
(b) Garrowhill  
(H = 2,500 ft.)



(c) Douglas Water (H = 3,000 ft.)



(d) Hunterston (H=6,000 ft.)



(e) Hunterston (H = 3,000 ft.)

Fig.9-7 The flight lines

It can be seen from Fig.9-7 above that the actual flight lines were not in sympathy with respect to the required lines. The following reasons for the poorly located flight lines can be offered:-

- (i) the navigation and flying of a pattern of parallel flight lines is not an easy task, especially when there is no sophisticated navigation equipment as in the case of a light aircraft such as the Cessna 172;
- (ii) a relatively inexperienced (amateur) crew conducted the survey;
- (iii) the use of a light aircraft, such as the Cessna 172 which has its restrictions in forward viewing and which can easily be drifted off course by any light wind was not an optimum solution for the flights;
- (iv) the complete dependence on the navigator to visually locate the aircraft's position on the flight lines was found to be unsatisfactory;
- (v) the scanner's field of view is very small which made it difficult to estimate the side lap between adjacent flight lines;and
- (vi) in the Hunterston area it was extremely difficult for the navigator to track the flight lines over the water since there were no ground features. For this reason, the direction of the planned flight lines had to be modified before the second flight over the same area since the poor navigation of the first flight was apparent from the replay of the imagery on the return of the plane and crew from the mission.

The main difficulty appeared to be the accurate positioning and navigation of the aircraft during the actual imaging runs. To overcome this problem, a small low-cost battery-operated position location device using a medium frequency continuous wave system such as Decca or Loran can be used. If one of these devices could be coupled up to a small battery-operated track plotter, this would help the pilot and the navigator to achieve correct tracking of the flight lines using a small aircraft.

Indeed, following on from the disappointing results of the flights carried out for this project, Dr. Ekin has carried out a number of flights using a low cost, light weight Decca navigator set manufactured by Polytechnic Marine.

The other alternative would be to get a professional aerial surveying company to conduct the test flights which of course would be at least 10 to 15 times more expensive.

Whatever the shortcomings of the flights, enough usable imagery was acquired by the IR-18 to allow a series of tests to be carried out to establish the geometric characteristics and the interpretational qualities of the video frame scanner imagery.

In Chapter VIII, the analytical techniques which can be applied to frame scanner imagery have been discussed. In this Chapter, the details of the flight mission which has been carried out to provide the imagery required for the test have been presented. In the next Chapter, the provision of the control and check points and the results of the geometric test are discussed in detail.



CHAPTER X

THE GEOMETRIC TEST- PROVISION OF THE CONTROL-  
RESULTS AND ANALYSIS

## CHAPTER X

### THE GEOMETRIC TEST- PROVISION OF THE CONTROL-

#### RESULTS AND ANALYSIS

##### 10.1 Introduction

The geometric test is concerned with establishing the accuracy which may be obtained when airborne video frame scanner imagery is used for large scale mapping. For this purpose, the analytical procedures which may be used to extract planimetric and height information from this type of imagery have been discussed in Chapter VIII. To test these procedures, a flight mission was planned and executed successfully as explained in the previous Chapter. This aerial mission provided the required image data which was used for the geometric test.

##### 10.1.1 Test Procedure

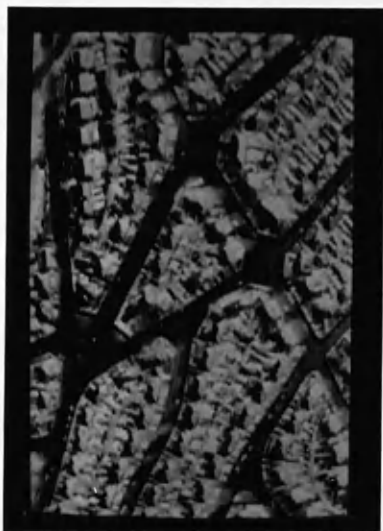
The procedure which was used in this project was to make measurements on video frame scanner images taken over test fields with numerous suitably positioned ground points whose terrain coordinates were already known. Using certain of these as control points, the devised analytical techniques were then applied to form a stereo-model and produce terrain coordinates for the test field. The next step was to compare these photogrammetrically derived coordinates for the control points with their corresponding known coordinates and to compute the discrepancies between the two sets of coordinates. Finally, an analysis of the residual errors was carried out to establish the extent and nature (i.e whether systematic or random) of these errors and to make comparisons of the various analytical procedures which have been applied with a view to establishing which are the most satisfactory for use with airborne thermal video frame scanner imagery.

##### 10.2 Provision of the Control Points For the Geometric Test

As mentioned in the previous Chapter, both the Queenslie industrial estate and the Garrowhill area were intended to be used for the geometric test. However, it turned out that the images covering the Queenslie area were not suitable for the test since the images of the large factory buildings often filled the whole or most of a single frame. Thus very few control points could be obtained in an individual frame. On the other hand, the Garrowhill area proved to be quite satisfactory for the purpose of the test, especially the images taken for Baillieston area. The main problem appeared to be the thermal shadows, since the imagery had been acquired at mid-day. This caused some features to be obscured. However, since the area is mainly residential, with a large number of varied and well defined features, it

was possible to define a sufficient number of objects on the video images to be used as control points.

Four stereo-models, (Figs.10-1a to 10-1d) widely separated from one another, were formed from the video images of this area. Suitable control and check points were identified and selected on both the video images and the O.S. 1:1,250 scale maps covering the area. Road intersections and corners of houses were found to be the most suitable points, and a series of these were selected to give a set of check and control points which were fairly evenly distributed over the images. A careful sketch was made for each of the control points so that it could be identified easily when measuring its coordinates on both images of the stereo-pair.



Model A



Model B



Model C



Model D

Fig.10-1 The four test areas

### 10.2.1 Video Image Coordinate Measurements

The selected set of check and control points in each image was measured by the video monocomparator described in Chapter VI. Two rounds of observations were made for each image and the mean value for each point was taken. The precision of the image coordinate measurements for each model is shown below in Table 10-1.

Model	No. of Points	rmse (pixel)		
		$m_x$	$m_y$	$m_p$
A	25	0.5	0.6	0.78
B	24	0.7	0.4	0.80
C	19	0.6	0.8	1.00
D	23	0.4	0.7	0.80

Table 10-1 Precision of image coordinate measurements

It can be seen from the table above that the precision of measurements on terrain images using the video-based monocomparator could be carried out to sub-pixel level.

### 10.2.2 Ground Coordinate Measurement

The planimetric ground coordinates of the check and control points were measured with reference to the nearest National Grid intersection given on the O.S. 1:1,250 scale maps. Each point was measured 3 times to avoid any blunder and the mean was adopted. A precise ruler was used to measure the coordinates to the nearest 0.2 mm between the grid lines shown on the O.S. plans. This is equivalent to  $\pm 0.25$  metre on the ground. Recalling that the ground resolution of the scanner at the flying height at which the images were acquired is 0.85 metre, it can be seen that this is a satisfactory accuracy for the purpose of the geometric test.

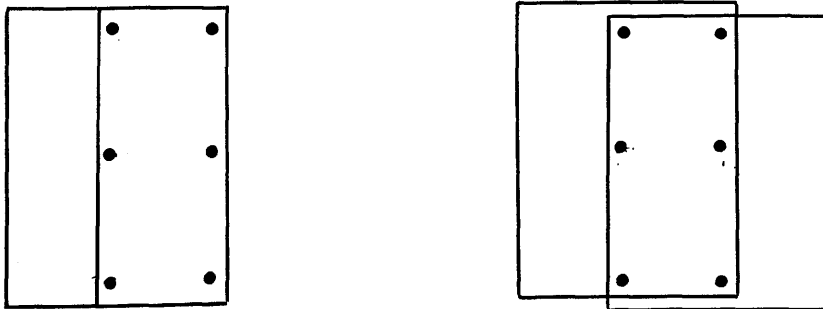
Since the O.S. 1:1,250 scale map does not contain any height information which can be used for this type of geometric test, the elevations of the check and control points had to be determined by practical levelling in the terrain. A sketch of each of the points was made and its location noted with respect to the nearest available Bench Mark (BM) in the area. A Kern GKO tilting level and a 4 metre staff were used to conduct the levelling with the help of two undergraduate students from the Department. The levelling started from a BM and closed at the same BM to check the results. The closing error was found to be + 5 cm. In fact the weather conditions were very bad at the time of running the levelling which

resulted in this relatively large closing error. However the accuracy was more than sufficient for the purpose of the geometric test. The closing error was distributed between the points relative to their distance from the closing BM.

### 10.3 Data Processing

Three approaches were used for the data processing. These are:-

- (i) Conventional space resection/intersection. This approach does not take into account the distortion introduced to the image as a result of the scanning geometry. It is normally applied with data measured on conventional photographs taken by a photogrammetric frame camera with its ideal imaging geometry. This technique has been implemented mainly to find out the difference between the analytical techniques specifically derived to deal with frame scanner imagery and the conventional techniques which are commonly used with photogrammetric frame camera images. This technique requires a minimum number of 3 control points (known in X,Y and Z) to solve for the six unknown parameters of an individual image. However, in order to minimise the effects of any observational error, 6 control points were used to solve for the exterior orientation parameters in a single frame scanner image using the least squares adjustment procedure. These were distributed as shown in Fig.10-2. It will be noted that these only cover part of the area of a single image(-that of the stereo-overlap) and are not distributed over the whole image area as would be ideal for the space resection of an individual photograph or image.



(a) single image  
(for space resection)

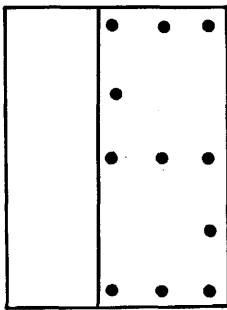
(b) stereo-model  
(for space intersection)

Fig.10-2 Distribution of the control points for the conventional space resection method

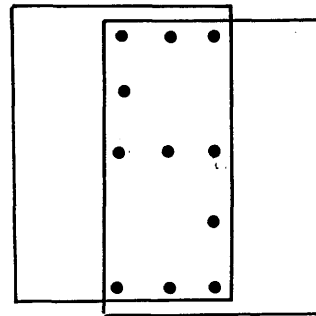
(ii) Space resection with additional parameters followed by space intersection. In this procedure, the additional parameters of equations 8-17, 8-18 have been included to take account of:-

- (a) the spherical recording surface of the frame scanner;
- (b) the changes in the exterior orientation parameters occurring during the image scan time; and
- (c) any error in the interior orientation parameters.

These additional parameters will be determined simultaneously with the exterior orientation elements during the space resection phase. This requires a minimum number of 8 control points. Again 11 points distributed as shown in Fig.10-3 were used in the least squares procedure.



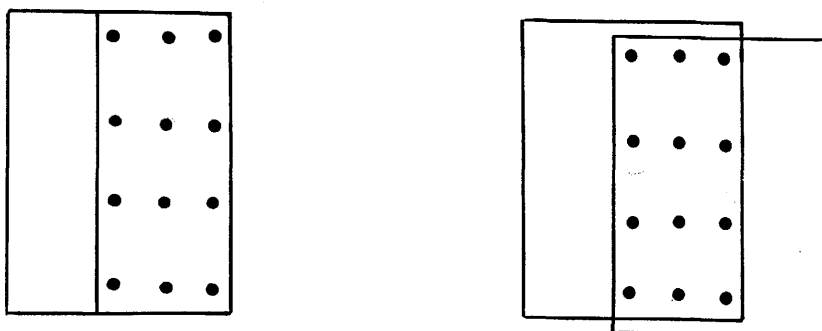
(a) single image  
(for space resection)



(b) stereo-model  
(for space intersection)

Fig.10-3 Distribution of the control points used for the additional parameters technique

(iii) Space resection point-by-point followed by space intersection. The image coordinates were transformed into a plane tangent to the spherical surface at its centre. The transformation procedure was carried out as a function of the scanner's focal length ( $f$ ) and the two scan angles ( $\beta$ ), ( $\theta$ ). To account for the changes in the exterior orientation parameters during the image scan time, each image point was treated individually as described in Section 8.5.3. This technique requires a minimum number of 9 control points to solve for the unknown parameters. Again, 12 control points were used for the same reason mentioned above. Fig.10-4 shows the distribution of these points for a single frame scanner video image and the resulting stereo-model.



(a) single image (for space resection)      (b) stereo-model (for space intersection)

Fig.10-4 Distribution of the control points used for the point-by-point technique

#### 10.4 Results and Analysis of the Geometric Test

The three analytical techniques mentioned above were used to process the data for the four test models. First the results for each of the four models will be presented and analysed for each technique individually. Next an overall analysis will be carried out in order to establish which of these techniques is the most satisfactory for use with frame scanner images. The following symbols are used during the presentation of the results:-

- Ch            Number of check points;
- Co            Number of control points;
- $m_x$  ( $m_x$ )    RMSE in x-direction expressed in pixels in the image scale (in metres on the ground);
- $m_y$  ( $m_y$ )    RMSE in y-direction expressed in pixels in the image scale (in metres on the ground);
- $m_p$  ( $m_p$ )    RMSE of the planimetric vector ( $m_p^2 = m_x^2 + m_y^2$ ) expressed in pixels in the image scale (in metres on the ground);
- $m_z$  ( $m_z$ )    RMSE in z-direction expressed in pixels in the image scale (in metres on the ground); and
- W.M.        Weighted mean for the four models. The number of points was taken as the weight for each model.

### 10.4.1 Results from the Use of the Conventional Space Resection/Intersection Technique

Model	Co	Ch	RMSE							
			Control Points				Check Points			
			$m_x$	$m_y$	$m_p$	$m_z$	$m_x$	$m_y$	$m_p$	$m_z$
			$m_x$	$m_y$	$m_p$	$m_z$	$m_x$	$m_y$	$m_p$	$m_z$
A	6	19	3.41	4.11	5.34	5.95	3.63	4.76	5.98	6.70
			4.01	4.83	6.28	7.93	4.27	5.60	4.03	8.93
B	6	18	2.67	3.22	4.18	4.21	2.93	3.70	4.71	5.70
			3.14	3.78	4.92	5.61	3.44	4.35	5.54	7.60
C	6	13	3.26	4.60	5.63	5.70	3.95	4.85	6.25	6.31
			3.83	5.41	6.63	7.60	4.60	5.70	7.35	8.41
D	6	17	2.39	3.41	4.16	4.71	2.96	3.47	4.56	5.17
			2.81	4.01	4.89	6.27	3.48	4.08	5.36	6.89
W.M.	24	67	2.93	3.83	4.82	5.14	3.32	4.16	4.92	5.96
			3.44	4.50	5.67	6.85	3.91	4.89	5.79	7.95

Table 10-2 Results from the use of the conventional space resection/intersection technique

As mentioned above, this technique does not take into account the special characteristics of the frame scanner geometry. The results for the four models showed large residual errors in X, Y and Z. The weighted means for the check points in the four models were  $\pm 3.32$ ,  $\pm 4.16$  and  $\pm 5.96$  m in X, Y and Z respectively. It can also be seen in the results obtained from each of the four models that the lowest magnitude of error was obtained in the X-direction followed by that obtained in the Y-direction and the largest magnitude of error was obtained in the Z-direction. This was quite an expected characteristic due to the aspect ratio of the video image format and the small B/H ratio. This particular point will be discussed in more detail later in this Chapter.



### 10.4.2 Results from the Use of Space Resection/Intersection with Additional Parameters

Model	Co	Ch	RMSE							
			Control Points				Check Points			
			$m_X$	$m_Y$	$m_P$	$m_Z$	$m_X$	$m_Y$	$m_P$	$m_Z$
$m_x$	$m_y$	$m_p$	$m_z$	$m_x$	$m_y$	$m_p$	$m_z$			
A	11	14	1.49	2.16	2.62	2.72	1.73	2.69	3.19	3.54
			1.75	2.54	3.08	3.62	2.03	3.16	3.75	4.72
B	11	13	0.89	1.22	1.51	2.54	0.84	1.77	1.95	3.29
			1.04	1.43	1.77	3.38	0.98	2.08	2.29	4.38
C	11	8	1.49	2.01	2.50	2.91	1.72	2.38	2.93	3.13
			1.75	2.36	2.94	3.87	2.02	2.80	3.44	4.17
D	11	12	1.44	2.53	2.91	2.19	1.60	2.40	2.88	2.70
			1.69	2.97	3.42	2.91	1.88	2.82	3.39	3.60
W.M.	44	47	1.32	1.98	2.37	2.59	1.44	2.30	2.71	3.18
			1.55	2.32	2.78	3.45	1.69	2.70	3.18	4.24

Table 10-3 Results from the use of space resection/intersection with additional parameters

The additional parameters were used in the space resection phase to take account of all the geometric distortion existing in the frame scanner imagery as a result of the scanning technique employed by these devices. This has resulted in a significant improvement in the accuracy as shown in the table above. The results for all the models were in very close agreement except the figure for  $m$  in model B. This was far too good which raised some suspicion about the observations made for this model. The image and ground coordinates were checked and reprocessed several times with an attempt to discover any error but the same result was obtained each time. Apart from this figure, all the results showed considerable and consistent improvement relative to those obtained by the conventional space resection/intersection as shown in Table 10-3 above.

Comparing the mean accuracy figures (in metres) for the check points obtained from the two techniques:-

Technique	$m_x$	$m_y$	$m_p$	$m_z$
Conventional space resection/intersection	3.32	4.16	4.92	5.96
Space resection/intersection with additional parameters	1.44	2.30	2.71	3.18

Table 10-4 Comparison between conventional and additional parameters space resection/intersection techniques

It can be seen that the figures for  $m_x$  improved from  $\pm 3.32$  m to  $\pm 1.44$  m (i.e. the accuracy improved by 1.88 m) in the X-direction. In the y-direction, the Figure for  $m_y$  was improved from  $\pm 4.16$  to 2.30 m (1.86 m), while in the Z-direction, the  $m_z$  figure was improved from  $\pm 5.96$  to 3.18 m (2.78 m). It is obvious that the use of the additional parameters had a significant effect in improving the results since these parameters had been precisely determined through the comprehensive scanner calibration which had been carried out and described in Chapters VI and VII.

#### 10.4.3 Results from the Use of the Point-by-Point Space Resection/Intersection Technique

Model	Co	Ch	RMSE							
			Control Points				Check Points			
			$m_x$	$m_y$	$m_p$	$m_z$	$m_x$	$m_y$	$m_p$	$m_z$
A	12	13	2.31	3.12	3.88	4.16	2.54	3.41	4.25	4.46
			2.71	3.67	4.56	5.54	2.98	4.01	4.99	5.94
B	12	7	2.51	3.37	4.20	4.01	2.94	3.88	4.86	4.93
			2.95	3.96	4.94	5.34	3.45	4.56	5.72	6.57
C	12	12	2.56	1.67	3.05	4.86	2.89	2.04	3.53	7.30
			3.01	1.96	3.59	6.48	3.40	2.40	4.16	9.73
D	12	11	2.12	3.22	3.85	2.16	2.17	3.05	3.74	3.88
			2.49	3.78	4.58	2.87	2.55	3.58	4.40	5.17
W.M.	48	43	2.36	2.78	3.64	3.81	2.60	3.01	3.97	5.18
			2.77	3.27	4.28	5.08	3.05	3.54	4.67	6.90

Table 10-5 Results from the use of the point-by-point space resection/intersection technique

The results obtained from applying this technique are progressing in the same manner as that obtained from the previous two techniques. However, the results from model C are quite peculiar and disturbing in that the figure for  $m_x$  is larger than that of  $m_y$ . Also the figure for  $m_z$  was relatively bigger than that obtained from the other models. A considerable time has been spent on checking the input data, the programs and in re-running the program in an attempt to locate any error which could have occurred and caused the results for this model to be much poorer and different to those obtained from the other three models; but unfortunately without any change in the results.

Comparing the mean result from the four models with the corresponding results obtained from the other two techniques in Table 10-6; then

Technique	RMSE			
	$m_x$	$m_y$	$m_p$	$m_z$
Conventional space resection/intersection	3.32	4.16	4.92	5.96
Space resection/intersection with additional parameters	1.44	2.30	2.71	3.18
Space resection/intersection point-by-point	2.60	3.01	3.97	5.18

Table 10-6 Comparison between the results from the three analytical techniques

It can be seen that the additional parameters technique still provides better accuracy than the other two techniques. The point-by-point space resection/intersection, although it resulted in a significant improvement in the accuracy as compared with the conventional technique, it gave much poorer results than the additional parameters technique. In fact the point-by-point technique takes into account the spherical recording surface and the changes in the exterior orientation parameters, but it does not account for the errors in the interior orientation parameters (focal length value and principal point position) or any lack of orthogonality in the video image.

Based on this result, the residual errors from the four models resulted using the additional parameters method were plotted out as vectors using program PLOTDT4. These plots, which are included in Appendix C, displayed a random pattern of distortion in both the planimetric and height directions, again pointing to the removal of the systematic errors by the additional parameters.

## 10.5 Overall Analysis

It can be seen from the results obtained from the use of the three analytical techniques that, as expected, considerably larger residual errors resulted from the conventional space resection/intersection method than occurring with the alternative two other techniques which were based on the geometrical analysis and calibration carried out for the frame scanners. When these were used, a considerable improvement in the accuracy was obtained. However, the space resection/intersection with additional parameters provided the best accuracy which could be obtained from thermal frame scanner imagery. It is quite understandable that the accuracy figures obtained during the test are considerably worse than the accuracy figures stated by the professional mapping agencies. Harley, 1975 stated that the O.S. accuracy figures for the 1:1,250 scale maps are  $\pm 0.40$ ,  $\pm 0.40$  and  $\pm 0.60$  m in X, Y and Z respectively (N.B. These figures apply to maps compiled by direct ground measurements and not by photogrammetric methods).

No doubt, the results from this test would have been slightly improved if the control points had been distributed all over the image which would have ensured better space resection. Another factor which could have improved the results is concerned with the nature of the control points themselves. Those used were well-defined natural points. If a test field consisting of numerous signalised points (i.e. artificial targets made up of highly thermal emissive material) had been specifically established for the geometric test, the errors in the image and ground control points measurements could have been reduced and hence the accuracy could have been improved. However, the expense and effort required to establish and maintain such a test field were such that it could not be contemplated. Nevertheless, the results obtained in this test are quite satisfactory in purely photogrammetric terms, especially when the low resolution, and the rather complex and unusual characteristics of the frame scanners are considered.

In order to assess the overall potential of this test, the mean of the results obtained from the four models using the additional parameters techniques will be compared and analysed relative to some photogrammetric standard tests, i.e. ISP tests.

### 10.5.1 ISP Standard Tests

Moller, 1964, 1968 carried out a comprehensive statistical analysis for some of the ISP standard tests. He based his analysis on the assumption that the standard deviation in

X, Y, P and Z could depend on the dimensions of the stereo-model. He considered the cases when a wide-angle vertical photography was used with overlaps of 60% (lateral) and 30% (longitudinal). Fig.10-5 shows the model area and the base-to-height ratio for wide-angle photography.

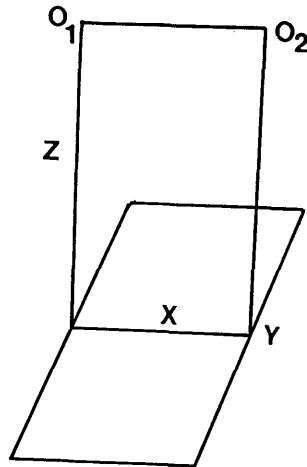


Fig.10-5 Model area for wide-angle photography

By ratioing the dimensions of the test area with respect to the photo-base (the photo-base is 40% of the photograph width in the x-direction), the following figures were obtained:-

$$x : y : z = 1.00 : 1.75 : 1.63$$

Based on the idea that the standard deviations are proportional to the square root of some model dimensions, the values above were used to obtain the following proportions :-

sx : sy : sz : sp	$\sqrt{x}$ : $\sqrt{y}$ : $\sqrt{x+y+z}$ : $\sqrt{x+y}$
sx : sy : sz : sp	1.00 : 1.32 : 2.09 : 1.67
sx : sy : sz : sp	0.76 : 1.00 : 1.58 : 1.25
sx : sy : sz : sp	0.48 : 0.63 : 1.00 : 0.79

Table 10-7 Proportional values between the model dimensions for wide-angle photography

Then, Moller checked this idea against some empirical results. The table below shows the proportional values for the accuracy results obtained from some well known ISP tests, together with the corresponding theoretical proportions related to the model dimensions.

Experiment	No. of points	$m_x/m_z$	$m_y/m_z$	$m_p/m_z$	$m_z/m_z$	$m_R/m_z$
Pecny 1966-1968	8,117	0.68	0.64	0.95	1.00	1.30
Reichenbach 1962-1964	13,320	0.48	0.58	0.77	1.00	1.27
Monti de Revoira	2,845	0.51	0.57	0.76	1.00	1.26
Weighted Mean	2,4282	0.54	0.60	0.83	1.00	1.31
Theoretical proportions from model dimensions		0.48	0.63	0.79	1.00	1.28

Table 10-8 Proportions of errors from ISP standard tests

Where R is the vector in space.

It can be seen that the theoretical proportions derived from the model dimensions are not far from the corresponding proportions obtained from the geometric tests. The same procedure was used to relate the proportions of errors obtained from the IR-18 geometric test to the model dimensions as explained below.

### 10.5.2 IR-18 Test

As mentioned earlier, the IR-18 frame scanner produces a rectangular frame size (500 X 767 pixel). For the analytical test, the whole model area which is 60% of the format size (in x-direction) was used. Fig.10-6. shows the model area and the base-to-height ratio in this case.

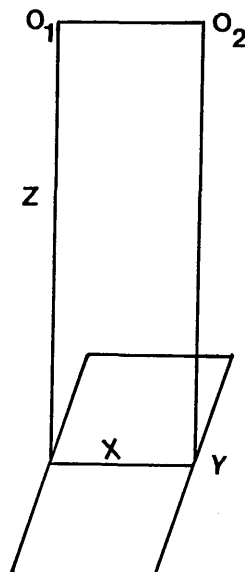


Fig.10-6 Model area for the IR-18 test

Thus the following ratios can be obtained:-

$s_x : s_y : s_z : s_p$	$\sqrt{x}$	$\sqrt{y}$	$\sqrt{x+y+z}$	$\sqrt{x+y}$
$s_x : s_y : s_z : s_p$	1.00	1.59	2.51	1.88
$s_x : s_y : s_z : s_p$	0.63	1.00	1.58	1.18
$s_x : s_y : s_z : s_p$	0.40	0.63	1.00	0.75

Table 10-9 proportional values between the model area for the IR-18 imagery

Now, using the same procedure as in Table 10-8 above;

Experiment	No. of Points	$m_X/m_Z$	$m_Y/m_Z$	$m_P/m_Z$	$m_Z/m_Z$	$m_R/m_Z$
Weighted Mean from the IR-18 Test	91	0.45	0.72	0.85	1.00	1.31
Theoretical Proportions from Model Dimensions		0.40	0.63	0.75	1.00	1.25

Table 10-10 Proportions of errors from the IR-18 geometric test

It can be noticed that the values worked out from the test results are consistently lower than the corresponding theoretical values. An obvious reason is that the theoretical values were derived by relating the model dimensions to the errors in height derived from the geometric test. As mentioned earlier, the IR-18 imagery has a very small base to height ratio (0.12) while the B/H ratio of the wide-angle photography used in the ISP tests was 0.6 (as shown in Figs.10-5 and 10-6). The small B/H ratio of the IR-18 imagery resulted in a small intersection angle between corresponding rays on the ground as discussed in Chapter VIII. This characteristic had a direct impact in producing a relatively large error in height which caused the theoretical values to be consistently lower than the actual values derived from the geometric test. In the case of the ISP tests, the B/H ratio resulted in a reasonable intersection angle on the ground and the magnitude of error in height is usually smaller than that of the narrow-angle imagery. This shows why the theoretical values derived by relating the model dimensions to the error in height were closer to the values obtained from the ISP tests than the corresponding values in case of the IR-18 test. Nevertheless, the results from the IR-18 test analysis showed that the magnitude of residual errors is related to the model dimensions in much the same manner as was the case with the ISP standard tests.

### 10.5.3 Accuracy of Parallax Measurements

The residual error in heights obtained from the geometric test can now be used to evaluate the use of the video monocomparator for parallax measurements. This can be achieved by the use of the general parallax-height formula:

$$m_z = \frac{H}{f \cdot B/H} \cdot d_p \dots\dots\dots 10-1$$

where:-

f is the sensor's focal length;  
 m<sub>z</sub> is the error in height;  
 d<sub>p</sub> is the residual parallax;  
 B is the air-base; and  
 H is the flying height.

Rearranging the above equation to solve for d<sub>p</sub>;

$$d_p = \frac{B}{H} \cdot \frac{m_z}{H} \cdot f \dots\dots\dots 10-2$$

Substituting for the known parameters of the IR-18 frame scanner when equipped with the 1.5X telescope magnifications (B/H = 0.12, H = 750 m and f = 833 pixel), and for the value for m<sub>z</sub> obtained by the geometric test (± 3.18 m) the accuracy of parallax measurements would be ± 0.42 pixel.

### 10.6 Conclusion

Airborne and spaceborne imagery is usually acquired to compile either topographic maps or thematic maps. These maps contain three kinds of information:-

- (i) position which relates the various features shown in the map to a ground coordinate system;
- (ii) elevation which is shown principally on topographic maps and is usually indicated by spot heights and by contour lines at a given vertical interval;
- (iii) content which defines the types of feature detail which have to be shown on the map.

For topographic maps, a very high positional accuracy and large amount of details have to be shown in the map. For thematic maps, the accuracy requirements are relaxed and the expected completeness of the detail is much less than that required for topographic maps.

Based on the results and analysis carried out in the present project, the positional and elevation accuracy are quite satisfactory and can further be improved as will be discussed in the recommendations given in Chapter XIV.

On the other hand, the content is related to the feature detail (such as roads, railways, buildings etc.) which can be detected and identified on the imagery so that it can be plotted on a topographic map. This depends entirely on the ground resolution of the sensor in use. This particular point will be discussed in more detail in the next Chapter which is devoted to the interpretation of frame scanner imagery for topographic mapping.



**CHAPTER XI**  
**INTERPRETATION OF THERMAL FRAME SCANNER VIDEO IMAGES**  
**FOR TOPOGRAPHIC MAPPING**

## CHAPTER XI

### INTERPRETATION OF THERMAL FRAME SCANNER VIDEO IMAGES FOR TOPOGRAPHIC MAPPING

#### 11.1 Introduction

Thermal infrared line scanner imagery has been used widely for qualitative interpretation purposes in many fields in remote sensing such as energy conservation, thermal discharge from power stations, identification of rock types and the location of fault lines in geology, leaks from dams, heat loss from buildings in residential areas, etc. For these applications, normally a thermal infrared line scanner has been used to acquire the imagery and the interpretation has been carried out using hard-copy images.

On the other hand, thermal video frame scanners have only been released or become available for non-military applications very recently and very little work has been published about their potential use in civilian remote sensing applications. The thermal images produced by a frame scanner are often of much better quality than those of the line scanner due to the perspective scanning technique which they employ to generate the thermal image. However, usually the images will still contain some distortion caused by the spherical recording image surface.

In this Chapter, the main factors which are likely to affect the interpretation of the video images produced by the thermal frame scanner are discussed. The principal concern will be with the analogue video image displayed on a video monitor screen since this will be the normal method of generating an image from the video tape used to record the frame scanner images. No attempt has been made in this study to produce or employ hard copy images for interpretation.

However, it should be noted that the results of the interpretation set out in this Chapter are not oriented towards the needs of specialised field scientists interested in the calibrated temperature values which can be extracted from thermal images, since the present author does not have the reference level required for such a specialised study. Instead, the studies have been concentrated on the basic question as to whether the objects which can be detected and identified on a video thermal image are useful in the context of the detail required for the construction of topographic maps at large scales.

## 11.2 Factors Affecting Interpretability of Thermal Images

Apart from the interpreter's own knowledge, abilities and aptitudes, there are four main factors which may affect the interpretability of the video thermal images. These are:-

- (i) the geometric and radiometric characteristics of the scanning system;
- (ii) environmental factors present during the acquisition of the aerial images;
- (iii) the thermal characteristics of the recorded objects ;and
- (iv) the resolution of the display monitor.

### 11.2.1 Geometric and Radiometric Characteristics of the Scanning System

Among the most important parameters for the image interpretation is the geometric resolution. The concept of the frame scanner resolution has been explained earlier in Chapter V. The size of the resolution element on the ground is a function of the flying height, the scanner's IFOV and the scan angles. The image scanning technique is also an important factor since it will introduce a geometric distortion to the object image due to the employment of a spherical image surface as discussed in Chapter V. The correction of these types of distortion would be possible if an image processing system was available so that the video images would be rectified geometrically before carrying out the interpretive process. If an image processing system is not available, care must be taken during the interpretation since the various types of geometric distortion may falsify the shape and size of certain objects.

The radiometric characteristics of the imaging system will also have an essential role to play in deciding the quality and hence the interpretability of the thermal images. Among the most important radiometric parameters is the temperature sensitivity of the scanner expressed in terms of the Minimum Resolvable Temperature Difference (MRTD) which has been discussed in Chapter IV. The high temperature sensitivity of a frame scanner will allow the fine details within the terrain features to be detected and identified in the thermal images.

### 11.2.2 Environmental Factors Affecting the Thermal Image

A variety of conditions outside the actual imaging system can produce unexpected and unwanted effects on thermal infrared imagery. Even though most thermal infrared systems operate in the relatively clear atmospheric window which exists at 8 to 14  $\mu\text{m}$  wavelength, weather effects can degrade the imagery. Clouds may result in a pattern of warm and less warm patches being generated in the scanner images. It is known that a heavy overcast layer will greatly reduce thermal contrast because of the re-radiation of energy between the terrain and the cloud layer even if the base of the overcast layer is above the planned flying height. Surface winds also produce changes in the temperature of ground objects which result in characteristic smears and streaks on the imagery.

Both the time of day and the season of the year are important parameters affecting image acquisition and subsequent interpretation. Radiant emission from surface objects varies with time of day as a result of differential heating and cooling, which in turn is related to Sun angle and the intensity of the solar radiation. Because surface temperature changes with time of day, an interpreter should be aware of the time when the imagery was obtained. For instance, at certain times due to the differential heating and cooling of certain objects and their backgrounds, a so called "cross over" period may occur. At these periods, an object's rate of heat emission will coincide with that of the background, producing the same degree of energy incident on the detector. This could lead to the object and the background having the same shade of grey on the imagery produced by the scanner, thus hiding the object. Usually there will be two periods of crossover per day, one in the morning and the other in the evening which must be considered during interpretation.

### 11.2.3 Thermal Characteristics of the Recorded Objects

The thermal properties of the surface materials determine how the heating from the various heat sources is distributed and stored in the surface layers and how the temperature varies as a function of time and depth in response to the heating. Different factors affect the heat distribution within the object and hence affect the amount of radiation emitted by this object. Among these factors are thermal conductivity, specific heat, density, heat capacity and thermal inertia. Thermal inertia is the most important factor and is defined as the measure of the resistance of a material to a change in temperature. Since the emissivity of an object is related to its temperature, this particular characteristic will have a significant effect on the image contrast.

The above mentioned factors will control the distribution of energy within a certain object and in turn control its radiant temperature. As has been mentioned earlier, the

amount of thermal radiation emitted by an object is related to its temperature and its emissivity. It may be useful to list the emissivity factors for different ground features which are likely to be encountered in the interpretation process. This is given in Table 3-1 below

Material	Temperature of Sample (° C)	Emissivity
Water	32	0.98
Wet Soil	20	0.95
Dry Soil	20	0.93
Glass	20	0.95
Brick	20	0.93
Concrete	20	0.93
Plaster	20	0.91
Sand	20	0.90
Wood	20	0.90
Snow	-10	0.85
Aluminium	100	0.55
Stainless Steel	20	0.16

Table 11-1 Typical emissivity factors of various common materials ( after Lillesand, 1979 )

#### 11.2.4 The Video Monitor

The use of a high resolution video monitor is an essential factor in a successful interpretation of a video image. The high resolution monitor will allow the identification of the fine details of the ground features which have already been detected by the scanner. The size of the display (i.e. 9",12",14" etc. diagonal length) may also have an effect on the interpretation process. A medium sized (14") monitor was found to be quite satisfactory in the case of the images utilized in this project.

#### 11.3 Elements of Thermal Image Interpretation

As can be seen from the preceding discussion, the thermal image of a specific area will be very different in appearance from the corresponding aerial photographic image of the same area taken by a conventional photogrammetric or reconnaissance camera. Thus the normal experiences and procedures derived from photographic interpretation will often have limited application to the interpretation of thermal images. However, it may be useful to review the usual set of factors (size, shape, shadow, tone, pattern and site) which are important in photographic image interpretation and assess their relevance to the particular case of thermal imagery.

**Size:** As with aerial photographic images, the size of an object on a thermal image is an important clue as to an object's identity. By measuring or estimating the dimensions of an unknown object in the video image, the interpreter can frequently eliminate from consideration certain possibilities as to the character of the objects imaged. For thermal images, the size of an object should normally be greater than the nominal resolution of the scanner for it to be detected and identified. If the thermal images taken by the frame scanner have not been rectified, the object images will certainly appear smaller than their expected size due to the compression in scale caused by the scanning geometry as explained in Chapter V.

**Shape:** Shape relates to the general form, outline or configuration of an individual object and, as such, these characteristics are just as important in recognising objects on a thermal video image as they are on photographic images. The shadows cast by the Sun which were present in conventional aerial photography will not be seen on thermal scanner images which eliminates an important set of clues as to the shape of an object. However, the direction of the solar radiation from the Sun can greatly affect the shape of that object when it is being recorded by the scanner because of differential heating of one part of the object against the rest. In this way, the shape of the recorded image may differ from that of the whole object. Furthermore, the object's shape may not be clearly distinguishable from its background if there was not enough difference in emissivity between them during the time of acquiring the imagery.

**Tone:** Tone is a very important element in the interpretation of thermal images. Different objects reflect, emit and transmit differing amounts of energy at different wavelengths. In thermal imaging, the tone or density value assigned to a particular object corresponds to the amount of radiation emitted from that object as received by the scanner. Thus the tone in fact reveals some of the thermal characteristics of the object at the time of collecting the imagery.

**Pattern:** Pattern is the repetition of the spatial arrangement of specific components of an object. It is usually a characteristic of many man-made

objects. However care must be taken since the pattern may change according to the temperature of the object. For example, in a residential area where all the houses were built to have the same shape and size, if some of these were not properly insulated for heat loss, they will take a different tone with respect to those which are properly insulated, arising in a disturbance in the pattern recorded on the thermal video image.

**Shadow:** Shadows are particularly helpful if the objects themselves are very small or lack tonal contrast relative to their background. Under these conditions, the sharp boundaries and shapes of the shadows enable the analyst to identify objects at the threshold of recognition. In the context of thermal images, shadows indicate a cool area shaded from the Sun by high objects or as a result of topography. Consideration must be given to differentiate between shadows and naturally cool or low emissive objects appearing in a thermal image.

**Site:** The location of objects with respect to terrain features or other objects is often helpful. For example, power stations need an abundant supply of coolant water and are usually found near major streams or at the coast. So the identification of a plume or different signatures of warm water in a stream or a water body often gives a clue to the possible existence of a power station or large industrial plant in this area.

#### 11.4 Interpretation of Thermal Imagery for Topographic Mapping Purposes

Having introduced the basic elements required to carry out the interpretation of the thermal images and the various factors which are likely to be involved in the process, it is now possible to see how the interaction of these factors has affected the interpretation of the thermal video images produced by frame scanners in the present project. Three specially flown areas were involved in the interpretation process- the Hunterston area, the Douglas Water area and the Garrowhill area. The first two were flown mainly to provide material for the interpretation test while the last one was chosen mainly for the geometric test but it will also be included in the interpretational study. As mentioned earlier, frame scanners operate in a continuous framing mode producing 25 frames per second (PAL TV-compatible). About 20 minutes of recorded images were obtained for each area during the aerial test. Moreover, the Hunterston area was flown twice at different flying altitudes and at different times of day. The

interpretation of each of the three areas was carried out separately and the results are summarized in Table 11-2 at the end of this Chapter.

The main interest was the interpretation of the video images which have been recorded for each area. The images were played back on the VTR, viewed monocularly and analysed visually. Thus no magnifiers or stereoscopes were used. Whenever necessary, the images were frozen on the video monitor screen using the frame memory to allow adequate time to examine the main features of interest from the point of viewing of compiling or revising a topographic map of the area.

## 11.5 Interpretation of the Video Images Covering the Hunterston Area

The images for this area were acquired at two different times and flight altitudes. The first flight was conducted on the 25th of August, 1984 at about 5.0 p.m. from a flight altitude of 6,000 ft (1,800 m). The second flight was conducted on the 26th of August, 1984 at about 11 a.m. from a flying altitude of 3,000 ft (900 m). The interpretation of different topographic details in this area are discussed below.

### 11.5.1 Man-Made Features

**Roads and Highways** These are smooth man-made features which generally speaking, should exhibit large amounts of emitted radiation since they are covered with a thick layer of asphalt. These features appear relatively warm both day and night since they heat up to a temperature higher than their surroundings during the daytime. Also they lose heat relatively slowly at night, thus always retaining a temperature higher than their surroundings. In the O.S. 1 : 25,000 scale topographic map series, the roads are classified into many categories- motorways (M-class), trunk and main roads (A-class), roads of 14 ft (4 m) or over of metalling, roads of 14 ft or under of metalling (B-class), minor roads and gravel paths. Each of these categories is well depicted on the map by using different symbols and colours. These all appeared very clearly in the video images. However, in the late morning images, roads appeared to exhibit a better contrast with respect to their backgrounds than those which appeared in the evening images. Obviously, the solar heating was responsible for this effect, since in the morning images the surroundings have been heated up for just 3 to 4 hours, while in the evening images, they have



been heated up for about 10 hours and the surrounding ground may have begun to cool. The classification of different types of roads as they appeared in the late morning and evening images is given in Table 11-2.

#### **Railway**

These features are classified on the O.S. map into single or multiple tracks. However, in this area, there was only a multiple track railway line running parallel to the coast. Railway lines are made of steel materials which are highly reflective and hence have a low emissivity factor. However they also exhibit a high thermal inertia which means that they can heat up very quickly. In the low flight imagery (3,000 ft), the railway line passing parallel to the coast was easily identified by its warm signature relative to its background, but it was not as warm as the roads. On the other hand, the same line was not identified at all in the high altitude images since the resolution was poor (2.1 m on the ground) at this flying height.

#### **Built-up Areas**

These comprise the towns and villages of which a number are scattered around within this test area. Buildings may vary in their appearance in thermal images according to their roof construction. For example, when covered with painted metal sheets, buildings would appear cold in thermal image since metals are highly reflective. On the other hand, if the roof was made of concrete, it would appear warm since this material has a relatively high thermal inertia. In this test area, buildings appeared very warm especially in the evening images. In general, the buildings which appeared in the video images were relatively easy to identify and interpret.

#### **Power Lines**

Many of these features exist in the test area and are shown in the 1:25,000 scale map. However it was extremely difficult to detect a power line without the help of the map, especially in the high altitude images.

Fig.11-1 below shows an image of a residential area acquired by the IR-18 frame scanner (N.B. the photograph was produced by photographing the video image displayed on the video monitor screen). The various man-made features discussed above can be seen in this image, especially the roads and the built-up areas. Also the effect of thermal shadows can be noticed very clearly in the image.



Fig.11-1 A thermal frame scanner image for a residential area

### 11.5.2 Hydrological Features

#### Discharge from the Power Station

This test area was mainly chosen to discover the effect of the thermal discharge from the Hunterston power station on the sea water. Power stations require very large volumes of cooling water. The water is discharged into the sea at a temperature higher than the ambient water temperature. During day time, water usually has a very cold signature since it is highly absorbent of radiation from the Sun and has a low thermal inertia. However, due to the discharge of the heated water from the power station, the water appeared to have different signatures. At the outlet point of the discharge pipes, the water appeared to exhibit a relatively high temperature signature. This warm signature appeared to get cooler away from the outlet point where the discharged warm water gets mixed with the ambient cold water, resulting in a less warm signature which gets colder as it goes away from the outlet point as shown in Fig.11-2.

The tracing of the subsequent pattern at different states of the tidal rate is not required for topographic mapping, but nevertheless the characteristic is a notable one and can be usefully employed in a suitable circumstances. The main difficulty lies in being able to position or locate each video image taken over the sea where there are no land features to aid the location.



Fig.11-2 Thermal discharge from Hunterston power station

**Reservoirs** These can be easily identified by their very cold signature in daytime imagery and warm signature in nighttime imagery. However, sometimes it may be difficult to differentiate between a reservoir and a small lake though the shape of the dam associated with the reservoir is an important clue in this respect. Several reservoirs have been identified very easily in both the high and low altitude images of this area.

**Natural Water Bodies** These are lakes, rivers, canals and streams which should appear very clearly in the daytime images due to the cold signature of water relative to the land. However, apart from the Firth of Clyde itself, no other natural water bodies exist in the area covered by the imageries. The Firth of Clyde was covered by several frames and the shore lines appeared very sharp and well-defined so that an accurate measurement of the land/water boundary can be compiled very easily in the plotting. This is an important and favourable characteristic of thermal video images, since normally, the O.S. has to fly special infrared photography to support the normal panchromatic photography, specifically for the purpose of locating the coast lines during its topographic mapping operations.

### 11.5.3 Vegetational Features

The various types of vegetation classified and shown on the O.S. 1:25,000 scale maps are woodlands, ornamental grounds or parks and orchards, all of which are well depicted on the map. On a thermal image, the woodlands and scattered trees would appear to have a relatively cold signature with respect to the terrain background since different types of vegetation contain differing amounts of water. During the daytime, the transpiration of water by the solar heating causes the vegetation to drop in temperature and hence radiate smaller amounts of thermal energy.

**Woodlands** These showed up strikingly well on these images ,e.g. Allan Wood just beside the Hunterston power station was very clearly distinguishable. Even the individual trees in the area could be recognised. They almost always produced very dark grey tones and could be identified by this tone together with their shape.

**Cultivated areas** With their recognisable landscape, cultivated areas appeared very clearly in the images. However, the tone appeared to vary from one area to the other, presumably according to its crop or the water content of the surface soil. For instance, a recently irrigated area would appear to exhibit darker tones than a relatively dry area. The actual crop or land use is not a characteristic which has to be recorded on a topographic map.

### 11.6 Interpretation of the Video Thermal Images Covering the Douglas Water Area

The imagery for this area was acquired on the 26th of August, 1984 at 12 noon from a flight altitude of 3,000 ft (900 m). Comments will only be made on those features which are different to those encountered on the Hunterston imagery.

**Roads and Highways** The area contains several types of roads and highways, including a dual-carriageway trunk road (A 74), other main roads (A 70) and secondary roads. All these different types of roads appeared very clearly so that even the individual cars running on these roads could be identified.

**Railways** Four single-track railway lines running through the area were very clearly identified in the images.

**Built-Up Areas**

Some scattered houses and buildings appeared in the images and were clearly identified.

**Vegetation**

The main vegetational features are several woods which were scattered about the area and could be identified and plotted readily. Cultivated land also showed up very clearly and could be plotted very easily.

**The Coal Bings**

The special heaps or bings associated with the large coal mines in this area are cooled down by spraying water on them since they are subject to spontaneous internal combustion. These bings were found to exhibit a very high contrast against their background, since they appeared extremely warm. Several bings were shown up in the images and were very easily recognised. However, this appeared to be due to the effects of solar heating and it would have required night-time imagery to detect whether or not internal combustion was present within the bings. Fig.11-3 shows how these coal bings appear very clearly in thermal frame scanner images.

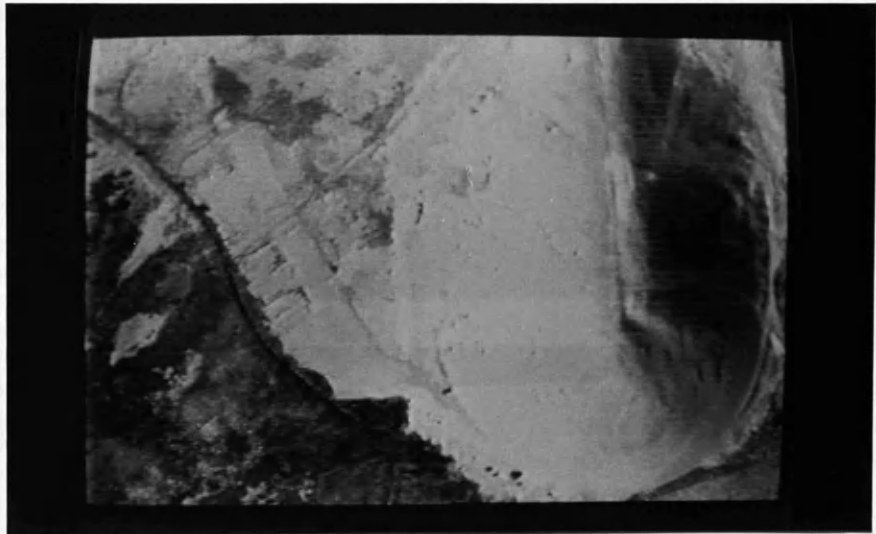


Fig.11-3 The coal bing

**Hydrological Features**

The main hydrological feature in this area is the River Clyde with its canals and streams. Because of their twisting pattern and cold signature during daytime, they could easily be recognised and plotted. Fig.11-4 shows a water stream from the River Clyde running beside a coal bing.

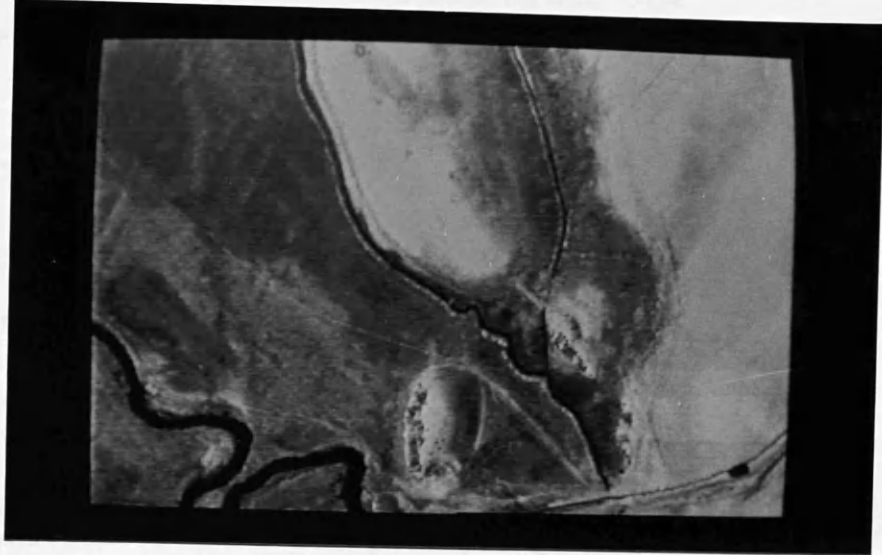


Fig.11-4 A water stream from the River Clyde

### 11.7 Interpretation of the Video Images Covering the Queenslie-Garrowhill Area

The imagery for this area was acquired on the 25th of August, 1984 at 2 p.m. from a flying altitude of 2,500 ft (750 m). As mentioned above, this residential area was chosen essentially for the geometric test. The low flying height which had to be used to acquire the imagery for this area resulted in large scale images (1:1,200) which were very easy to interpret. The pattern of houses was very clear and the outlines of the individual houses appeared very sharp and easy to plot. All classes of roads appeared very wide and distinct. In fact, the only problem in the interpretation of this area was the effect of thermal shadows which resulted in a change in the shape of some of the ground features. Obviously, this was the consequence of acquiring the imagery at this time of the day. However, it was still possible to recognise all the features which have been discussed in the previous two areas.

### 11.8 Conclusion

Table 11-2 below summarizes the interpretation results set out in this chapter. It can be seen from this table that the detectability of objects is largely dependent on the ground resolution of the scanner being used for the survey together with some previous knowledge about the thermal characteristics of the terrain features. In fact, the ability of the scanner to detect small differences in temperature (as a function of the amount of emitted radiation), made the interpretation process quite similar to that of a black and white image produced by a vidicon tube camera operating in the visible light band of the spectrum. In general, it can be said that interpretation and plotting of the detail required for topographic mapping from video frame scanner imagery appeared to be quite feasible and causes no specific problems to the topographic scientist.

Feature Mapped in 1:25,000 Scale Map	Area	Hunterston 6,000	Hunterston 3,000	Douglas Water 3,000	Queenslie-Garrowhill 2,500
	H(ft) (m)	1,800	900	900	750
<b>1. Communication Features</b>					
Roads & Highways		I	I	I	I
Railway Lines		D	I	I	I
Bridges		D	I	I	I
Foot Paths		N	I	I	I
Ferry Location		I	I	---	---
Railway Station		D	I	I	I
<b>2. Man-Made Features</b>					
Houses		I	I	I	I
Towers		I	I	---	---
Lighthouses		I	I	---	---
Storage Tanks		D	I	I	---
Power Lines		D	I	I	I
Reservoirs		I	I	I	---
Coal Bings		---	---	I	---
<b>3. Hydrological Features</b>					
Rivers		I	I	I	I
Lakes		I	I	I	I
Shorelines		I	I	---	---
Water Delineation		I	---	---	---
Harbours		I	I	---	---
<b>4. Vegetation</b>					
Woodland		I	I	I	I
Scattered Trees		I	I	I	I
Orchard		---	---	---	I

Table 11-2 Summary of the detectability and interpretability of topographic details in the thermal video frame scanner images

Where:-

H is the flying height;  
 I = Identified;  
 D = Detected;  
 N = Neither identified nor detected; and  
 --- = not existing in the area.

**CHAPTER XII**  
**DIGITAL GEOMETRIC RECTIFICATION**  
**OF FRAME SCANNER IMAGERY**



## CHAPTER XII

### DIGITAL GEOMETRIC RECTIFICATION OF FRAME SCANNER IMAGERY

#### 12.1 Introduction

The purpose of the digital geometric rectification is to remove different types of distortion introduced to the image during the imaging process such as optical elements distortion, scan geometry, tilts and image motion distortion.

In the present project, geometric rectification was carried out with a view to constructing a three-dimensional (stereoscopic) video model using the facilities of a GEMS image processing system, by overlaying two digitally rectified video images of a stereopair. The digital geometric rectification was carried out on the ICL 2988 mainframe computer of the University of Glasgow. The rectified images were then transferred onto magnetic tape which was read into the Prime 300 minicomputer attached to the GEMS system and used to construct the stereo-video model.

This Chapter will be devoted to the digital geometric rectification of the digitized images. In the next Chapter, methods of carrying out stereo-video viewing will be discussed in detail.

#### 12.2 Digitization of the Video Images

After the images have been acquired and recorded, they must be digitized for processing by a digital computer. Digitization consists of sampling the grey levels in an image at constant intervals to produce an M by N matrix of pixels and quantizing the grey level at each sampled pixel.

The analogue to digital conversion of the video images is carried out by a digital frame store (DFS). This operates in the same manner as the frame buffer discussed in Section 2.5 of Chapter II. However, the DFS accepts the analogue video signal from the video tape recorder which is then converted into digital form and stored in the image planes. The digital information could then be transferred into the computer memory via an input-output (I/O) data bus. These devices are now widely available at relatively low costs.

A digital image as it is handled in the computer can be described as a two-dimensional array of integer values. Each value (digital number), represents the average brightness in the image at one location (i.e within a single pixel).

In the present project, several video frame scanner images have been digitized at the National Remote Sensing Centre (NRSC), Farnborough using the Quantel 3001 DFS image digitizer controlled by a Plessey IDP 3000 image processing system. Each image was transformed into 512 by 512 format (262,144 pixels per frame). The intensity or brightness of each pixel was quantized over the range  $2^8$  bits, giving 256 different shades or grey levels.

Since the results of the analytical techniques derived in the previous chapters were used for the digital rectification, each digital image had to be brought to the same scale as the corresponding video image which was used for the analytical rectification. Methods of reducing or enlarging the digital image scale are explained below.

### 12.2.1 Digital Image Reduction and Enlargement

The vertical dimension of the video image measured by the video mono-comparator during the analytical rectification was 250 lines, each line consisting of 384 (square) pixels. However, when the frame scanner image was digitized at NRSC, the resultant digital image comprised 512 lines, each line consisting of 512 (rectangular) pixels. Thus, the digital image has to be reduced by a factor of 2.048 in the vertical direction and by a factor of 1.333 in the horizontal direction. However, after the appropriate digital rectification has been carried out, the rectified digital image has to be enlarged back to its original digitized format in order to achieve the correct size on the display.

#### (i) Digital Image Reduction

A digital image reduction algorithm served to represent the image with fewer pixels. Integer reductions (in which the reduction factor is an integer number) can easily be accomplished by pixel and line deletions. For example, to reduce a digital image by a factor of three, two out of each three pixels in each line and two out of each three lines may be deleted. Alternatively, integer reductions may be achieved by averaging. For example, each block of 3 x 3 pixels may be replaced by a single pixel having the average grey level value of the 9 pixels. Non-integer reduction can be achieved by interpolation. Different methods of interpolation will be explained later in this Chapter.

#### (ii) Digital Image Enlargement

In this procedure, pixels are added to the image to increase its scale, either to improve the display or to match the scale of another image. Just as pixel

and line deletion offers the simplest way of image reduction, so pixel and line replication offers the simplest form of image enlargement. To enlarge a digital image by a factor of three, each pixel is replaced by 3 x 3 block of pixels, all with the same grey level value as the replaced pixel. Interpolation methods can also be used to enlarge the digital image when the enlargement factor is a fractional value.

### 12.3 Digital Geometric Rectification

The purpose of the digital rectification is to reduce the digitized frame scanner image (which will be called the input image) into an equivalent distortion-free vertical image, i.e. the image which would have been recorded instantaneously on a flat image plane in a horizontal position with the scanner's optical axis pointing vertically downward. This will be called the output image. It will be noted that this image would then be identical to that produced by a photographic frame camera, i.e. it would be a truly perspective projection on a flat image plane. It further follows that, if the terrain is perfectly flat, the output image will have the geometry of a map. If the terrain is not perfectly flat, the output image will still contain the relief displacements induced by the terrain elevations above or below the datum. These will not be rectified; indeed their retention is a necessity if a stereoscopic video image of the terrain is to be produced. This rectification can be carried out in two stages:-

- (i) analytical rectification, in which each pixel position in the digital image is corrected for the geometric distortion existing in the frame scanner images as a result of the scanning geometry; and
- (ii) for each corrected pixel location a digital number or brightness value is assigned, as will be explained later in this chapter.

#### 12.3.1 Analytical Rectification

Analytical rectification requires a mathematical model to remove geometric distortion. A suitable model for rectification can only be decided upon after geometrical analysis so that the chosen mathematical model takes into consideration the geometric characteristics of the imaging sensor. Based on the discussion in the previous Chapters, the digitized frame scanner images have to be corrected for the following effects:-

- (i) image displacement caused by the spherical recording surface of the frame scanner;

- (ii) tilts of the scanner occurring during the frame scan time;
- (iii) scanner distortion such as the distortion introduced by the scanner's optical components and any distortion introduced by the scanner's electronic components or circuitry; and
- (iv) image motion during the image scan time.

### 12.3.1.1 Correction for the Effect of the Spherical Image Surface

As mentioned in Chapter V, the effect of the scanning technique employed by frame scanners is that the size of the ground resolution element varies with the scan angles while each element is recorded on the image with a constant pixel size producing a spherical image surface. To remove the spherical effect, the size of each pixel in the image must be made to correspond to a constant resolution element on the ground. In other words, transforming the spherical image surface into an equivalent flat image surface tangent at the centre point of the spherical surface.

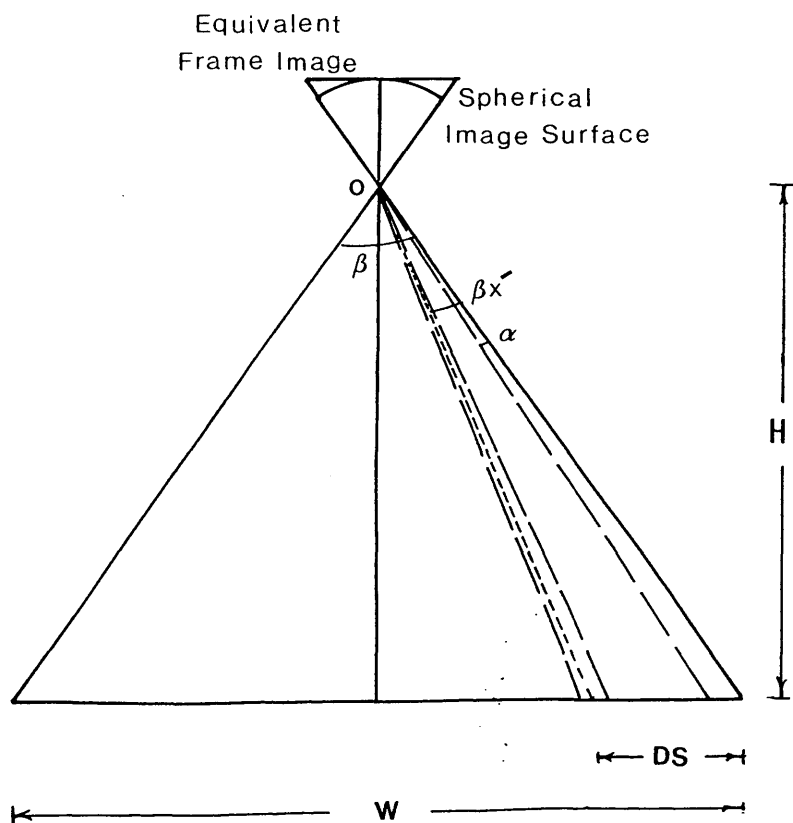


Fig.12-1 Digital correction for the spherical surface

In Fig.12-1 above,

$$W = 2 H \tan \beta/2 \dots\dots\dots 12-1$$

where W is the width of the frame in the frame scan direction on the ground;

H is the flying height;and

$\beta$  is the scan angle in the frame scan direction.

Thus the dimension of each pixel on the ground in this direction will be

$$Y = W/M$$

Where Y is the dimension of the pixel on the ground;and  
M is the number of lines/frame.

In Fig.12-1, if DS is the distance on the ground from the beginning of the frame scan to the position corresponding to line  $x'$  in the output image, then

$$\begin{aligned} DS &= x' (W/M) - 1/2 (W/M) \\ &= (2x'-1)/2 \cdot (W/M) \dots\dots\dots 12-2 \end{aligned}$$

This distance may also be expressed in terms of the scan angle as follows:-

$$DS = H \tan \beta/2 - ( H \tan (\beta/2 - \beta x') \dots\dots\dots 12-3$$

Equating the right hand sides of equations 12-2 and 12-3 and solving for  $\beta x'$ , then:-

$$\beta x' = \beta/2 + \tan^{-1} [ (2x'-1)/2H \cdot (W/M) - \tan \beta/2 ] \dots\dots 12-4$$

Substituting for W in equation 12-1 and for  $\beta x' = x \cdot \alpha$ , where  $\alpha$  is the scanner's IFOV, then:-

$$x = M/2 + (1/\alpha) \tan^{-1} [(2x'-1)/M \tan \beta/2 - \tan \beta/2] \dots\dots 12-5$$

In the same manner, the position of pixel  $y'$  in line  $x'$  of the output image can be found in the input image except that the width of the line on the ground (W) will be a function of the two scanning angles  $\beta$  and  $\theta$ . Thus;

$$W = 2 H \sec \beta \tan \theta/2$$

and,

$$y = N/2 + (1/\alpha) \tan^{-1} [(2y'-1)/N \sec \beta/2 \tan \theta/2 - \tan \theta/2] \dots\dots\dots 12-6$$

### Example

As a simplified example, consider a frame scanner with a field of view of  $11.5^\circ \times 17^\circ$  and an IFOV of 0.01 radians. It is required to determine the grey level for pixel (3,3) in the output image. Thus;

$$\text{No. of lines/frame (M)} = 20$$

$$\text{No. of pixels/line (N)} = 30$$

$$\begin{aligned} x &= 20/2 + 1/0.01 \tan^{-1} [(2 \times 3 - 1)/20 \tan 0.01 - \tan 0.01] \\ &= 2.489 \end{aligned}$$

$$\begin{aligned} y &= 30/2 + 1/0.01 \tan^{-1} [(2 \times 3 - 1)/30 \sec 0.1 \tan 0.15 - \tan 0.15] \\ &= 2.483 \end{aligned}$$

N.B. the angles in the above equations are expressed in radians.

Thus the grey level value of pixel (2.489, 2.483) in the input image will be assigned to pixel (3,3) in the output image.

#### **12.3.1.2 Digital Correction for Scanner Attitude and Change of Attitude during the Image Scan Time**

The purpose of this correction is to remove the effects of tilt from the input image so that it conforms to that of an instantaneously recorded image taken with the optical axis of the scanner pointing vertically downwards.

In Chapter VIII, the space resection procedure was used to solve for the exterior orientation parameters. Two different techniques have been used to model the changes in these parameters during the image scan time. The technique of space resection with additional parameters proved to be more satisfactory and gave better accuracy than the point-by-point space resection/intersection. It also involves less computer storage and computational effort. The results from the additional parameters technique were used to correct for the effects of tilt. This was carried out in two stages:-

- (i) each pixel location was corrected for the initial tilts which occurred during the recording of the image's geometric centre. This was achieved by rotating each pixel in three dimensions. The initial tilt values have been solved for during the space resection phase as described in Chapter VIII; and

- (ii) the rotated pixel positions were further corrected for the changes in the tilt parameters which occurred during the image scan time using the known coefficients of equations 8-17,8-18 which have also been obtained during the space resection phase.

The general three dimensional transformation has the form:-

$$\begin{vmatrix} x' \\ y' \\ z' \end{vmatrix} = \lambda A \begin{vmatrix} x \\ y \\ z \end{vmatrix} + \begin{vmatrix} dx \\ dy \\ dz \end{vmatrix} \dots\dots\dots 12-6$$

Where:-

- x,y,z are the coordinates in the input image;
- x',y',z' are the coordinates in the output image;
- dx,dy,dz represent the shifts or translations between the two coordinate systems;
- λ is a scale factor;and
- A is a 3 x 3 rotation matrix. Its elements are functions of the three angular rotations about x,y and z respectively.

However, in the present situation, it is required to rotate the input image so that the reproduced image (output image) will have the same scale and it is also necessary to ensure that its coordinate system's origin coincides with that of the input image origin. In other words, the scale factor λ in the above equation will be set to unity, while the translation elements (dx,dy and dz) will be set to zero. So rearranging equation 12-6 above and solving for the input image coordinates yields the following equation:-

$$\begin{vmatrix} x \\ y \\ z \end{vmatrix} = A^{-1} \begin{vmatrix} x' \\ y' \\ -f \end{vmatrix} \dots\dots\dots 12-7$$

**12.3.1.3 Correction for the Scanner Distortion Determined during the Calibration Process**

The analytical technique described in Section 8.3.1 can be used to correct for this distortion.

#### 12.3.1.4 Digital Correction for Image Motion during the Scan Time

Again the technique described in Section 5.6.4 using equation 5-6 can be used for this correction.

#### 12.3.2 Assignment of Digital Brightness Values

So far, the method of correcting each pixel location for the various types of geometric distortion has been discussed. Now, each corrected pixel must be assigned a digital brightness value. This can be achieved by two different ways. In the first, the actual locations of the picture elements (pixels) are changed but each element retains its brightness value. This situation is shown in Fig.12-2 where the input image (distorted) is considered to have a regular pixel size relative to the output image which will then be represented by a series of pixels of irregular shape and size. Because of its limited accuracy, this method tends to be used only for simple geometric corrections such as those concerned with the aspect ratio of the image.

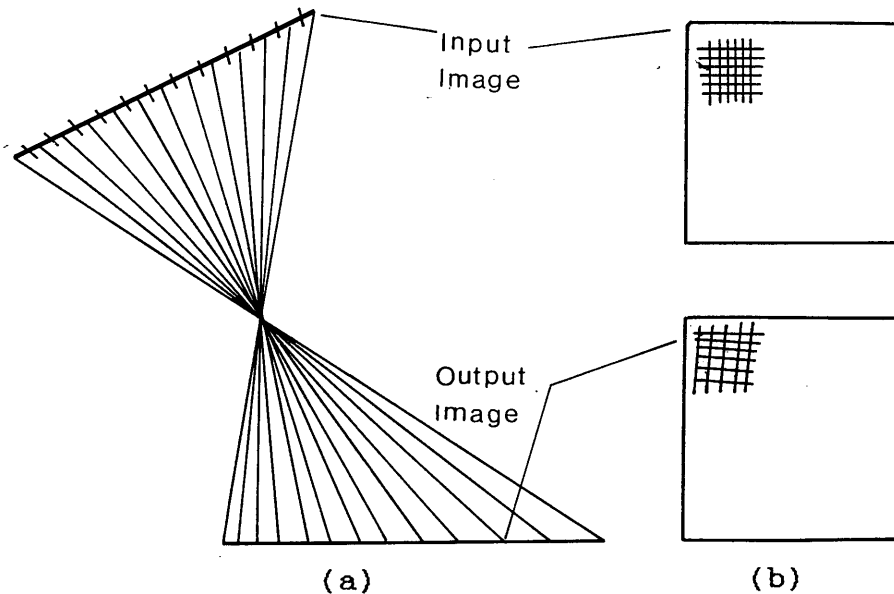


Fig.12-2 Regular input pixel and irregularly-shaped output pixel

Alternatively, the input image may be considered to have an irregular pixel size relative to an output image consisting of a series of pixels of regular shape and size as shown in Fig.12-3. The brightness value to be assigned for each pixel in this case is obtained by interpolation in the input image. This method is known as resampling and is explained in detail below.



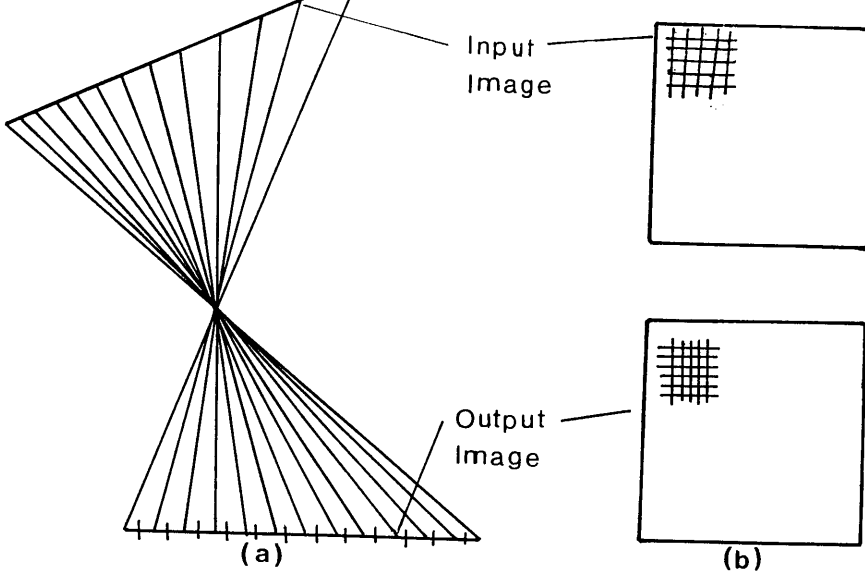


Fig.12-3 Irregularly-shaped input pixel and regular output pixel

### 12.4 Resampling Methods

As mentioned above, resampling is the process by which a brightness value or digital number (DN) is assigned to the geometrically corrected pixel location. Referring to Fig.12-4, a pixel at location  $(x',y')$  in the geometrically corrected image (output image) corresponds to pixel  $(x,y)$  in the distorted image (input image). Because the values of  $x,y$  do not necessarily occur exactly at the coordinates of an original pixel, interpolation in the input image at  $(x,y)$  is necessary to calculate the brightness value to be assigned to pixel  $(x',y')$  in the output image.

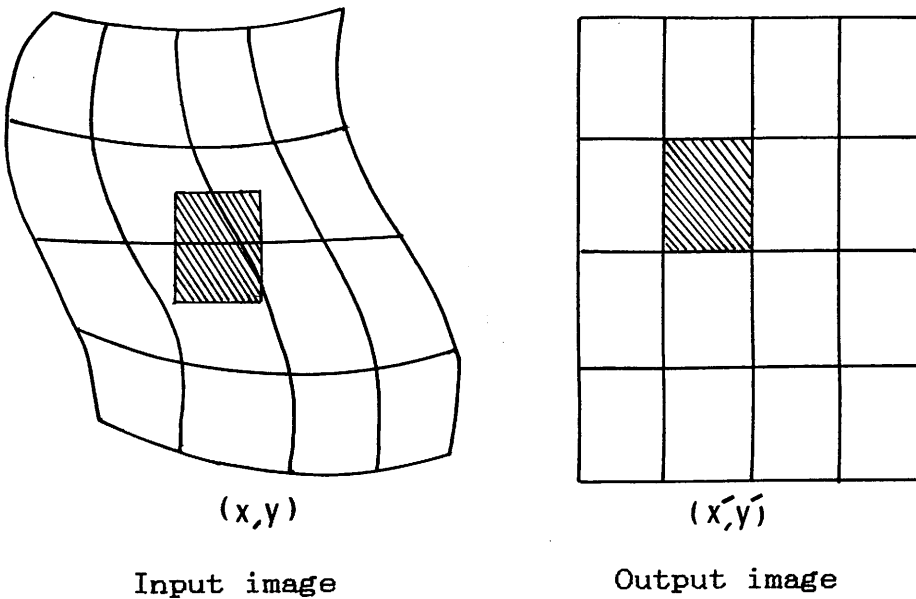


Fig.12-4 Corresponding locations of pixels in the input and output images

There are three different methods of interpolation which are commonly used for this particular task in the processing of remotely sensed images. These are :-

- (i) nearest neighbour interpolation;
- (ii) bilinear interpolation; and
- (iii) bicubic interpolation

However, it must be noted here that these methods of interpolation are being used to carry out a completely different set of operations to those carried out by the transformation equations described in Section 7.1.2 of Chapter VII. The purpose of the transformation procedure is to transform the image coordinates from one coordinate system to another. On the other hand, the purpose of the present interpolation procedure is to assign a digital value (of intensity or brightness) to a known pixel position by averaging the surrounding pixels.

### 12.4.1 Nearest Neighbour Interpolation

In the nearest neighbour interpolation (sometimes called zero-order interpolation), a value equal to that of the nearest input pixel is assigned to the output pixel as shown in Fig.12-5a.

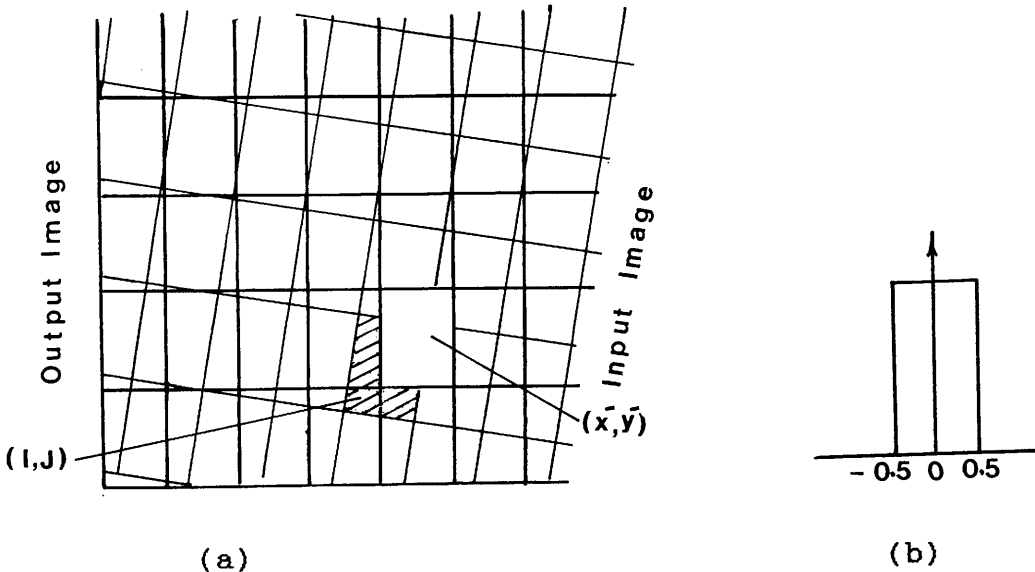


Fig. 12-5 Nearest neighbour interpolation

Thus if pixel  $(x', y')$  in the output image corresponds to location  $(x, y)$  in the input image, the digital brightness number (DN) for pixel  $(I, J)$  - where  $I$  is the integer number of  $(x + 0.5)$  and  $J$  is the integer number of  $(y + 0.5)$  in the input image assigned to pixel  $(x', y')$  in the output image.

The interpolation function of this method is shown in Fig.12-5b. For example, if pixel (3,5) in the output image was transformed to the input image as pixel (3.6,5.1), then:-

$$I = \text{the integer number of } (3.6 + 0.5) = 4$$

$$J = \text{the integer number of } (5.1 + 0.5) = 5$$

Thus, the digital brightness value of pixel (4,5) in the input image is assigned to pixel (3,5) in the output image.

In this method, the resulting intensity values correspond to true input pixel values, but the geometric location of an individual pixel may be displaced by as much as  $\pm 0.5$  pixel. The resulting shift of the true pixel values caused by the employment of such an interpolation method causes a blocky appearance to the linear features present in the image. The computational requirements for the nearest neighbour interpolation are relatively low because only one data value is required to determine a resampled pixel value.

#### 12.4.2 Bilinear Interpolation

Bilinear (first-order) interpolation involves finding the four pixels on the input image closest to location (x,y) and obtaining the required digital brightness value by the weighted average of the four pixels as shown in Fig.12-6a. The most suitable weight which can be used would be a function of the respective distances between the centre of the transformed pixel and the centres of the surrounding four pixels.

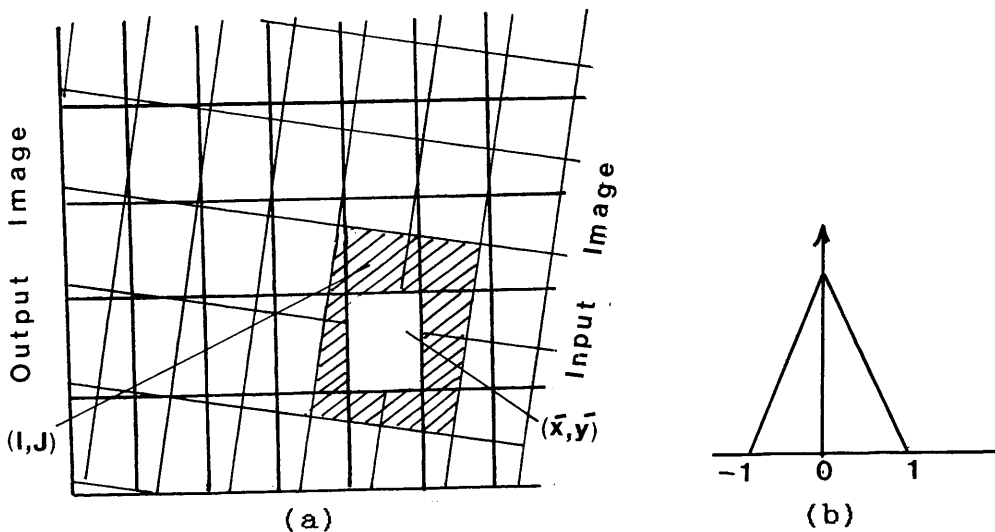


Fig.12-6 Bilinear interpolation

From Fig.12-6a above, the digital brightness value (DN) to be assigned to pixel  $(x', y')$  in the output image can be found from the input image as follows:-

$$DN(\bar{x}, \bar{y}) = (1-a)(1-b) DN(I, J) + a(1-b) DN(I+1, J) + b(1-a) DN(I, J+1) + a b DN(I+1, J+1) \dots\dots\dots 12-8$$

Where:- I = Integer x ;and a = x - I  
 J = Integer y ;and b = y - J

The interpolation function of this method is shown in Fig.12-6b.

Bilinear interpolation may cause a small loss of image resolution due to its smoothing nature. On the other hand, the blocky appearance of the linear features associated with the nearest neighbour interpolation is reduced. However, the computational cost of this method is higher because of the additional operations required.

### 12.4.3 Bicubic Interpolation

This second-order interpolation method (sometimes called cubic convolution resampling) assigns new values to the output pixels in much the same manner as bilinear interpolation, except that the weighted values of 16 input pixels are used to determine the value of each output pixel as shown in Fig.12-7a.

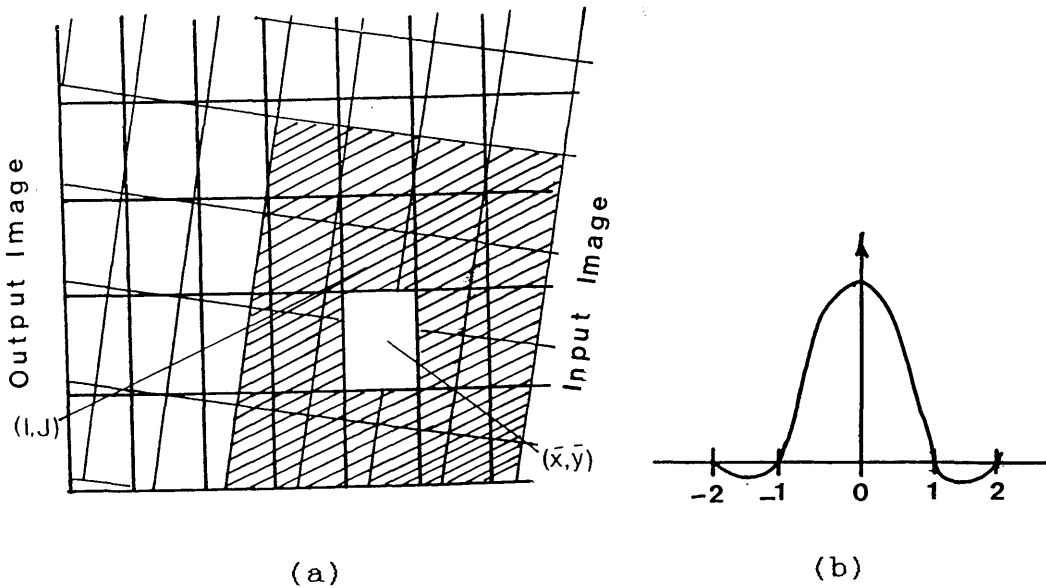


Fig.12-7 Bicubic interpolation

This interpolation can be achieved in two stages- firstly to interpolate in the line direction to obtain pixel values at locations (x, J-1), (x, J), (x, J+1), (x, J+2) and then to interpolate in the sample direction to obtain  $DN(\bar{x}, \bar{y})$  (Moik, 1980). Thus,

$$DN(x, m) = -a(1-a)^2 DN(I-1, m) + (1-2a^2+a^3) DN(I, m) + \\ a(1+a-a^2) DN(I+1, m) - a^2 (1-a) DN(I+2, m)$$

Where  $m = J-1, J, J+1, J+2$ . The final interpolated value  $DN(x, y)$  is obtained by:-

$$DN(\bar{x}, \bar{y}) = -b(1-b)^2 DN(x, J-1) + (1-2b^2+b^3) DN(x, J) + \\ b(1+b-b^2) DN(x, J+1) - b^2 (1-b) DN(x, J+2) \dots 12-11$$

The cubic convolution is continuous in value and slope as shown in Fig.12-7b. This type of interpolation is free from the dislocation of values characteristic of nearest neighbour interpolation, while the resolution degradation associated with bilinear interpolation is reduced.

## 12.5 Description of the Digital Rectification Process Carried out for the Video Frame Scanner Images

As mentioned above, the digital geometric rectification was carried out with a view to investigating the possibility of stereo-video viewing using frame scanner images. For this purpose, the two overlapping images forming model I which were used for the geometric test were digitized at the NRSC as mentioned earlier. The exterior orientation parameters which had been determined for each image individually during the space resection procedure were used to correct the digital image for the initial tilts which took place at the moment of recording the geometric centre of the video image. The additional parameters were used to correct for the various types of distortion introduced to the image such as tilt variations during the image scan time and the errors in the position of the principal point. Other types of distortion were corrected as described in Section 12.3.1 above.

After each correction, the bicubic resampling method described above was used to assign a digital number for each corrected pixel location.

### 12.5.1 Computer Processing of the Digital Images

To perform the digital rectification procedure described above, a computer program was written in Fortran 77 by the present author to run on the ICL 2988 mainframe computer of the University of Glasgow. A complete listing and description of the program (program DICOR) is given in Appendix A. However, it might be useful to record and discuss some of the difficulties which arose during the computer processing of the image data.

(i) **Data Transfer**

The video images which were to be used for the stereo-video viewing were recorded on a U-matic video tape and were sent to the Environmental Remote Sensing Application Centre (ERSAC) in Livingston which arranged for them to be digitized at the NRSC in Farnborough. The digitized images received from NRSC were written on a magnetic tape which was then read into the ICL 2988. However it took quite an effort to read the tape since ERSAC people knew very little about the format and the machine language which had been used to write the information on the magnetic tape. After quite an effort, the staff in the computer centre of the University of Glasgow succeeded in interpreting the machine code by which the data were written onto the tape (binary code) and a small program was written to read the data.

After the appropriate analytical rectification and resampling process had been carried out using the specific program written by the author, it was necessary to write the digitally corrected images onto a magnetic tape so that it could be read by the Prime computer attached to the GEMS image processing system. After several trials during which the images were written using different formats, it was found that an IBM format was the only one which could be read and written by both the ICL 2988 and the Prime computer.

(ii) **Difficulties during the Running of Program DICOR**

The main problem which arose during the use of program DICOR was the large computer storage required to store and process the two digital images. As mentioned earlier in this Chapter, the video images were digitized into 512 x 512 pixels, i.e. each image was stored in the computer memory as an array consisting of 262,144 elements. Thus for the two images, 524,528 pixels required to be corrected and each input image resulted in a corresponding rectified output image, i.e. in total, 1,048,576 pixels had to be handled by the program. Although, the ICL 2988 has an enormous storage capacity, the storage space allocated to an individual user was not enough to perform the data processing taking into consideration the other computer programs and the data which already existed in the computer memory for the author. In fact, many times a penalty was imposed in the form of a limited OCP time (time allowed to use the computer in one session) due to the exceedingly large storage space occupied by the image

data. The problem was solved when the author was allowed the use of another user number which was normally allocated to the undergraduate students during their practical training in the remote sensing course.

In this chapter, the various procedures which have been used to digitize, correct and resample the video frame scanner images have been discussed. In the next Chapter, the method which had been used to form a stereo-video model using the two digitally rectified images will be explained in detail.

**CHAPTER XIII**  
**THREE DIMENSIONAL VIDEO VIEWING**  
**USING AIRBORNE FRAME SCANNER IMAGERY**



## CHAPTER XIII

### THREE-DIMENSIONAL VIDEO VIEWING USING AIRBORNE FRAME SCANNER IMAGERY

In the previous Chapter, a suitable procedure which can be used for the digital rectification of frame scanner video images was explained. Two overlapping images were digitized, and corrected for geometric distortion. These two rectified images were then used to create a three-dimensional model on a video monitor screen. As explained earlier, the digital rectification was carried out on the ICL 2988 mainframe computer of the University of Glasgow. The two rectified images were transferred onto magnetic tape (in IBM format) which was then read into the Prime minicomputer attached to the GEMS image processing system which was then used to generate and display the three-dimensional image.

In this Chapter, different methods of creating a three-dimensional video model will be explained. Also the initial plan which was intended to create such a model will be discussed. Finally, the actual procedure which has been adopted for this purpose will be discussed with detailed analysis of the various difficulties which arose during the different stages of the process.

#### 13.1 Methods of Achieving Stereo-video Viewing

Before describing the actual procedure which was implemented to form the stereo-video model, it is necessary to review the different possible techniques which can be used to form such a three-dimensional model. There are in fact a wide variety of possible methods, many of which are very similar to those used in existing analogue stereo-plotting machines. These methods were classified by Petrie, 1983 as follows:-

- (i) The use of a single screen on which the two component images appear side-by-side and are viewed by a hood containing two lenses with prismatic wedges which may be directed towards the two component images making up the stereo-model (Fig.13-1). A disadvantage of the arrangement is that it reduces the coverage to only half the width of the video monitor screen.

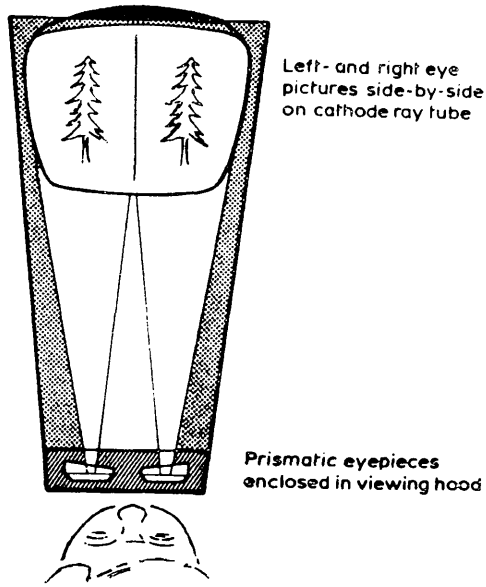


Fig.13-1 Split screen with lens stereoscope

- (ii) This latter difficulty can of course be overcome by using two separate screens viewed simultaneously using a semi-reflecting mirror as shown in Fig.13-2. The required image separation is produced by insertion of horizontally and vertically polarised sheets in front of the two screens, the operator wearing spectacles with corresponding filters to produce the three-dimensional effect. This arrangement has in fact already been adopted by Matra in its Video Correlator Compiler (VCC).

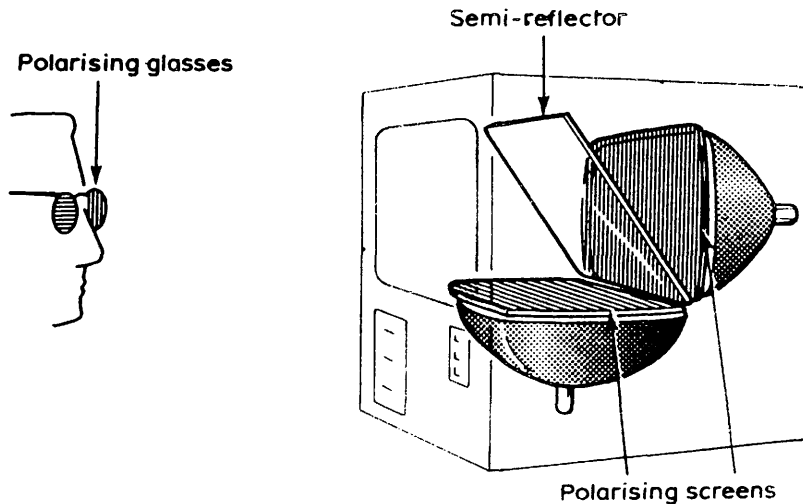


Fig.13-2 Dual screens + semi-reflecting mirror + polarising filters

(iii) It is also possible to use a single screen with a semi-reflecting mirror and polarising filters for stereoscopic viewing. As shown in Fig.13-3, this requires the two component images to be displayed simultaneously on the upper and lower halves of the screen (the upper image being inverted). Three-dimensional viewing is again achieved by the observers using polarising filters. Like solution (i), the availability of only half the screen is a disadvantage in terms of either coverage or resolution.

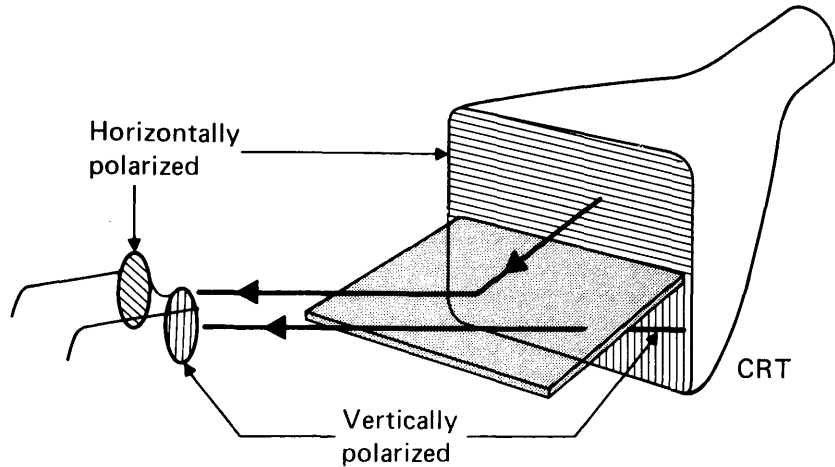


Fig.13-3a Single split-screen + semi-reflecting mirror + polarising filters (perspective view)

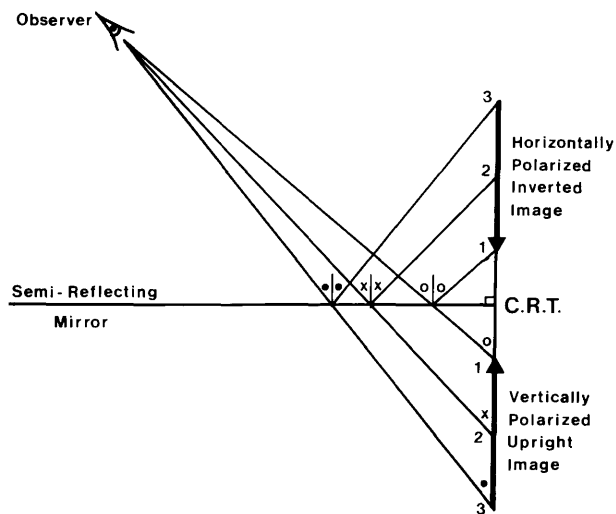


Fig.13-3b Single split-screen + semi-reflecting mirror (sectional diagram)

- (iv) Another solution familiar to photogrammetrists from optical projection stereo-plotting machines is the use of complementary (red/green) anaglyphic images. Applied to stereo-television, this requires the use of a single colour video monitor, in which the red gun displays the left hand image and the green, the right hand image. The operator views the screen with the familiar anaglyphic filters as shown in Fig.13-4.

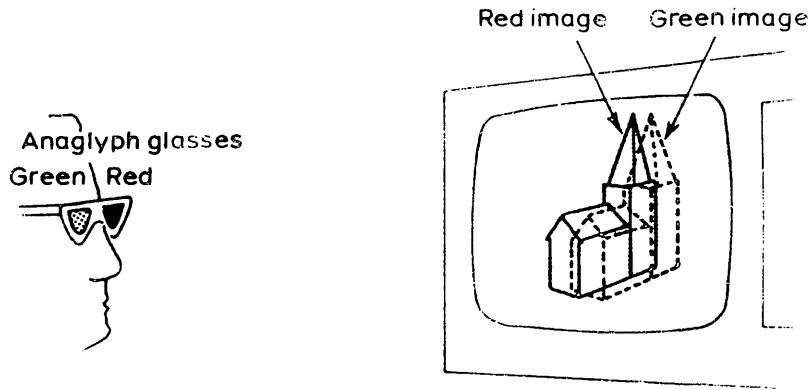


Fig.13-4 Use of anaglyphic system with single screen (colour monitor)

- (v) An alternative approach is that of the so-called "direction selective method" (Fig.13-5). The two component images are displayed as alternating vertical strips of information (image data) on the video monitor tube. A lenticular screen consisting of an array of cylindrical lenses directs left and right hand images to the left and right hand eyes of the observer.

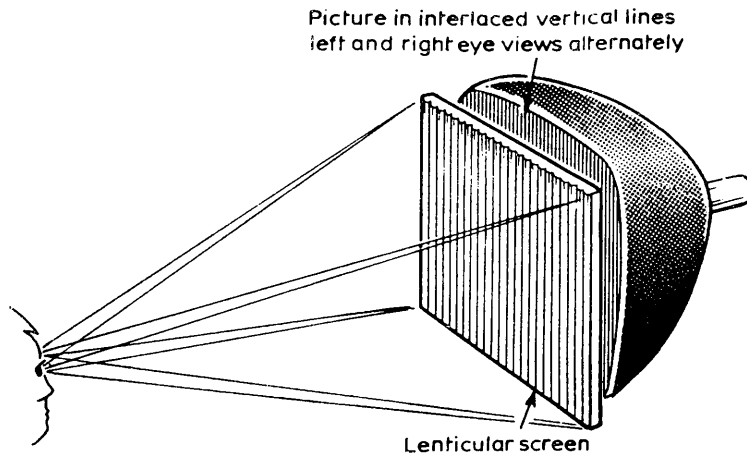


Fig.13-5 Single screen with lenticular screen

Suitable screens are being developed which will allow two perfectly matched pictures to be produced. While this solution gets rid of the need for spectacles, it is rather restrictive in terms of the observer's position and the resolution is reduced in the horizontal direction. These difficulties may be removed by the use of two projection television tubes rear-projecting the two images onto a dual lenticular screen with a diffusing layer sandwiched between them as shown in Fig.13-6.

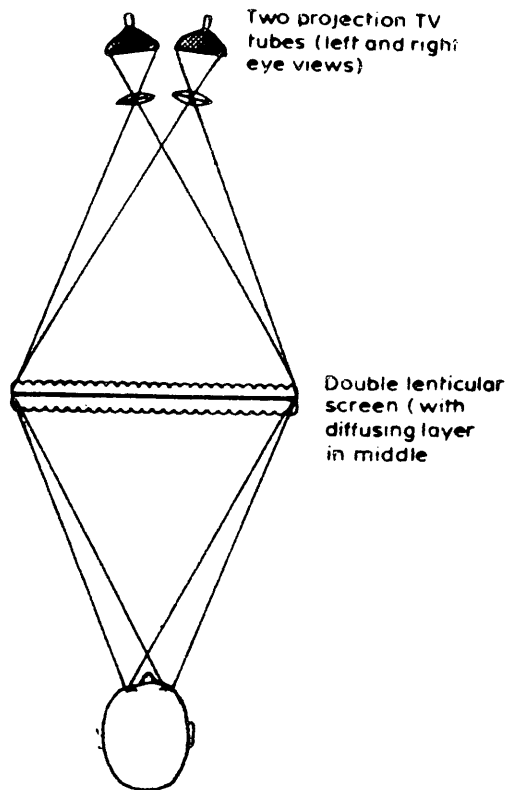


Fig.13-6 Two televisions rear projecting on to dual lenticular screens

- (vi) Finally another solution which is already known to photogrammetrists is to use alternating shutters. On the video monitor screen, the two component left and right hand images of the stereo-model are displayed at the video refresh rate (50 Hz). All the odd numbered fields display the left hand image and all the even numbered fields display the right hand image. Viewing is achieved by using spectacles equipped with high-speed electronic shutters employing lead lanthanum zirconate titanate (PLZT) ferro-electric ceramics which can switch their state (open or closed) in one millisecond (Figs.13-7,13-8)

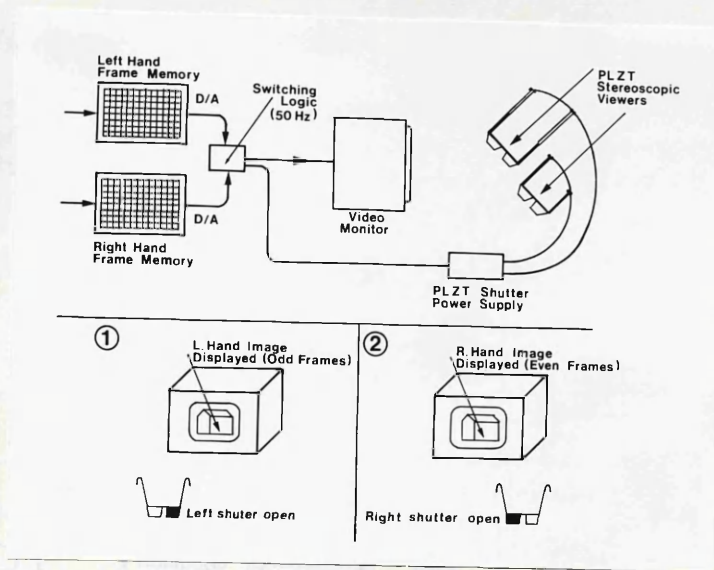


Fig.13-7 Use of PLZT Spectacles (alternating shutters)

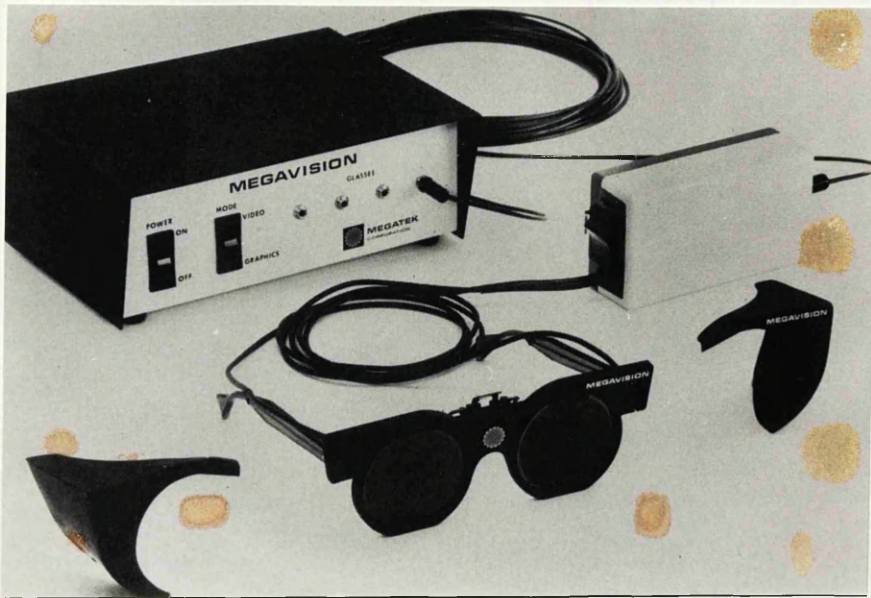


Fig.13-8 PLZT control unit and spectacles

Petrie also concluded that there is a particular merit to most of these systems in that they allow several observers to view the stereo-model simultaneously. The lack of expensive optical components and trains can only be an advantage also. These various possibilities discussed above offer the photogrammetric systems designers a wide choice of methods by which users may continue to employ stereoscopic viewing for both the measurement and interpretation of digital image data with all the advantages of the three-dimensional presentation.

## 13.2 Actual Implemented Procedure

The initial plan which was suggested to form a video stereocomparator was based on the use of a video stereocomparator. This is shown in Fig.13-9 and functions in the following way:-

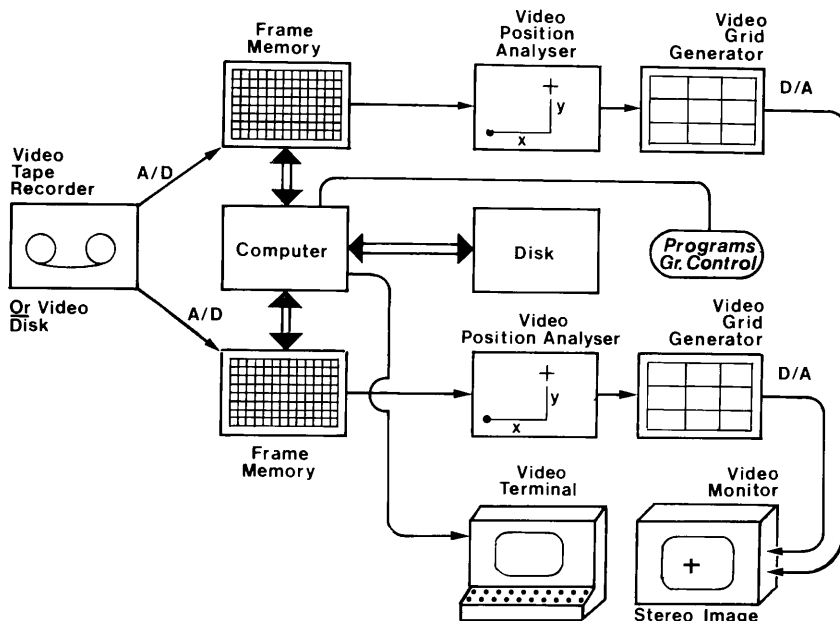


Fig.13-9 The video stereocomparator connected on-line to a computer

- (i) The video cassette tape containing the video images recorded during the aerial flight test is played back in the VTR.
- (ii) Two frame memories are used so that one contains the LH image, while the other contains the RH image of the stereopair.
- (iii) Image coordinate measurement is carried out in each image to provide the control points required for the rectification procedure. The coordinate measurement is carried out using two video position analysers, each coupled to one of the frame memories.
- (iv) The images which have been stored in the frame memories (now in digital form) are transferred to the computer together with the measured video image coordinates.

- (v) The rectification of the two images is carried out by first performing the space resection procedure to obtain the scanner's exterior orientation elements. Then a digital rectification of each image is carried out in the same manner as explained in the previous chapter.
- (vi) The two rectified images are then transferred back into the frame memories.
- (vii) The alternating shutters method described above (method vi) could be used to create the stereo-viewing on the video monitor screen.

However, some problems arose during the preliminary construction of the system. At the time when this project started, suitable video frame memories which could be directly interfaced to the computer were very expensive. A further difficulty was that the only supplier who responded to the request to supply an alternating shutters system was Megatek and their system was designed to be used only with their vector refresh graphics terminals. It was known from the literature that other suppliers exist, e.g. Honeywell in the United States, but no response was received from them. It is probable also that these systems are quite expensive to buy at the moment and will remain so until there is a wider demand.

Arising from the above difficulties, the initial plan had to be changed to implement the video monocoparator described in Chapter VI. The images were rectified as described in the previous chapter and then transferred to the Prime computer attached to a GEMS image processing system which was used to form the three-dimensional video model.

### 13.2.1 The GEMS Image Processing System

GEMS is a general purpose digital image processing system on which a software package (GEMSTONE) has been specially developed for remote sensing applications. This package system was developed in association with the National Remote Sensing Centre (NRSC), Farnborough. This system provides the user with a powerful set of image processing facilities. It allows any form of digital image data- raster or vector- to be handled and processed. The basic memory module is designed to hold a picture of up to 1,024x 1,024 x 8 bit for each primary colour, giving a full 24-bit image with 16,777,216 possible colours. A high resolution colour monitor displays the images which are controlled from the operator's console with its integral tracker ball and illuminated push buttons. The configuration of the system is shown in Fig.13-10.





Fig.13-10 The GEMS image processing system

### 13.2.2 Stereo-video Viewing using the GEMS System

The two digitally rectified images of the stereo model had been read into the Prime computer and were displayed first separately on the video monitor. The preliminary work was done on the GEMS system of the Environmental Remote Sensing Application Centre (ERSAC) in Livingston, while the actual procedure was carried out on another similar GEMS system located at the Macaulay Institute for Soil Research in Aberdeen. The following procedure was used:-

- (i) An extract was taken from each image which is the area of overlap between the two images.
- (ii) The two images were overlaid by identifying two common points in each image and registering the two images at these two points.
- (iii) The LH image was then projected onto the colour video monitor screen using the green gun while the RH image was similarly projected using the red gun. By viewing the model using anaglyphic spectacles, the model appeared in three-dimensions.
- (iv) Several photographs of the combined red/green image (shown in Section 4.3 at the end of this Chapter) were taken at different stages during this procedure using the Ramtek colour film camera attached to the GEMS system. The RGB video signals which are sent to the

video monitor are also directed to the Ramtek camera as shown in the block diagram of Fig.13-11. The camera is equipped with a small high resolution flat-screen CRT on which the image is displayed. By the use of appropriate filters and a suitable shutter, the red, green and blue components of the colour image are overlaid on the film via a lens which is located in front of the CRT, i.e., the film is held stationary and is exposed three successive times, once for each primary colour. When this process is completed, the film is then advanced to the next shot.

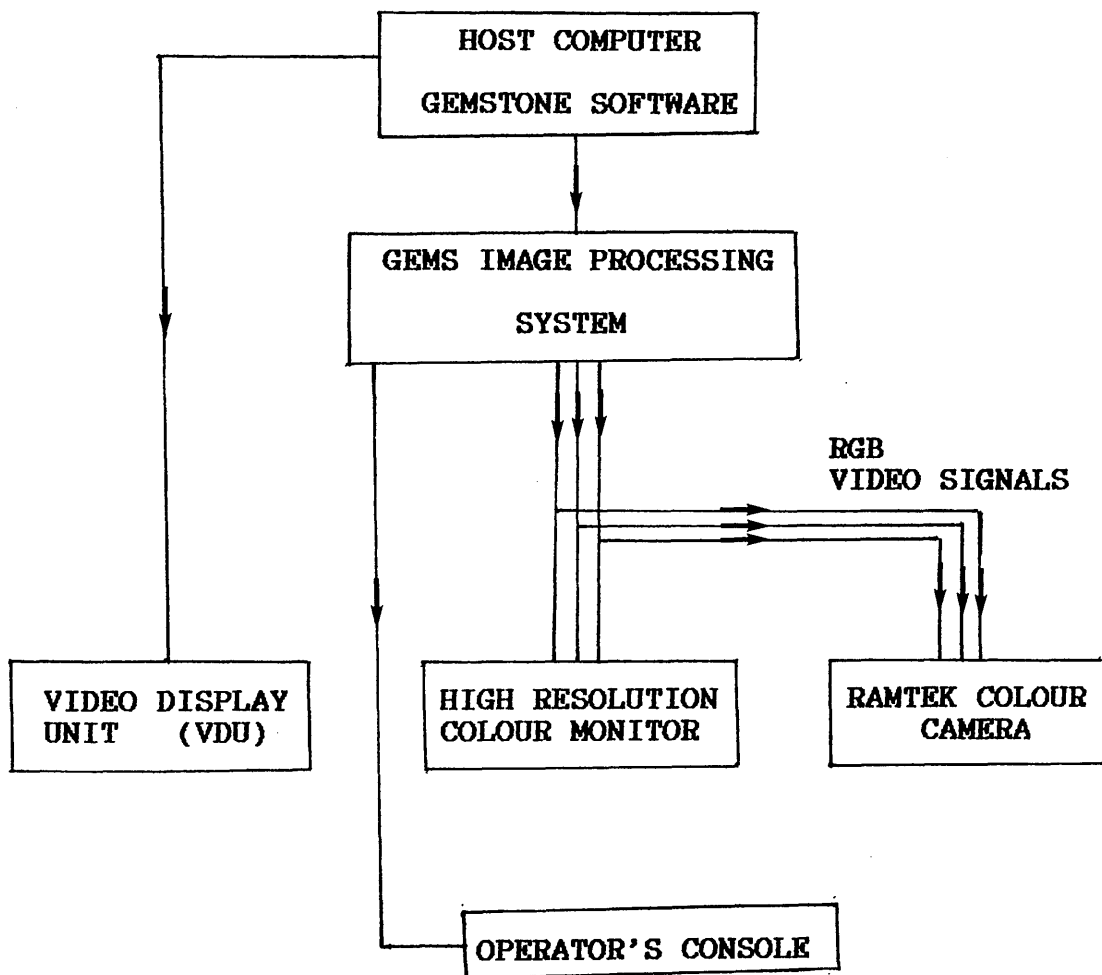


Fig.13-11 Configuration of the GEMS system and the Ramtek colour camera

### 13.3 Flexibility and Limitations

The method described above was very easy to implement especially with the GEMS image processing system with its powerful hardware and software which provided a great deal of flexibility to move the images across the video monitor screen and also to extract a particular part of the image and rotate or translate this part into a position appropriate to the needs of stereo-viewing. Also the relatively large storage of the system was very useful. The use of the anaglyphic technique to form the three-dimensional model was an adequate one since it allowed several viewers to see the stereo-model simultaneously.

In fact, the three-dimensional effect appeared very clearly. Since the area covered by the images was a residential one, the houses and other buildings appeared quite distinctly in three-dimensions. Also the shape of the topography of the area appeared clearly. In particular, the slope of the roads was a quite notable feature of the video stereo-model. It was soon realized that the observer must position himself at an appropriate distance (about 0.4 m) from the video monitor screen in order to be able to get the best impression of the video viewing.

Several attempts were made to improve the model by shifting the RH image relative to the LH image by intervals of 3, 6 and 12 pixels respectively. This is a similar procedure to that employed when a mirror stereoscope is used to observe two overlapping photographs where the two photographs are shifted along the photo-base to achieve the best stereo-viewing. The shifting of the RH image by 6 pixels appeared to give the best stereo-model.

However, it was not possible to make sure that the stereo-model was free from distortion. The only way to check this would be to carry out stereoscopic measurements on some well defined points in the model and compare the measured coordinates with their corresponding ground coordinates measured from an existing map for the area. Unfortunately this feature of stereoscopic measurement is not available in the GEMS system.

Nevertheless, the model appeared in three-dimensions which proved that the actual procedure and techniques which have been devised and used have been successful and quite practical and extremely useful when interpreting video frame scanner imagery for topographic mapping.

### 13.4 Photographs of the Video Stereo-Models

The figures below show a sample of the photographs of the video stereo-model taken using the Ramtek camera. Although the quality of the model which appeared on the video monitor was fairly good, the photographs below do not represent the same quality due to technical difficulties experienced during exposure. In fact several attempts have been made to improve the quality of the photographs but without success. Nevertheless, these photographs show the model in three-dimensions and give an idea about the work which has been done in this respect.

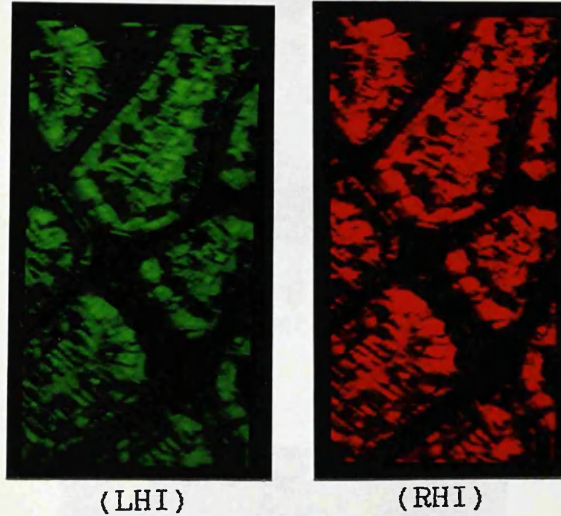


Fig.13-12 The two images of the steropair

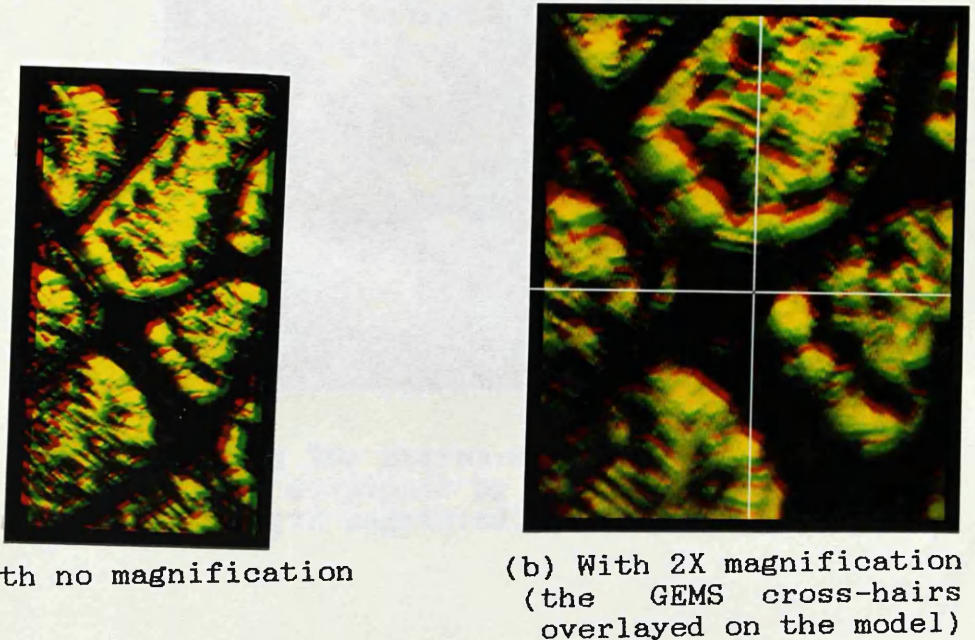


Fig.13-13 The stereo-model with no displacement

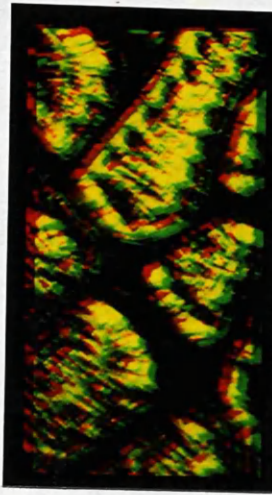


Fig.13-14 The stereo-model with  
the RHI displaced by 3-pixels

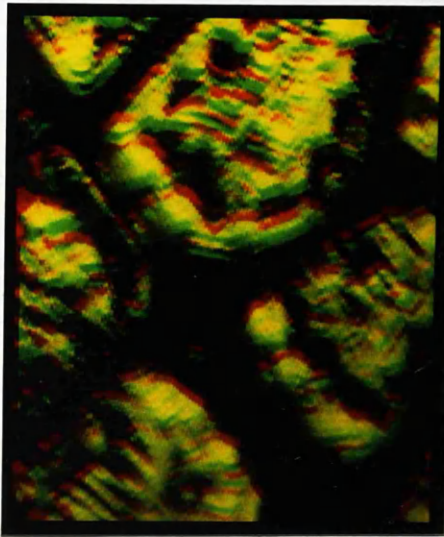


Fig.13-15 The stereo-model with  
the RHI displaced by 6-pixels  
(2X magnified)

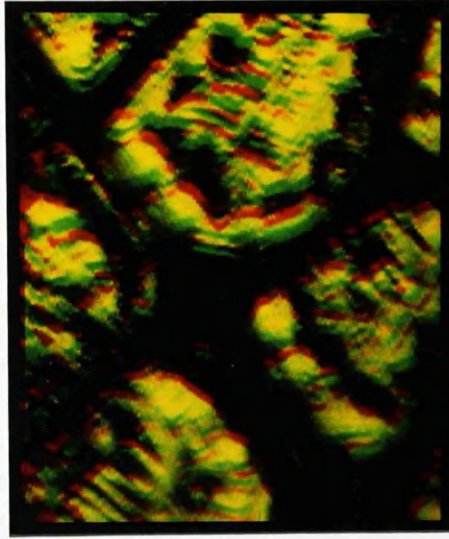


Fig.13-16 The stereo-model with  
the RHI displaced by 9-pixels  
(2X magnified)

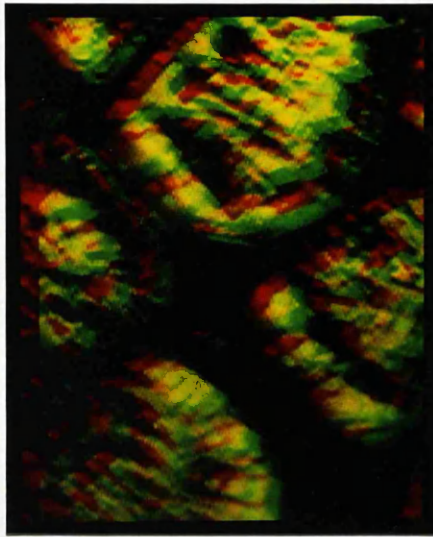


Fig.13-17 The stereo-model with  
the RHI displaced by 12-pixels  
(2X magnified)



## CHAPTER XIV

### CONCLUSIONS AND RECOMMENDATIONS

#### 14.1 General Conclusions

Since the results obtained during the various stages of the present project have been reported and analysed in the relevant Chapters, it is not necessary to repeat them in this concluding Chapter. However, it is quite appropriate to attempt to draw some general conclusions regarding the possibilities of carrying out topographic mapping operations using airborne video frame scanner imagery based on the research work carried out and the results obtained during the present project.

- (i) Thermal video frame scanners produce an image of relatively high quality but of relatively small format size since at present it is associated with broadcast television technology. However, although the image quality cannot be matched with a photogrammetric film camera image, it can be said that the frame scanner images are of superior quality in both radiometric and geometric terms as compared with those resulting from other remote sensing sensors such as the optical-mechanical line scanner. Certainly this is the case in terms of the production of images in the thermal infrared part of the electromagnetic spectrum.
- (ii) The geometric calibration of these scanners can be readily achieved to determine the magnitude and pattern of distortion existing in the frame scanner images as a result of the scanning geometry. The method which has been devised and used in the present project was very flexible. This method showed that the distortion pattern is highly systematic, mainly as a result of the displacement caused by the scanning technique. When the appropriate mathematical model was used to correct for this systematic pattern, the magnitude of distortion was reduced to less than 0.5 of a pixel and the plots of the residuals displayed a random pattern of distortion.
- (iii) The results from the calibration of four different frame scanners showed that all optical-mechanical frame scanners produce images which have the same



geometric characteristics, since basically they all use the same scanning technique in which two scanning elements scan the object in two directions to produce a spherical image surface. In this respect, two polynomial equations were formed to model the systematic distortion in frame scanner images and proved to be effective in removing this distortion. Furthermore, the results of the calibration showed that the geometric characteristics remained fairly stable over a considerable period of time e.g. over the period of an individual flight. Calibration over an extended period of time would be necessary to establish whether this stability occurred over a still longer period.

- (iv) The perspective geometry of the video frame scanners allowed the images to be processed analytically in the same way as photogrammetric camera images when an appropriate technique was used to account for the special characteristics e.g. the spherical image surface of the frame scanner images. Two different techniques have been used as described in Chapter VIII. These are the space resection with additional parameters and the point-by-point space resection. Both techniques were followed by a conventional space intersection procedure to produce the ground coordinates of the control and check points. The results showed that the use of conventional analytical photogrammetric procedures is quite appropriate to frame scanner imagery provided that a preliminary pre-processing of the measured image data takes place and is supplemented by the use of one or other of these techniques.
  
- (v) The results from the use of the additional parameters technique showed the best accuracy which could be obtained from this type of imagery. However, this accuracy falls substantially below that of conventional photographic images and is not compatible with the accuracy standards specified by the professional surveying companies or a national mapping agency such as the Ordnance Survey. However, the accuracy figures obtained from the geometric test are very satisfactory considering the lower resolution of the scanner and also the lower resolution of the devices used to measure the image coordinates of the control and check points.
  
- (vi) The comprehensive analysis carried out for the results of the geometric test showed that the residual errors in position and height are related to the model dimensions in much the same manner as

has previously been shown in ISP standard tests of photogrammetric frame photography.

- (vii) In spite of the various limitations noted above, it is indeed possible to extract metric and topographic information from video frame scanner imagery which can be used by a wide spectrum of users from military personnel through Earth scientists to topographic scientists.
  
- (viii) The flight planning required to provide the necessary image data using airborne thermal video frame scanners was found to be similar to that carried out for missions using a photogrammetric frame camera. Apart from the difficulties reported towards the end of Chapter IX which are mainly concerned with the use of a light aircraft which was not equipped with suitable tracking and navigation devices and the dependence on an inexperienced amateur pilot and navigator to conduct the aerial survey, the flight missions went very smoothly and no problems or difficulties were encountered during the flight missions. The use of an on-board portable video monitor greatly helped the scanner operator in adjusting the scanner's controls (i.e thermal sensitivity, focussing, etc) to achieve the best possible image quality and contrast. Also the immediate playback of the recorded images on the return of the crew from the flight mission was found to be very useful as in the case of the Hunterston area where the directions of the flight lines had to be changed and the imaging of this particular area needed to be repeated.
  
- (ix) The fast and easy image digitization is an important characteristic of video frame scanner imagery, especially in these days when efficient and relatively cheap image processing systems and frame memories allied to computers with large storage are coming into widespread use in the remote sensing field. The availability of this cheap hardware will help greatly in the geometric and radiometric processing of the video frame scanner images with a view to extracting metric, qualitative and quantitative information.
  
- (x) The possibility exists to create a three-dimensional video model if a suitable image processing system is available. The method which has been used in this project using the GEMS system was very simple and easy to implement. This 3-D effect will be very

useful in the interpretation side where the third dimension (height) may play an important role in providing a clue as to the identity of a particular feature in the image. On the other hand, due to the current lack of height measurement facilities (floating marks) in these systems, 3-D video viewing does not offer any advantages from the point of view of mapping applications. However, this difficulty must surely be very easy to overcome and if suitable measuring marks are incorporated in an image processing system, then the plotting of the planimetric detail, the measurement of spot heights and contours and the implementation of terrain modelling techniques would be natural applications of video frame scanner imagery.

- (xi) Finally, the results obtained from the comprehensive interpretation of the video frame scanner imagery were found to be very satisfactory. The ability of the scanner to detect small variations in temperature (MRTD = 0.17 C) within the object made the ground features show up very clearly in the images. In fact, the only limitation was the scanner's geometric resolution. It is obvious that the size of an object on the ground has to be greater than the size of the ground resolution of the scanner to be detected and identified on the image.

#### 14.2 Assessment of the Video Technique

The use of an all-video technology for image acquisition, image measurements and image display was found to be very simple and easy to implement. The use of the video technique for the image acquisition has provided an enormous amount of image data suitable for processing and analysis. This is a characteristic of the video imaging where the sensor produces continuous imaging in the form of a series of heavily overlapped successive frames. As has been shown by the present research, this allows the selection and implementation of optimised three-dimensional viewing of the terrain imaged by the scanner.

The video-based monocomparator which was specifically assembled and used in this project was an easy and cheap way of carrying out measurements on video images. Its only limitation was its low measuring accuracy (one pixel). However, since this was in fact matched to the relatively low resolution of the frame scanners, this proved to be a very adequate solution.

### 14.3 Recommendations for Future Work

Based on the difficulties or problems which arose during the various stages of the present project, the following points may be made regarding work which could be undertaken in the future:-

- (i) At present, there is an almost total lack of information concerning the interior orientation parameters of video frame scanner. If measurements or mapping from frame scanner imagery is to be contemplated on a regular basis, then it will be necessary to determine these parameters initially during the manufacture of the device and regularly on an operational basis thereafter. The incorporation of a single cross on the scanner optical axis appears to be a satisfactory solution to determine the position of the principal point. However, as mentioned in Chapter VI, these scanners do not have an image plane (as in the case of the film cameras) on which a register glass with a pattern of calibrated reseau marks could be fitted. Thus the only obvious solution to determine the scanner's focal length and geometric distortion would be the method which has been devised and used in this project. However, if the distance between the scanner and the calibration target plate can be measured more accurately using some kind of measuring device, this will have a significant effect on the accuracy of the computed focal length and hence in the overall accuracy obtained from a geometric test.
  
- (ii) The use of the Barr & Stroud IR-18 fitted with 1.5X telescope magnification provided a small field of view and hence a small base-to-height ratio in terms of stereo-coverage. This had a significant effect both on the stereo-viewing and on the accuracy obtained from this type of imagery. Any future researcher into this subject is recommended to use a scanner with the widest possible field of view. However, it must be noted that there is a trade-off between the field of view and the IFOV and hence the ground resolution. Since the number of lines per frame is limited to around 500, if broadcast television technology is used, the wider the field of view, the larger the IFOV, hence the poorer will be the ground resolution.
  
- (iii) Notwithstanding the advantages of using inexpensive, well understood and commonly available broadcast television technology in conjunction with video frame scanners, there are obvious advantages in using much

higher resolution such as would result from the employment of high definition television (HDTV) technology in association with video frame scanners. Indeed this would appear to be an obvious future development with enormous advantages to be gained in terms of either ground resolution or coverage and in terms of stereo-coverage and viewing.

- (iv) The lack of well-defined signalized points in the test field meant that the precision of measuring the ground coordinates of the check and control points in the present project was relatively low which had a significant effect on the accuracy obtained in the geometric test. In this context, it is recommended to establish a special test field consisting of an appropriate number of targets distributed over the area to be imaged. These targets should be made of a suitable thermal material (such as a black painted block of concrete). The size of the individual targets should be determined bearing in mind the ground resolution of most video frame scanners at the intended flying height.

#### 14.4 A Final Note

Ending this thesis in a final note, the author has greatly benefited from undertaking this research work in various ways. Before commencing this work, he had very limited experience in computing science. However, during the project he has been able to make full use of the extensive facilities available in the Department and in the Computing Service. While much use was made of relevant software in the form of existing packages, the author has also succeeded in writing several computer programs in two versatile languages- Fortran 77 and Algol 60 - during his research work. As a result, the techniques of devising suitable algorithms and of writing the appropriate computer programs to solve such algorithms have been thoroughly grasped.

Furthermore, the author had only a limited knowledge of and experience of analytical photogrammetric techniques prior to undertaking this project. This knowledge has been greatly enhanced and expanded as a result of the project described in this dissertation. This can only be beneficial since the photogrammetry of the future will be largely analytical in nature.

The field of remote sensing was also a relatively new area for the author. By the end of this work, he has become very familiar with the different aspects of remote sensing, in

particular with the geometrical aspects of the data acquisition systems which are commonly used in this field. It goes without saying the specific field of thermal frame scanners and the associated video technology and techniques were totally unknown to the author before undertaking this research. However, the execution of this research project has resulted in him gaining an insight into what must be an important field of remote sensing in the future.

Finally, the most important benefit which the author has gained from carrying out this project is that his ability to tackle the different problems which may arise during research work has been greatly enhanced. This will undoubtedly be of great benefit to the author's future career as a university lecturer.

## BIBLIOGRAPHY

Abraham, V., 1961 - "Relative Geometric Strength of Frame, Strip and Panoramic Cameras". Photogrammetric Engineering, Vol.27 , No.5, p755-766.

American Society of Photogrammetry, 1983, Manual of Remote Sensing, Second Edition, Volumes I and II.

Bauer, H. and Muller, J., 1972 - "Height Accuracy of Blocks and Bundle Adjustment with Additional Parameters". Presented Paper, Commission III, 12th Congress of the International Society of Photogrammetry, Ottawa.

Bernstein, R., 1975 - "Digital Image Processing". Photogrammetric Engineering and Remote Sensing, Vol.41, No.12, p1465-1476.

Borg, S., 1968 - "Thermal Imaging with Real Time Picture Presentation". Applied Optics, Vol.7, No.9, p1697-1703.

Brown, E., 1965 - " V/H Image Motion in Aerial Cameras". Photogrammetric Engineering, Vol.31, No.2, p308-323.

Brown, D., 1976 - " The Bundle Adjustment - Progress and Prospects". Invited Paper, Commission III, 13th Congress of the International Society of Photogrammetry, Helsinki.

Brunsveld, H. W., 1984 - "Contributions to Remote Sensing Applications of Thermal Infrared". Rijkswaterstaat. Communications, No.34.

Case, J., 1967 - "The Analytical Reduction of Panoramic and Strip Photography". Photogrammetria, Vol.22, p127-141.

Colvocoresses, A., 1970 - " ERTS-A Satellite Imagery". Photogrammetric Engineering, Vol.36, No.4, p555-560.

Crandon, C., 1985 - "Thermal Imaging Common Modules Class II (TICM II), High performance Thermal Imagers". Sira Course Notes, Introduction to Military Thermal Imaging, Sira Ltd., p8-1:8-39.

Cuthbertson, G. M., 1983 - "Thermal Imaging for Avionic Applications". Agardograph, No.272, p1:11.

Davis, W., 1978 - "Registration of Digital Images". 5th Canadian Symposium on Remote Sensing, p48-52.

Dean, R., 1982 - "Home Video". Newnes Technical Books, London.

- Derenyi, E. and Konecny, G., 1964 - "Geometry of Infrared Imagery". Canadian Surveyor, Vol.18, No.3, p279-290.
- Derenyi, E. and Konecny, G., 1966 - "Infrared Scan Geometry". Photogrammetric Engineering, Vol.32, No.5, p773-778.
- Derenyi, E., 1972 - "Geometric Considerations in Remote Sensing". 1st Canadian Symposium on Remote Sensing, p547-550.
- Derenyi, E., 1974 - "Planimetric Accuracy of Infrared line Scan Geometry". Canadian Surveyor, Vol.28, No.3, p247-254.
- Derenyi, E., 1974 - "Metric Evaluation of Radar and Infrared Imageries". 2nd Canadian Symposium on Remote Sensing, p643-647.
- Doyle, F. J., 1983 - "Film Cameras for the Space Shuttle". Proceedings of the Conference on Techniques of Extraction of Information from Remotely Sensed Images, American Society of Photogrammetry, p3-13.
- Ebner, H., 1976 - "A Mathematical Model for Digital Rectification of Remote Sensing Data". Presented Paper, Commission III, 13th Congress of the International Society of Photogrammetry, Helsinki.
- Ekin W. H., 1984 - "The Development of an Inexpensive Retractable Vertical Camera Rig for a Light Aircraft". Photogrammetric Record, Vol.11, No.63, p311-317.
- El Hassan, I. M., 1978 - "Metric Aspects of Reconnaissance Frame Photography". Ph.D Thesis, University of Glasgow. 403 pages.
- Elms, D., 1962 - "Mapping with a Strip Camera". Photogrammetric Engineering, Vol.28, No.3, p638-653.
- Forrest, R. B., 1974 - "Geometric Correction of Erts-1 MSS Images". Proceedings of the International Society of Photogrammetry, Commission III, Stuttgart.
- Gambino, L., 1974 - "Digital Mapping and Digital Image Processing". Photogrammetric Engineering, Vol.40, No.7, p1259-1264.
- Gordon, W., 1982 - "Video Techniques". Newnes Technical Books Inc., London.
- Harely, J. B., 1975 - "Ordnance Survey Maps" Southampton Ordnance Survey.
- Karizhenskiy, G., 1970 - "Scanning Systems for Thermal imaging Devices". Soviet Journal of Optical Technology, Vol.37, p600-603.



- Konecny, G. and Derenyi E., 1966 - "Geometrical Considerations for Mapping from Scan Imagery". 4th International Symposium on Remote Sensing of the Environment, p-327-338.
- Konecny, G., 1970 - "Metric Problems in Remote Sensing". ITC Series A, No.50, p152-177.
- Konecny, G., 1972 - "Geometrical Aspects of Remote Sensing". Invited Paper, Commission IV, 12th congress of the International Congress of Photogrammetry, Ottawa.
- Konecny, G., 1974 - "Approach and Status of Geometric Restitution for Remote Sensing Imagery". Proceedings of the International Society of Photogrammetry, Commission III, Stuttgart.
- Konecny, G., 1975 - "Analytical Relations for the Restitution of Dynamic Remote Sensing Imagery". Report Submitted to ERD-ETL Conference, University of Glasgow.
- Konecny, G., 1976 - "Mathematical Models and Procedures for the Geometric Restitution of Remote Sensing Imagery". Invited Paper, Commission III, 13th Congress of the International Society of Photogrammetry, Helsinki.
- Konecny, G., 1979 - "Methods and Possibilities for Digital Differential Rectification". Photogrammetric Engineering and Remote Sensing Vol.45, No.6, p727-734.
- Kratky, V., 1971 - "Precision Processing of ERTS Imagery". Technical Papers, 1971 Fall Convention, American Society of Photogrammetry, p481-489.
- Kratky, V., 1972 - "Photogrammetric Aspects of Precision Processing of ERTS-1 Images". 1st Canadian Symposium on Remote Sensing, p505-513.
- Kratky, V., 1974 - "Cartographic Accuracy of ERTS". Photogrammetric Engineering, Vol.40, No.2, p203-212.
- Kulikovskaya, N. I., 1970 - "Optical Characteristics of Thermal Infrared Scanning Systems". Soviet Journal of Optical Technology, Vol.37, p646-648.
- Lawson, W. D., 1984 - "Introduction to Thermal Imagers and Their Design". Sira Course Notes, Introduction to Military Thermal Imaging, Sira Ltd., p1-1: 1-9.
- Leberl, F., 1971 - "Metric Properties of Imagery Produced by Side-looking Airborne Radar and Infrared Line Scan Systems". ITC Series A, No.50, p125-151.

- Lillesand, T. and Kiefer, R., 1979 - "Remote Sensing and Image Interpretation". John Wiley and Sons, New York.
- Lindberg, P. J., 1966 - "A Prism Line Scanner for High Speed Thermography". Optica Acta, Vol.15, No.3 p305-316.
- Lloyd, J. M., 1975 - "Thermal Imaging Systems". Plenum Press
- Masry, S. and Gibbons, J., 1973 - "Distortion and Rectification of IR-Imagery". Photogrammetric Engineering, Vol.39, No.8, p845-849.
- Moffit, F. H. and Mikhail, E. M., 1980 - "Photogrammetry". Harper & Row Publishers, New York.
- Mohamed, M. A., 1981 - "Photogrammetric Analysis and Rectification of Landsat MSS and Seasat-SAR Imageries". Ph.D. Thesis, University College London.
- Moik, G. J., 1980 - "Digital Processing of Remotely Sensed Images". National Aeronautics and Space Administration (NASA), Publication No.SP-431, Washington, DC.
- Moller, G., 1964 - "Report of the International Experiment Rechenbach". Commission IV, 10th International Archives of Photogrammetry, Lisbon.
- Moller, G., 1968 - "Report of the Experiment Pecny". Commission IV, 11th International Congress of Photogrammetry, Lausanne.
- Money, S., 1981 - "Video". Newnes Technical Books, London.
- Petrie, G., 1970 - "Some Considerations Regarding Mapping from Earth Satellites". Photogrammetric Record, Vol.6, No.36, p590-624.
- Petrie, G., 1981 - "Hardware Aspects of Digital Mapping". Photogrammetric Engineering and Remote Sensing, Vol.47, No.3, p307-320.
- Petrie, G., 1983 - "The Philosophy of Digital and Analytical Photogrammetric Systems". Proceedings of the 39th Photogrammetric Week, University of Stuttgart, 27 pages.
- Petrie, G., Hsu, A. and Ali, A. E., 1984 - "Geometric Accuracy Testing of SAR-580 and Seasat-SAR Imagery". Investigators Final Report, The European SAR-580 Experiment, Vol.1, p71-101.
- Petrie, G., 1985 - "Remote Sensing and Topographic Mapping". Remote Sensing in Civil Engineering, Edited by T. Kennie and M. Matthews, Chapter 6, John Wiley and Sons, New York.

- Runciman, H. M., 1984 - "Theoretical Considerations in the Design of Thermal Imaging Systems". Sira Course Notes, Introduction to Military Thermal Imaging, Sira Ltd., p2-1:2-17.
- Sabins, F., 1967 - "IR- Imagery and Geologic Aspects". Photogrammetric Engineering, Vol.33, No.4, p743-750.
- Sabins, F., 1973 - "Flight Planning and Navigation for Thermal-IR Surveys". Photogrammetric Engineering, Vol.39 No.1, p49-58.
- Sabins, F., 1973 - "Recording and Processing Thermal IR Imagery". Photogrammetric Engineering, Vol.39, No.5, p839-844.
- Stark, E., 1975 - "The Effect Of Angular Field on Horizontal and Vertical Accuracy in Photogrammetric Plotting". Proceedings of the 35th Photogrammetric Week, Stuttgart.
- Sundstrom, E., 1968 - "Wide Angle Infrared Camera for Industry and Medicine". Applied Optics, Vol.7, No.9, p1763-1768.
- Taranik, J., 1978 - "Principles of Computer Processing of Landsat Data for Geologic Applications". U.S. Geological Survey, Departement of the Interior, Open File Report 78/117.
- Thurgood, J. and Mikhail, E., 1982 - "Photogrammetric Analysis of Digital Images". Technical Papers, 48th Annual Meeting, American Society of Photogrammetry, Denver, p295-304.
- Utz, P., 1980 - "Video Users Handbook". Prectice-Hall Inc., New Jersey.
- Waddle, E., 1966 - "Rotating Prism Design". Applied Optics, Vol.5, No.7, p1211-1223.
- Welch, R., 1975 - "Photogrammetric Image Evaluation Techniques". Photogrammetria, Vol.31, No.2, p161-190.
- Williams, T., 1975 - "Assesment of Materials, Components, and Systems for Use in Thermal Imaging". Optica Acta, Vol.22, No.4, p327-337.
- Wolf, P. R., 1983 - Elements of Photogrammetry, McGraw-Hill Book Co. Inc., New York.
- Wolfe, W. L., 1965 - "Handbook Of Military Infrared Technology". Office of Naval Research, Department of the Navy, Washington, D.C.

Wong, K. W., 1968 - "Geometric Calibration of Television Systems for Photogrammetric Applications". Civil Engineering Studies, Photogrammetry Series, No.16, Department of Civil Engineering, University of Illinois.

Wong, K. W., 1968 - "Photogrammetric Quality of Television Pictures". Civil Engineering Studies, Photogrammetry Series No.17. Department of Civil Engineering, University of Illinois.

Wong, K. W., 1970 - "Fidelity of Space TV". Photogrammetric Engineering, Vol.36, No.5, p491-497.

Wong, K. W., 1971 - "Television Display of Topographic Maps". Journal of the Surveying and Mapping Division, Proceedings of the American Society of Civil Engineering, November 1971, p273-281.

Wong, K. W., 1972 - "Geometric Analysis of the RBV Television System". Civil Engineering Studies, Photogrammetry Series, No.35, Department of Civil Engineering, University of Illinois.

Wong, K. W., 1975 - "Geometric and Cartographic Accuracy of ERTS-1 Imagery". Photogrammetric Engineering, Vol.41, No.3, p621-635.

**APPENDIX A**  
**DESCRIPTION OF THE COMPUTER PROGRAMS**

## Appendix A

### Description of the Computer Programs

In this Appendix, different computer programs which have been developed and used by the present author will be explained in detail. All the programs were developed in standard Fortran 77 to run in an interactive mode in the ICL 2988 mainframe computer of the University of Glasgow.

#### A.1 Program CON

This program was developed to perform linear conformal transformation in order to establish the magnitude and nature of the systematic and random distortions present in frame scanner imagery. The mathematical basis of the program has been discussed in Section 7.2.

##### A.1.1 Definition of Variables

N        Number of points whose calibrated and measured coordinates are known ( number of crosses).

$m_x$      r.m.s.e. in the x-direction.

$m_y$      r.m.s.e. in the y-direction.

$m_p$      r.m.s.e. in the vector direction.

##### A.1.2 Definition of Arrays

A        Coefficient matrix of transformation parameters.

AT       Transpose matrix of A.

AN       Inverse matrix of A.

COB     Matrix of measured image coordinates corrected for systematic distortion.

DX       Matrix of transformation parameters ( $a_0, b_0, a_1, a_2$ )

OB       Matrix of measured video image coordinates.

RE       Matrix of calibrated target plate coordinates.

- SV Matrix of systematic distortion in x,y at each image point.
- V Matrix of random distortion in x,y at each image point.

### A.1.3 Explanation of Program CON

The program is listed below. As can be seen in the listing, the program is broken up into a number of blocks to assist the explanation of the sequence of operations carried out by the program.

- Block 1. In this first block, the program name is defined and the arrays required for input data are dimensioned. The COMMON/BLOCK command has been used in order to reduce the required storage space in the computer during the running of the program.
- Block 2. In this block, the program asks for the total number of points and for the data file name. If a wrong data file name is given, the program will display an error message and gives the operator two alternatives - either to continue and give the correct file name, or to quit. The data file name should be arranged in (I4, 4F10.3) format, where I4 is the point number followed by the calibrated target plate coordinates x,y written in F10.3 each and finally, the measured video image coordinates  $x',y'$  written also in F10.3 each.
- Block 3. Least squares computations after which the residual errors at each image point are computed.
- Block 4. Transformation parameters for the first image are printed together with the residual errors at each point if required.
- Block 5. The program asks if this is the last image to be calibrated. If the answer is YES. the residual errors at the corresponding image points are added to these from the previous images and the mean (systematic) distortion is computed and printed. If the answer is NO, the residuals are added and the program starts again from Block 2.

- Block 6. The program asks if it is required to correct any image for systematic distortion and then compute the random distortion. If the answer is YES, the program proceeds to the next block. If the answer is NO, the program ends.
- Block 7. In this block, the program asks for the data file name, reads the calibrated and measured coordinates, and corrects these measured coordinates for the systematic distortion.
- Block 8. The least squares procedure is used to transform the calibrated coordinates into the image coordinate system. This time the corrected image coordinates are used for the transformation procedure. After the transformation, the residual errors at each image point are computed and printed.
- Block 9. In this block, the random distortion values for the image are printed out. Then the program asks if it is required to correct any other image for systematic distortion. If the answer is YES, the program starts again from Block 7. If the answer is NO, the program ends.
- Block 10. Contains the subroutines used for matrix operations. These are:-
- (1) **FORM** which is used to form the matrix of the coefficients of the unknown parameters;
  - (2) **MATINV** to perform matrix inversion;
  - (3) **MATVEC** to carry out the multiplication of a matrix array by a vector array;
  - (4) **MATMAT** to carry out the multiplication of two matrices;
  - (5) **MATSUB** to subtract two matrices from each other;
  - (6) **RMSE** to compute the root mean square error using the computed residuals at each image point; and
  - (7) **CORR** to correct the measured image coordinates of the video image for the systematic distortion.



#### A.1.4 Listing of Program CON

```
PROGRAM CON
PARAMETER(NR=260)
COMMON/BLOCK1/OB(NR, 2), RE(NR, 2), A(NR, NR), SF(NR)
DIMENSION AT(NR, NR), AN(NR, NR), ANT(NR, NR), F(NR),
*DX(NR), ADX(NR), V(NR), H(NR), NO(NR)
DIMENSION SUMV(NR), SV(NR), COB(NR, NR)
CHARACTER*32NAME1, NAME2
CHARACTER*1ANS
```

C ----- END OF BLOCK 1.

```
T=0.0
1 PRINT*, 'PLEASE ENTER THE NUMBER OF CONTROL POINTS'
  READ*, N
  DO 77, I=1, 2*N
77 SUMV(I)=0
145 PRINT*, 'PLEASE ENTER THE CONTROL POINTS FILE NAME'
  READ (5, 990)NAME1
  OPEN(3, FILE=NAME1, STATUS='OLD', FORM='FORMATTED', ERR=150)
  T=T+1
  GO TO 155
150 PRINT*, 'CAN NOT FIND THE CONTROL POINTS FILE '
  GO TO 145
155 DO 15, I=1, N
  READ(3, 1000)NO(I), RE(I, 2), RE(I, 1), OB(I, 2), OB(I, 1)
  15 CONTINUE
  CLOSE(UNIT=3)
```

C ----- END OF BLOCK 2.

```
CALL FORM(N)
CALL MATRAN(A, AT, 2*N, 4)
CALL MATMAT(AT, A, AN, 4, 2*N, 4)
CALL MATINV(AN, 4, ANT)
CALL MATVEC(AT, SF, F, 4, 2*N)
CALL MATVEC(ANT, F, DX, 4, 4)
CALL MATVEC(A, DX, H, 2*N, 4)
CALL MATSUB(H, SF, V, 2*N)
```

C ----- END OF BLOCK 3.

```
PRINT*, '*****'
WRITE(6, 700)T
700 FORMAT(/2X, 'TRANSFORMATION PARAMETERS FOR IMAGE NO.', F4.0)
  DO 60, I=1, 4
  PRINT*, DX(I)
60 CONTINUE
```

```

PRINT*, '*****'
PRINT*, 'DO YOU WANT TO PRINT THE SYSTEMATIC DISTORTION'
READ(5,255)ANS
IF(ANS.EQ.'N')GO TO 62
WRITE(6,710)T
710 FORMAT(/2X, '*RESIDUAL ERRORS FOR IMAGE NO.',F4.0, '**')
WRITE(6,280)
280 FORMAT(/3X, 'PT. NO. ', 2X, 'X', 9X, 'Y', 6X, 'DX', 7X, 'DY')
DO 70, I=1, 2*N, 2
J=I/2+1
70 WRITE(6,274) J,OB(J,1),OB(J,2),V(I),V(I+1)
62 CALL RMSE(V,N, RMSEX, RMSEY, RMSEP)
990 FORMAT(A32)
1000 FORMAT(I4, 4F10.3)
WRITE(6,357)
WRITE(6,377)RMSEX, RMSEY, RMSEP
357 FORMAT(/, '          MX          MY          MP')
377 FORMAT(/, 3F13.2)
DO 250, I=1, 2*N
250 SUMV(I)=SUMV(I)+V(I)
WRITE(6,144)
274 FORMAT(I4, 2F10.0, 2F8.2)

```

```

C
C ----- END OF BLOCK 4.
C

```

```

144 FORMAT(/, 'IS THIS THE LAST IMAGE ?')
READ(5,255)ANS
IF(ANS.EQ.'N') GO TO 145
DO 260, I=1, 2*N
260 SV(I)=SUMV(I)/T
WRITE (6,290)
290 FORMAT(/3X, '**SYSTEMATIC DISTORTION **')
WRITE(6,280)
DO 270, I=1, 2*N, 2
J=I/2+1
270 WRITE(6,274)J,OB(J,1),OB(J,2),SV(I),SV(I+1)
81 CALL RMSE(SV,N, RMSEX, RMSEY, RMSEP)
WRITE(6,357)
WRITE(6,377)RMSEX, RMSEY, RMSEP
275 FORMAT(3X, I3, 3X, F14.8, 3X, F14.8)
255 FORMAT(A1)

```

```

C
C ----- END OF BLOCK 5.
C

```

```

WRITE(6,156)
156 FORMAT(/, 'DO YOU WANT TO COMPUTE THE RANDOM DISTORTION
* FOR ANY * IMAGE ?')
READ(5,255)ANS
IF(ANS.EQ.'N') GO TO 999

```

```

C
C ----- END OF BLOCK 6.
C

```

```

66 PRINT*, 'PLEASE ENTER THE IMAGE FILE NAME'
   READ(5, 990)NAME2
   OPEN(9, FILE=NAME2, STATUS='OLD', FORM='FORMATTED', ERR=819)
   GO TO 820
819 PRINT*, ' CAN NOT FIND THE DATA FILE NAME'
   GO TO 66
820 DO 600, I=1, N
600 READ(9, 1000)NO(I), RE(I, 2), RE(I, 1), OB(I, 2), OB(I, 1)
   CALL CORR(OB, SV, COB, N)

```

C  
C  
C

----- END OF BLOCK 7.

```

CALL FORM(N)
CALL MATRAN(A, AT, 2*N, 4)
CALL MATMAT(AT, A, AN, 4, 2*N, 4)
CALL MATINV(AN, 4, ANT)
CALL MATVEC(AT, SF, F, 4, 2*N)
CALL MATVEC(ANT, F, DX, 4, 4)
CALL MATVEC(A, DX, H, 2*N, 4)
CALL MATSUB(H, SF, V, 2*N)

```

C  
C  
C

----- END OF BLOCK 8.

```

WRITE(6, 157)
157 FORMAT(/, 'DO YOU WANT TO PRINT THE RANDOM DISTORTION ?')
   READ(5, 255)ANS
   IF(ANS.EQ. 'N')GO TO 113
   PRINT*, ' **** RANDOM DISTORTION ****'
   WRITE(6, 280)
   DO 133, I=1, 2*N, 2
   J=I/2+1
   WRITE(6, 274)J, COB(J, 1), COB(J, 2), V(I), V(I+1)
133 CONTINUE
113 CALL RMSE(V, N, RMSEX, RMSEY, RMSEP)
   WRITE(6, 357)
   WRITE(6, 377)RMSEX, RMSEY, RMSEP
   PRINT*, 'DO YOU WANT TO CORRECT ANY OTHER IMAGE?(Y/N)'
   READ(5, 255)ANS
   IF(ANS.EQ. 'Y') GO TO 66
999 END

```

C  
C  
C

----- END OF BLOCK 9.

```

SUBROUTINE CORR(OB, SV, COB, N)
PARAMETER(NR=260)
DIMENSION OB(NR, 2), SV(NR), COB(NR, NR)
DO 700, I=1, 2*N, 2
J=I/2+1
COB(J, 1)=OB(J, 1)+SV(I)
700 COB(J, 2)=OB(J, 2)+SV(I+1)
RETURN
END

```

```

SUBROUTINE FORM(N)
C
PARAMETER(NR=260)
COMMON/BLOCK1/OB(NR, 2), RE(NR, 2), A(NR, NR), SF(NR)
DO 10, I=1, 2*N, 2
  J=I/2+1
  A(I, 1)=1
  A(I, 2)=RE(J, 1)
  A(I, 3)=-RE(J, 2)
  A(I, 4)=0
  A((I+1), 1)=0
  A((I+1), 2)=RE(J, 2)
  A((I+1), 3)=RE(J, 1)
  A((I+1), 4)=1.0
10 CONTINUE
DO 20, I=1, 2*N, 2
  J=I/2+1
  SF(I)=+OB(J, 1)
  SF(I+1)=+OB(J, 2)
20 CONTINUE
RETURN
END

```

```

C
SUBROUTINE MATINV(A, N, AINV)

```

```

C
PARAMETER (NR=260)
DIMENSIONA(NR, NR), AINV(NR, NR), B(NR, NR), X(NR, NR)
M=2*N
DO 600, I=1, N
DO 605, J=1, N
605 B(I, J)=A(I, J)
DO 600, J=N+1, M
IF((I+N).EQ.J)THEN
B(I, J)=1.
ELSE
B(I, J)=0.0
END IF
600 CONTINUE
DO 610, I=1, N
PIVOT=B(I, I)
DO 615, J=I+1, N
IF(ABS(PIVOT).LT.ABS(B(J, I))) THEN
DO 620, K=1, M
TT=B(I, K)
B(I, K)=B(J, K)
B(J, K)=TT
620 CONTINUE
PIVOT=B(J, I)
END IF
615 CONTINUE
DO 625, K=M, I, -1
625 B(I, K)=B(I, K)/B(I, I)

```

```

DO 630, J=I+1, N
DO 630, K=M, I, -1
B(J, K)=B(J, K)-B(I, K)*B(J, I)
630 CONTINUE
610 CONTINUE
DO 640, J=1, N
K=N+J
X(N, J)=B(N, K)
640 CONTINUE
DO 650, I=N-1, 1, -1
DO 655, J=1, N
M=N+J
X(I, J)=B(I, M)
655 CONTINUE
DO 660, K=N, I+1, -1
DO 660, J=1, N
X(I, J)=X(I, J)-B(I, K)*X(K, J)
660 CONTINUE
650 CONTINUE
DO 670, I=1, N
DO 670, J=1, N
670 AINV(I, J)=X(I, J)
RETURN
END

```

```

C
SUBROUTINE MATVEC(A, X, Z, N, M)

```

```

C
PARAMETER(NR=260)
DIMENSION A(NR, NR), X(NR), Z(NR)
INTEGER M, N, AN
DO 5, I=1, N
SUM=0.0
DO 5, J=1, M
SUM=SUM+A(I, J)*X(J)
5 Z(I)=SUM
RETURN
END

```

```

C
SUBROUTINE MATMAT(A, U, T, N, M, IP)

```

```

C
PARAMETER(NR=260)
DIMENSION A(NR, NR), U(NR, NR), T(NR, NR)
DO 10, J=1, N
DO 10, K=1, IP
T(J, K)=0.0
DO 10, I=1, M
T(J, K)=T(J, K)+A(J, I)*U(I, K)
10 CONTINUE
RETURN
END

```

```

C      SUBROUTINE MATRAN(A1, A1T, N, M)
C
C      PARAMETER(NR=260)
C      DIMENSION A1(NR, NR), A1T(NR, NR)
C      DO 11, I=1, N
C      DO 11, J=1, M
11  A1T(J, I)=A1(I, J)
C      RETURN
C      END
C
C      SUBROUTINE MATSUB(A, B, C, N)
C
C      PARAMETER(NR=260)
C      DIMENSION A(NR), B(NR), C(NR)
C      DO 95, I=1, N
95  C(I)=A(I)-B(I)
C      RETURN
C      END
C
C      SUBROUTINE RMSE(X, N, RMSEX, RMSEY, RMSEP)
C
C      PARAMETER(NR=260)
C      DIMENSION X(NR)
C      SUMXX=0.0
C      SUMYY=0.0
C      DO 900, I=1, 2*N, 2
C      SUMXX=SUMXX+X(I)**2
900  SUMYY=SUMYY+X(I+1)**2
C      RMSEX=SQRT(SUMXX/(N-1))
C      RMSEY=SQRT(SUMYY/(N-1))
C      RMSEP=SQRT(RMSEX**2+RMSEY**2)
C      RETURN
C      END
C
C      ----- END OF BLOCK 10.

```

### A.1.5 Sample Input Data for Program CON

The data below is for one frame and represents the target plate coordinates  $(x,y)$  measured by the Ferranti monocomparator and the video image coordinates  $(x^-,y^-)$  measured by the video monocomparator. However, the systematic distortion is computed for five frames while the random distortion is for this particular frame.

PT. NO.	x	y	$x^-$	$y^-$
1	-179.687	-135.564	-122.750	-112.250
2	-149.690	-135.429	-102.750	-111.750
3	-119.690	-135.379	-82.250	-111.250
4	-89.698	-135.284	-62.250	-111.250
5	-59.647	-135.096	-41.500	-111.250
6	-29.669	-135.011	-20.250	-110.500
7	0.313	-134.966	-0.250	-110.250
8	30.312	-134.896	20.250	-110.750
9	60.302	-134.854	40.750	-110.750
10	90.330	-134.667	61.250	-111.250
11	120.345	-134.599	81.750	-111.250
12	150.326	-134.512	101.750	-111.250
13	180.276	-134.482	121.750	-111.250
14	180.252	-104.492	121.750	-86.250
15	150.276	-104.548	101.750	-86.250
16	120.282	-104.627	81.750	-86.250
17	90.295	-104.691	61.750	-86.250
18	60.261	-104.858	40.750	-86.250
19	30.286	-104.894	20.250	-86.250
20	0.288	-104.990	0.250	-86.250
21	-29.707	-105.060	-21.250	-86.250
22	-59.677	-105.115	-41.750	-86.250
23	-89.716	-105.298	-62.250	-86.250
24	-119.722	-105.374	-82.750	-87.250
25	-149.687	-105.459	-103.250	-87.250
26	-179.696	-105.534	-123.250	-87.250
27	-179.837	-75.519	-123.750	-62.250
28	-149.798	-75.455	-103.750	-62.250
29	-119.803	-75.382	-83.250	-62.250
30	-89.846	-75.338	-62.750	-62.250
31	-59.764	-75.135	-42.250	-61.250
32	-29.777	-75.054	-21.250	-61.250
33	0.179	-74.988	-0.250	-61.250
34	30.180	-74.932	20.750	-61.250
35	60.224	-74.876	40.750	-61.500
36	90.211	-74.672	61.750	-61.750
37	120.187	-74.581	82.750	-61.750
38	150.174	-74.521	102.750	-62.000
39	180.148	-74.491	122.750	-62.250

40	180.074	-44.470	123.750	-37.250
41	150.124	-44.528	103.750	-36.750
42	120.143	-44.579	83.250	-36.750
43	90.156	-44.703	62.250	-37.250
44	60.120	-44.895	41.750	-37.250
45	30.130	-44.880	21.250	-37.250
46	0.133	-44.979	0.250	-37.250
47	-29.853	-45.041	-20.750	-37.250
48	-59.821	-45.097	-41.250	-37.250
49	-89.862	-45.335	-62.250	-37.250
50	-119.851	-45.381	-82.750	-37.250
51	-149.836	-45.462	-103.250	-37.250
52	-179.845	-45.519	-123.750	-37.250
53	-179.949	-15.531	-124.250	-12.750
54	-149.974	-15.446	-103.750	-12.750
55	-119.972	-15.384	-83.750	-12.250
56	-89.991	-15.331	-62.750	-12.250
57	-59.968	-15.106	-41.750	-12.250
58	-29.975	-15.040	-20.750	-12.250
59	0.018	-14.993	0.250	-12.250
60	30.004	-14.921	20.750	-12.250
61	60.010	-14.898	41.750	-12.250
62	90.025	-14.650	62.750	-12.250
63	119.968	-14.599	83.750	-12.250
64	149.966	-14.539	103.750	-12.000
65	179.946	-14.496	123.750	-12.250
66	179.911	15.534	123.750	12.750
67	149.932	15.467	103.250	12.750
68	119.950	15.413	83.250	12.750
69	89.964	15.333	62.250	12.750
70	59.933	15.197	42.000	12.750
71	29.991	15.127	20.750	12.750
72	-0.017	14.993	-0.250	12.250
73	-30.025	14.923	-20.750	12.750
74	-60.012	14.890	-41.750	12.750
75	-90.031	14.661	-62.750	12.750
76	-120.003	14.603	-83.750	11.750
77	-150.010	14.537	-103.750	11.750
78	-180.021	14.467	-124.750	11.750
79	-180.127	44.481	-124.250	36.750
80	-150.134	44.534	-104.250	36.750
81	-120.169	44.599	-83.250	36.750
82	-90.177	44.659	-62.750	36.750
83	-60.098	44.869	-41.750	36.750
84	-30.145	44.926	-21.250	37.250
85	-0.163	44.990	-0.250	37.750
86	29.833	45.087	20.750	37.750
87	59.812	45.083	41.250	37.750
88	89.857	45.348	62.250	37.750
89	119.825	45.364	82.750	37.750
90	149.796	45.409	102.750	37.750
91	179.749	45.503	123.250	37.750
92	179.734	75.482	122.750	63.750
93	149.765	75.399	102.750	62.750
94	119.771	75.408	82.750	62.750



95	89.793	75.345	62.250	62.750
96	59.786	75.124	41.250	62.750
97	29.765	75.051	20.750	62.500
98	-0.221	74.978	0.250	61.750
99	-30.220	74.917	-21.250	61.750
100	-60.214	74.845	-41.750	61.750
101	-90.226	74.630	-62.250	61.750
102	-120.217	74.576	-82.750	61.750
103	-150.216	74.507	-103.750	61.750
104	-180.201	74.435	-123.750	61.750
105	-180.324	104.434	-123.250	86.750
106	-150.329	104.499	-102.750	86.750
107	-120.333	104.583	-82.750	86.750
108	-90.300	104.600	-62.250	86.750
109	-60.309	104.838	-41.750	86.250
110	-30.357	104.905	-20.750	86.750
111	-0.385	104.960	-0.750	86.750
112	29.640	105.058	20.250	86.750
113	59.639	105.117	41.250	86.750
114	89.628	105.304	61.250	87.750
115	119.646	105.379	82.250	87.750
116	149.618	105.437	102.250	87.750
117	179.593	105.473	122.250	87.750
118	179.555	135.475	121.250	111.750
119	149.575	135.395	101.250	111.750
120	119.570	135.355	81.250	110.750
121	89.606	135.282	61.250	111.250
122	59.568	135.103	40.250	110.750
123	29.594	135.087	20.250	110.750
124	-0.414	134.963	-0.750	110.750
125	-30.390	134.896	-20.750	109.750
126	-60.407	134.824	-41.750	109.750
127	-90.407	134.623	-61.750	109.750
128	-120.381	134.559	-82.750	109.750
129	-150.399	134.484	-102.750	109.750
130	-180.374	134.415	-122.750	110.750

### A.1.6 Sample Output Data from Program CON

\*\*\*\* SYSTEMATIC DISTORTION \*\*\*\*

PT. NO.	x'	y'	dx	dy
1	-113.	-120.	11.91	-10.97
2	-112.	-100.	11.39	-9.04
3	-112.	-80.	11.31	-7.20
4	-111.	-59.	11.17	-5.67
5	-111.	-39.	11.29	-3.95
6	-111.	-18.	11.19	-2.78
7	-111.	3.	11.15	-1.05
8	-111.	23.	11.39	0.38
9	-111.	44.	11.50	1.81
10	-111.	64.	11.92	3.67
11	-111.	85.	12.26	5.51
12	-112.	104.	12.70	7.84
13	-112.	124.	12.91	9.74
14	-87.	124.	10.14	9.43
15	-87.	104.	10.01	7.32
16	-86.	84.	9.67	5.58
17	-86.	63.	9.54	3.86
18	-86.	42.	9.23	2.50
19	-86.	22.	9.32	1.08
20	-87.	1.	9.07	-0.26
21	-87.	-20.	8.94	-1.49
22	-87.	-41.	8.81	-2.70
23	-87.	-61.	8.69	-4.37
24	-87.	-82.	8.85	-6.01
25	-87.	-103.	8.91	-7.42
26	-88.	-123.	9.17	-9.56
27	-63.	-124.	6.32	-9.05
28	-63.	-103.	6.45	-7.28
29	-62.	-82.	6.38	-5.45
30	-62.	-62.	6.50	-4.05
31	-62.	-41.	6.33	-2.75
32	-62.	-20.	6.28	-1.52
33	-62.	1.	6.41	-0.32
34	-62.	21.	6.53	0.92
35	-62.	42.	6.71	2.59
36	-62.	63.	6.89	4.11
37	-62.	83.	7.14	5.53
38	-62.	103.	7.32	7.46
39	-62.	124.	7.47	9.47
40	-37.	124.	4.63	9.14
41	-37.	104.	4.30	7.04
42	-37.	84.	4.08	5.21
43	-37.	63.	4.20	3.89
44	-37.	42.	3.98	2.43

45	-37.	21.	3.91	1.20
46	-37.	1.	3.85	-0.14
47	-37.	-20.	3.72	-1.26
48	-37.	-41.	3.70	-2.68
49	-37.	-62.	3.64	-3.84
50	-38.	-83.	3.72	-5.47
51	-38.	-103.	3.58	-7.09
52	-38.	-124.	3.45	-8.94
53	-13.	-124.	0.88	-8.60
54	-13.	-103.	1.03	-7.18
55	-13.	-83.	0.86	-5.04
56	-13.	-62.	0.98	-3.92
57	-13.	-41.	1.23	-2.77
58	-12.	-21.	1.26	-1.24
59	-12.	0.	1.28	-0.11
60	-12.	21.	1.21	1.22
61	-12.	42.	1.31	2.46
62	-12.	63.	1.58	4.01
63	-12.	83.	1.70	5.50
64	-12.	104.	1.58	7.04
65	-12.	124.	1.74	9.16
66	13.	124.	-1.30	9.05
67	13.	103.	-1.23	7.43
68	13.	83.	-1.35	5.71
69	13.	62.	-1.30	4.08
70	13.	42.	-1.48	2.67
71	12.	21.	-1.32	1.43
72	12.	0.	-1.30	0.09
73	12.	-21.	-1.53	-1.16
74	12.	-42.	-1.64	-2.48
75	12.	-63.	-1.89	-3.53
76	12.	-83.	-1.42	-5.15
77	12.	-104.	-1.95	-6.69
78	12.	-124.	-1.88	-8.53
79	37.	-123.	-4.64	-9.00
80	37.	-103.	-4.52	-7.16
81	37.	-83.	-4.29	-5.45
82	37.	-62.	-4.16	-4.22
83	37.	-41.	-4.12	-3.03
84	37.	-21.	-4.09	-1.03
85	37.	0.	-4.16	0.09
86	37.	21.	-4.11	1.23
87	37.	42.	-4.03	2.65
88	37.	62.	-3.85	4.12
89	38.	83.	-4.15	5.83
90	38.	103.	-4.14	7.85
91	38.	123.	-3.99	9.95
92	63.	123.	-7.06	9.95
93	63.	103.	-7.01	7.84
94	63.	82.	-6.99	6.11
95	62.	62.	-6.62	4.29
96	62.	42.	-6.86	2.75
97	62.	21.	-6.95	1.49
98	62.	0.	-6.74	-0.13
99	62.	-21.	-6.76	-1.17

100	62.	-41.	-6.60	-2.80
101	61.	-62.	-6.74	-4.44
102	61.	-83.	-6.77	-5.87
103	61.	-103.	-6.90	-7.61
104	61.	-124.	-7.24	-9.33
105	86.	-124.	-9.90	-9.81
106	86.	-103.	-9.77	-7.97
107	86.	-83.	-9.62	-6.04
108	86.	-62.	-9.53	-4.58
109	86.	-42.	-9.17	-2.65
110	86.	-21.	-9.14	-1.45
111	86.	-1.	-9.01	0.06
112	86.	20.	-8.96	1.82
113	86.	41.	-9.03	2.95
114	86.	62.	-9.31	4.78
115	87.	82.	-9.37	6.63
116	87.	102.	-9.35	8.55
117	87.	122.	-9.64	10.67
118	111.	121.	-11.20	11.75
119	111.	101.	-11.34	9.43
120	111.	81.	-11.15	7.29
121	110.	61.	-10.79	5.28
122	110.	40.	-10.81	3.82
123	110.	20.	-10.70	1.70
124	109.	-1.	-10.67	0.56
125	109.	-21.	-10.41	-1.56
126	109.	-42.	-10.54	-2.81
127	109.	-62.	-10.68	-4.84
128	109.	-82.	-10.81	-6.56
129	109.	-103.	-10.94	-8.31
130	110.	-123.	-11.78	-10.43

\*\*\*\* RMSE (PIXEL) \*\*\*\*

mx	my	mp
5.80	7.50	9.48

\*\*\*\* RANDOM DISTORTION \*\*\*\*

PT. NO.	$\bar{x}$	$\bar{y}$	$d\bar{x}$	$d\bar{y}$
1	-100.	-134.	0.45	0.83
2	-100.	-112.	0.56	1.03
3	-100.	-89.	0.16	0.83
4	-100.	-68.	0.37	1.43
5	-100.	-45.	0.38	1.13
6	-99.	-23.	-0.21	0.83
7	-99.	-1.	-0.41	1.23
8	-99.	21.	-0.10	1.42
9	-99.	43.	-0.19	1.62
10	-99.	65.	0.01	1.42
11	-99.	87.	-0.28	1.22
12	-99.	110.	-0.67	1.02
13	-98.	131.	-0.86	1.22
14	-76.	131.	-0.97	1.51
15	-76.	109.	-0.87	1.51
16	-77.	87.	-0.58	1.11
17	-77.	66.	-0.49	0.72
18	-77.	43.	-0.29	0.92
19	-77.	21.	-0.40	0.72
20	-77.	0.	-0.21	-0.08
21	-77.	-23.	-0.12	0.52
22	-77.	-44.	-0.02	0.12
23	-78.	-67.	-0.03	0.12
24	-78.	-89.	0.76	0.12
25	-78.	-111.	0.66	-0.08
26	-78.	-133.	0.35	-0.08
27	-56.	-133.	0.35	-0.18
28	-56.	-111.	0.25	0.22
29	-56.	-89.	0.36	0.02
30	-56.	-67.	0.27	0.21
31	-55.	-45.	-0.42	0.61
32	-55.	-23.	-0.32	0.51
33	-55.	-1.	-0.41	0.41
34	-55.	22.	-0.50	0.31
35	-55.	43.	-0.40	0.81
36	-55.	66.	-0.19	0.41
37	-55.	88.	-0.38	0.11
38	-55.	110.	-0.27	0.31
39	-55.	132.	-0.17	0.40
40	-33.	133.	-0.17	-0.30
41	-32.	111.	-0.37	-0.30
42	-33.	88.	-0.18	-0.10
43	-33.	66.	0.11	0.10
44	-33.	44.	0.20	-0.10
45	-33.	22.	0.30	-0.50
46	-33.	0.	0.29	-0.30
47	-34.	-22.	0.38	-0.29
48	-34.	-44.	0.37	-0.49

49	-34.	-66.	0.27	-0.49
50	-34.	-88.	0.16	-0.49
51	-34.	-110.	0.25	-0.49
52	-34.	-133.	0.35	-0.29
53	-12.	-133.	0.55	-0.20
54	-12.	-111.	0.45	0.00
55	-11.	-89.	0.16	0.00
56	-11.	-67.	0.07	0.00
57	-11.	-45.	-0.03	0.00
58	-11.	-22.	-0.02	-0.40
59	-11.	0.	-0.01	-0.40
60	-11.	22.	0.10	-0.10
61	-11.	44.	0.00	-0.21
62	-11.	67.	-0.09	-0.61
63	-11.	89.	-0.18	-1.01
64	-10.	111.	-0.28	-0.41
65	-11.	133.	-0.17	-0.41
66	11.	133.	0.03	-0.32
67	12.	111.	-0.08	-0.32
68	11.	89.	0.02	-0.71
69	11.	66.	-0.09	-0.21
70	11.	45.	0.00	-0.71
71	11.	22.	-0.21	-0.31
72	11.	0.	0.19	-0.11
73	11.	-22.	-0.12	-0.51
74	11.	-44.	-0.03	-0.31
75	11.	-66.	0.07	-0.41
76	10.	-89.	0.56	0.09
77	10.	-110.	1.05	-0.51
78	10.	-133.	0.94	0.20
79	32.	-133.	0.84	0.09
80	32.	-111.	0.75	0.39
81	32.	-89.	0.56	-0.21
82	33.	-67.	0.46	0.19
83	33.	-45.	0.57	0.18
84	33.	-22.	0.08	-0.22
85	34.	0.	-0.31	-0.22
86	34.	22.	-0.31	-0.22
87	34.	44.	-0.40	-0.02
88	34.	66.	-0.39	-0.32
89	34.	89.	-0.09	-0.42
90	34.	111.	-0.08	-0.32
91	34.	133.	-0.17	-0.82
92	57.	133.	-0.97	-0.33
93	56.	111.	-0.08	-0.33
94	56.	89.	-0.09	-0.73
95	56.	67.	-0.49	-0.53
96	56.	44.	-0.40	-0.13
97	56.	22.	-0.11	-0.53
98	55.	0.	0.39	-0.52
99	55.	-22.	0.38	-0.12
100	55.	-45.	0.17	-0.12
101	55.	-67.	0.16	-0.12
102	55.	-89.	0.16	-0.32
103	55.	-111.	0.25	0.28

104	55.	-133.	0.54	-0.12
105	77.	-133.	0.34	-0.23
106	77.	-111.	0.25	-0.43
107	77.	-89.	0.16	-0.23
108	77.	-67.	0.06	-0.03
109	77.	-44.	0.37	-0.33
110	78.	-22.	-0.12	-0.43
111	78.	-1.	-0.22	0.17
112	78.	22.	-0.21	-0.43
113	78.	44.	-0.10	-0.43
114	78.	66.	-0.69	-0.14
115	78.	89.	-0.59	-0.84
116	78.	111.	-0.58	-0.64
117	78.	133.	-0.27	-0.64
118	101.	133.	-0.57	-0.75
119	100.	111.	-0.48	-0.54
120	100.	89.	0.31	-0.54
121	100.	67.	-0.60	-0.64
122	100.	44.	-0.20	-0.34
123	100.	22.	-0.31	-0.34
124	100.	0.	-0.42	-0.34
125	99.	-22.	0.28	-0.34
126	99.	-45.	0.37	-0.24
127	99.	-67.	0.36	-0.34
128	99.	-89.	0.45	0.26
129	99.	-111.	0.55	-0.13
130	99.	-133.	0.34	-0.13

\*\*\*\*\* RMSE (PIXEL) \*\*\*\*\*

mx	my	mp
0.28	0.31	0.41

## A.2 Program POLY25

This program was written and used to perform a polynomial transformation for any number of points using a 25-term polynomial equation in such a manner that the user can specify any number of terms between 3 and 25 to be used in each individual run. However, another version of the program was modified to use a continuous DO-LOOP to use all the possible number of terms starting with the simple 3-term (6-unknowns) affine transformation and increasing one term at a time up to the full 25-term (50-unknown) polynomial transformation. Thus the program can carry out all the possible transformation equations discussed in Section 7.1.2.

### A.2.1 Definition of Variables

- NR is the maximum possible number of points which may be used in this program. This is limited only by the storage capacity defined by the operating system.
- N is the number of points used in each individual run.
- NTERM is the number of polynomial terms to be used in a specific run of the program.
- $m_x$  r.m.s.e. in the x-direction.
- $m_y$  r.m.s.e. in the y-direction.
- $m_p$  r.m.s.e. in the vector direction.

### A.2.2 Definition of Arrays

- A Coefficient matrix of transformation parameters.
- AT Transpose matrix of A.
- AN Inverse matrix of A.
- COB Matrix of measured image coordinates corrected for systematic distortion.
- DX Vector of transformation parameters. The number of parameters depends on the specified number of terms.
- OB Matrix of measured video image coordinates.
- RE Matrix of calibrated target plate coordinates.



- SV Matrix of systematic distortion in x,y at each image point.
- V Matrix of random distortion in x,y at each image point.

### A.2.3 Detailed Description of Program POLY25

Once again, the listing of the program below has been divided into a number of blocks to facilitate the explanation of the program.

- Block 1. In this first block, the name of the program is defined and the arrays which are to be used are dimensioned.
- Block 2. The name of the file containing the calibrated and measured coordinates is given. The program opens the file and reads the data in (I4, 4F10.3) format.
- Block 3. The number of terms to be used in this particular run is defined and read in this block.
- Block 4. In this block, the least squares procedure is used by calling a sequence of subroutines for matrix operations.
- Block 5. The transformation parameters are printed out.
- Block 6. The distortion values in x,y are printed if required, followed by the r.m.s.e. in x,y and p. There is also the possibility of creating a special plotting file for the input of the residuals which can be used later for vector plots.
- Block 7. The systematic distortion of the system is computed which is the mean distortion value at each image point determined from every frame.
- Block 8. The program asks the user if he requires to correct any image points for the computed systematic distortion with a view to computing the magnitude of the random distortion at each point in a particular frame. If the answer is YES, the program proceeds to correct the measured image coordinates of the specified frame and uses these corrected coordinates to perform another least squares procedure by calling a number of subroutines for matrix operations.

- Block 9. The random distortion at each image point is printed followed by the r.m.s.e. in x,y and p.
- Block 10. In this block, there is the option of:-
- (i) correcting any other image for systematic distortion and computing the random distortion in which case the program starts again from Block 6;
  - (ii) starting the whole calibration procedure from the beginning, in which case the program starts from block 2; or
  - (iii) the program ends.
- Block 11. The same matrix operations listed above for program CON are used in this block.

#### A.2.4 Listing of Program POLY25

```
PROGRAM POLY25
PARAMETER(NR=300)
DIMENSION OB(NR, 2), RE(NR, 2), A(NR, 50), SF(NR),
*AT(NR, NR), AN(NR, NR), ANT(NR, NR), F(NR),
*DX(NR), ADX(NR), V(NR), H(NR), NO(NR)
DIMENSION SUMV(NR), SV(NR), COB(NR, NR)
CHARACTER*32NAME1, NAME2
CHARACTER*1ANS
```

C ----- END OF BLOCK 1.

```
T=0.0
1 PRINT*, 'PLEASE ENTER THE NUMBER OF CONTROL POINTS'
  READ*, N
  DO 77, I=1, 2*N
77 SUMV(I)=0
145 PRINT*, 'PLEASE ENTER THE CONTROL POINTS FILE NAME'
  READ (5, 990)NAME1
  OPEN(3, FILE=NAME1, STATUS='OLD', FORM='FORMATTED', ERR=150)
  T=T+1
  GO TO 155
150 PRINT*, 'CAN NOT FIND THE CONTROL POINTS FILE '
  GO TO 145
155 DO 15, I=1, N
  READ(3, 1000)NO(I), RE(I, 1), RE(I, 2), OB(I, 1), OB(I, 2)
15 CONTINUE
  CLOSE(UNIT=3)
```

C ----- END OF BLOCK 2.

```
PRINT*, 'THE PROGRAM USES 25 TERM POLYNOMIAL'
PRINT*, 'HOW MANY TERMS DO YOU WANT TO USE?'
READ*, NTERM
```

C ----- END OF BLOCK 3.

```
CALLFORM20(RE, A, N, OB, SF, NTERM)
CALL MATRAN(A, AT, 2*N, 2*NTERM)
CALL MATMAT(AT, A, AN, 2*NTERM, 2*N, 2*NTERM)
CALL MATINV(AN, 2*NTERM, ANT)
CALL MATVEC(AT, SF, F, 2*NTERM, 2*N)
CALL MATVEC(ANT, F, DX, 2*NTERM, 2*NTERM)
CALL MATVEC(A, DX, H, 2*N, 2*NTERM)
CALL MATSUB(H, SF, V, 2*N)
```

C ----- END OF BLOCK 4.

```

C      PRINT*, '*****'
      WRITE(6,700)T
700  FORMAT(/, ' TRANSFORMATION PARAMETERS FOR IMAGE
      * NO. ', F4.0)
      DO 60, I=1, NTERM
      WRITE(6,776)DX(I), DX(NTERM+I)
      60  CONTINUE
776  FORMAT(2F12.6)
      PRINT*, '*****'

C
C      ----- END OF BLOCK 5
C
      PRINT*, 'DO YOU WANT TO PRINT THE SYSTEMATIC DISTORTION
      * VALUES'
      READ(5,255)ANS
      IF(ANS.EQ.'N') GO TO 62
      WRITE(6,710)T
710  FORMAT(/2X, '**SYSTEMATIC DISTORTION FOR IMAGE
      * NO. ', F4.0, ' **')
      WRITE(6,280)
280  FORMAT(/3X, 'PT.NO. ', 6X, 'OX', 16X, 'OY')
      DO 70, I=1, 2*N, 2
      J=I/2+1
      70  WRITE(6,274)J, OB(J,1), OB(J,2), V(I), V(I+1)
      62  PRINT*, 'DO YOU WANT TO CREATE A PLOTTING FILE FOR THIS
      *IMAGE'
      READ(5,255)ANS
      IF (ANS.EQ.'Y') THEN
      PRINT*, 'INPUT THE PLOTTING FILE NAME'
      READ(5,990)NAME1
      OPEN(1, FILE=NAME1, FORM='FORMATTED', STATUS='NEW')
      DO 877, I=1, 2*N, 2
      J=I/2+1
      877  WRITE(1,274)J, OB(J,1), OB(J,2), V(I), V(I+1)
      END IF
      CLOSE(UNIT=1)
      CALL RMSE(V, N, RMSEX, RMSEY)
      WRITE(6,357)RMSEX
      WRITE(6,377)RMSEY
      357  FORMAT(/, 'ROOT MEAN SQUARE ERROR IN X DIRECTION=', F6.2)
      377  FORMAT(/, 'ROOT MEAN SQUARE ERROR IN Y DIRECTION=', F6.2)
      990  FORMAT(A32)
1000  FORMAT(I4, 4F10.3)

C
C      ----- END OF BLOCK 6.
C
      DO 250, I=1, 2*N
      250  SUMV(I)=SUMV(I)+V(I)
      PRINT*, 'DO YOU WANT TO CONTINUE'
      READ(5,255)ANS
      IF(ANS.EQ.'N') GO TO 999
      PRINT*, 'IS THIS THE LAST IMAGE ?'

```

```

      READ(5,255)ANS
      IF(ANS.EQ.'N') GO TO 145
      DO 260, I=1, 2*N
260  SV(I)=SUMV(I)/T
      WRITE (6,290)
290  FORMAT(/3X, '***SYSTEMATIC DISTORTION ***')
      WRITE(6,280)
      DO 270, I=1, 2*N, 2
      J=I/2+1
270  WRITE(6,274)NO(J),OB(J,1),OB(J,2),SV(I),SV(I+1)
C    PRINT*, 'PLEASE INPUT THE PLOTTING FILE NAME'
      READ(5,255)NAME1
      OPEN(3, FILE=NAME1, STATUS='NEW', FORM='FORMATTED')
      DO 456, I=1, 2*N, 2
      J=I/2+1
C 456 WRITE(3,274)NO(J),OB(J,1),OB(J,2),SV(I),SV(I+1)
      CLOSE(UNIT=3)
      CALL RMSE(SV,N, RMSEX, RMSEY)
      WRITE(6,357)RMSEX
      WRITE(6,377)RMSEY
274  FORMAT(I4,2F10.3,2F8.2)
275  FORMAT(3X,I3,3X,F14.8,3X,F14.8)
255  FORMAT(A1)
C
C ----- END OF BLOCK 7.
C
      PRINT*, 'DO YOU WANT TO CORRECT ANY IMAGE FOR SYSTEMATIC
*DISTORTION AND THEN COMPUTE THE RANDOM DISTORTION?(Y/N)'
      READ(5,255)ANS
      IF(ANS.EQ.'N') GO TO 8
66  PRINT*, 'PLEASE ENTER THE IMAGE FILE NAME'
      READ(5,990)NAME2
      OPEN(9, FILE=NAME2, STATUS='OLD', FORM='FORMATTED', ERR=819)
      GO TO 820
819 PRINT*, ' CAN NOT FIND THE DATA FILE NAME'
      GO TO 66
820 DO 600, I=1, N
600 READ(9,1000)NO(I),RE(I,2),RE(I,1),OB(I,2),OB(I,1)
      CALL CORR(OB,SV,COB,N)
      CALL FORM20(RE,A,N,COB,SF,NTERM)
      CALL MATRAN(A,AT,2*N,2*NTERM)
      CALL MATMAT(AT,A,AN,2*NTERM,2*N,2*NTERM)
      CALL MATINV(AN,2*NTERM,ANT)
      CALL MATVEC(AT,SF,F,2*NTERM,2*N)
      CALL MATVEC(ANT,F,DX,2*NTERM,2*NTERM)
      CALL MATVEC(A,DX,H,2*N,2*NTERM)
      CALL MATSUB(H,SF,V,2*N)
C
C -----END OF BLOCK 8.
C
      PRINT*, ' **** RANDOM DISTORTION ****'
      PRINT*, 'DO YOU WANT TO PRINT THE RANDOM DISTORTION
*VALUES?'

```

```

READ(5,255)ANS
IF(ANS.EQ.'N')GO TO 117
WRITE(6,280)
CLOSE(UNIT=9)
DO 133,I=1,2*N,2
J=I/2+1
WRITE(6,274) NO(J),OB(J,1),OB(J,2),V(I),V(I+1)
133 CONTINUE
117 CALL RMSE(V,N, RMSEX, RMSEY)
WRITE(6,357)RMSEX
WRITE(6,377)RMSEY

```

```

C
C ----- END OF BLOCK 9.
C

```

```

PRINT*, 'DO YOU WANT TO CORRECT ANY OTHER IMAGE?(Y/N)'
READ(5,255)ANS
IF(ANS.EQ.'Y') GO TO 66
8 PRINT*, 'DO YOU WANT TO START AGAIN?(Y/N)'
READ(5,255)ANS
IF(ANS.EQ.'Y') GO TO 1
999 END

```

```

C
C ----- END OF BLOCK 10.
C

```

```

SUBROUTINE CORR(OB, SV, COB, N)
PARAMETER(NR=300)
DIMENSION OB(NR,2), SV(NR), COB(NR,NR)
DO 700,I=1,2*N,2
J=I/2+1
COB(J,1)=OB(J,1)-SV(I)
700 COB(J,2)=OB(J,2)-SV(I+1)
RETURN
END

```

```

C
SUBROUTINE FORM20(RE, BT, N, OB, SF, NTERM)
C

```

```

PARAMETER(NR=300)
DIMENSION BT(NR,NR), OB(NR,2), SF(NR), A(NR,50), RE(NR,2)
DO 10,I=1,2*N,2
K=I/2+1
X=RE(K,1)
Y=RE(K,2)
A(I,1)=1.
A(I,2)=X
A(I,3)=Y
A(I,4)=X*Y
A(I,5)=X**2
A(I,6)=Y**2
A(I,7)=(X**2)*Y
A(I,8)=X*(Y**2)
A(I,9)=X**2*Y**2
A(I,10)=X**3
A(I,11)=Y**3

```

```

A(I,12)=X**3*Y
A(I,13)=Y**3*X
A(I,14)=X**3*Y**2
A(I,15)=X**2*Y**3
A(I,16)=X**3*Y**3
A(I,17)=X**4
A(I,18)=Y**4
A(I,19)=X**4*Y
A(I,20)=X*Y**4
A(I,21)=X**4*Y**2
A(I,22)=X**2*Y**4
A(I,23)=X**4*Y**3
A(I,24)=X**3*Y**4
A(I,25)=X**4*Y**4
DO 15,J=26,50
15 A(I,J)=0.0
DO 20,J=1,25
A((I+1),J)=0.0
20 CONTINUE
DO 10,L=26,50
J=L-25
A((I+1),L)=A(I,J)
10 CONTINUE
DO 35,I=1,2*N,2
J=I/2+1
SF(I)=OB(J,1)
SF(I+1)=OB(J,2)
35 CONTINUE
DO 50,I=1,2*N
DO 50,J=1,NTERM
BT(I,J)=A(I,J)
50 CONTINUE
DO 60,I=1,2*N
DO 60,J=26,(25+NTERM)
M=J-25+NTERM
BT(I,M)=A(I,J)
60 CONTINUE
RETURN
END

```

C

```
SUBROUTINE MATVEC(A,X,Z,N,M)
```

C

```

PARAMETER(NR=300)
DIMENSION A(NR,NR),X(NR),Z(NR)
INTEGER M,N,AN
DO 5,I=1,N
SUM=0.0
DO 5,J=1,M
SUM=SUM+A(I,J)*X(J)
5 Z(I)=SUM
RETURN
END

```

```

SUBROUTINE MATMAT(A, U, T, N, M, IP)
C
PARAMETER(NR=300)
DIMENSION A(NR, NR), U(NR, NR), T(NR, NR)
DO 10, J=1, N
DO 10, K=1, IP
T(J, K)=0.0
DO 10, I=1, M
T(J, K)=T(J, K)+A(J, I)*U(I, K)
10 CONTINUE
RETURN
END

```

```

C
SUBROUTINE MATRAN(A1, A1T, N, M)
C
PARAMETER(NR=300)
DIMENSION A1(NR, NR), A1T(NR, NR)
DO 11, I=1, N
DO 11, J=1, M
11 A1T(J, I)=A1(I, J)
RETURN
END

```

```

C
SUBROUTINE MATSUB(A, B, C, N)
C
PARAMETER(NR=300)
DIMENSION A(NR), B(NR), C(NR)
DO 95, I=1, N
95 C(I)=A(I)-B(I)
RETURN
END

```

```

C
SUBROUTINE RMSE(X, N, RMSEX, RMSEY)
C
PARAMETER(NR=300)
DIMENSION X(NR)
SUMXX=0.0
SUMYY=0.0
DO 900, I=1, 2*N, 2
SUMXX=SUMXX+X(I)**2
900 SUMYY=SUMYY+X(I+1)**2
RMSEX=SQRT(SUMXX/(N-1))
RMSEY=SQRT(SUMYY/(N-1))
RETURN
END

```

```

C
SUBROUTINE MATINV(A, N, X2)
C
PARAMETER(NR=300)
DIMENSION A(NR, NR), X2(NR, NR)
DO 5, I=1, N
DO 5, J=1, N

```



```

5 X2(I, J)=0.0
  X2(1, 1)=1./A(1, 1)
  IF(N-1)500, 501, 500
500 DO 40, M=2, N
    K=M-1
    EK=A(M, M)
    DO 10, I=1, K
    DO 10, J=1, K
  10 EK=EK-A(M, I)*X2(I, J)*A(J, M)
    X2(M, M)=1./EK
    DO 30, I=1, K
    DO 20, J=1, K
  20 X2(I, M)=X2(I, M)-X2(I, J)*A(J, M)/EK
  30 X2(M, I)=X2(I, M)
    DO 40, I=1, K
    DO 40, J=1, K
    X2(I, J)=X2(I, J)+X2(I, M)*X2(M, J)*EK
  40 CONTINUE
501 RETURN
  END

```

```

C -----
C ----- END OF BLOCK 11.

```

### A.2.5 Sample Input Data for Program POLY25

The same sample input data listed above for program CON was used in this run of program PLOY25.

### A.2.6 Sample Output Data From Program POLY25

\*\*\*\* SYSTEMATIC DISTORTION \*\*\*\*

PT. NO.	x'	y'	dx	dy
1	-120.000	-113.000	0.17	0.34
2	-100.000	-112.500	-0.06	0.05
3	-80.000	-112.000	-0.18	0.14
4	-59.000	-111.500	-0.44	0.12
5	-39.000	-111.000	-0.39	0.32
6	-18.000	-111.000	-0.81	0.23
7	3.000	-111.000	-0.63	0.16
8	23.000	-111.000	-0.73	0.31
9	44.000	-111.000	-0.89	0.29
10	64.000	-111.000	-0.70	0.52
11	85.000	-111.000	-0.64	0.62
12	104.000	-112.000	-0.28	0.78
13	124.000	-112.000	-0.54	0.64
14	124.000	-87.000	-0.22	0.15
15	104.000	-87.000	-0.30	0.30
16	84.000	-86.500	-0.19	0.20
17	63.000	-86.000	-0.25	0.27
18	42.000	-86.500	-0.06	0.11
19	22.000	-86.500	-0.01	0.33
20	1.000	-87.000	0.08	0.15
21	-20.000	-87.000	0.27	0.05
22	-41.000	-87.000	0.52	-0.07
23	-61.000	-87.000	0.41	-0.24
24	-82.000	-87.000	0.44	-0.16
25	-103.000	-87.000	0.87	-0.23
26	-123.000	-88.000	0.77	-0.13
27	-124.000	-63.000	0.66	-0.43
28	-103.000	-63.000	0.46	-0.20
29	-82.000	-62.000	0.54	-0.19
30	-62.000	-62.000	0.37	-0.04
31	-41.000	-62.000	0.20	-0.18
32	-20.000	-62.000	0.05	-0.25
33	1.000	-62.000	-0.08	-0.16
34	21.500	-62.000	-0.18	-0.11
35	42.000	-62.000	0.11	-0.04
36	63.000	-62.000	0.18	0.02

37	83.000	-62.000	0.01	0.12
38	103.500	-62.000	0.19	0.11
39	124.000	-62.000	0.26	0.05
40	124.000	-37.000	0.18	-0.04
41	104.000	-37.000	-0.03	-0.22
42	84.000	-37.000	-0.16	-0.30
43	63.000	-37.000	0.04	-0.06
44	42.000	-37.000	-0.03	-0.20
45	21.000	-37.000	0.06	-0.18
46	1.000	-37.000	0.00	-0.17
47	-20.000	-37.000	0.15	-0.25
48	-41.000	-37.000	0.06	-0.24
49	-62.000	-37.500	0.29	-0.30
50	-83.000	-38.000	0.19	-0.22
51	-103.000	-38.000	0.26	-0.38
52	-124.000	-38.000	0.31	-0.54
53	-124.000	-13.000	0.38	-0.24
54	-103.000	-13.000	-0.07	-0.12
55	-83.000	-13.000	0.41	-0.32
56	-62.000	-13.000	0.03	-0.24
57	-41.000	-13.000	-0.19	-0.02
58	-21.000	-12.500	0.06	-0.04
59	0.000	-12.000	-0.06	-0.08
60	21.000	-12.000	0.02	-0.20
61	42.000	-12.000	-0.02	-0.17
62	63.000	-12.000	0.15	0.04
63	83.000	-12.000	0.15	0.08
64	104.000	-12.000	0.03	-0.12
65	124.000	-12.000	0.28	-0.05
66	124.000	13.000	0.07	-0.17
67	103.000	13.000	0.32	-0.08
68	83.000	13.000	0.26	-0.17
69	62.500	13.000	0.12	-0.08
70	42.000	13.000	0.09	-0.22
71	21.000	12.000	0.13	-0.01
72	0.000	12.000	0.04	0.06
73	-21.000	12.000	0.04	-0.12
74	-42.000	12.000	0.00	-0.16
75	-63.000	12.000	0.32	-0.35
76	-83.000	12.000	0.20	0.20
77	-104.000	12.000	0.32	-0.25
78	-124.000	12.000	0.34	-0.09
79	-123.000	37.000	-0.04	0.03
80	-103.000	37.000	-0.10	0.00
81	-83.000	37.000	-0.08	0.10
82	-62.000	37.000	-0.37	0.11
83	-41.000	37.000	-0.58	0.06
84	-21.000	37.000	0.10	0.00
85	0.000	37.000	-0.05	-0.14
86	21.000	37.000	-0.19	-0.13
87	42.000	37.000	-0.09	-0.09
88	62.000	37.000	-0.02	0.09
89	83.000	38.000	0.17	-0.22
90	103.000	38.000	0.50	-0.18
91	123.000	38.000	0.70	0.01

92	123.000	63.000	0.25	-0.32
93	103.000	63.000	0.09	-0.36
94	82.000	63.000	0.11	-0.40
95	62.000	62.000	-0.13	-0.08
96	42.000	62.000	-0.21	-0.35
97	21.000	62.000	-0.08	-0.42
98	0.000	62.000	-0.37	-0.16
99	-21.000	62.000	-0.07	-0.12
100	-41.000	62.000	-0.33	0.15
101	-62.000	61.500	-0.51	0.12
102	-83.000	61.000	-0.36	0.26
103	-103.000	61.000	-0.34	0.31
104	-124.000	61.000	-0.11	0.19
105	-124.000	86.000	-0.15	0.09
106	-103.000	86.000	-0.36	-0.06
107	-83.000	86.000	-0.26	-0.15
108	-62.000	86.000	-0.48	-0.26
109	-42.000	86.000	-0.10	-0.05
110	-21.000	86.000	-0.36	-0.14
111	-1.000	86.000	-0.27	-0.09
112	20.000	86.000	0.06	-0.07
113	41.000	86.000	-0.27	-0.15
114	62.000	86.000	0.01	-0.38
115	82.000	87.000	0.19	-0.36
116	102.000	87.000	0.26	-0.21
117	122.000	87.000	0.34	-0.34
118	121.000	111.000	0.62	0.37
119	101.000	111.000	0.46	0.00
120	81.000	111.000	0.28	0.02
121	61.000	110.000	0.06	0.26
122	40.000	110.000	0.27	0.17
123	20.000	110.000	-0.27	0.26
124	-1.000	109.000	0.13	0.32
125	-21.000	109.000	-0.44	0.67
126	-42.000	109.000	-0.11	0.67
127	-62.000	109.000	-0.48	0.72
128	-82.000	109.000	-0.40	0.83
129	-103.000	109.000	-0.20	0.98
130	-123.000	110.000	-0.15	0.49

\*\*\*\* RMSE (PIXEL) \*\*\*\*

mx	my	mp
0.39	0.30	0.49

\*\*\*\* RANDOM DISTORTION \*\*\*\*

Pt. NO.	$x'$	$y'$	$dx'$	$dy'$
1	-112.250	-122.750	0.01	0.18
2	-111.750	-102.750	0.12	0.42
3	-111.250	-82.250	0.01	0.00
4	-111.250	-62.250	0.52	0.34
5	-111.250	-41.500	0.75	-0.14
6	-110.500	-20.250	0.56	-0.80
7	-110.250	-0.250	0.20	-0.18
8	-110.750	20.250	0.84	-0.26
9	-110.750	40.750	0.97	-0.22
10	-111.250	61.250	1.32	-0.50
11	-111.250	81.750	1.15	-0.76
12	-111.250	101.750	0.65	-0.76
13	-111.250	121.750	0.67	-0.68
14	-86.250	121.750	0.02	0.66
15	-86.250	101.750	0.25	0.42
16	-86.250	81.750	0.24	0.22
17	-86.250	61.750	0.37	-0.30
18	-86.250	40.750	0.13	0.24
19	-86.250	20.250	0.10	-0.11
20	-86.250	0.250	-0.05	-0.63
21	-86.250	-21.250	-0.33	0.27
22	-86.250	-41.750	-0.68	0.25
23	-86.250	-62.250	-0.82	0.31
24	-87.250	-82.750	-0.05	0.27
25	-87.250	-103.250	-0.73	0.56
26	-87.250	-123.250	-0.91	0.36
27	-62.250	-123.750	-1.01	0.49
28	-62.250	-103.750	-0.61	0.49
29	-62.250	-83.250	-0.50	0.38
30	-62.250	-62.750	-0.19	0.26
31	-61.250	-42.250	-0.78	0.64
32	-61.250	-21.250	-0.51	0.47
33	-61.250	-0.250	-0.31	0.15
34	-61.250	20.750	-0.17	-0.09
35	-61.500	40.750	-0.20	0.63
36	-61.750	61.750	0.09	0.24
37	-61.750	82.750	0.24	-0.31
38	-62.000	102.750	0.25	0.10
39	-62.250	122.750	0.32	0.36
40	-37.250	123.750	0.27	-0.15
41	-36.750	103.750	0.01	-0.22
42	-36.750	83.250	0.16	-0.10
43	-37.250	62.250	0.41	0.04
44	-37.250	41.750	0.35	-0.10
45	-37.250	21.250	0.29	-0.45
46	-37.250	0.250	0.27	-0.33

47	-37.250	-20.750	0.06	-0.11
48	-37.250	-41.250	0.08	-0.43
49	-37.250	-62.250	-0.40	-0.15
50	-37.250	-82.750	-0.40	-0.36
51	-37.250	-103.250	-0.61	-0.16
52	-37.250	-123.750	-0.81	0.22
53	-12.750	-124.250	-0.49	0.19
54	-12.750	-103.750	0.07	-0.14
55	-12.250	-83.750	-0.82	0.57
56	-12.250	-62.750	-0.38	0.14
57	-12.250	-41.750	0.04	-0.27
58	-12.250	-20.750	-0.13	-0.39
59	-12.250	0.250	0.03	-0.45
60	-12.250	20.750	0.01	0.07
61	-12.250	41.750	0.08	-0.09
62	-12.250	62.750	0.10	-0.50
63	-12.250	83.750	0.13	-0.92
64	-12.000	103.750	0.04	-0.20
65	-12.250	123.750	0.04	0.02
66	12.750	123.750	0.19	0.17
67	12.750	103.250	-0.14	0.28
68	12.750	83.250	-0.16	-0.13
69	12.750	62.250	-0.12	0.12
70	12.750	42.000	-0.21	-0.30
71	12.750	20.750	-0.33	-0.09
72	12.250	-0.250	0.15	-0.06
73	12.750	-20.750	-0.42	-0.30
74	12.750	-41.750	-0.40	-0.12
75	12.750	-62.750	-0.91	0.27
76	11.750	-83.750	0.18	0.07
77	11.750	-103.750	0.02	0.00
78	11.750	-124.750	-0.04	0.53
79	36.750	-124.250	0.26	0.09
80	36.750	-104.250	0.28	0.39
81	36.750	-83.250	0.25	-0.26
82	36.750	-62.750	0.54	-0.14
83	36.750	-41.750	0.89	-0.28
84	37.250	-21.250	-0.26	0.08
85	37.750	-0.250	-0.56	0.08
86	37.750	20.750	-0.32	-0.06
87	37.750	41.250	-0.40	0.22
88	37.750	62.250	-0.20	-0.18
89	37.750	82.750	-0.32	0.24
90	37.750	102.750	-0.53	0.66
91	37.750	123.250	-0.56	0.21
92	63.750	122.750	-1.27	0.66
93	62.750	102.750	-0.34	0.52
94	62.750	82.750	-0.48	0.16
95	62.750	62.250	-0.39	-0.22
96	62.750	41.250	-0.57	0.36
97	62.500	20.750	-0.55	0.16
98	61.750	0.250	0.41	-0.39
99	61.750	-21.250	0.07	0.26
100	61.750	-41.750	0.30	-0.26
101	61.750	-62.250	0.37	-0.43

102	61.750	-82.750	0.26	-0.63
103	61.750	-103.750	0.30	-0.09
104	61.750	-123.750	0.15	-0.17
105	86.750	-123.250	-0.04	0.02
106	86.750	-102.750	0.03	-0.23
107	86.750	-82.750	-0.16	0.16
108	86.750	-62.250	-0.06	0.25
109	86.250	-41.750	0.17	0.12
110	86.750	-20.750	-0.07	-0.17
111	86.750	-0.750	-0.13	0.47
112	86.750	20.250	-0.35	0.17
113	86.750	41.250	0.09	-0.10
114	87.750	61.250	-0.93	0.70
115	87.750	82.250	-0.91	0.16
116	87.750	102.250	-0.77	0.29
117	87.750	122.250	-0.60	0.51
118	111.750	121.250	-0.21	-0.01
119	111.750	101.250	-0.39	0.41
120	110.750	81.250	0.53	0.23
121	111.250	61.250	0.02	-0.31
122	110.750	40.250	0.04	0.31
123	110.750	20.250	0.48	-0.29
124	110.750	-0.750	-0.05	0.09
125	109.750	-20.750	1.49	-0.81
126	109.750	-41.750	1.16	-0.34
127	109.750	-61.750	1.48	-0.84
128	109.750	-82.750	1.52	-0.26
129	109.750	-102.750	1.46	-0.59
130	110.750	-122.750	0.62	-0.05

\*\*\*\* RMSE (PIXEL) \*\*\*\*

mx	my	mp
0.40	0.22	0.45

### A.3 Program DISTCOR

This program was written to correct the measured video image coordinates for the systematic distortion and for the image motion distortion. The mathematical basis is discussed in Section 8.3 of Chapter VIII.

#### A.3.1 Definition of Variables

- N Number of points.
- FL Scanner focal length.
- V Aircraft ground speed.
- H Flying height.

#### A.3.2 Definition of Arrays

- A Working array in which the coordinates and the distortion values of each of the four closest cross images (known from the scanner calibration) to the point to be corrected are stored.
- B Array containing the coordinates x,y of the control and check points.
- CB Array containing the corrected image coordinates.
- D Array representing the distortion table. This consists of the x,y coordinates of the 130 cross images as measured by the video position analyser, together with the distortion values dx,dy at each cross image as determined by the scanner calibration.
- NO1 Array containing the points number.

#### A.3.3 Detailed Description of Program DISTCOR

A listing of the program is shown below. The main blocks of this listing will be explained in detail.

- Block 1. In this first block, the program name is defined and the different arrays are dimensioned.
- Block 2. In which the different files used during the running of the program are defined. These are the image coordinates file name, the distortion table file name, and the output file name. The image coordinates should be written in (I3, 2F10.3) format where I3 is the point number and



2F10.3 represents the measured x and y video image coordinates. The distortion table file should be arranged in (I4, 4F10.3) representing the point number, x,y (measured coordinates of the cross image), and dx,dy (the distortion values at each cross as determined during the scanner calibration). The output file will be opened automatically by the system and the user is only required to assign a name for this file.

**Block 3.** In this block, the closest four crosses to the first image point are found and their coordinates and the distortion values at each of them are retrieved. This is achieved by opening the file containing the distortion table and locating the closest cross coordinates. The coordinates and the distortion values of this cross are stored in separate arrays. The distortion table file is then closed. The procedure is repeated 3 times to obtain the information about the other three crosses.

**Block 4.** The least squares procedure is used to solve for the unknown parameters ( $a_0, a_1, a_2, b_0, b_1$ , and  $b_2$ ) of an affine transformation equation using the known coordinates and distortion values of the four cross images. Having determined these parameters, the correction values for the measured coordinates of any point on the image can be computed by back substitution in the same polynomial equations. These correction values are added to the measured image coordinates to produce the corrected image coordinates.

**Block 5.** In this block, the image coordinates are corrected for the image motion distortion during the image scan time. After this correction, the program starts again from Block 2 to correct the second point and the process is repeated until all the measured coordinates are corrected for both types of distortion.

**Block 6.** This contains the subroutines required to solve the various matrix operations during the different stages of the program. The same subroutines listed above in program POLY25 were used to carry out the various matrix operations required in this case.

### A.3.4 Listing of Program DISTCOR

```
C   DISTORTION CORRECTION PROGRAM FOR THE IR-18 IMAGES
PROGRAM DISTCOR
PARAMETER(NR=200)
DIMENSION B(NR,NR),D(150,NR),R(NR,NR),A4(NR,NR)
1, A(NR,NR),AT(NR,NR),AN(NR,NR),ANT(NR,NR),SF(NR),F(NR)
1,NO1(NR),NO2(NR),DX(NR),CB(NR,3)
CHARACTER*32NAME1,NAME2,NAME3
CHARACTER*1ANS

C   ----- END OF BLOCK 1.
C
C   PRINT*, 'PLEASE INPUT THE DATA FILE NAME'
READ(5,820)NAME1
OPEN(1,FILE=NAME1,STATUS='OLD',FORM='FORMATTED')
READ(1,150)N
DO 10,I=1,N
10 READ(1,800)NO1(I),B(I,2),B(I,3)
READ(1,155)XC,YC
CLOSE(UNIT=1)
ND=130
PRINT*, 'PLEASE ENTER THE DISTORTION VALUES FILE NAME'
READ(5,820)NAME2
PRINT*, 'PLEASE INPUT THE OUTPUT FILE NAME'
READ(5,820)NAME3
OPEN(2,FILE=NAME3,STATUS='OLD',FORM='FORMATTED')
DO 20,K=1,N
IX=(B(K,2)-14)/21
IY=(B(K,3)-11)/25
IX=IX*21+14
IY=IY*25+11
IF(IX.LE.14) THEN
IX=IX+21
ELSE IF(IX.GE.266)THEN
IX=IX-21
END IF
IF(IY.LE.11) THEN
IY=IY+25
ELSE IF(IY.GE.236)THEN
IY=IY-25
END IF

C   ----- END OF BLOCK 2.
C
C   OPEN(3,FILE=NAME2,STATUS='OLD',FORM='FORMATTED')
DO 30,I=1,ND
READ(3,810)NO2(I),(D(I,J),J=2,5)
```

```

IF(D(I, 2).EQ. IX.AND. D(I, 3).EQ. IY) THEN
  A4(1, 1)=D(I, 2)
  A4(1, 2)=D(I, 3)
  R(1, 1)=D(I, 4)
  R(1, 2)=D(I, 5)
  END IF
30 CONTINUE
  CLOSE(UNIT=3)
  OPEN(3, FILE=NAME2, STATUS='OLD', FORM='FORMATTED')
  DO 35, I=1, ND
  READ(3, 810)NO2(I), (D(I, J), J=2, 5)
  IF(D(I, 2).EQ. (IX+21).AND. D(I, 3).EQ. (IY)) THEN
  A4(2, 1)=D(I, 2)
  A4(2, 2)=D(I, 3)
  R(2, 1)=D(I, 4)
  R(2, 2)=D(I, 5)
  END IF
35 CONTINUE
  CLOSE(UNIT=3)
  OPEN(3, FILE=NAME2, STATUS='OLD', FORM='FORMATTED')
  DO 40, I=1, ND
  READ(3, 810)NO2(I), (D(I, J), J=2, 5)
  IF(D(I, 2).EQ. (IX+21).AND. D(I, 3).EQ. (IY+25)) THEN
  A4(3, 1)=D(I, 2)
  A4(3, 2)=D(I, 3)
  R(3, 1)=D(I, 4)
  R(3, 2)=D(I, 5)
  END IF
40 CONTINUE
  CLOSE(UNIT=3)
  OPEN(3, FILE=NAME2, STATUS='OLD', FORM='FORMATTED')
  DO 45, I=1, ND
  READ(3, 810)NO2(I), (D(I, J), J=2, 5)
  IF(D(I, 2).EQ. IX.AND. D(I, 3).EQ. (IY+25)) THEN
  A4(4, 1)=D(I, 2)
  A4(4, 2)=D(I, 3)
  R(4, 1)=D(I, 4)
  R(4, 2)=D(I, 5)
  END IF
45 CONTINUE
  CLOSE(UNIT=3)

```

C  
C  
C

----- END OF BLOCK 3.

```

DO 11, I=1, 4
  A4(I, 1)=A4(I, 1)-IX
11 A4(I, 2)=A4(I, 2)-IY
  CALL FORM(A4, A, R, SF, 4)
  CALL MATRAN(A, AT, 8, 6)
  CALL MATMAT(AT, A, AN, 6, 8, 6)
  CALL MATINV(AN, 6, ANT)
  CALL MATVEC(AT, SF, F, 6, 8)
  CALL MATVEC(ANT, F, DX, 6, 6)
  X=DX(1)+DX(2)*(B(K, 2)-IX)+DX(3)*(B(K, 3)-IY)

```

```
Y=DX(4)+DX(5)*(B(K,2)-IX)+DX(6)*(B(K,3)-IY)
CB(K,2)=B(K,2)-X
CB(K,3)=B(K,3)-Y
```

```
20 CONTINUE
```

```
C
C
C
```

```
----- END OF BLOCK 4.
IMAGE MOTION CORRECTION
```

```
PRINT*, 'INPUT THE SCANNERS'S FOCAL LENGTH
READ *, FL
PRINT*, INPUT THE AIRCRAFT SPEED IN METRES/SEC'
READ*, V
PRINT*, 'INPUT THE FLYING HEIGHT IN METRES'
READ*, H
XR=CB(I,2)-XC
YR=CB(I,3)-YC
KC=(ABS(YR)+2)/4
C=(.000868*FL*V*KC)/H
IF(YR) 1,2,2
2 YR=YR+C
GO TO 7
1 YR=YR-C
7 CB(I,3)=YR
CB(I,2)=CB(I,2)-XC
510 WRITE(2,810)NO1(I),CB(I,2),CB(I,3)
CLOSE(UNIT=2)
150 FORMAT(I3)
155 FORMAT(2F10.3)
820 FORMAT(A32)
800 FORMAT(I3,2F10.3)
810 FORMAT(I4,4F10.3)
999 END
```

```
C
C
C
C
```

```
----- END OF BLOCK 5.
```

```
SUBROUTINE FORM(RE, A, OB, SF, N)
```

```
PARAMETER(NR=200)
DIMENSION OB(NR, NR), SF(NR), A(NR, NR), RE(NR, NR)
DO 10, I=1, 8, 2
K=I/2+1
X=RE(K, 1)
Y=RE(K, 2)
A(I, 1)=1.
A(I, 2)=X
A(I, 3)=Y
A(I, 4)=0.0
A(I, 5)=0.0
A(I, 6)=0.0
A((I+1), 1)=0.0
A((I+1), 2)=0.0
A((I+1), 3)=0.0
A((I+1), 4)=1.
A((I+1), 5)=X
```

```

A((I+1),6)=Y
  SF(I)=OB(K,1)
  SF(I+1)=OB(K,2)
10 CONTINUE
  RETURN
  END
C
  SUBROUTINE MATINV(A,N,X2)
C
  PARAMETER(NR=200)
  DIMENSION A(NR,NR),X2(NR,NR)
  DO 5,I=1,N
  DO 5,J=1,N
5 X2(I,J)=0.0
  X2(1,1)=1./A(1,1)
  IF(N-1)500,501,500
500 DO 40,M=2,N
  K=M-1
  EK=A(M,M)
  DO 10,I=1,K
  DO 10,J=1,K
10 EK=EK-A(M,I)*X2(I,J)*A(J,M)
  X2(M,M)=1./EK
  DO 30,I=1,K
  DO 20,J=1,K
20 X2(I,M)=X2(I,M)-X2(I,J)*A(J,M)/EK
30 X2(M,I)=X2(I,M)
  DO 40,I=1,K
  DO 40,J=1,K
  X2(I,J)=X2(I,J)+X2(I,M)*X2(M,J)*EK
40 CONTINUE
501 RETURN
  END
C
  SUBROUTINE MATVEC(A,X,Z,N,M)
C
  PARAMETER(NR=200)
  DIMENSION A(NR,NR),X(NR),Z(NR)
  INTEGER M,N,AN
  DO 5,I=1,N
  SUM=0.0
  DO 5,J=1,M
  SUM=SUM+A(I,J)*X(J)
5 Z(I)=SUM
  RETURN
  END
C
  SUBROUTINE MATMAT(A,U,T,N,M,IP)
C
  PARAMETER(NR=200)
  DIMENSION A(NR,NR),U(NR,NR),T(NR,NR)
  DO 10,J=1,N

```

```
DO 10, K=1, IP
T(J, K)=0.0
DO 10, I=1, M
T(J, K)=T(J, K)+A(J, I)*U(I, K)
10 CONTINUE
RETURN
END
```

C

```
SUBROUTINE MATRAN(A1, A1T, N, M)
```

C

```
PARAMETER(NR=200)
DIMENSION A1(NR, NR), A1T(NR, NR)
DO 11, I=1, N
DO 11, J=1, M
11 A1T(J, I)=A1(I, J)
RETURN
END
```

C

```
SUBROUTINE MATSUB(A, B, C, N)
```

C

```
PARAMETER(NR=200)
DIMENSION A(NR), B(NR), C(NR)
DO 95, I=1, N
95 C(I)=A(I)-B(I)
RETURN
END
```

### A.3.5 Sample Input Data For Program DISTCOR

PT. NO.	x	y
15	129.0	200.5
17	106.5	197.5
105	103.0	182.5
19	125.0	171.0
29	29.0	127.0
30	29.0	149.5
26	43.5	153.0
25	60.5	150.5
1	167.5	110.0
2	176.0	122.5
3	169.5	146.0
4	207.5	133.0
5	244.5	119.0
12	212.0	215.0
10	248.0	193.0
11	212.0	185.0
40	99.0	231.0
31	28.0	182.0
34	11.5	204.0
16	129.0	211.0
24	74.0	145.5
8	244.5	163.5
42	79.5	223.0
210	13.0	217.0
32	11.0	124.0
21	111.5	113.0
201	264.0	106.5
700	258.0	241.0
	130.0	138.0

A.3.6 Sample Output Data from Program DISTCOR

PT. NO.	x	y
15	-0.999	63.368
17	-23.593	60.247
105	-26.948	44.911
19	-5.195	33.334
29	-100.860	-11.141
30	-101.070	11.711
26	-86.558	15.073
25	-69.562	12.412
1	37.546	-28.301
2	45.988	-15.697
3	39.433	7.993
4	77.412	-5.163
5	114.593	-19.294
12	81.993	78.026
10	118.058	55.720
11	82.021	47.551
40	-31.124	93.820
31	-101.876	44.324
34	-118.366	66.901
16	-0.953	74.004
24	-56.098	7.553
8	114.303	25.730
42	-50.378	86.034
210	-117.081	79.967
32	-118.603	-14.030
21	-18.392	-25.418
201	134.082	-31.878
700	128.015	103.786



#### A.4 Space Resection/Intersection Program

As mentioned in Chapter VIII, this program was written originally for the processing of reconnaissance frame photography. A complete description of the program is given in El Hassan, 1978. The modifications which have been introduced by the present author to the program to account for the additional and unique characteristics of frame scanners are discussed below.

##### A.4.1 Space Resection with Additional Parameters

For the conventional space resection case, the linearized collinearity equations can be written in matrix form as follows:-

$$V = B X_1 - L \quad \dots\dots\dots A-1$$

in which

$$V = \begin{bmatrix} v_x \\ v_y \end{bmatrix} ; \quad L = \begin{bmatrix} j \\ k \end{bmatrix} ;$$

$$X_1^T = [ d\omega \quad d\phi \quad dK \quad dX_0 \quad dY_0 \quad dZ_0 ] ; \text{ and}$$

B represents the coefficients of the partial derivatives derived from equations 8-19,8-20

The least squares procedure can then be used to solve Equation A-1 to give the unknown corrections for the orientation elements. Thus

$$X_1 = ( B^T B )^{-1} B^T L \quad \dots\dots\dots A-2$$

When the parameters of equations 8-17,8-18 are added to the observation equations, the resulting equation can be written in the form:

$$V = B X_1 + C X_2 - L \quad \dots\dots\dots A-3$$

or

$$V = DX - L \quad \dots\dots\dots A-4$$

In which C X2 represents the additional parameters of equations 8-17,8-18.

Where:-

$$C = \begin{vmatrix} 1 & x & y & xy^2 & x^3 & 0 & 0 & 0 & 0 & 0 \\ 0 & 0 & 0 & 0 & 0 & 1 & x & -y & x^2y & y^3 \end{vmatrix}$$

and;

$$X2^T = [ a_0 \ a_1 \ a_2 \ a_3 \ a_4 \ b_0 \ b_1 \ b_2 \ b_3 \ b_4 ]$$

Using least squares; the solution is given by;

$$X = (D^T D)^T . D^T L \dots\dots\dots A-5$$

**A.4.2 Space Resection Point by Point**

In this case, the exterior orientation elements are expressed as a function of the image coordinates. The observation equation can be written in the following matrix form:-

$$V = B X1 + F X3 - L \dots\dots\dots A-6$$

or  $V = D X - L \dots\dots\dots A-7$

Where:-

B is matrix of the partial derivatives derived from equations 8-24,8-25;

$$F = [ 1 \quad x \quad y ]$$

$$X3 = \begin{vmatrix} a_0 & a_1 & a_2 \\ b_0 & b_1 & b_2 \\ c_0 & c_1 & c_2 \\ d_0 & d_1 & d_2 \\ e_0 & e_1 & e_2 \\ f_0 & f & f_2 \end{vmatrix}$$

Again, using least squares procedure to solve for the unknown parameters, equations A-6 can be rewritten in the form:-

$$X = ( B^T B )^T B^T L \dots\dots\dots A-7$$

## A.5 Program DIGCOR

This program was written to correct the digitized frame scanner images for various types of geometric distortion. The mathematical basis and procedure of this correction have been discussed in Chapter XII.

### A.5.1 Definition of Variables

- N1 is the number of lines per frame in the original image;
- N2 is the number of pixels per line in the original image;
- N3 is the number of lines per frame in the digitized image (square image);
- FL is the scanner's focal length;
- V is the platform ground speed in metres/second; and
- H is the flying height.

### A.5.2 Definition of Arrays

- ADD is the matrix of the additional parameters which will be used to correct for the changes of the exterior orientation parameters during the scan time. These parameters have been determined during the space resection phase.
- D is the matrix containing the distortion table;
- IM is the matrix representing the digitized frame scanner image before any geometric rectification (input image);
- IM2 is the matrix of the rectified digital image (output image);
- ROT1 is the orthogonal rotation matrix. This 3x3 matrix is a function of the three rotations , , of the scanner which occurred at the moment of recording the principal point of the video image.

The remaining arrays are working arrays used by the program during the various stages of the digital correction.

### A.5.3 Explanation of Program DIGCOR

- Block 1.** This contains the name of the program, defines the dimensions of the various variables and arrays, asks for the input of the data file containing the digital image to be corrected and reads the digital brightness value for all the pixels in the image. The data file should be arranged as a matrix of 512x512 with each brightness value written in I3 format.
- Block 2.** In this block, the input image scale is reduced to the original size as produced by the frame scanner. This reduced image is used throughout the program as the input image. After all the corrections have been carried out, the image will be enlarged back to its digitized size to produce the correct size of display.
- Block 3.** Each pixel is corrected for the scanner tilts which occurred at the moment of recording the video image principal point and also for the changes in these tilts during the image scan time.
- Block 4.** The image motion correction is carried out using equation 5-6.
- Block 5.** In this block, the digital image is corrected for the spherical imaging surface using equations 11-5, 11-6.
- Block 6.** Each pixel is corrected for the distortion introduced to the video image by the optical components and any distortion introduced by the scanner's electronic circuits. The magnitude and nature of this distortion have been determined during the scanner calibration. The same procedure explained above in Blocks 3, 4 of Section A.3.3 is used here.
- Block 7.** In this block, the corrected image is enlarged back to its original digitized size.
- Block 8.** This block is concerned with the output of the digitally corrected image. The user is required to choose a name for the output file. This file is then created automatically by the program.

**Block 9.** Here, the formats of all the input and output data are declared.

**Block 10.** This block contains the following subroutines:-

- (1) **FORM1** which is used to correct each pixel for the scanner tilts;
- (2) **FORM** used to form the matrix of the unknown parameters during the least squares solution;
- (3) **MATINV** to inverse a matrix;
- (4) **MATVEC** to multiply a matrix by a vector;
- (5) **MATMAT** to multiply a matrix by a matrix;
- (6) **MATRAN** to transpose a matrix;
- (7) **MATSUB** to subtract two matrices from each other;and
- (8) **RESAMP** which is used to assign the digital brightness value for each corrected pixel. The bicubic resampling method which was explained in Section 12.4.3 and based on the use of equations 12-11,12-12 has been used.

#### A.5.4 Listing of Program DIGCOR

```

PROGRAM DIGCOR
PARAMETER (NL=512, NP=767, NR=20)
COMMON/BLOCK1/IM(NL, NP), LIM(NL, NP), IM2(NL, NP)
DIMENSION D(130, 5), R(NR, NR), A4(NR, NR)
1, A(NR, NR), AT(NR, NR), AN(NR, NR), ANT(NR, NR), SF(NR), F(NR)
1, ROT1(3, 3), ROT2(3, 3), NO2(130), DX(NR)
1, ADD(10), AH(3), AB(3)
CHARACTER*32NAME1, NAME2, NAME3
CHARACTER*1ANS
N1=500
N2=512
N3=767
PRINT*, 'INPUT THE DIGITAL IMAGE FILE NAME'
READ(5, 820)NAME1
OPEN(1, FILE=NAME1, STATUS='OLD', FORM='FORMATTED')
DO 10, I=1, N2
10 READ(1, 800)(IM(I, J), J=1, N2)
CLOSE(UNIT=1)

C
C ----- END OF BLOCK 1
C
C DIGITAL IMAGE REDUCTION
C
DO 20, I=1, N1
DO 20, J=1, N3
X=I*N2/N1
Y=I*N2/N3
20 CALL RESAMP (I, J, X, Y)
DO 25, I=1, N1
DO 25, J=1, N3
IM(I, J)=IM2(I, J)
25 IM2(I, J)=0

C
C ----- END OF BLOCK 2
C
C CORRECTION FOR THE SCANNER TILT AND CHANGES IN TILT
C DURING THE SCAN TIME
C
PRINT*, 'PLEASE INPUT THE TILTS FILE NAME. THIS SHOULD
*CONTAIN THE SCANNER ROTATIONS AND THE ADDITIONAL
*PARAMETERS'
READ(5, 820)NAME2
OPEN(3, FILE=NAME2, STATUS='OLD', FORM='FORMATTED')

```

```

DO 30, I=1, 10
READ(3, 840)ADD(I)
30 CONTINUE
DO 40, I=1, 3
40 READ(3, 860)(ROT1(I, J), J=1, 3)
CLOSE(UNIT=3)
DO 50, I=1, N1
DO 50, J=1, N3
CALL MATINV(ROT1, 3, ROT2)
CALL FORM1(I, J, X, Y)
50 CALL RESAMP(I, J, X, Y)

```

C  
C  
C  
C  
C

----- END OF BLOCK 3

IMAGE MOTION CORRECTION

THE

PRINT\*, 'INPUT THE FOCAL LENGTH, THE PLATFORM SPEED AND

\*FLYING HEIGHT'

```

READ*, FL, V, H
DO 60, I=1, N2
DO 60, J=1, N3
CX=0.00064*FL*V*I/H
IX=I+CX
IF (IX.LT.1.OR.IX.GT.N1) THEN
IM2(I, J)=0
GO TO 60
END IF
IY=J
CALL RESAMP(I, J, X, Y)
60 CONTINUE
DO 65, I=1, N1
DO 65, J=1, N3
IM(I, J)=IM2(I, J)
65 IM2(I, J)=0

```

C  
C  
C  
C  
C

----- END OF BLOCK 4

CORRECTION OF THE SPHERICAL IMAGING SURFACE

```

V=1.73/1.5
NM=N1
NN=767
DO 75, I=1, N1
DO 75, J=1, N3
AX=I*V
AY=J*V
X=(NM/2)+(1/V)*(ATAN((2*I-1)/NM*TAN AX/2 - TAN AX/2))
Y=(NN/2)+(1/V)*(ATAN((2*J-1)/NN*SEC AX/2 * TAN AY/2 -
*TAN AY/2))
CALL RESAM (I, J, X, Y)
75 CONTINUE

```

```
DO 85, I=1, N1
DO 85, J=1, N3
IM(I, J)=IM2(I, J)
85 IM2(I, J)=0
```

C  
C  
C  
C  
C

----- END OF BLOCK 5

### DISTORTION CORRECTION

```
PRINT*, 'PLEASE ENTER THE DISTORTION VALUES FILE NAME'
READ(5, 820)NAME2
DO 70, I=1, N1
DO 70, J=1, N3
IX=(I-14)/21
IY=(J-11)/25
IX=IX*21+14
IY=IY*25+11
IF(IX.LE.14) THEN
IX=IX+21
ELSE IF(IX.GE.N2) THEN
IX=IX-21
END IF
IF(IY.LE.11) THEN
IY=IY+25
ELSE IF(IY.GE.N3) THEN
IY=IY-25
END IF
OPEN(3, FILE=NAME2, STATUS='OLD', FORM='FORMATTED')
DO 80, K=1, 130
READ(3, 900)NO2(K), (D(K, L), L=2, 5)
IF(D(K, 2).EQ. IX.AND.D(K, 3).EQ. IY) THEN
A4(1, 1)=D(K, 2)
A4(1, 2)=D(K, 3)
R(1, 1)=D(K, 4)
R(1, 2)=D(K, 5)
END IF
80 CONTINUE
CLOSE(UNIT=3)
OPEN(3, FILE=NAME2, STATUS='OLD', FORM='FORMATTED')
DO 90, K=1, 130
READ(3, 900)NO2(K), (D(K, L), L=2, 5)
IF(D(K, 2).EQ. (IX+21).AND.D(K, 3).EQ. (IY)) THEN
A4(2, 1)=D(K, 2)
A4(2, 2)=D(K, 3)
R(2, 1)=D(K, 4)
R(2, 2)=D(K, 5)
END IF
90 CONTINUE
CLOSE(UNIT=3)
OPEN(3, FILE=NAME2, STATUS='OLD', FORM='FORMATTED')
DO 100, K=1, 130
READ(3, 900)NO2(K), (D(K, L), L=2, 5)
```



```

IF(D(K, 2).EQ.(IX+21).AND.D(K, 3).EQ.(IY+25)) THEN
A4(3, 1)=D(K, 2)
A4(3, 2)=D(K, 3)
R(3, 1)=D(K, 4)
R(3, 2)=D(K, 5)
END IF
100 CONTINUE
CLOSE(UNIT=3)
OPEN(3, FILE=NAME2, STATUS='OLD', FORM='FORMATTED')
DO 110, K=1, 130
READ(3, 900)NO2(K), (D(K, L), L=2, 5)
IF(D(K, 2).EQ.IX.AND.D(K, 3).EQ.(IY+25)) THEN
A4(4, 1)=D(K, 2)
A4(4, 2)=D(K, 3)
R(4, 1)=D(K, 4)
R(4, 2)=D(K, 5)
END IF
110 CONTINUE
CLOSE(UNIT=3)
DO 120, IL=1, 4
A4(IL, 1)=A4(IL, 1)-IX
120 A4(IL, 2)=A4(IL, 2)-IY
CALL FORM(A4, A, R, SF, 4)
CALL MATRAN(A, AT, 8, 6)
CALL MATMAT(AT, A, AN, 6, 8, 6)
CALL MATINV(AN, 6, ANT)
CALL MATVEC(AT, SF, F, 6, 8)
CALL MATVEC(ANT, F, DX, 6, 6)
X=DX(1)+DX(2)*(B(K, 2)-IX)+DX(3)*(B(K, 3)-IY)
Y=DX(4)+DX(5)*(B(K, 2)-IX)+DX(6)*(B(K, 3)-IY)
X=I-X
Y=J-Y
CALL RESAMP(I, J, X, Y)
70 CONTINUE
DO 95, I=1, N1
DO 95, J=1, N3
IM(I, J)=IM2(I, J)
95 IM2(I, J)=0

```

C  
C  
C  
C  
C

----- END OF BLOCK 6

DIGITAL IMAGE ENLARGEMENT

```

DO 125, I=1, N1
DO 125, J=1, N2
X=I*N1/N2
Y=J*N3/N2
125 CALL RESAMP(I, J, X, Y)
DO 135, I=1, N1
DO 135, J=1, N3
IM(I, J)=IM2(I, J)
135 IM2(I, J)=0

```

C  
C

----- END OF BLOCK 7

```

C      PRINT*, 'ENTER THE OUTPUT FILE NAME - THIS FILE WILL BE
      CREATED AUTOMATICALLY BY THE PROGRAM'
      READ(5, 820)NAME2
      OPEN(2, FILE=NAME2, STATUS='NEW', FORM='FORMATTED')
      DO 130, I=1, N2
130    WRITE(2, 800)(IM2(I, J), J=1, N2)
C
C      ----- END OF BLOCK 8
C
800    FORMAT(5I2I3)
820    FORMAT(A32)
840    FORMAT(F10.7)
860    FORMAT(3F10.7)
900    FORMAT(I4, 4F10.3)
999    END
C
C      ----- END OF BLOCK 9
C
      SUBROUTINE FORM1(I, J, X, Y)
C
      DIMENSIONS ROT2(3, 3), AH(3), AB(3)
      AH(1)=I
      AH(2)=J
      AH(3)=833
      CALL MATVEC(ROT2, AH, AB, 3, 1)
      X=AB(1)
      Y=AB(2)
      X=ADD(1)+ADD(2)*X+ADD(3)*Y+ADD(4)*Y**2*X+ADD(5)*X**3
      Y=ADD(6)+ADD(7)*X+PA(8)*Y+ADD(9)*X**2*Y+ADD(10)*Y**3
      RETURN
      END
C
      SUBROUTINE FORM(RE, A, OB, SF, N)
C
      PARAMETER(NR=20)
      DIMENSION OB(NR, NR), SF(NR), A(NR, NR), RE(NR, NR)
      DO 10, I=1, 8, 2
      K=I/2+1
      X=RE(K, 1)
      Y=RE(K, 2)
      A(I, 1)=1.
      A(I, 2)=X
      A(I, 3)=Y
      A(I, 4)=0.0
      A(I, 5)=0.0
      A(I, 6)=0.0
      A((I+1), 1)=0.0
      A((I+1), 2)=0.0
      A((I+1), 3)=0.0
      A((I+1), 4)=1.
      A((I+1), 5)=X
      A((I+1), 6)=Y

```

```

SF(I)=OB(K,1)
SF(I+1)=OB(K,2)
10 CONTINUE
RETURN
END

```

C

```

SUBROUTINE MATINV(A,N,X2)

```

C

```

PARAMETER(NR=20)
DIMENSION A(NR,NR),X2(NR,NR)
DO 5,I=1,N
DO 5,J=1,N
5 X2(I,J)=0.0
X2(1,1)=1./A(1,1)
IF(N-1)500,501,500
500 DO 40,M=2,N
K=M-1
EK=A(M,M)
DO 10,I=1,K
DO 10,J=1,K
10 EK=EK-A(M,I)*X2(I,J)*A(J,M)
X2(M,M)=1./EK
DO 30,I=1,K
DO 20,J=1,K
20 X2(I,M)=X2(I,M)-X2(I,J)*A(J,M)/EK
30 X2(M,I)=X2(I,M)
DO 40,I=1,K
DO 40,J=1,K
X2(I,J)=X2(I,J)+X2(I,M)*X2(M,J)*EK
40 CONTINUE
501 RETURN
END

```

C

```

SUBROUTINE MATVEC(A,X,Z,N,M)

```

C

```

PARAMETER(NR=20)
DIMENSION A(NR,NR),X(NR),Z(NR)
INTEGER M,N,AN
DO 5,I=1,N
SUM=0.0
DO 5,J=1,M
SUM=SUM+A(I,J)*X(J)
5 Z(I)=SUM
RETURN
END

```

C

```

SUBROUTINE MATMAT(A,U,T,N,M,IP)

```

C

```

PARAMETER(NR=20)
DIMENSION A(NR,NR),U(NR,NR),T(NR,NR)
DO 10,J=1,N
DO 10,K=1,IP

```

```

T(J,K)=0.0
DO 10, I=1, M
T(J,K)=T(J,K)+A(J,I)*U(I,K)
10 CONTINUE
RETURN
END

```

```

C
SUBROUTINE MATRAN(A1, A1T, N, M)

```

```

C
PARAMETER(NR=20)
DIMENSION A1(NR, NR), A1T(NR, NR)
DO 11, I=1, N
DO 11, J=1, M
11 A1T(J, I)=A1(I, J)
RETURN
END

```

```

C
SUBROUTINE MATSUB(A, B, C, N)

```

```

C
PARAMETER(NR=20)
DIMENSION A(NR), B(NR), C(NR)
DO 95, I=1, N
95 C(I)=A(I)-B(I)
RETURN
END

```

```

C
SUBROUTINE RESAMP(I, J, X, Y)

```

```

C
PARAMETER (NL=512, NP=767)
COMMON/BLOCK1/IM(NL, NP), LIM(NL, NP), IM2(NL, NP)
IX=X
IY=Y
C1=X-IX
C2=Y-IY
DO 10, L=IY-1, IY+2
LIM(IX, L)=C1*(1-C1)**2*IM(IX-1, L)+(1-2*C1**2
* +C1**3)*IM(IX, L) +C1*(1+C1-C1**2)*IM(IX+1, L)
* +C1**2*(1-C1)*IM(IX+2, L)
10 CONTINUE
IM2(I, J)=-C2*(1-C2)**2*LIM(IX, IY-1)+(1-2*C2**2*C2**3)*
* LIM(IX, IY) +C2*(1+C2-C2**2)*LIM(IX, IY+1)
* +C2**2*(C2-1)*LIM(IX, IY+2)
RETURN
END

```

```

C
C ----- END OF BLOCK 10

```

### A.5.5 Sample Input Data for Program DIGCOR

Since the size of the digitized frame scanner images was 512 x 512 (=262,144) pixels, it is inconvenient to list all the pixel values. Only a small part will be listed from the input image and the corresponding rectified part from the output image. Fig.A-1 shows the particular part of the image whose brightness values are listed below.

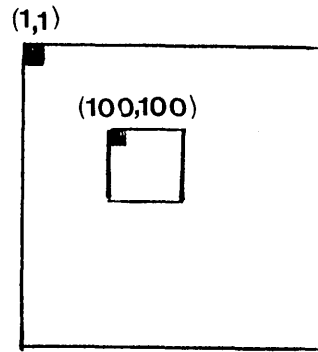


Fig.A-1 Sample Input data

23	18	21	20	25	22	23	20	22	22	22	20	20	24	21	22	24	18	22	21
20	20	22	22	22	18	23	20	24	20	20	18	21	24	21	18	18	19	23	19
19	22	25	24	17	18	22	19	22	21	25	23	22	21	18	18	23	20	22	23
23	22	20	21	17	21	23	19	20	19	24	20	23	18	22	23	22	20	23	23
23	22	20	22	23	23	22	17	21	23	25	20	21	18	26	19	20	22	23	23
23	19	20	24	22	21	16	18	21	22	24	17	20	21	23	19	23	20	21	20
20	19	22	22	20	21	20	22	22	22	22	20	23	18	26	20	25	19	23	23
21	20	24	20	19	23	20	24	20	20	22	23	21	21	24	20	22	18	24	21
23	18	24	20	20	24	22	21	19	22	22	22	22	19	19	20	21	20	25	21
24	19	19	16	21	22	21	19	18	25	22	23	20	20	23	25	20	18	26	19
21	16	20	20	24	18	21	20	22	21	19	20	18	26	21	24	23	20	23	18
20	19	22	24	21	18	19	22	23	23	20	22	19	25	21	24	24	22	20	20
18	22	23	23	20	20	24	20	23	19	18	20	20	24	19	24	22	18	18	19
22	21	19	21	22	21	24	20	22	21	23	22	20	23	22	24	19	20	19	21
22	23	20	19	20	24	21	22	21	18	27	22	22	17	21	23	18	20	18	21
23	23	23	23	19	24	20	22	21	19	21	20	24	20	22	22	21	21	19	20
20	20	22	24	19	24	19	23	24	19	20	19	23	18	23	20	22	21	17	21
21	20	23	19	21	22	23	23	20	19	19	20	25	21	24	18	21	17	21	22
21	18	24	20	21	25	19	23	19	20	23	23	22	20	23	22	24	17	22	19
27	19	20	22	23	23	23	22	19	25	21	24	20	22	20	20	24	21	26	17
24	19	24	20	23	18	22	23	21	24	20	22	20	22	22	21	21	19	21	19
23	21	21	23	23	20	20	22	24	20	23	19	19	24	21	22	24	21	19	15
20	20	23	23	23	19	23	24	24	21	23	24	24	23	21	24	21	18	18	21
24	21	20	20	22	23	23	21	24	20	20	22	22	22	21	25	20	19	19	21
22	24	23	21	25	23	18	20	24	21	25	19	24	22	20	24	20	21	19	21
20	21	20	26	19	22	21	18	24	23	23	21	22	21	23	21	20	18	18	22
22	20	21	25	21	24	18	20	23	25	22	18	24	22	24	24	20	20	17	23
21	23	21	24	17	19	22	24	18	21	20	25	24	21	24	19	26	19	22	20
24	22	20	22	21	19	19	23	20	23	23	23	20	20	23	23	21	25	19	24
24	21	22	19	19	20	24	22	21	19	22	25	22	23	22	18	23	20	22	20

A.5.6 Sample Output Data from Program DIGCOR

23 19 23 22 21 16 18 21 22 24 17 20 21 23 19 23 20 21 20 24  
23 18 21 25 22 23 20 22 22 22 20 20 24 21 22 24 18 22 21 20  
20 19 22 23 21 20 22 22 22 22 20 23 18 26 20 25 19 23 23 22  
20 20 22 22 18 23 20 24 20 20 18 21 24 21 18 18 19 23 19 22  
21 20 24 19 23 20 24 20 20 22 23 21 21 24 20 22 18 24 21 20  
23 18 24 20 24 22 21 19 22 22 22 22 19 19 20 21 20 25 21 20  
24 19 19 21 22 21 19 18 25 22 23 23 20 23 25 20 18 26 19 16  
21 16 20 24 18 21 20 22 21 19 20 18 26 21 24 23 20 23 18 20  
20 19 22 21 18 19 22 23 23 20 22 19 25 21 24 24 22 20 20 24  
18 22 23 20 20 24 20 23 19 18 20 20 24 19 24 22 18 18 19 23  
22 21 19 22 21 24 20 22 21 23 22 20 23 22 24 19 23 19 21 21  
22 23 20 20 24 21 22 21 18 27 22 22 17 21 23 18 20 18 21 19  
23 23 23 19 24 20 17 21 19 21 20 24 20 22 22 21 21 19 20 23  
20 20 22 19 24 19 23 24 19 20 19 23 18 23 20 22 21 17 21 24  
21 20 23 21 22 23 23 20 19 19 20 25 21 24 18 21 17 21 22 19  
21 18 24 21 25 19 23 19 23 23 23 22 20 23 22 24 17 22 19 20  
27 19 20 23 23 23 22 19 25 21 24 20 22 20 20 24 21 26 17 22  
24 19 24 23 18 22 23 21 24 20 22 20 22 22 21 21 19 21 19 20  
23 21 21 23 20 20 22 24 20 23 19 19 24 21 22 24 21 19 15 23  
20 20 23 23 19 23 24 24 21 23 24 24 23 21 24 21 18 18 21 23  
23 23 20 18 21 23 19 20 17 24 20 23 18 22 23 22 24 20 19 22  
24 21 20 22 23 23 21 24 20 20 17 22 22 21 25 20 19 19 21 20  
22 24 23 25 23 18 20 24 21 25 19 24 22 20 24 20 21 19 21 21  
20 21 20 19 22 21 18 24 23 23 21 22 21 23 21 23 18 18 22 26  
22 20 21 21 24 18 20 23 25 22 18 24 22 24 24 20 20 17 23 25  
21 23 21 17 19 22 24 18 21 20 25 24 21 24 19 26 19 22 20 24  
24 22 20 21 19 19 23 20 23 23 23 20 20 23 23 21 25 19 24 22  
24 21 22 19 20 24 22 21 19 22 25 22 23 22 18 23 20 22 20 19  
23 22 20 17 21 23 19 20 19 24 20 23 18 17 23 22 20 23 23 21  
23 22 20 23 23 22 17 21 23 25 20 21 18 26 19 20 22 23 23 22

**APPENDIX B**  
**VECTOR PLOTS OF RESIDUAL ERRORS FROM THE**  
**CALIBRATION OF THERMAL VIDEO FRAME SCANNERS**

The error vectors resulting from the calibration of the four frame scanners were plotted using program PLOTDT4 as mentioned in Chapter VII. Those which are shown in this Appendix are for the cases where an improvement in the accuracy has occurred by adding a specific term to the polynomial equation. The vectors in these figures are 3X magnified.

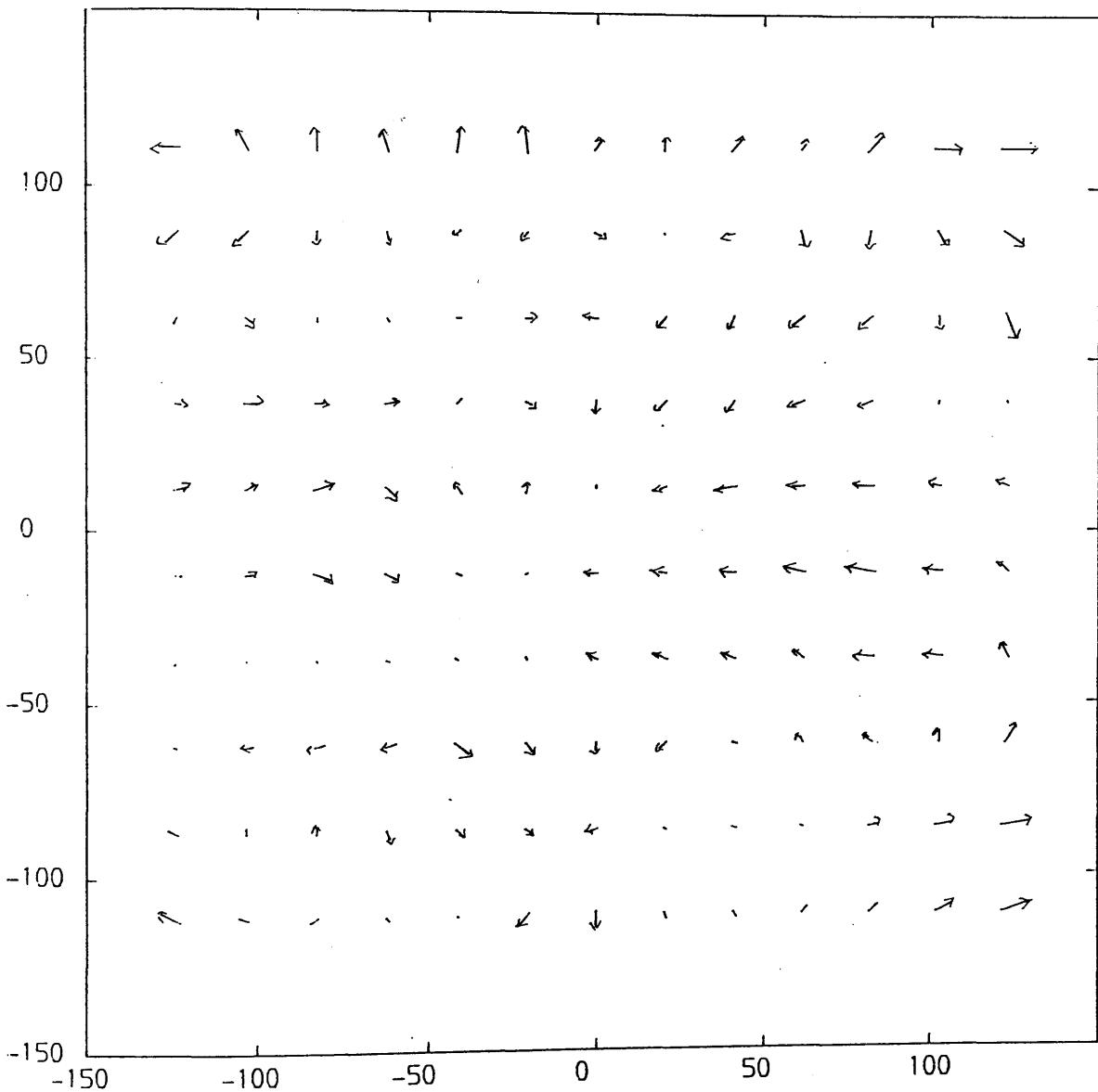


Fig.B-1 Vector plot of residual errors from the calibration of Barr & Stroud IR-18 frame scanner using affine transformation



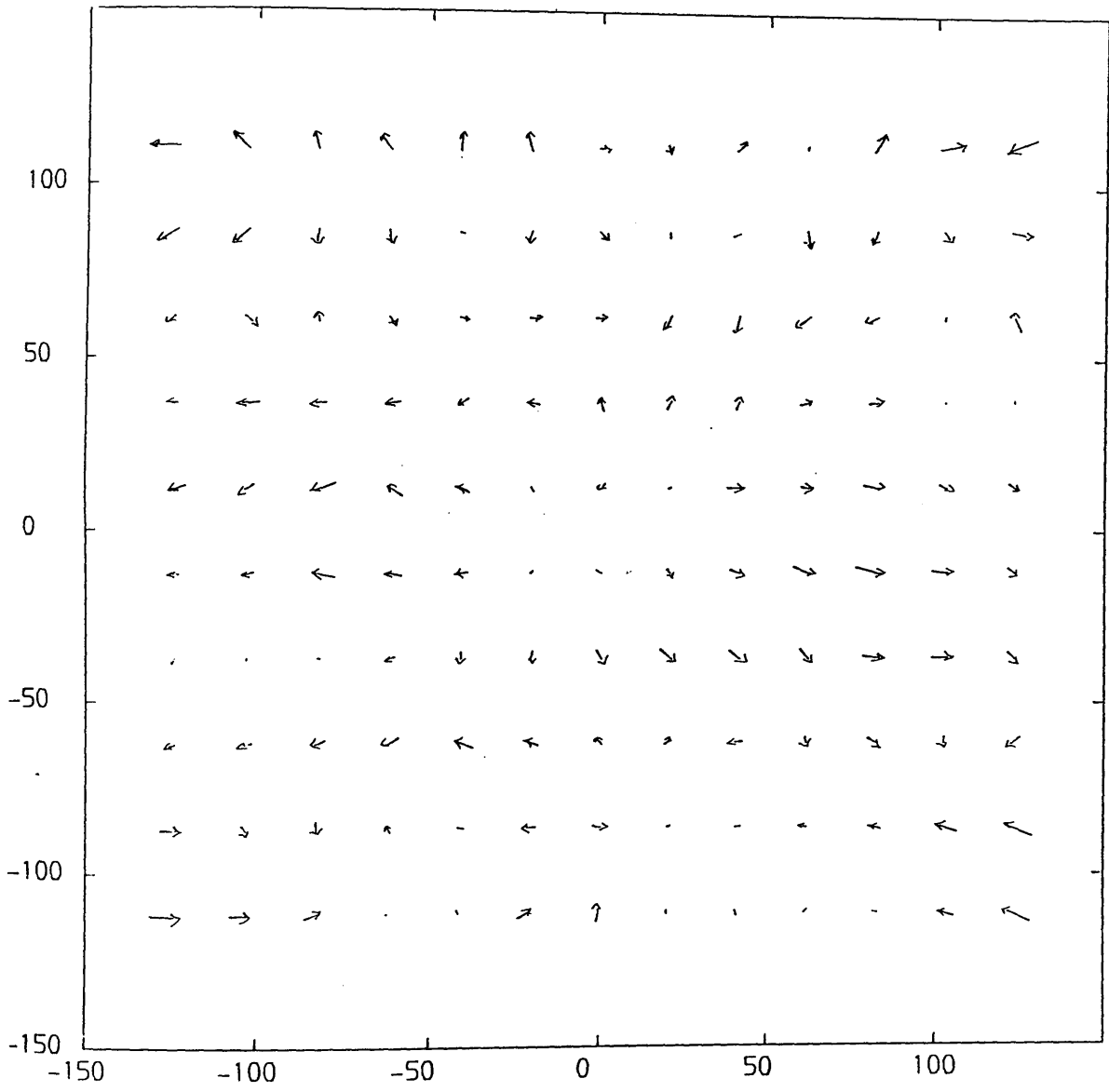


Fig.B-2 Vector plot of residual errors from the calibration of Barr & Stroud IR-18 frame scanner using 7-parameter polynomial transformation

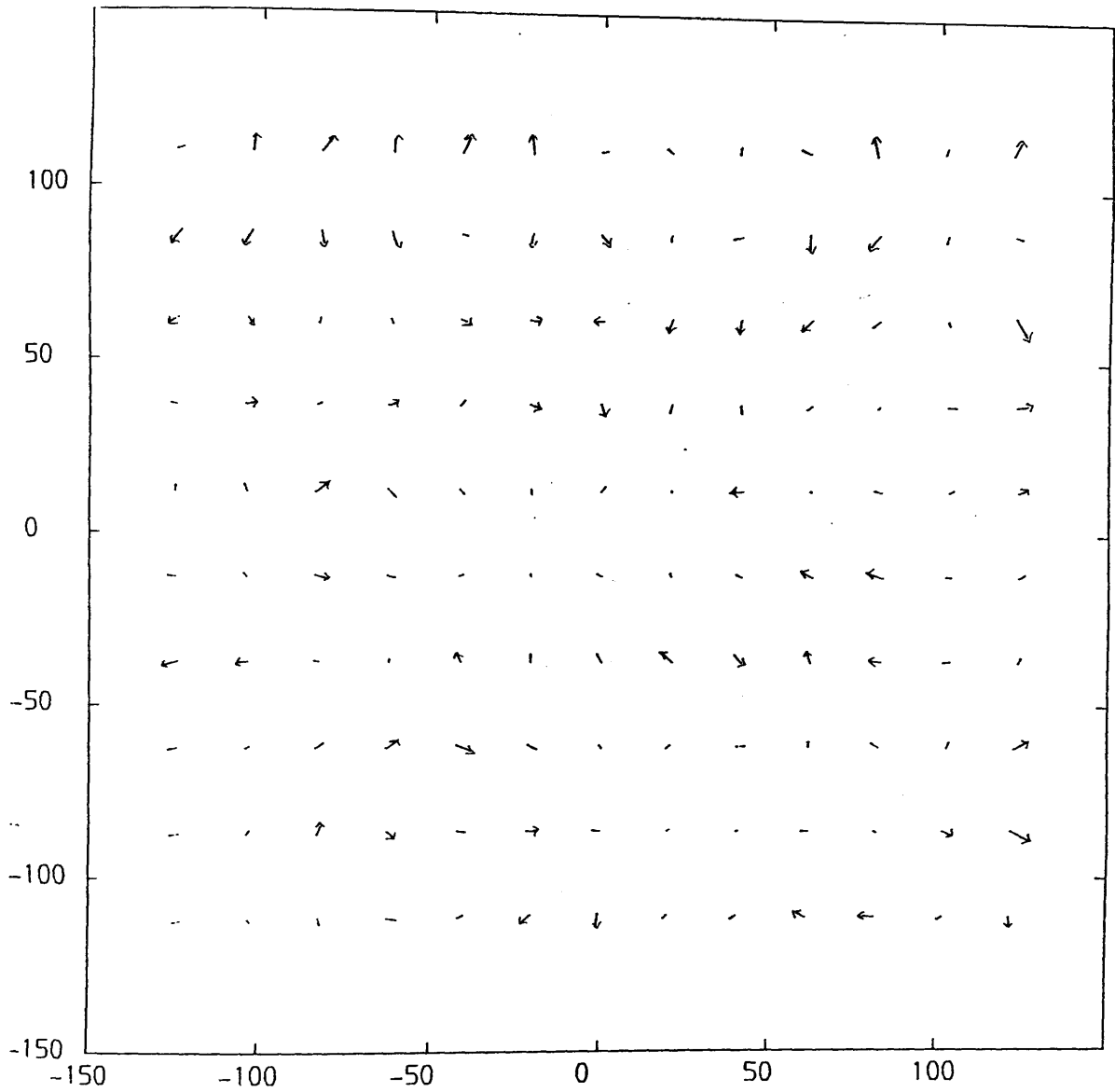


Fig.B-3 Vector plot of residual errors from the calibration of Barr & Stroud IR-18 frame scanner using 8-parameter polynomial transformation

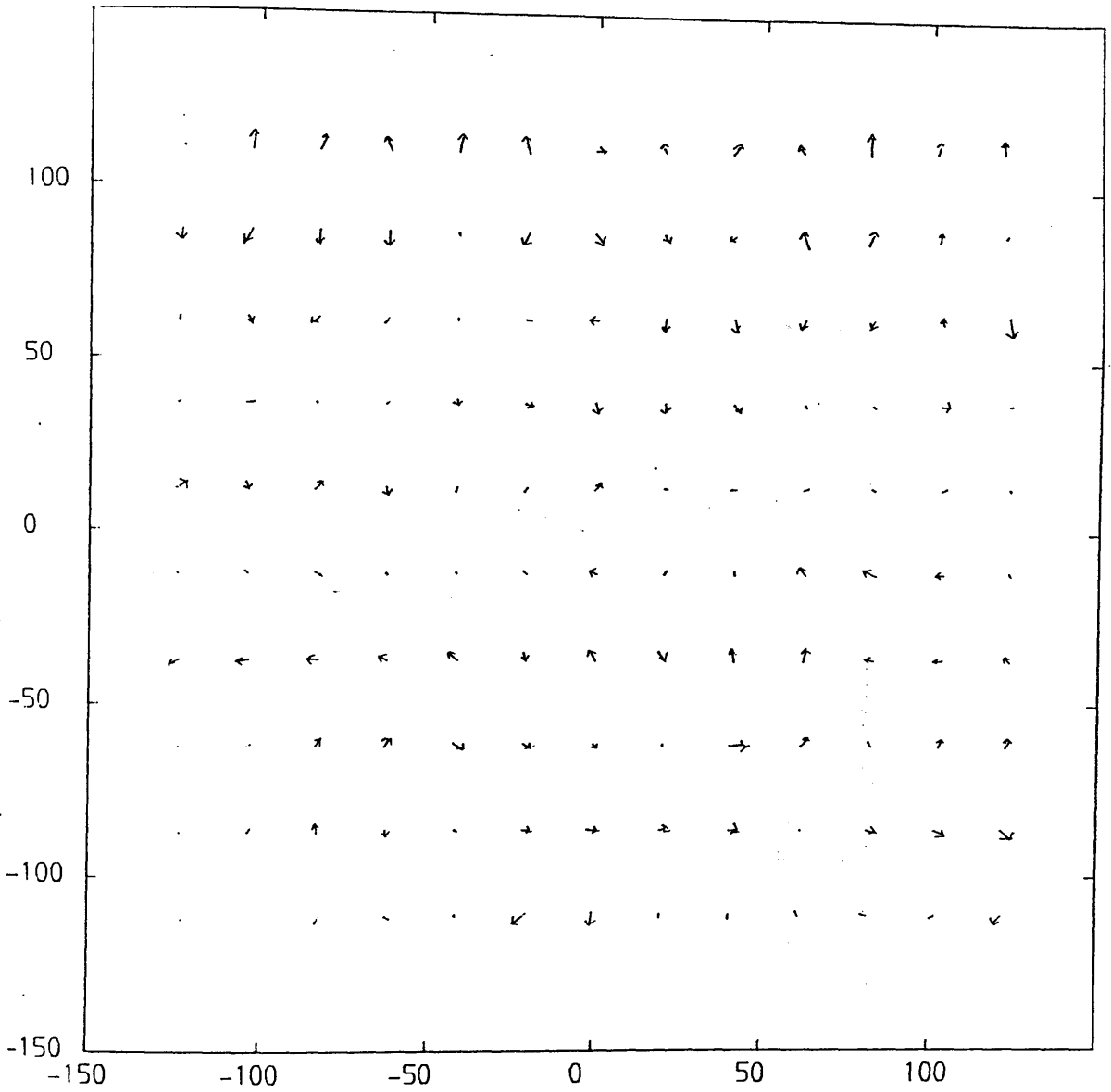


Fig.B-4 Vector plot of residual errors from the calibration of Barr & Stroud IR-18 frame scanner using 10-parameter polynomial transformation

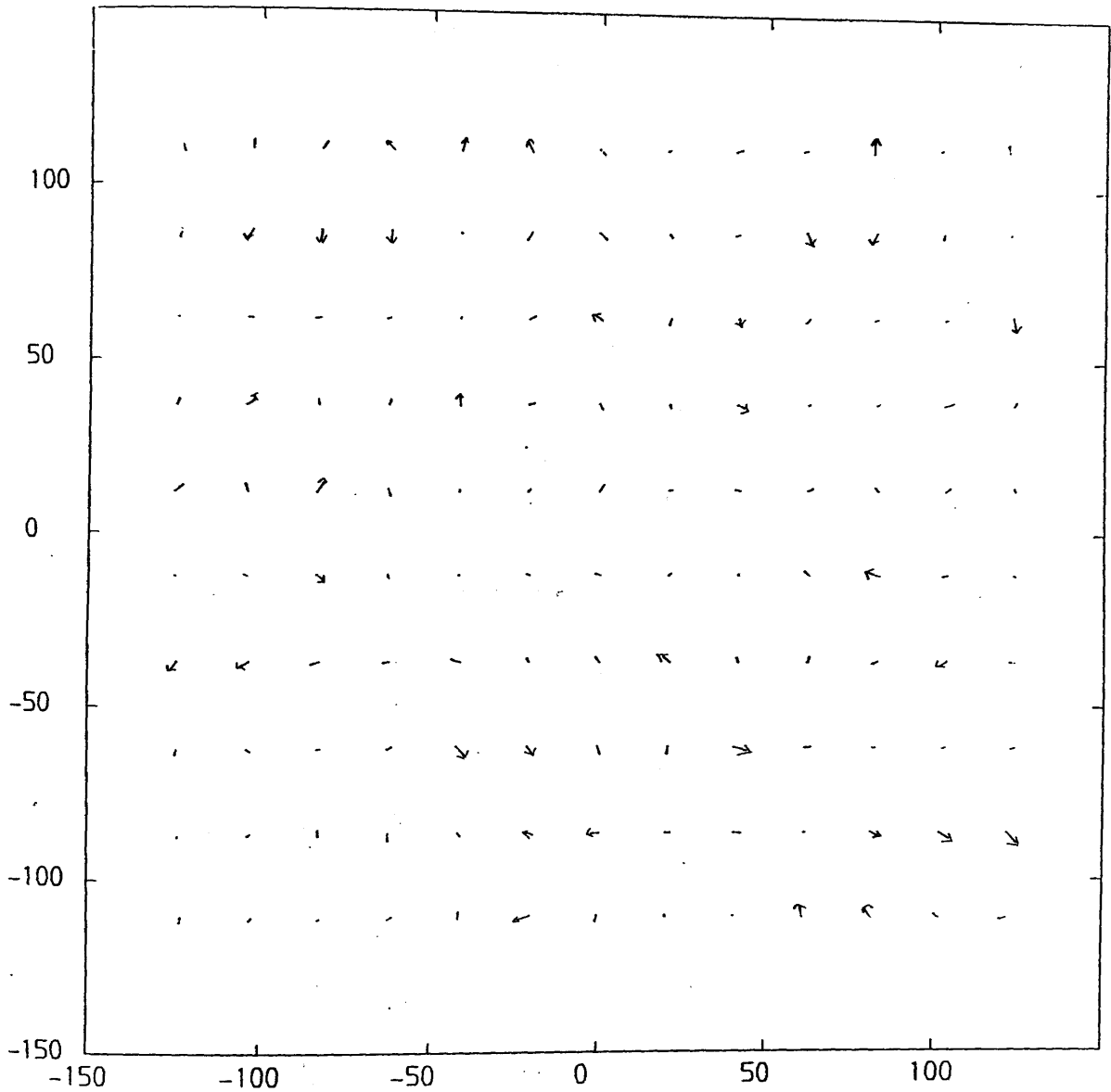


Fig.B-1 Vector plot of residual errors from the calibration of Barr & Stroud IR-18 frame scanner using 11-parameter polynomial transformation

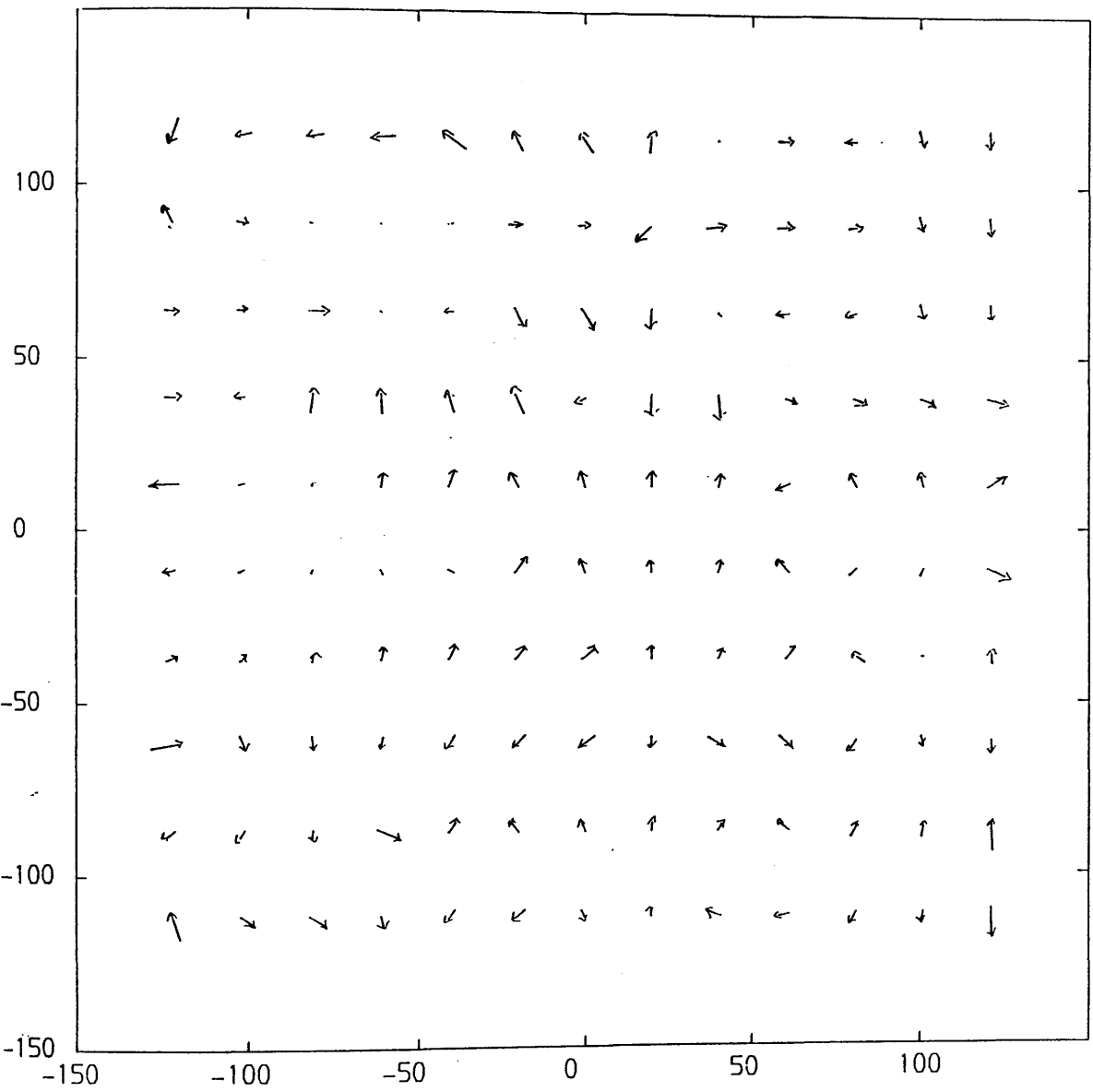


Fig.B-6 Vector plot of residual errors from the calibration of Rank Pullin Controls frame scanner using affine transformation

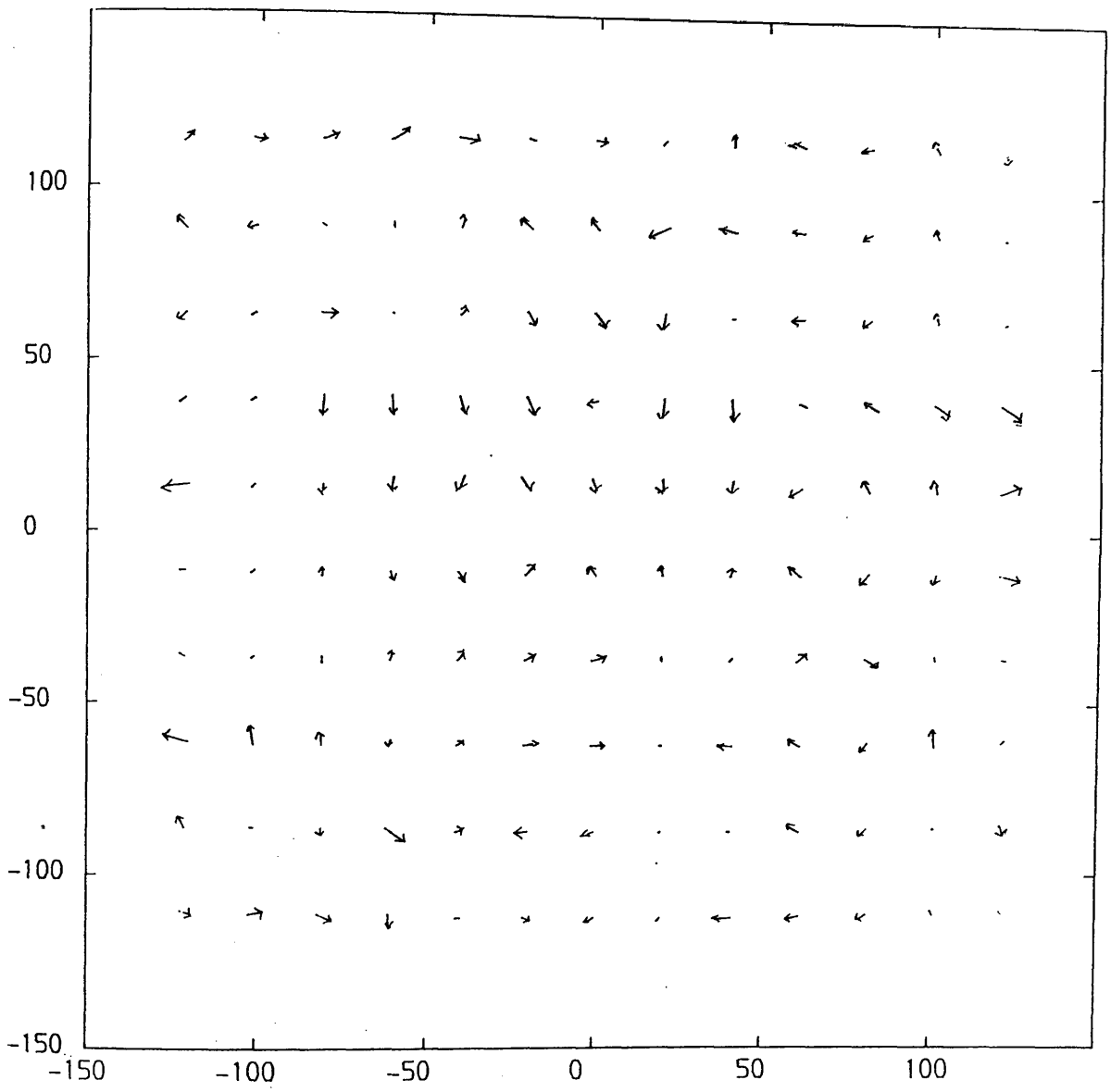


Fig.B-7 Vector plot of residual errors from the calibration of Rank Pullin Controls frame scanner using 7-parameter polynomial transformation

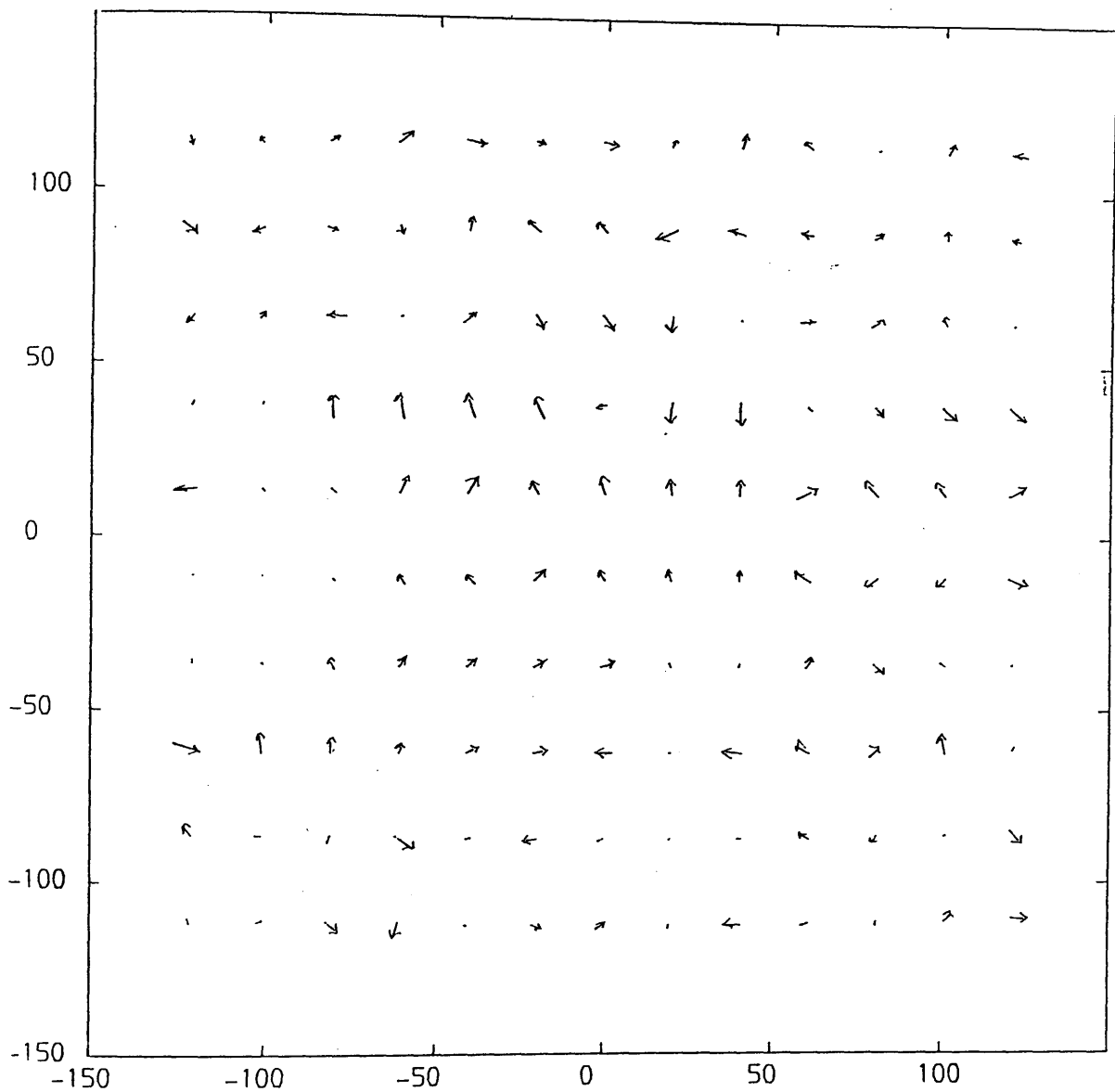


Fig.B-8 Vector plot of residual errors from the calibration of Rank Pullin Controls frame scanner using 8-parameter polynomial transformation

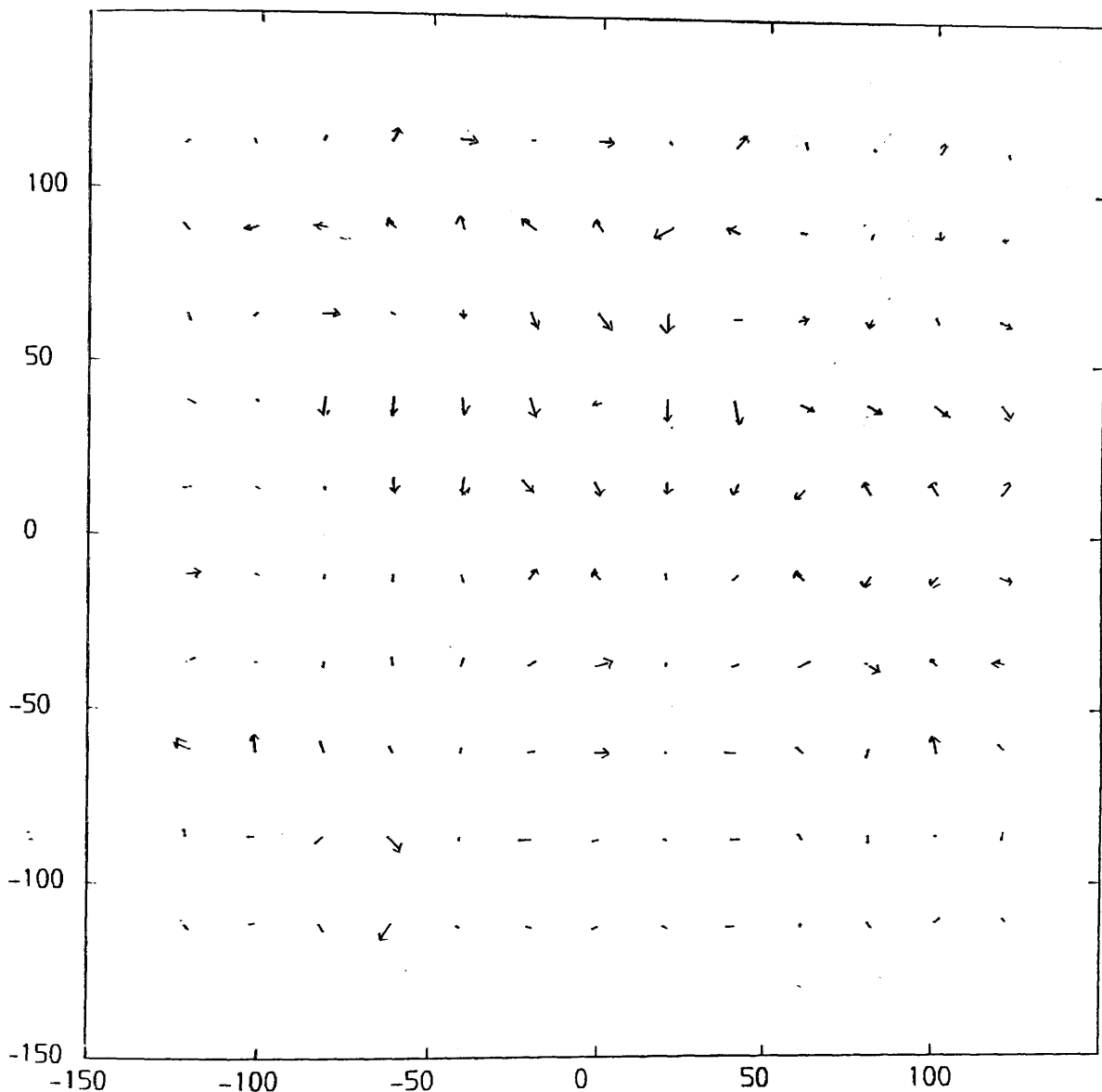


Fig.B-9 Vector plot of residual errors from the calibration of Rank Pullin Controls frame scanner using 10-parameter polynomial transformation



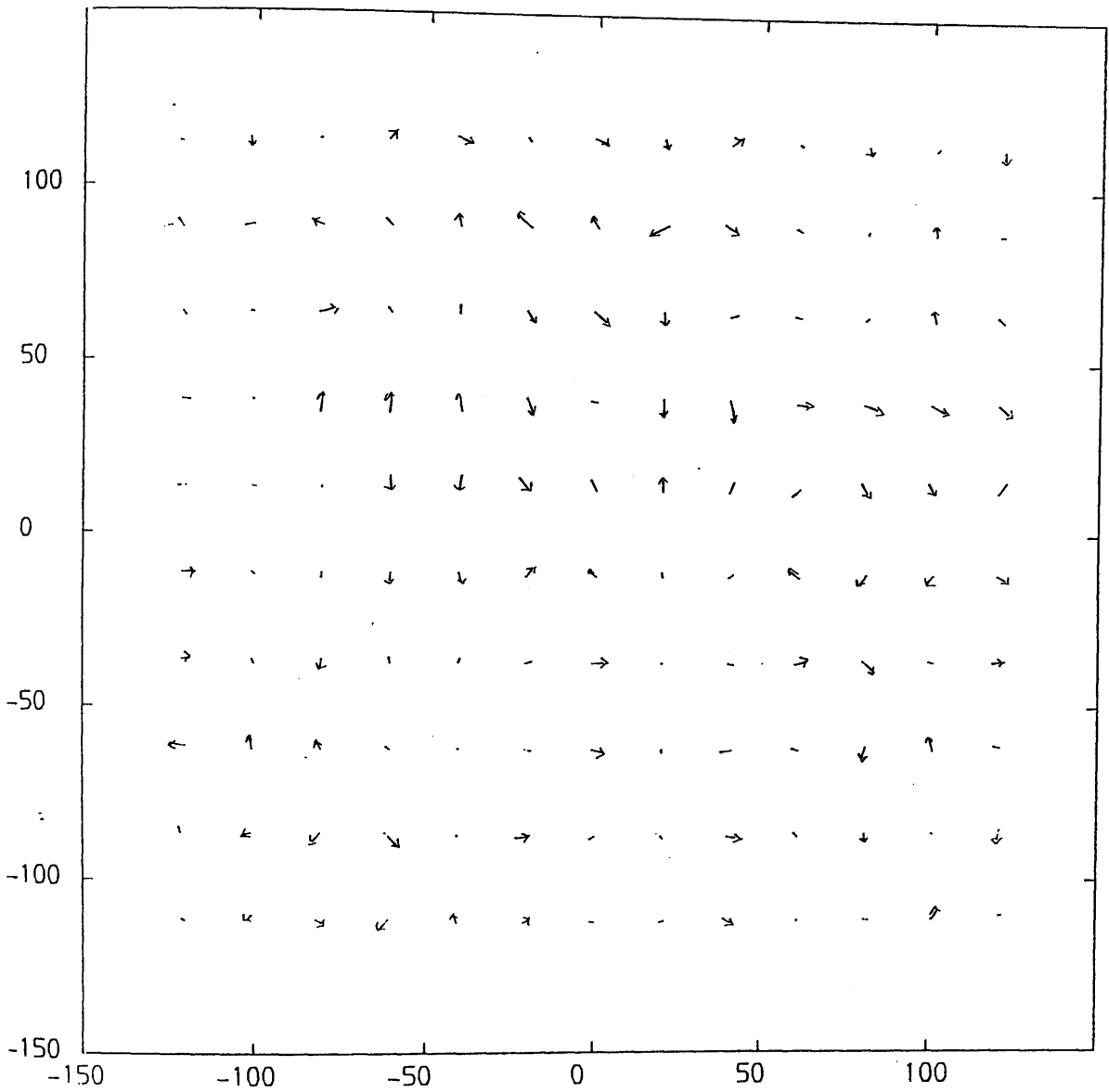


Fig.B-10 Vector plot of residual errors from the calibration of Rank Pullin Controls frame scanner using 11-parameter polynomial transformation

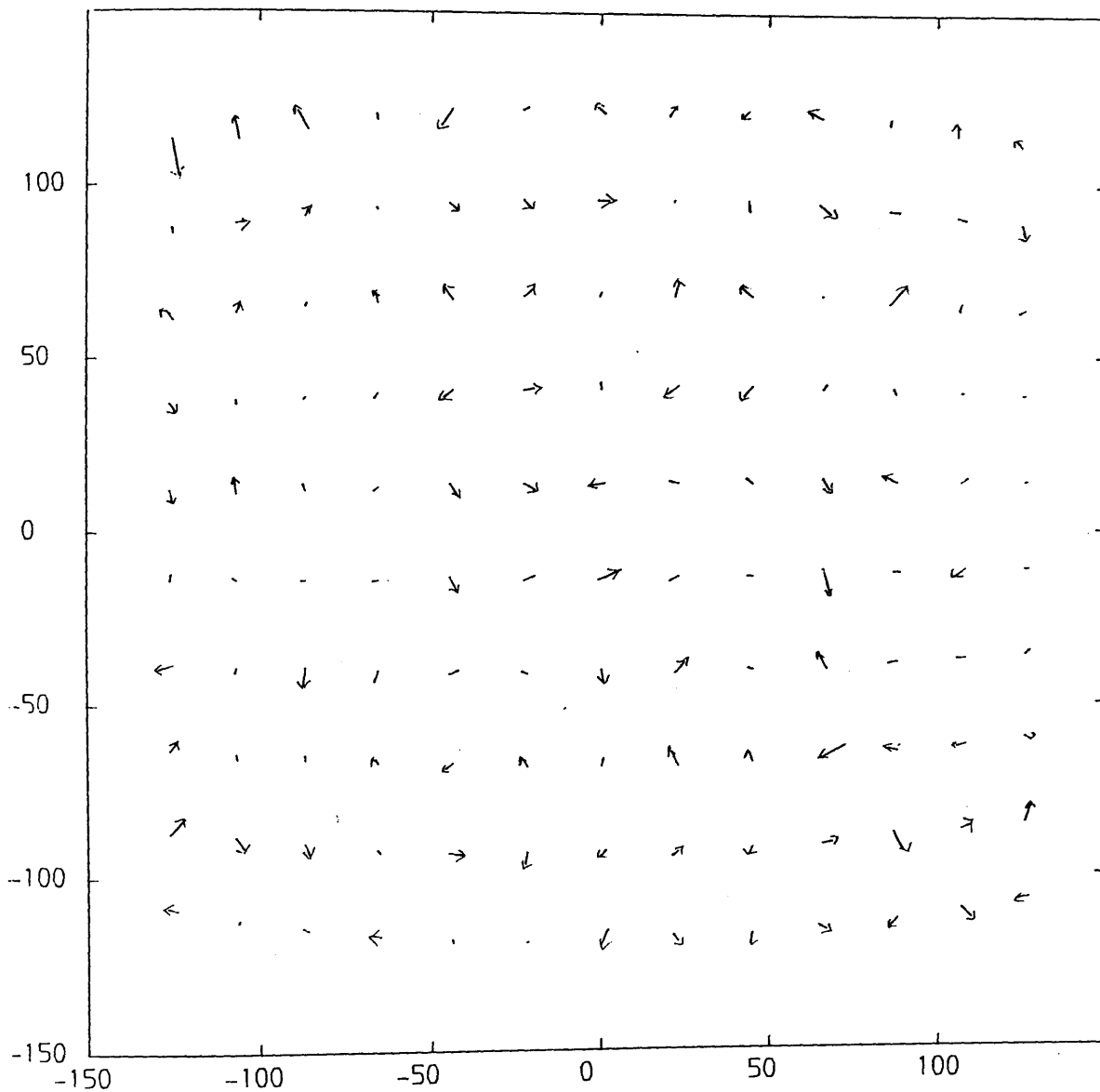


Fig.B-11 Vector plot of residual errors from the calibration of GEC Avionics/Rank Taylor Hobson (TICM II) frame scanner using affine transformation

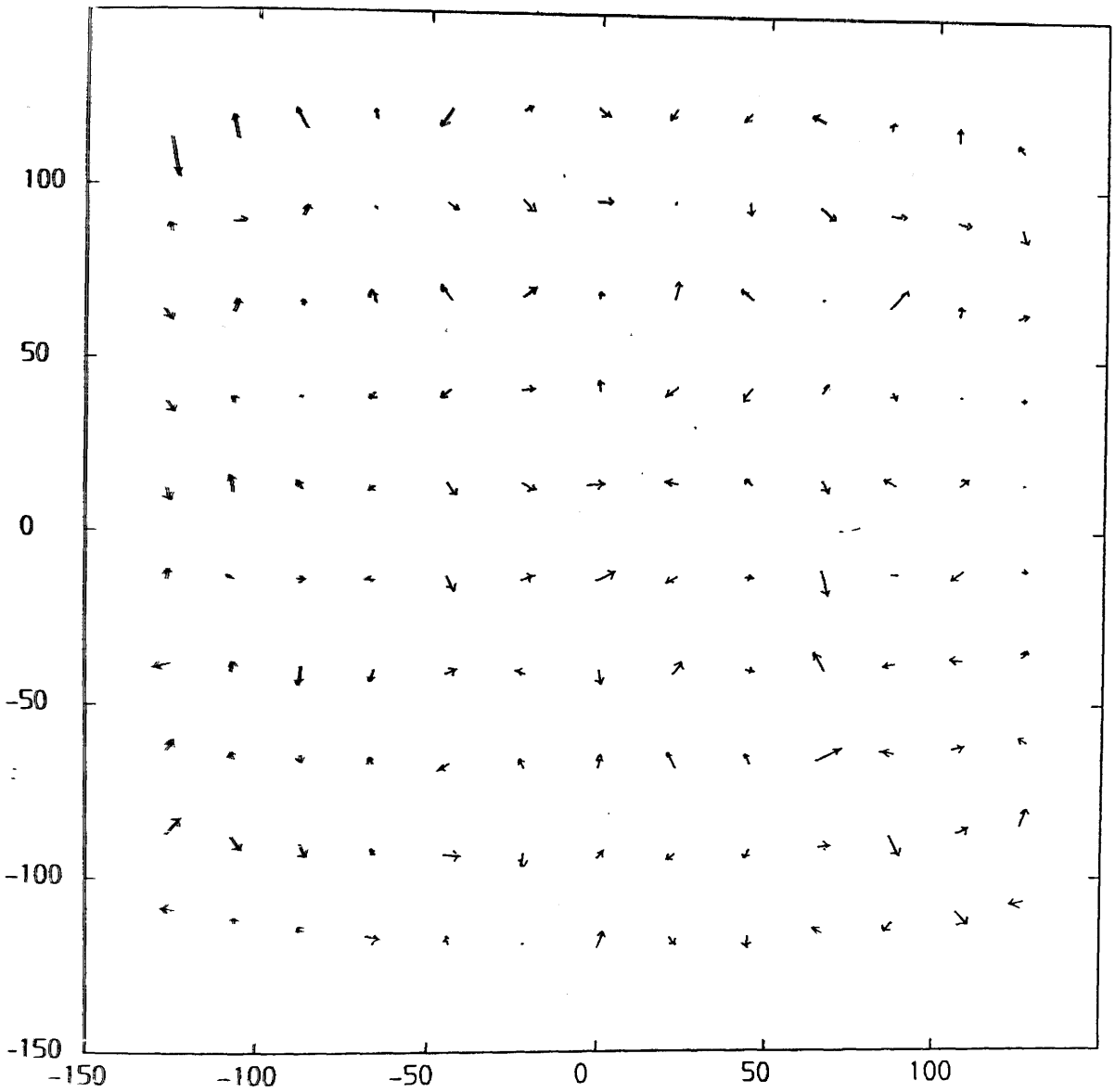
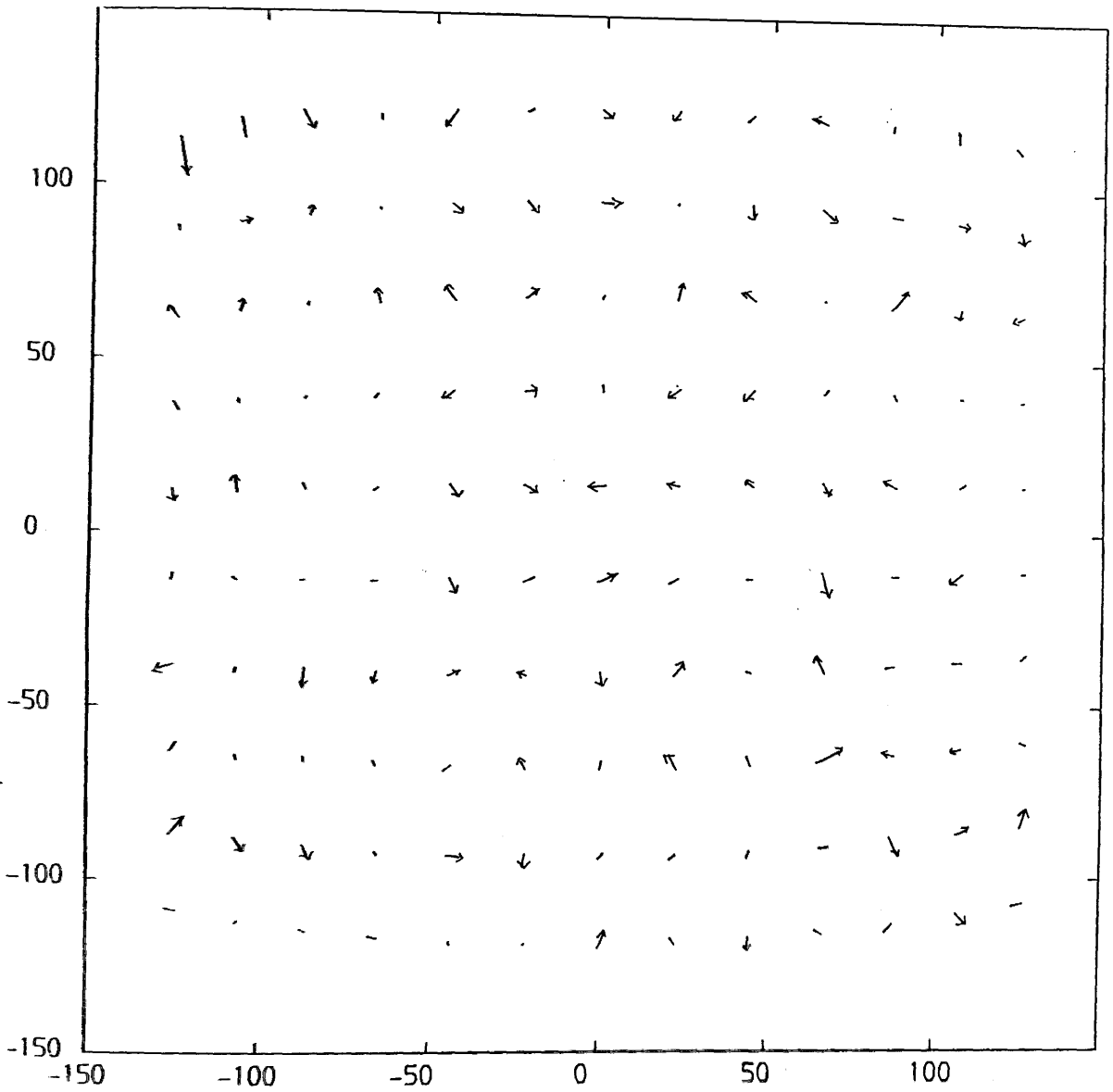


Fig.B-12 Vector plot of residual errors from the calibration of GEC Avionics/Rank Taylor Hobson (TICM II) frame scanner using 7-parameter polynomial transformation



**Fig.B-13 Vector plot of residual errors from the calibration of GEC Avionics/Rank Taylor Hobson (TICM II)frame scanner using 8-parameter polynomial transformation**

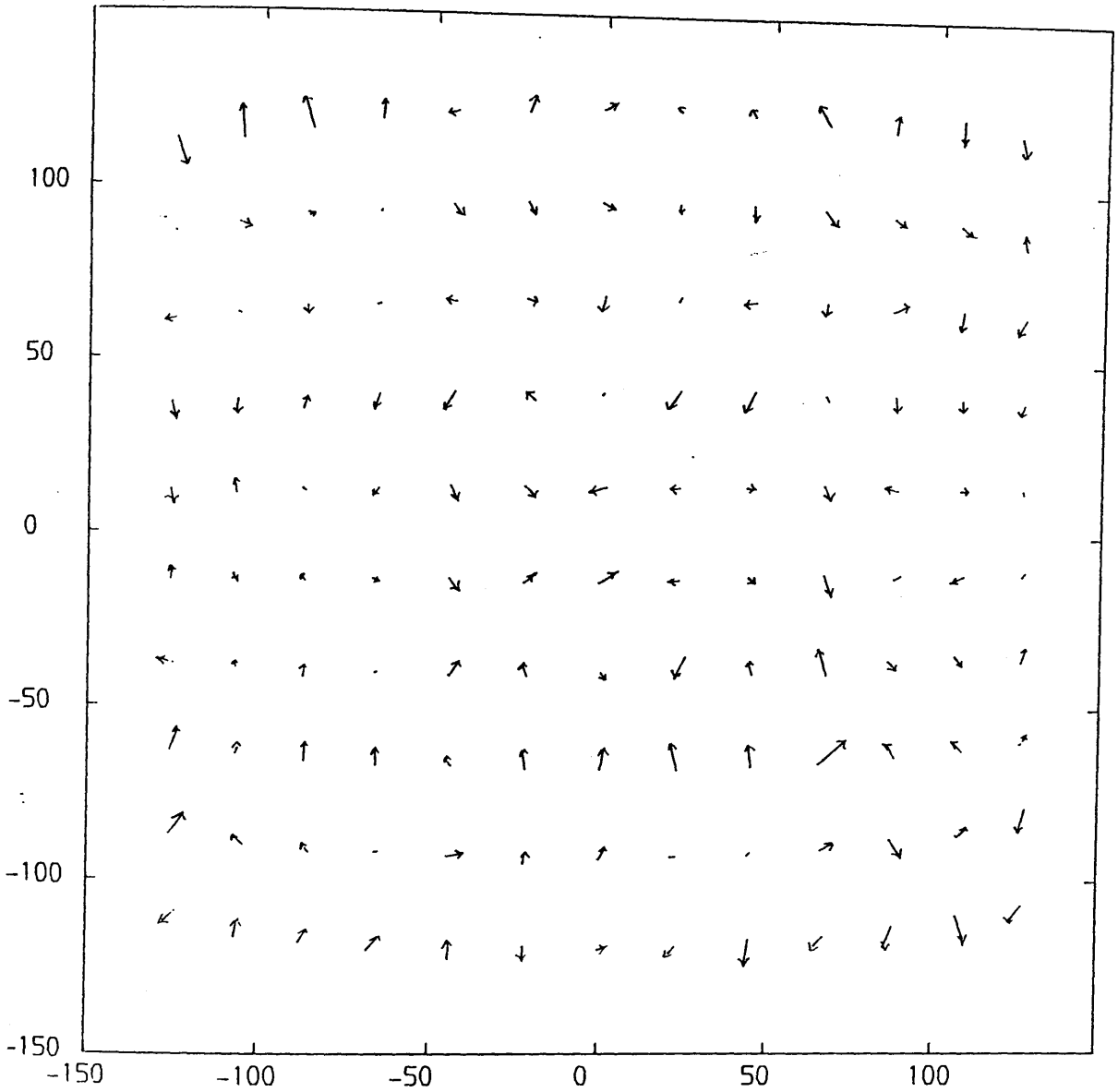


Fig.B-14 Vector plot of residual errors from the calibration of GEC Avionics/Rank Taylor Hobson (TICM II) frame scanner using 10-parameter polynomial transformation

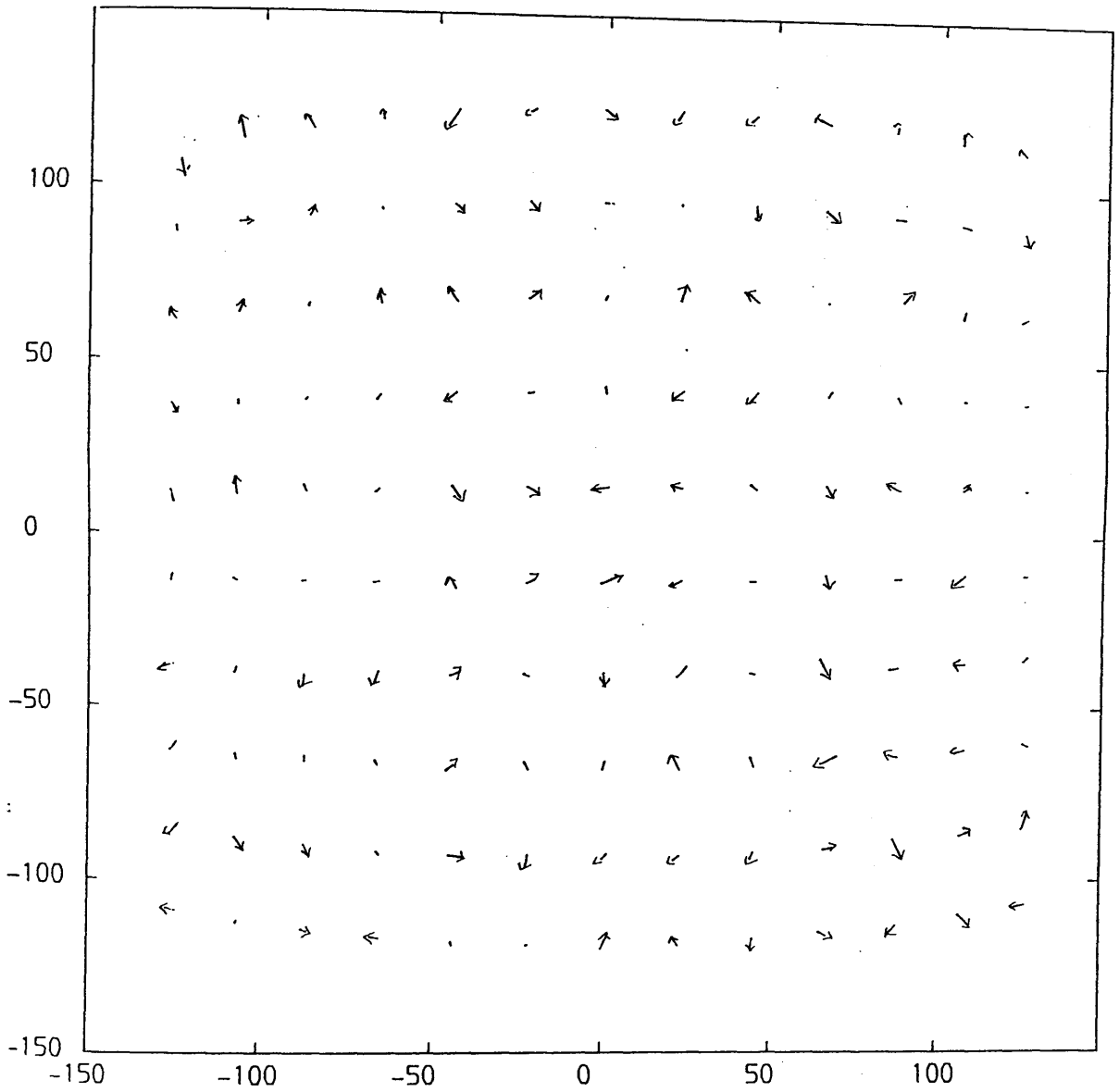


Fig.B-15 Vector plot of residual errors from the calibration of GEC Avionics/Rank Taylor Hobson (TICM II) frame scanner using 11-parameter polynomial transformation

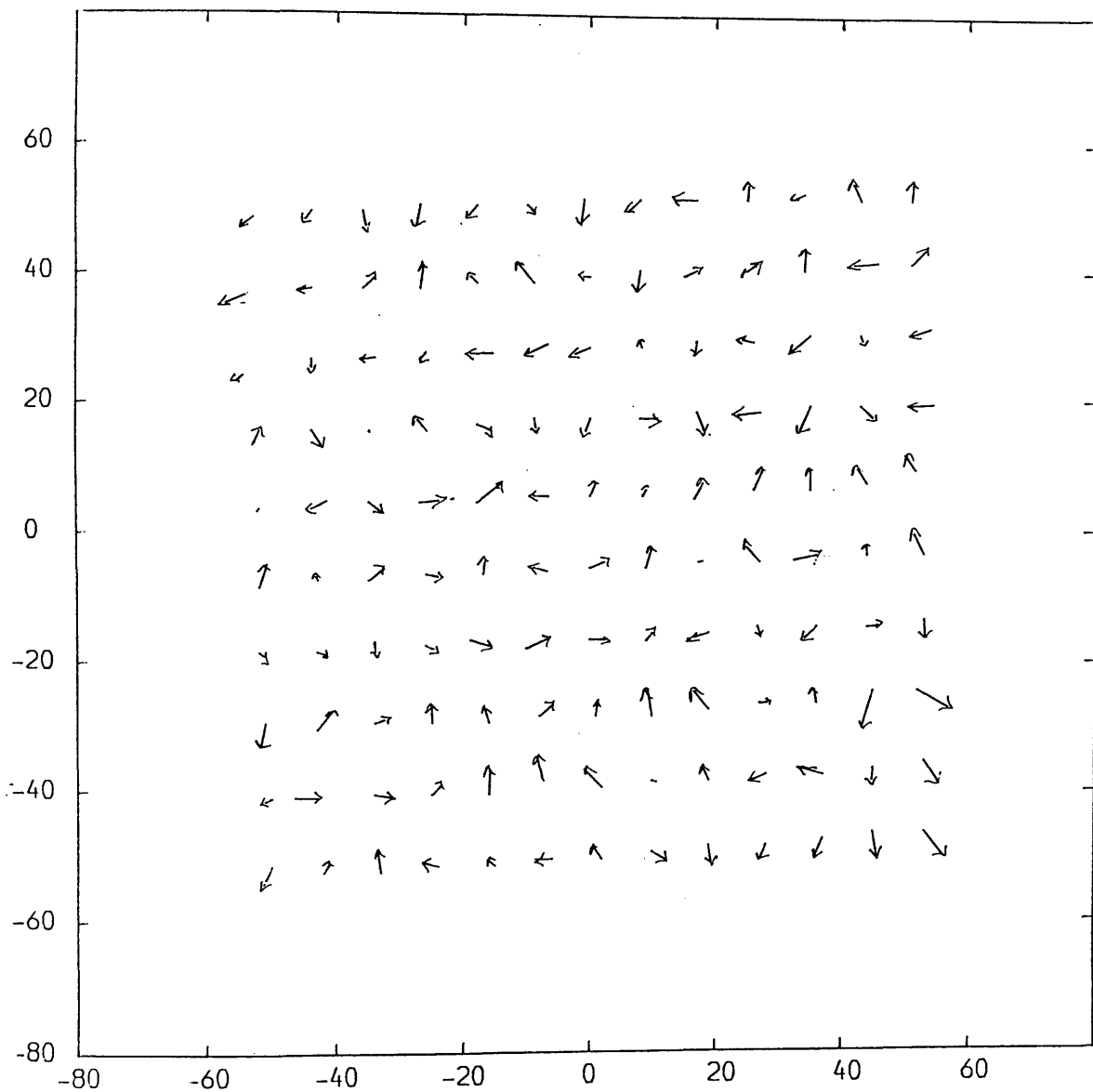


Fig.B-16 Vector plot of residual errors from the calibration of AGA Thermovision frame scanner using affine transformation

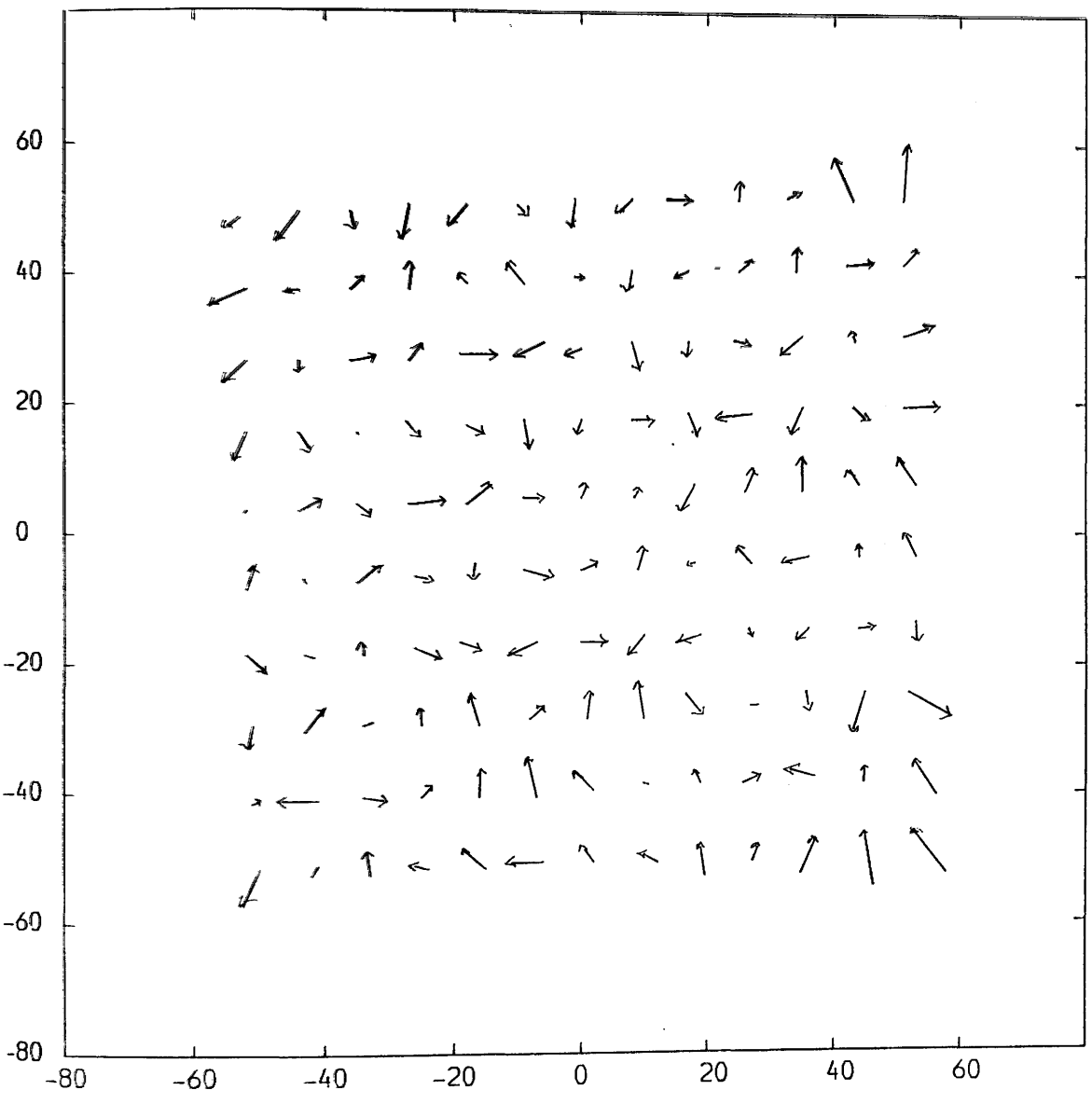


Fig.B-17 Vector plot of residual errors from the calibration of AGA Thermovision frame scanner using 7- parameter polynomial transformation



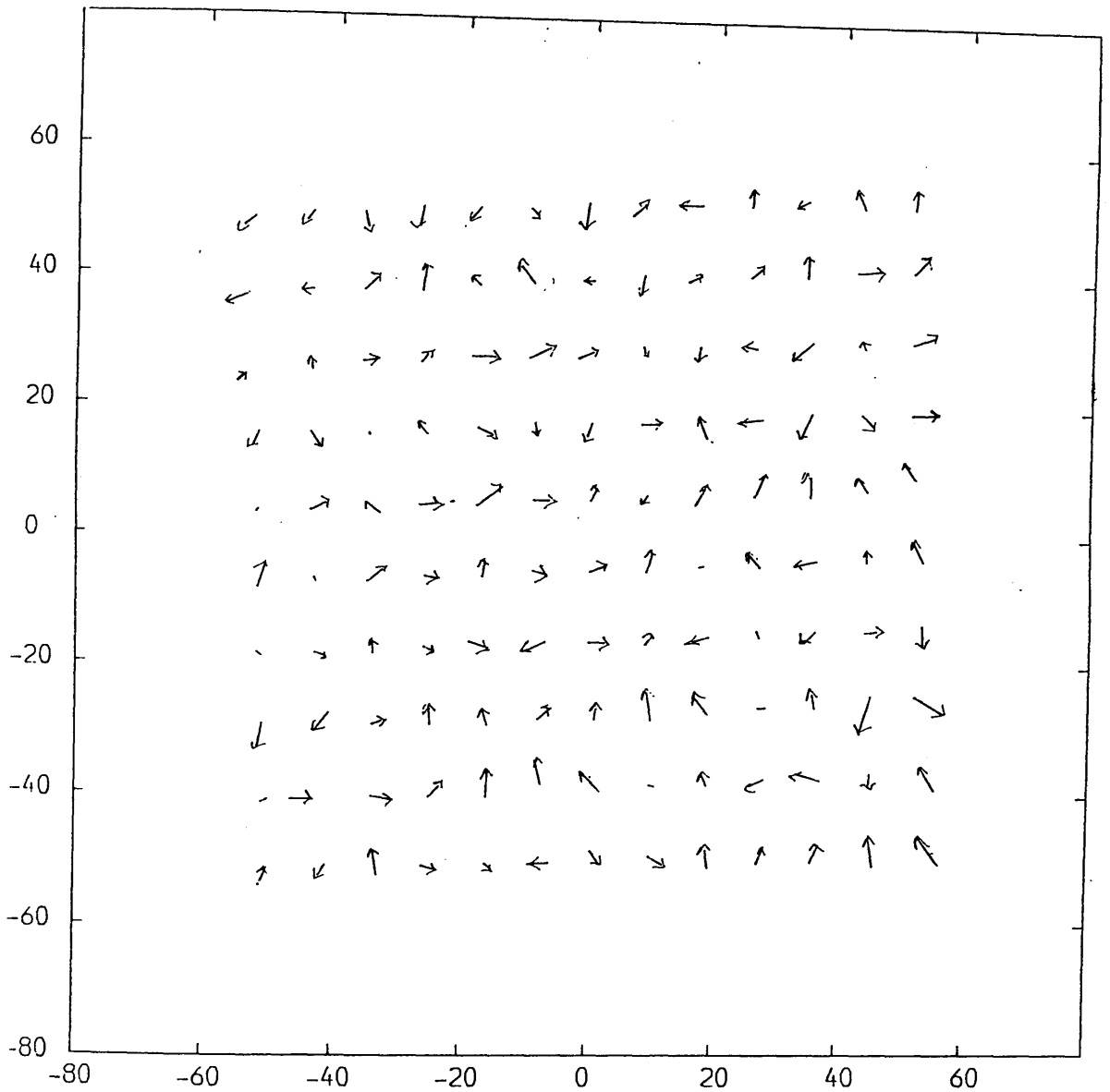


Fig.B-18 Vector plot of residual errors from the calibration of AGA Thermovision frame scanner using 8-parameter polynomial transformation

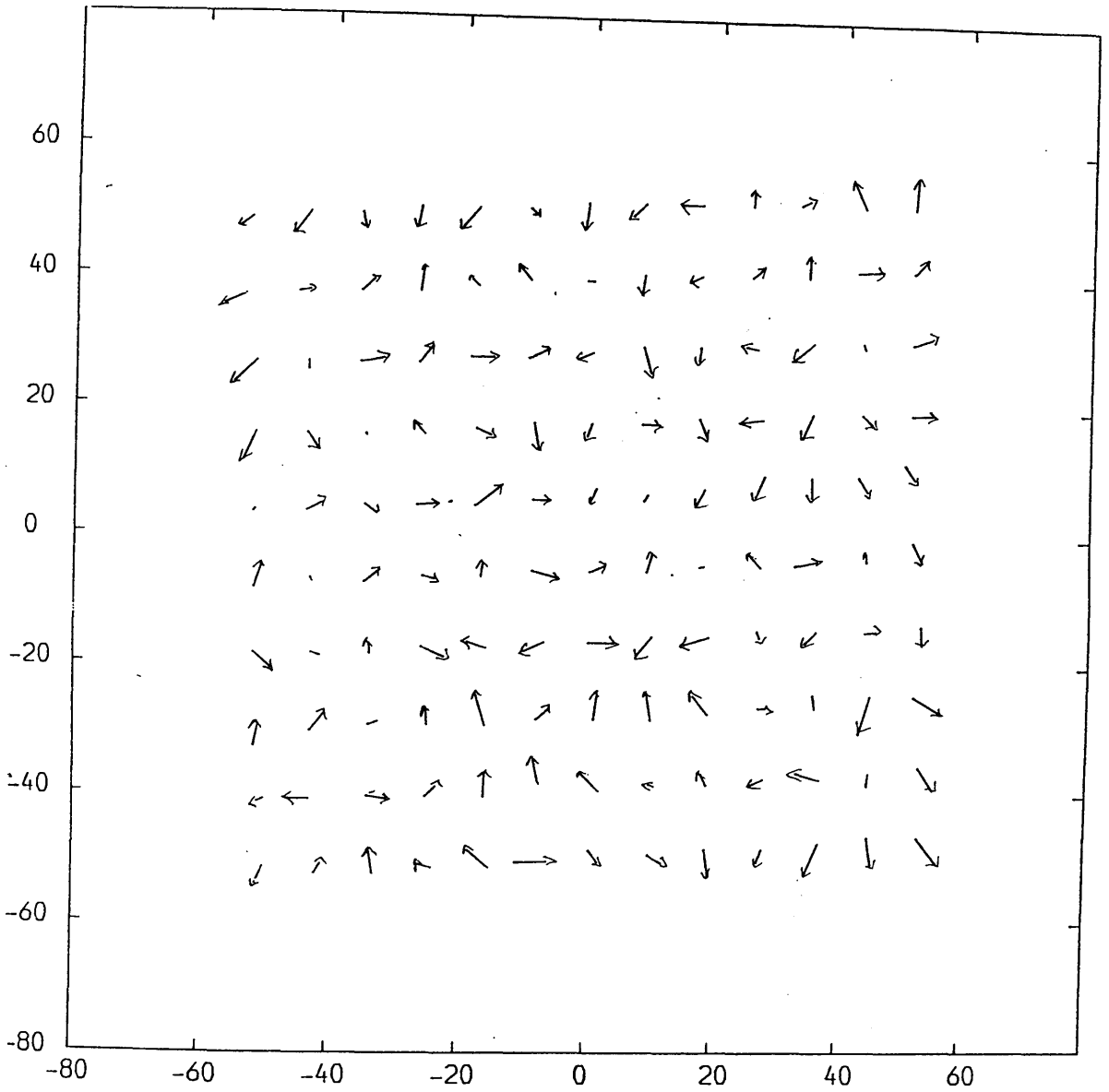


Fig.B-19 Vector plot of residual errors from the calibration of AGA Thermovision frame scanner using 10-parameter polynomial transformation

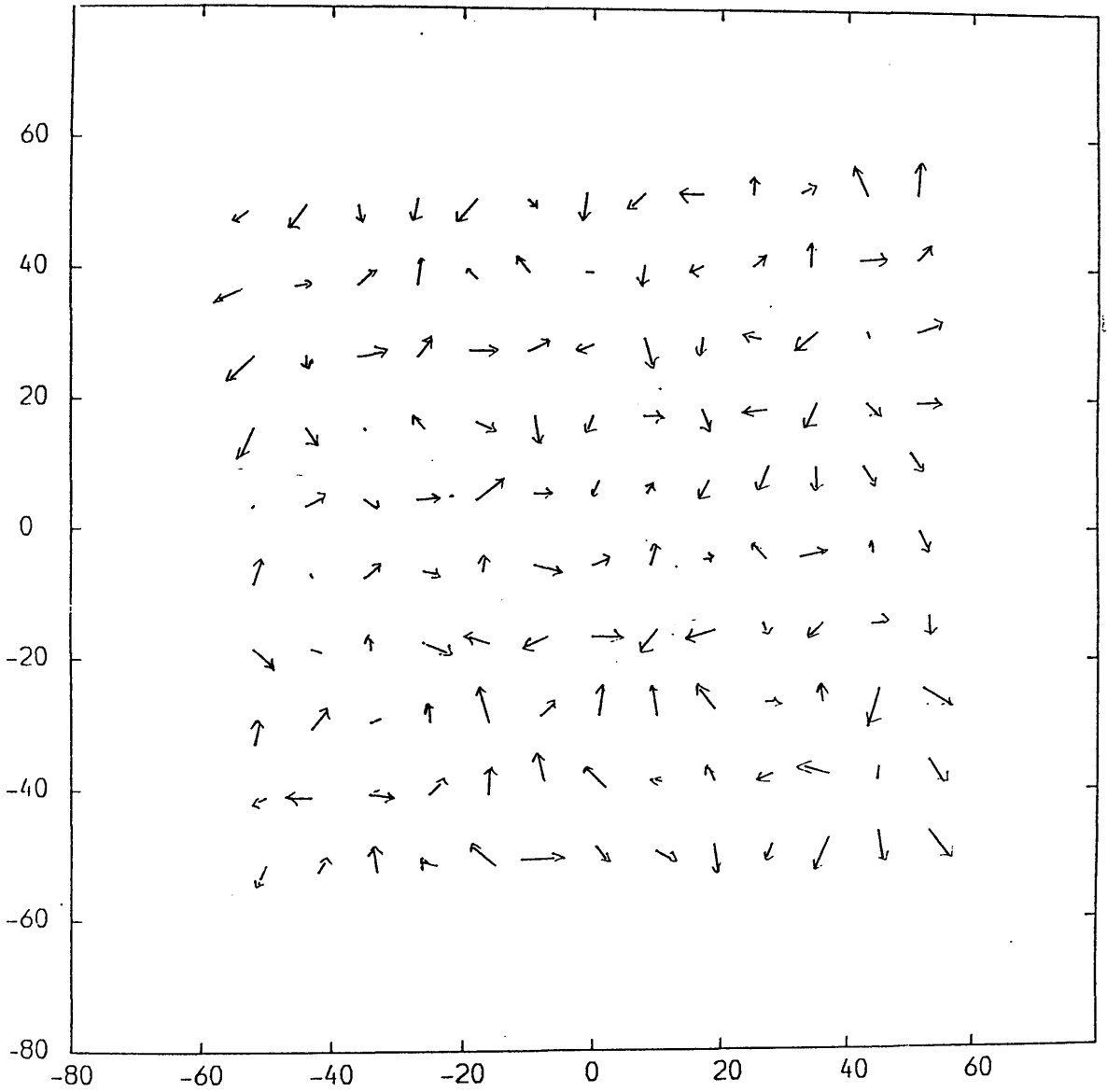


Fig.B-20 Vector plot of residual errors from the calibration of AGA Thermovision frame scanner using 11-parameter polynomial transformation